
Design and Synthesis of Purely Organic Chromophores for Ambient Triplet Harvesting

A Thesis

Submitted for the Degree of

Doctor of Philosophy

By

SUMAN KUILA



New Chemistry Unit

Jawaharlal Nehru Centre for Advanced Scientific Research

(A Deemed University)

Bangalore - 560064 (INDIA)

JULY 2020

Design and Synthesis of Purely Organic Chromophores for Ambient Triplet Harvesting

A Thesis

Submitted for the Degree of

Doctor of Philosophy

By

SUMAN KUILA

UNDER THE SUPERVISION OF

Dr. SUBI J. GEORGE

New Chemistry Unit

Jawaharlal Nehru Centre for Advanced Scientific Research

(A Deemed University)

Bangalore-560064 (INDIA)

JULY 2020

To My Family and Aishu

DECLARATION

I hereby declare that the thesis entitled “*Design and Synthesis of Purely Organic Chromophores for Ambient Triplet Harvesting*” is an authentic record of research work carried out by me at the New Chemistry Unit, Jawaharlal Nehru Centre for Advanced Scientific Research, Bangalore, India under the supervision of **Prof. Subi J. George** and that it has not been submitted elsewhere for the award of any degree or diploma.

In keeping with the general practice in reporting scientific observations, due acknowledgment has been made whenever the work described is based on the findings of other investigators. Any omission that might have occurred due to oversight or error in judgment is regretted.

Suman Kuila

Suman Kuila



**Jawaharlal Nehru Centre for
Advanced Scientific Research**

Dr. Subi J. George
New Chemistry Unit
Jawaharlal Nehru Centre for Advanced
Scientific Research (JNCASR)
Bangalore-560064, India
Phone : +91 80 2208 2964
Fax: + 91 80 22082627
E-mail: george@jncasr.ac.in

Date

December 26, 2020

CERTIFICATE

I hereby certify that the work described in this thesis titled “**Design and Synthesis of Purely Organic Chromophores for Ambient Triplet Harvesting**” has been carried out by **Suman Kuila** at the New Chemistry Unit, Jawaharlal Nehru Centre for Advanced Scientific Research, Bangalore, India under my supervision and it has not been submitted elsewhere for the award of any degree or diploma.

Prof. Subi J. George
(Research Supervisor)

ACKNOWLEDGEMENTS

*First and foremost, I would like to thank my research supervisor **Dr. Subi J. George** for his constant guidance, encouragement and support, leading to the successful completion of this work.*

*I would like to express my sincere gratitude to **Prof. C. N. R. Rao, FRS** for being a constant source of inspiration and providing necessary facilities for carrying out this work.*

I am thankful to all the faculty members of NCU for their guidance and support. I have also received immense support from all the present and past Presidents, JNCASR, which I gratefully acknowledge.

It is a great pleasure to thank all my collaborators: Prof. K. S. Narayan and his students; Dr. Prashant and Anaranya -CPMU Prof. M. Eswaramoorthy and his students; Dr. Amrit -CPMU Prof. S. K. Pati and his students; Dr. Pralok, Dr. Shubhajit and Bidhan -TSU. Prof. S. Peter and his student; Dr. Soumyabrata -NCU. Prof. Dinesh Kabra and his student; Gangadhar -IITB. Prof. Jyotishman Dasgupta and his student; Arup-TIFR-Mumbai, for fruitful collaborations.

I am thankful to Prof. Subi J. George, Prof. Sridhar Rajaram and all the other NCU faculty members from JNCASR and, Dr. Mahavir Singh and Prof. Siddharth P. Sharma from IISc for their coursework.

I express my sincere thanks to all my teachers, especially Prof M. Periyasamy from School of Chemistry, University of Hyderabad and Mr. Kaushik Basu from St. Paul's College, Calcutta for their encouragement at various stages of my academic career. I am grateful to all my present and past lab members, The SupraChem Group (Dr. Venkat, Dr. Mohit, Dr. Ankit, Dr. Chidambar, Dr. Bhawani, Dr. Krishnendu, Dr. Ananya, Dr. Shikha, Aritra, Swadhin, Souvik, Angshuman, Satyajit, Darshana, Anjali, Jagannath, Dr. Srinu, Akhil, Dr. Chandan Giri, Dr. Raja Siram, Dr. Kamna, Dr. Surbhi, Dr. Rita, Dr. Meenal) for their support at various levels and creating a joyful atmosphere in the lab. I am grateful to SRFP/POCE students: Shiva, Raushan, Sayantani, Tarun, Writam and Ankita for working with me on various projects.

I want to express my gratitude to Prof. Andrew P. Monkman, Prof. Fernando B. Dias and Dr. Marc K. Etherington (Durham University, UK) for useful discussions and their guidance.

I am thankful to the following people for timely assistance in various measurements: Prof. Ranjani V., Kushagra and Pradeep (lifetime); Mrs. Usha (TEM), Mr. Anil (XRD); Mr. Mahesh (NMR); Dr. Amrit and Dr. Sonu (DLS); Mr. Shivkumar (HRMS and MALDI); Dr. Sashidhara, Mr. Athul and Mrs. Gayathri (PL measurements in Edinburgh Instrument). I am thankful to academic and administrative staff of JNCASR for their assistance.

I thank all my friends Sudip, Viveka, Sarika, Shree, Mandar, Srinu, Bijit, Jyotirmoy, The Mad Folks group of NVSH and all other friends of JNCASR.

Besides the research life, I am thankful to Prof. Subi J. George and his family members for their hospitality and affection.

I am deeply grateful to my parents, sister (Sneha) and Aishwariya for their support, love and affection throughout this journey.

Financial assistance from University Grants Commission (UGC), India and Department of Science and Technology (DST), Government of India is gratefully acknowledged.

Suman

Preface

This thesis presents novel design strategies and synthesis of metal-free organic chromophores for triplet state emission via room temperature phosphorescence (RTP) and thermally activated delayed fluorescence (TADF).

The thesis is divided into six major chapters.

Chapter-1 is an introduction to the field summarizing the strategies employed in harvesting the triplet state excitons of organic chromophores (e. g. RTP and TADF) and their important applications in modern lighting devices. Along with that, a general outline of the methods (design principles) used in order to stabilize the triplet excitons to obtain efficient RTP and TADF under ambient conditions is discussed in the context of the present thesis.

Part-A deals with the direct transition from an excited triplet state to ground singlet state as room temperature phosphorescence (RTP).

In **chapter-2**, we have utilized a simple crystalline chromophore, carbazole, and introduced heavy-atoms like Bromine (Br) in order to enhance spin-orbit coupling (SOC). Although carbazole is well studied for its strong excimer “fluorescence” emission, with this “heavy-atom effect” strategy we have been successful to achieve strong red-emitting RTP with quantum yield ~15 % in air.

In **chapter-3**, we moved towards developing methods for organic long persistent luminescence (OLPL) under air- and solution-processed thin films. Here, we utilized polyvinyl alcohol as a rigid host which accommodates metal-free organic phosphors via non-covalent interactions e. g. H-bonding or ion-dipole interactions and reduces the aggregation caused quenching as well as vibrational dissipations. These materials are shown to show strong blue, greenish yellow and even white long-persistent phosphorescence with quantum yield over 20 % in air with lifetime up to 2.5 s. Further a unique “phosphorescence energy transfer strategy” has been applied which has never been done for any metal-free organic systems, for color-tunable “delayed fluorescence” from commercially available dyes like Sulpharhodamine G.

In **chapter-4**, we solved a long-standing problem of “solution-state” room temperature phosphorescence by a novel organic-inorganic hybrid self-assembly approach. Here, inorganic nanoparticles (LP) are shown to form rigid supramolecular microenvironment with charged organic chromophores having aromatic carbonyl groups and bromine atoms in their core. These functional groups provide a good excited triplet yield via efficient SOC and stabilized by the reduced vibrational motion of the rigid organic-inorganic supramolecular network and limited oxygen permeability.

Part-B deals with the strategy of harvesting excited triplet states *indirectly* via a reverse intersystem crossing process to result in thermally activated delayed fluorescence (TADF).

In **chapter-5**, we have utilized a donor-acceptor, charge-transfer molecular design strategy to tune the excited singlet and triplet energy gap (a newly developing field of research) for harvesting triplet excitons via delayed fluorescence. In this way, we could successfully achieve efficient TADF from a novel class of electron-deficient molecular system, namely, arylene diimides when conjugated with a donor molecule, carbazole. Detailed theoretical and spectroscopic analysis suggested that the locally excited triplet energy of these materials play a very important role for both TADF efficiency as well as color-tunability from blue to NIR region.

In **chapter-6**, we utilized triazatruxene (TAT) based donor-acceptor chromophores to get efficient cyan and green-emitting TADF in air. The high triplet state energies of TAT and other constituting acceptor motifs (benzophenone and triazine) are proposed to be playing a key role for their efficient delayed fluorescence feature. Since, pure blue-emitting materials are still a difficult task to solve in commercially available phosphorescence OLED materials, TAT based systems shown here are promising for further development. In addition, a synthetic strategy to substitute the core of TAT with acceptor units (e. g. naphthalene monoimide) has been done to improve the solution-processability of this class of materials which are otherwise difficult to achieve.

TABLE OF CONTENTS

Declaration	i
Certificate	iii
Acknowledgments	v
Preface	vii
Table of contents	x

CHAPTER 1

Introduction

Ambient Triplet Harvesting: Design Principles and Applications

Abstract	1
1. Introduction	2
1.1. Singlet and Triplet states	2
1.2. Excited-state Processes	4
1.3. Harvesting Triplet Excitons by Phosphorescence Process: Key Parameters and Molecular Design	7
1.4. Ambient Organic Phosphors	10
1.4.1. Organometallic Phosphors	10
1.4.2. Purely (metal-free) Organic Phosphors	11
1.4.2.1. Purely Organic Phosphorescence in Crystalline Assembly	12
1.4.2.1.1. Crystallization-induced RTP	12
1.4.2.1.2. Directed Heavy-atom Effect	13
1.4.2.1.3. Stabilizing Triplet Excitons through Intermolecular Electronic Coupling	15
1.4.2.1.3.1. H-aggregation Induced RTP	15
1.4.2.1.3.2. Intermolecular Electronic Coupling between $n-\pi^*$ and $\pi-\pi^*$ States	16

1.4.2.2.	Amorphous State Metal-free RTP	18
1.4.2.3.	Organic RTP in Solution State	20
1.5.	Applications of Organic Phosphors	22
1.5.1.	Organic Light Emitting Diodes (OLEDs)	22
1.5.2.	Optical Sensing and Bio-imaging	26
1.6.	Ambient Triplet Harvesting via Thermally Activated Delayed Fluorescence	30
1.6.1.	Triplet-triplet Annihilation Delayed Fluorescence (TTA-DF)	30
1.6.2.	Upper Triplet Crossing	31
1.6.3.	Thermally Activated Delayed Fluorescence (TADF)	32
1.6.3.1.	Basic Rules for Designing the TADF molecules	34
1.6.3.2.	Application of TADF materials	36
1.7.	Conclusions and Outlook	38
1.8.	References	39

CHAPTER 2

Ambient Room Temperature Phosphorescence in Heavy-atom Substituted Crystalline Carbazole Derivatives with Simple Molecular Design

Abstract		46
2.1.	Introduction	47
2.2.	Design Strategy and Synthesis	48
2.3.	Spectroscopic Studies in Solution-state	48

2.4.	Time-dependent Density Functional Theory (TDDFT) Calculations	49
2.5.	Ambient RTP in Crystalline State	51
2.6.	Single-Crystal X-Ray Diffraction Studies	52
2.7.	Origin of the Phosphorescence in Crystals	57
2.8.	Conclusions	58
2.9.	Experimental Section	59
2.10.	References	69

CHAPTER 3

Organic Long Persistent Luminescence in Solution Processable Amorphous Films

Chapter 3.1. Long Persistent Phosphorescence from Functionalized Coronenes

Abstract		74
3.1.1.	Introduction	75
3.1.2.	Design Strategy	76
3.1.3.	Ambient Triplet Harvesting from CS	77
3.1.3.1.	Solution-state Photophysical Properties of CS	78
3.1.3.2.	Ultralong Room Temperature Phosphorescence (Afterglow) of CS-PVA hybrid	78
3.1.4.	Orange-emitting Phosphorescence Afterglow of CC-PVA hybrids	81
3.1.5.	Conclusions	83
3.1.6.	Experimental Section	83
3.1.7.	References	84

Chapter 3.2. Activating “Afterglow Delayed Fluorescence” via Phosphorescence Energy Transfer

Abstract		86
3.2.1.	Introduction	87
3.2.2.	Design Strategy and Prerequisites for Triplet-to-singlet FRET	88

3.2.3.	Red-emitting Ambient Afterglow Fluorescence in CS-SR101-PVA Hybrid Films	90
3.2.4.	Yellow Afterglow Fluorescence Using SRG dye as FRET-acceptor	93
3.2.5.	Afterglow Hybrids as Encryption Materials	96
3.2.6.	Conclusions	98
3.2.7.	Experimental Section	99
3.2.8.	References	100

Chapter 3.3. Temporally-pure White Afterglow Using Complementary Blue and Greenish-Yellow Ultralong Room Temperature Phosphors

Abstract		102
3.3.1.	Introduction	103
3.3.2.	Design Strategy and Synthesis	104
3.3.3.	Deep-blue Phosphorescence from TAT	106
3.3.3.1.	Photophysical Properties of TAT in Solution-state	106
3.3.3.2.	Deep-blue Emitting TAT-PVA Afterglow Hybrids at Room Temperature	107
3.3.4.	Temporally-pure White Afterglow	110
3.3.5.	Excitation Dependent Colour-tunable Afterglow	114
3.3.6.	Conclusions	115
3.3.7.	Experimental Section	116
3.3.8.	References	119

CHAPTER 4

Aqueous Phase and Ambient Room Temperature Phosphorescence via Supramolecular Self-assembly

Abstract		122
4.1.	Introduction	123
4.2.	Design Strategy and Synthesis	124

4.3.	Previous Work on pNDI-LP Self-assembly	125
4.3.1	Solution-state Self-assembly	125
4.3.2.	Excimer Fluorescence in Solid-state Thin-films	126
4.3.3.	Morphology Studies	127
4.4.	Time-dependent Density Functional Theory Calculations to Understand the Implication of Heavy-atom Effect	128
4.5.	Aqueous and Amorphous Phase RTP from BrNDI-LP hybrids	129
4.6.	Role of Anion- π Charge-transfer States on the ISC Process	130
4.7.	Aqueous Phase and Amorphous-state RTP of BrPhS via Self-assembly	134
4.8.	Conclusions	137
4.9.	Experimental Section	137
4.10.	References	146

CHAPTER 5

Efficient Thermally Activated Delayed Fluorescence (TADF) from Donor-Acceptor Arylene Diimides

Abstract		152
5.1.	Introduction	154
5.2.	Design Strategy and Synthesis	155
5.3.	Thermally Activated Delayed Fluorescence and Room Temperature Phosphorescence from Core-substituted Naphthalene Diimides : A Structure-property Study	155
5.4.	Triplet Harvesting from Core-substituted Pyromellitic Diimide via TADF and RTP	164
5.5.	Blue-emitting solid-state Charge-transfer Emission from Donor-Acceptor Core-substituted Naphthalene Monoimide	165
5.6.	Conclusions	172
5.7.	Experimental Section	173
5.8.	References	185

CHAPTER 6**Triazatruxene Based Donor-Acceptor Charge-transfer Chromophores: A Step Towards Efficient Blue-emissive Thermally Activated Delayed Fluorescent Molecules**

Abstract	190
6.1. Introduction	191
6.2. Design Strategy and Synthesis	192
6.3. Blue-emitting TADF and RTP from Benzophenone-substituted Triazatruxene (TAT-3BP)	192
6.4. Green-emitting Ambient TADF and RTP from Triazine-substituted Triazatruxene (TAT-3TRZ)	198
6.5. Yellow-emissive Solution-processable TADF from Core-substituted Triazatruxene (TAT-NMI)	203
6.6. Conclusions	206
6.7. Experimental Section	207
6.8. References	219
Curriculum Vitae	224
List of Publications	226

CHAPTER 1

Introduction

Abstract

Harvesting the triplet excitons from organic chromophores is the key for achieving maximum efficiency in modern electroluminescent display devices such as organic light emitting diodes (OLEDs). In addition, due to the high sensitivity to air and slow-emitting characteristics of triplet excitons, organic triplet emitters are also very promising for various optical sensing and bio-imaging applications. Until recently, such triplet emitting phenomena (as phosphorescence) from purely organic molecules could only be observed under inert atmosphere and cryogenic conditions to prevent the non-radiative pathways that deactivate the excited triplets as heat. In addition, small organic chromophores generally lack strong spin-orbit coupling (SOC) which is the key for efficient triplet emission. In this regard, organometallic complexes have been utilized as phosphorescent emitting materials due to their high SOC strength and therefore, high ambient phosphorescence efficiency. In fact, especially due to this ambient triplet stability they have been widely explored as OLED materials for past two decades and commercialized as modern display devices. However, their potential toxicity as well as high-cost and instability especially in the blue-region still remains a grand challenge for these materials to be mass produced. Hence, developing alternative “metal-free” organic triplet emitters are more interesting although it is a highly challenging task. There are two major pathways by which ambient triplet harvesting can be done from metal-free organic chromophores, namely, room temperature phosphorescence (RTP) and thermally activated delayed fluorescence (TADF). In this introduction Chapter, we will be discussing the fundamental theory of phosphorescence and various mechanisms for delayed fluorescence in detail. In addition, we will also provide an overview on the design principles of such triplet emitting materials and their various state-of-the-art applications ranging from OLEDs, optical sensing and in vivo bio-imaging.

1. Introduction

1.1. Singlet and Triplet States

In order to fully describe an electronic state of an organic molecule, one needs to include the spin wavefunction into the total electronic wavefunction that usually considers the electron's spatial coordinates and the position of the nuclei.^[1] Spin is a quantum mechanical expression of the electron's angular momentum and a fundamental property like its mass and charge. The spin of an electronic state considers the total spin of all electrons present in all the orbitals. However, the electrons which reside in the filled orbitals are always paired with anti-parallel spins and hence they contribute zero to the total spin (e. g. the ground singlet state, S_0). For the analogous excited states, the spin is determined by considering a two-electron system which are residing in two different orbitals as an unpaired set of electrons. For instance, the unpaired electrons of an excited state configuration, one electron reside in a π^* -orbital and the other one in a π -orbital. To understand this arrangement in a simpler way, one can refer this excited state configuration to a singlet (or triplet) state when the spin of electron in the π^* orbital and that of its partner electron in the π -orbital are antiparallel (parallel) and leading to a total spin of zero (one) in the units of \hbar (Figure 1.1a). The numbering of different excited states is done in an ascending energetic order, for example, S_1 , S_2 , or T_1 , T_2 , and so on, for the energetically lowest or second lowest singlet or triplet excited states of the molecule. Spin angular momentum is a vector quantity that couples according to the rules of quantum mechanics and designated by the operator \hat{S} . There are four possible spin eigenstates of \hat{S} for a two electron system (e. g. one electron in a π^* -orbital and one in a π -orbital and each having spin $1/2$). The first spin wavefunction has eigenvalue of $S = 0$, and spin multiplicity $M = 1$ ($M = 2S + 1$). It has only a single possible value of its z-component, i.e. eigenvalue $M_S = 0$, and is therefore this is called singlet. The next three spin wavefunctions have eigenvalues $S = 1$ and $M = 3$. They only differ in the z-component of the spin, which can take one of three eigenvalues ($M_S = 1, 0, -1$). This arrangement is therefore called triplet. A vectorial representation is given in the Figure 1.1b. It is worthwhile to mention that the designation of these different configurations is a direct manifestation of the principle of indistinguishability in quantum mechanics which suggests that the wavefunction of a system must be symmetric or antisymmetric with respect to exchange of two electrons. In this case, two electrons with two possible spin states can have four possible spin combinations: $|\uparrow\uparrow\rangle$, $|\downarrow\downarrow\rangle$, $|\uparrow\downarrow\rangle$ and $|\downarrow\uparrow\rangle$. The first two states are symmetric with respect to exchange of the two electrons whereas the last two states are neither symmetric nor antisymmetric. Linear combinations of the last two states in the following form will make one of them symmetric and the other one antisymmetric:

$\frac{1}{\sqrt{2}} \{ |\uparrow\downarrow\rangle + |\downarrow\uparrow\rangle \}$ and $\frac{1}{\sqrt{2}} \{ |\uparrow\downarrow\rangle - |\downarrow\uparrow\rangle \}$; Where, $\frac{1}{\sqrt{2}}$ is the normalization constant. The three symmetric states form the triplet states and the only antisymmetric state forms the singlet state.

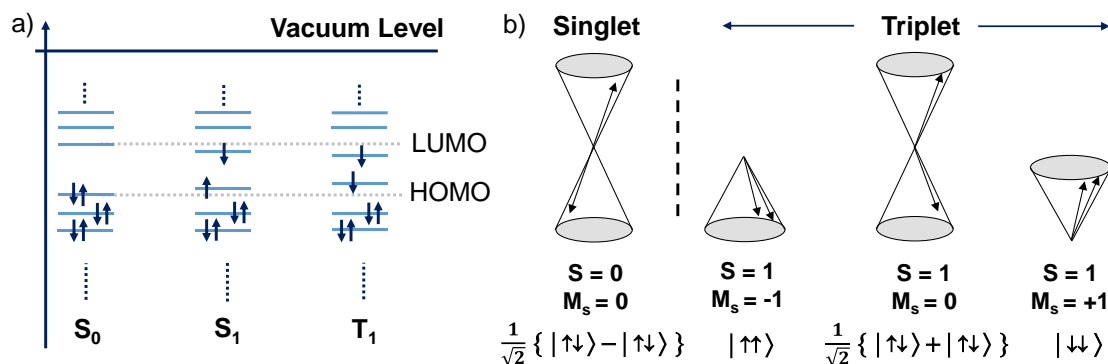


Figure 1.1. a) Singlet and triplet excited states in an orbital configuration scheme. Only one spin configuration is shown for the triplet state. b) A vector diagram illustration for the relative orientations of the two electron spins in the singlet and the triplet states. These two spins are indicated by the arrows which precess around a local magnetic field in the z -direction. The antiparallel and 180° out-of-phase configuration is designated as a singlet state and the other three configurations are designated as triplet state. (Figures reproduced with permission from Reference 1).

In the context of the present Thesis, it is very important to understand the various excited state transitions which occur upon the photo-excitation of the molecule. Before we understand these processes, it has to be noted that in the ground state of organic molecules the electrons share an orbital as a pair of bonded electrons or non-bonded lone-pairs. Therefore, the ground state of an organic molecule is generally a singlet state and hence the electrons will have antiparallel paired spins. However, in the excited state, the spin-orientation rule is no longer restricted because electrons are now sharing two different orbitals. As can be evident from Figure 1.1a, in the ground state two electrons share same orbitals in the highest occupied molecular orbital (HOMO). Upon photoexcitation, the electrons are residing in HOMO of the excited molecule and the other one in the lowest unoccupied molecular orbital (LUMO) which was empty prior to the photoexcitation. Importantly, these electrons can either be antiparallel (singlet) or parallel to each other (triplet). However, direct population of the triplet state is quantum mechanically forbidden and generally occur via a process called intersystem crossing. This process is of particular importance within the context of the present Thesis work and will be clearer in the later part of this discussion. Nonetheless, when there is a direct transition from the lowest excited singlet (S_1) state to ground singlet state (S_0), the process is called fluorescence and similarly from

the lowest excited triplet (T_1) to S_0 is called phosphorescence. There are many fundamental differences between these photo-processes which will be discussed in the next section with a special attention to the excited triplet states and their radiative decay pathways (phosphorescence and delayed fluorescence).

1.2. Excited-state Processes

Since in this Thesis we try to achieve the radiative decay of the triplet excited state under ambient conditions, it is a good starting point to analyse the photophysical processes when an organic molecule is excited by a photon (Figure 1.2). According to Boltzmann distribution (at room temperature), the majority of molecules will be in the lowest vibrational level of the ground state and as a result the absorption is always shown to start from this level. When an organic molecule absorbs a photon, it gets promoted from the S_0 (lowest vibrational level) to one of the vibrational levels of the excited singlet states (S_n , $n>0$). The timescale of this process is very fast, in the order of 10^{-15} s. Since, absorption strictly follow the total angular momentum conservation rule, only singlet-singlet transition is allowed whereas the singlet-triplet transition is forbidden.^[2]

After the molecule is promoted to an excited state following the absorption of a photon (with similar or higher energy than the energy gap of the S_n and S_0 states), it reaches a non-equilibrium state and need to dissipate the energy it has acquired and eventually return to the ground state. The first way it follows in order to dissipate the energy is called vibrational relaxation (VR), which is defined as a non-radiative transition to a lower vibrational level within the same electronic state. By this process, the excess vibrational energy is lost as heat to the vibrational modes within the same molecule (an intramolecular process) or to the neighbouring molecules such as solvent (intermolecular), until it reaches the lowest vibrational level of that particular electronic state (this is applicable to the ground singlet state as well). The timescale of vibrational relaxation is extremely fast in the order of 10^{-12} - 10^{-10} s.

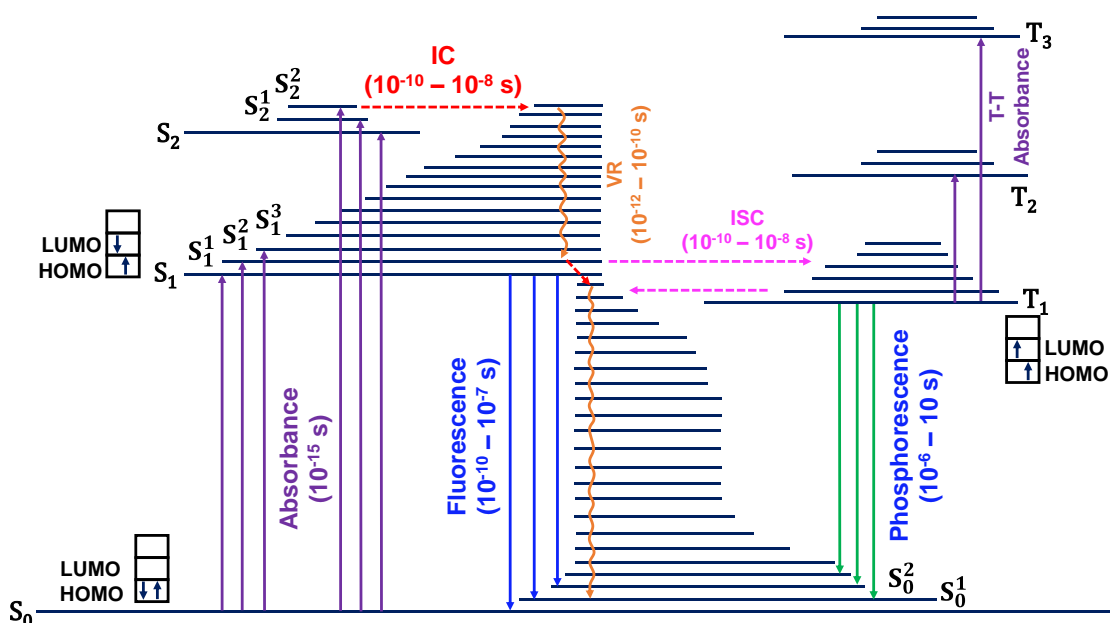


Figure 1.2. The Perrin-Jablonski diagram showing the most important excited state transitions (both radiative and non-radiative) upon absorption of photon. Typical rates of these transitions are shown in the diagram. The spin configurations are also shown for the S_0 , S_1 and T_1 state. It is to be noted that, the $S_0 \rightarrow T_1/T_n$ absorption is forbidden, however, $T_1 \rightarrow T_2/T_n$ transitions (absorption) are allowed under certain experimental set-up.

Once the molecule reaches the lowest vibrational level of the higher-lying excited singlet state (e. g. S_2 state), it will quickly undergo a process called internal conversion (IC) to reach lowest excited singlet state (S_1), followed by quick vibrational relaxation to the lowest vibrational level of S_1 . Internal conversion (IC) is defined as a non-radiative transition between two electronic states of the same spin-multiplicity. Hence, the process is applicable to the triplet excited states as well. It should be mentioned here, all higher-lying singlet/triplet states (upon absorption of photon) will eventually relax back to the lowest excited singlet/triplet state by the IC mechanism. The rate at which the IC takes place depend on the energy gap between the initial and final electronic states. For example, the rate is much faster (usually in the order of 10^{-10} to 10^{-8} s) between closely-spaced higher-lying singlet states (i. e. S_3 to S_2 , S_2 to S_1 etc.) as compared to S_1 to S_0 , because of the much wider energy gap. Therefore, when the molecule reaches the lowest excited singlet state, the IC competes with other relaxation processes such as fluorescence and intersystem crossing (ISC). Both these processes are extremely important in the context of this Thesis and will be discussed briefly in the following paragraph.

Fluorescence is a radiative transition between two electronic states of the same spin-multiplicity.^[3] In this discussion we will consider $S_1 \rightarrow S_0$ transition as fluorescence process. The

timescale of fluorescence is usually 10^{-10} to 10^{-7} s. As a consequence of the previously discussed vibrational relaxation and internal conversion, fluorescence always takes place from the lowest vibrational level of the first excited singlet state to the ground singlet state. This is an empirical rule given by Michael Kasha and is famously known as Kasha's rule.^[4] The Kasha's rule states that "luminescence (fluorescence or phosphorescence) only occurs with appreciable yield from the lowest excited state of a given multiplicity". This also explains the origin of Stokes-shift where the fluorescence emission takes place at the longer wavelengths as compared to the absorption (i. e. excitation wavelength).

There is another common route, alternative to the internal conversion and fluorescence from the S_1 state. This is a process called ISC and defined as a non-radiative transition between two isoenergetic vibrational levels that belong to electronic states with "different" spin-multiplicity (e. g. transition from S_1 to T_2 or T_1 , whichever is isoenergetic to the vibrational levels of S_1). This process is a formally forbidden process as there is a change in spin-multiplicity and hence the total angular momentum is not conserved. The process is therefore very inefficient in general and require strong spin-orbit coupling strength in order to become competitive to spin-allowed transitions like internal conversion or fluorescence. As mentioned earlier once the triplet state (T_n , $n>0$, e. g. T_2 or T_1) will relax to lowest vibrational level following internal conversion/vibrational relaxation (Kasha's rule). Typical timescale of ISC (provided the molecule has strong spin-orbit coupling strength, e. g. transition metal complexes) is 10^{-10} to 10^{-8} s.

Once the molecule reaches the lowest vibration level of T_1 , it can have the similar fate of S_1 excited state as discussed earlier. We can either see a radiative transition from $T_1 \rightarrow S_0$ state which is known as phosphorescence. However, the transition is a spin-forbidden process similar to the ISC (*vide supra*) and hence the timescale of phosphorescence is extremely slow (10^{-6} to 10^8 s) and typical lifetime of phosphorescence emission is in the range of μ s-s. Because of long lifetime, triplets are highly susceptible to intermolecular collisions (e. g. with solvent molecules) that activates non-radiative vibrational relaxations and the excited triplet energy is simply lost as heat. The most efficient way to prevent such vibrational (or collisional) quenching/dissipation is to freeze the molecular motion (of both solvent and phosphor molecules) under cryogenic conditions, in a glassy solvent matrix. In addition, because of the spin-allowed triplet-triplet energy transfer to molecular oxygen (ground state of molecular oxygen is of triplet character), triplets are quenched rapidly under aerated conditions. In this Thesis, we have taken these factors into account and developed new design strategies to prevent the non-radiative quenching of

triplets for efficient phosphorescence emission under fully ambient conditions (i. e. in air and room temperature).

Considering the theme of this particular Thesis work, there is another important process that the lowest triplet excited state (T_1) can undergo, which is a reverse intersystem crossing (RISC) to S_1 state. In this way the triplets are harvested indirectly as delayed fluorescence (DF). A more comprehensive description of this highly desirable process will be outlined in the later part of this Chapter.

1.3. Harvesting Triplet Excitons by Phosphorescence Process: Key Parameters and Molecular Design

Transition from singlet to triplet state (e. g. S_1 to T_1) is a forbidden process because there is a change in the spin angular momentum when the spin-flipping takes place. However, spin-flipping/intersystem crossing can take place when the electron experiences strong spin-orbit coupling (SOC) effect. SOC takes place due to coupling of spin and orbital angular momenta of the electron. In this way, a strong electromagnetic force created by the atomic nucleus on the rotating electron causes a change on the orientation of its spin. The extent or rate of intersystem crossing depends proportionally to the SOC strength and inversely proportional to the gap between the singlet-triplet states. The quantum mechanical relationship can be expressed by the following equation:

$$\delta = \frac{\langle {}^3\Psi | H_{SO} | {}^1\Psi \rangle}{|E_{S_1} - E_{T_1}|} \quad (1.1)$$

Here, the perturbation factor δ describes the singlet–triplet mixing by first-order spin–orbit coupling according to the First-order Perturbation Theory.^[5] ${}^1\Psi$ and ${}^3\Psi$ are the wavefunctions of the singlet and triplet states participating in the intersystem crossing, respectively. H_{so} is the spin–orbit Hamiltonian and E_{S_1} and E_{T_1} are the energy levels for singlet and triplet states. This mathematical expression describe that a greater spin–orbit matrix value (in Chapters 2 and 4 we shall see this is quantified by the spin-orbit coupling matrix element or SOCME) and a smaller energy gap (ΔE_{ST}) between the singlet and triplet states correspond to a larger δ ; which in turn suggests a high probability of electronic transition between singlet and triplet states. In the following discussion we will describe how the SOC can be increased along with the strategies for lowering the energy gap (ΔE_{ST}). The mathematical expression of spin-orbit coupling Hamiltonian is given in equation:

$$H_{SO} = -\frac{z^4 e^2}{8\pi\epsilon_0 m_e^2 c^2} \mathbf{l} \cdot \mathbf{s} \quad (1.2)$$

From equation 1.2 it is clearly evident that the SOC depends primarily on two parameters:

(i) The co-efficient which is basically a collection of many constants (e is the elementary charge of an electron, ϵ_0 is the permittivity of the vacuum, m_e is the mass of an electron, and c is the speed of light) and the atomic number of the nucleus, Z . This particular factor (Z) is the most important one in tuning the magnitude of SOC, since H_{SO} is proportional to Z^4 and highly sensitive to the charge/size of the nucleus. The change in the orientation of the electron spin is facilitated by the strong electromagnetic field of heavy-atomic nucleus such as Pt, Ir or halogens like Br or I. Since the first demonstration of an internal heavy atom-effect by McClure in 1949,^[6] various halogen or large-atomic-number metal atoms have been incorporated into luminescent organic molecules to enhance phosphorescence intensity relative to fluorescence.

(ii) The dot product of orbital and spin angular momentum ($\mathbf{L}\cdot\mathbf{S}$). This factor is comparatively weaker in magnitude in terms of facilitating the spin-flipping process as compared to the previous one (i. e. atomic number of the nucleus). However, in this Thesis, we would be discussing that the ISC and phosphorescence intensity can be strongly influenced without the aid of any heavy-atom effect. Interestingly, the rate of the phosphorescence emission can be slowed down in comparison to the examples which utilizes the heavy-atom effect. From an application point of view, the rate of phosphorescence emission should ideally be slow for encryption or bio-imaging studies; whereas, for lighting applications (e. g. OLEDs) faster lifetime (i. e. fast phosphorescence decay) is desirable to circumvent the efficiency roll-off at high brightness.

Nonetheless, as mentioned earlier, in an intersystem crossing (ISC) process, we see a change in the spin angular momentum. Therefore, in order to conserve the total angular momentum of the electronic transition (i. e. ISC in the present case), the orbital angular momentum has to be changed as well. This particular rule has been postulated by Mostafa El-Sayed in his seminal works in the 1960s.^[7] The rule can be simply understood by the following: the rate of ISC is large when the transition takes place between the electronic states of different multiplicity with a change in their respective orbital configuration. A schematic diagram is given in Figure 1.3 to explain this rule.^[8] The ISC will be fast and efficient when transition involves a change in the orbital type; i. e. the singlet is of $\pi\text{-}\pi^*$ and triplet is of $n\text{-}\pi^*$ in nature or vice versa. On the other hand, the rate will be slow when the single and triplet both are $\pi\text{-}\pi^*$ or $n\text{-}\pi^*$.

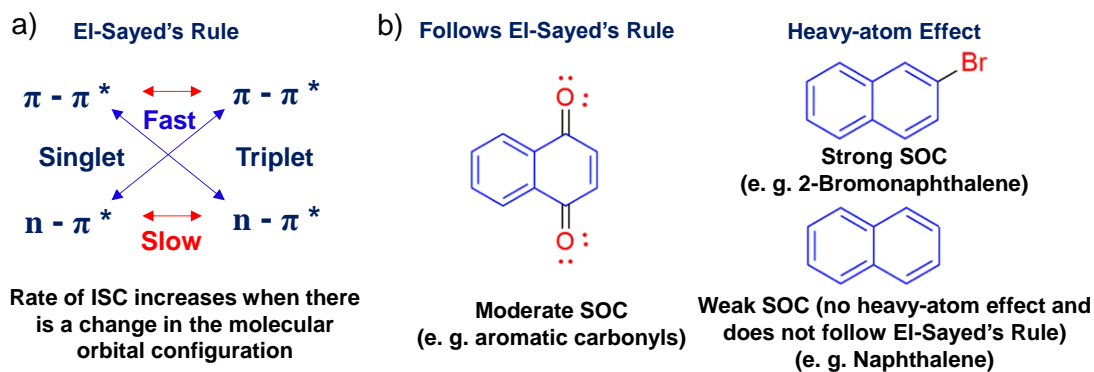


Figure 1.3. a) Schematic description of El-Sayed's Rule. B) Molecular examples showing different extent of spin-orbit coupling.

According to equation 1.1, we must also take into account the energy gap between the singlet and triplet states. However, in the present discussion on the phosphorescence emission we assume a small gap of lowest excited singlet and nearest excited triplet state. However, the importance of this particular factor will be explained on the mechanism and design strategy of thermally activated delayed fluorescence (TADF) emitting molecules.

Now, we have understood the extent of triplet population is largely determined by the extent of SOC. However, it is not wrong to think that the transition of $T_1 \rightarrow S_0$ as similar ISC process in the context of another spin-flipping requirement. Therefore, this transition again is spin forbidden and hence a relatively slow process as compared to the fluorescence (typical rates given in the previous section). Both the slowness of the phosphorescence transition and its spin-forbidden nature and the relatively large energy gap between the ground singlet state makes the triplets highly susceptible to various quenching pathways as outlined earlier leading to non-radiative deactivation. In fact, only feeble phosphorescence emission could be achieved in most of the common small organic molecules even under cryogenic/inert conditions and therefore, the practical applications of organic phosphors has long been neglected. Until recently, the phosphorescence emission has been relied on the organometallic phosphors. However, a significant improvement in the understanding and consequent design principles has been achieved with metal-free organic chromophores which exhibit phosphorescence under ambient conditions. Some of these breakthrough examples are outlined in the next sections.

1.4. Ambient Organic Phosphors

The organic material that exhibit phosphorescence mainly classified into two parts:

- a) Organometallic phosphors

- b) Metal-free/purely organic phosphors

1.4.1. Organometallic Phosphors

Organometallic complexes have been utilized as most efficient organic phosphors as they are capable of producing high triplet density due to strong spin-orbit coupling effects provided by the heavy-nucleus of the transition metals.^[9] This in turn ensure high phosphorescence quantum efficiency and short emission lifetime, both are highly desired for applications in solid-state lighting materials such as OLEDs. Another important aspect of these class of phosphors is their colour tunability which is achieved easily by modulating the ligand structure and their subsequent excited state energy profiles. Among various organometallic complexes studied until now, transition metals like Pt, Ir, Ru and Os; Ir-complexes has been explored as best molecular systems for lighting applications. Ir-complexes are easily synthesized and their emission can be tuned from blue to red with excellent quantum yields. However, organometallic complexes have certain limitations such as choice of limited numbers of metals, high cost (Ir is 6th rarest metal on earth) and most importantly their instability in the UV/blue-region of the emission spectrum which require strong metal-ligand bonds. Therefore, these drawbacks have prompted the researchers around the world to explore more alternatives which would be cost-effective, environmentally benign and equally efficient. In that regard, metal-free or purely organic phosphors (or TADF emitters) are attractive alternatives which would provide easy and flexible synthetic protocols (hence chemical tunability), low cost and wide-range colour-tunability by modulation of the π -conjugation length. A list of representative organometallic phosphor materials^[10] are given in Figure 1.4 and a detailed survey of the organometallic phosphors is beyond the scope of this thesis.

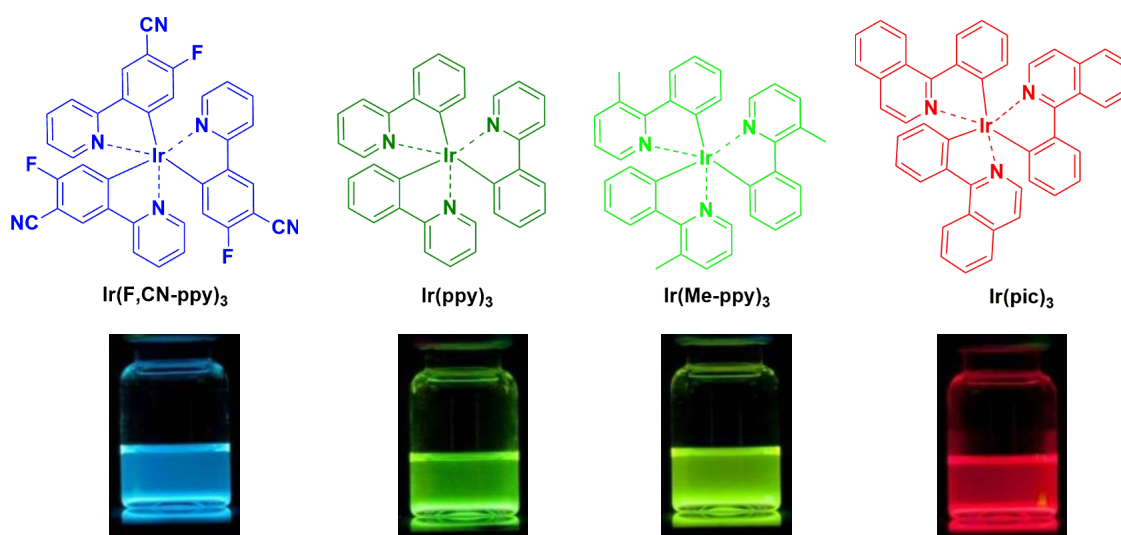


Figure 1.4. Examples of organometallic-complexes based on Ir showing bright phosphorescence. (Reproduced with permission from Reference 10).

1.4.2. Purely (metal-free) Organic Phosphors

Since the pioneering works of Lewis and Kasha in the 1940s,^[11] detectable organic phosphorescence has been achieved in many simple chromophores like naphthalene, carbazole etc. at cryogenic temperatures in glassy matrix. However, the practical application of purely organic phosphors have been realized recently, majorly in crystalline organic materials with certain functional groups.^[12] Among these, most commonly explored molecular systems are aromatic carbonyls. There are many advantages utilizing the carbonyl functional group in a phosphor design. The lone pair on the oxygen atom can bring about favourable orbital characteristics required for efficient ISC process to occur according to El-Sayed's rule.^[13] For example, in case of benzophenone, the S_1 state is of $n-\pi^*$ in character, whereas nearest T_2 state is of $\pi-\pi^*$ character (Figure 1.5a). Next, relatively small singlet triplet gap would also help in accelerating the process and it has been shown that the ISC is nearly 100 % for benzophenone.^[14] Although aromatic carbonyls facilitate ISC by following the El-Sayed's rule, their energy landscape cannot be predicted in a straightforward fashion. As evident from Figure 1.5b, increased ΔE_{ST} in case of pyrenealdehyde slows down the ISC rate to at least 5 folds as compared to the benzophenone. In addition, all these examples the phosphorescence was detected only at low temperature and in glassy matrix (77 K). Nonetheless, aromatic carbonyls (and structurally similar functional groups with lone pair of electrons, e. g. thiones, sulphonyls etc.) offered a suitable model system for the development of modern room temperature phosphorescence (RTP) systems which is outlined in the following discussions.

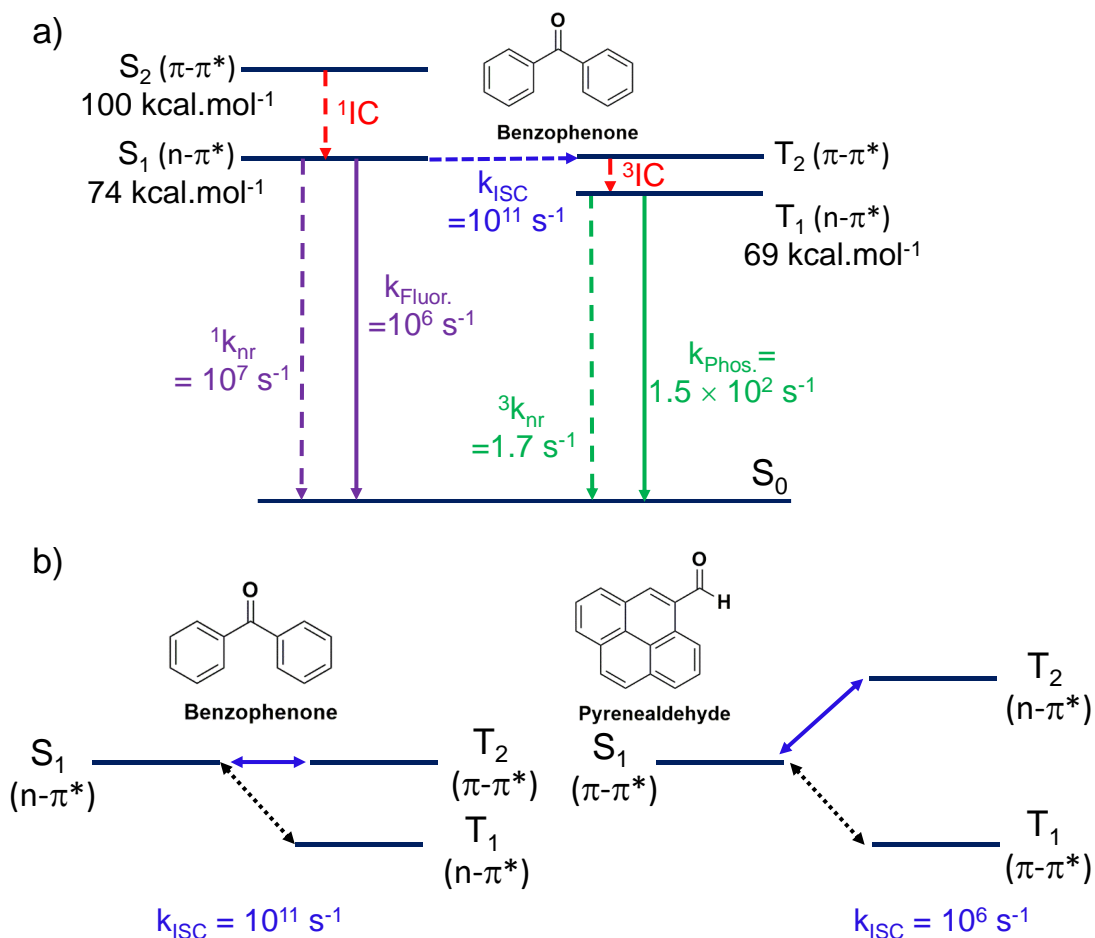


Figure 1.5. a) Jablonski diagram for benzophenone at 77 K. b) Examples of different rates of intersystem crossing for $S_1(n-\pi^*) \rightarrow T_2(\pi-\pi^*)$ and $S_1(\pi-\pi^*) \rightarrow T_1(\pi-\pi^*)$ transitions in carbonyl compounds. (Reproduced with permission from Reference 14)

1.4.2.1. Purely Organic Phosphorescence in Crystalline Assembly

1.4.2.1.1. Crystallization-induced RTP

The basic reason behind non-emissive nature of phosphorescence under ambient conditions stems from the rapid non-radiative decay pathways and poor spin-orbit coupling. Therefore, reducing the molecular motion of organic molecules in a rigid crystalline assembly has been exploited by Tang and co-workers, where they successfully achieved “Crystallization-induced Phosphorescence or CIP” in various benzophenone derivatives with excellent quantum efficiency (~40 %) at room temperature.^[15a] Detailed single crystal analysis of these molecules show numerous non-covalent interactions, particularly, C-H \cdots O, N-H \cdots O, C-H \cdots X (X = F, Cl, Br), C-Br \cdots Br-C, and C-H \cdots π hydrogen bonding, which effectively lock the conformational flexibility of the phosphors and lead to such unprecedented RTP properties under ambient

conditions (Figure 1.6). Many different ways of colour-tunability and lifetime modulation from organic phosphorescence systems utilizing this so-called “crystallization induced phosphorescence” has been exploited successfully since-then.^[15]

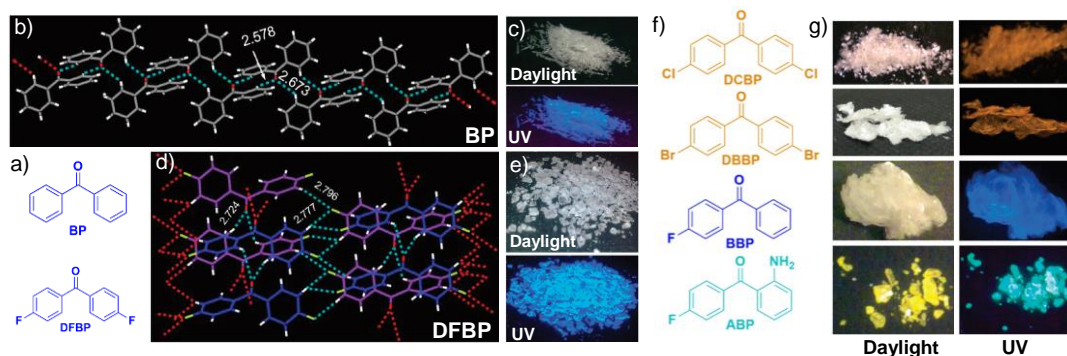


Figure 1.6. Crystallization induced phosphorescence from benzophenone and its derivatives. *a)* Molecular structure of **BP** and difluorobenzophenone (**DFBP**). *b)* Single crystal structure of benzophenone (**BP**) showing different intermolecular interactions. *c)* Photographs of the crystals of **BP** both under daylight and 365 nm UV-lamp (blue RTP). *d)* Single crystal structure of **DFBP** showing more intermolecular interactions than the parent **BP**. This leads to a better rigidification of the crystalline network in **DFBP** and increases the phosphorescence quantum yield to 39.7 % in comparison to **BP** (16 %). *e)* Photographs of the crystals of **BP** both under daylight and 365 nm UV-lamp (blue RTP). *f)* List of some other phosphorescent crystals studied in this work and *g)* their photographs taken under 365 nm UV-lamp also show bright ambient RTP. (Reproduced with permission from Reference 15a)

1.4.2.1.2. Directed Heavy-atom Effect

Parallel to the reports of CIP, Kim and co-workers have reported more comprehensive and systematic approach towards harnessing bright RTP from pure organic molecules.^[16] They developed a unique “directed heavy-atom effect” strategy in a bicomponent crystalline assembly.^[16a] Halogen-bonding between the host matrix (a dibromo-substituted aromatic compound) and guest phosphor (an aromatic bromoaldehyde) was utilized to rigidify the bicomponent assembly, in addition to promote simultaneous internal and external heavy-atom effects. Both these factors helped in activating a strong RTP by increasing the overall SOC in the system and reduced vibrational quenching. The reduced vibrational quenching and enhanced SOC was reiterated by the absence of any phosphorescence in solution state (Figure 1.7a-d). Moreover, this particular system also showed the importance of solid state dilution effect, since the crystalline samples of pure phosphor molecules (i. e. without the host co-crystal) exhibited very weak RTP because of excimer-induced self-quenching or plausibly triplet-triplet

annihilation processes (Figure 1.7c and 1.7d). Nonetheless, their work showed the bicomponent co-crystals could achieve phosphorescence quantum efficiency to as high as 55 %. The authors also attempted the colour-tunability of organic phosphors by tuning the π -conjugation length of the aromatic core to obtain blue and orange emission (Figure 1.7e-g). However, the phosphorescence efficiency reduced dramatically ($\sim 1\%$ for both blue and orange phosphors) and the reason behind this observation was not very clear. In fact, a rational design of crystalline phosphors based on a particular class of molecular unit, that show high quantum efficiency as well as colour-tunability is yet to be developed. Hence, other means of achieving these properties are being investigated by many groups.

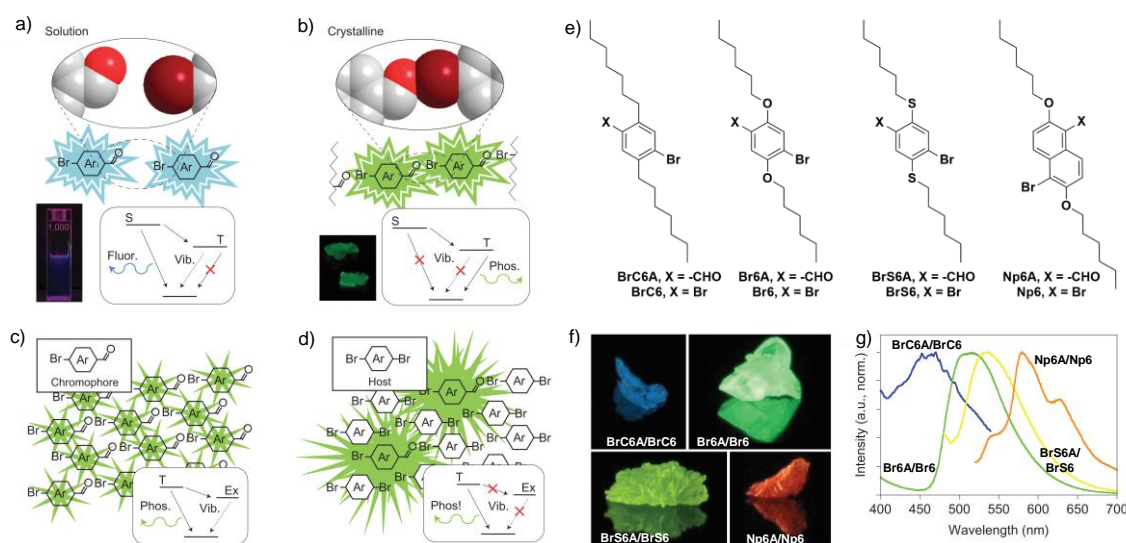


Figure 1.7. Design Principle for Directed Heavy-atom Effect and the molecular examples. a) In solution state, aromatic bromoaldehydes undergoes intersystem crossing but the triplets are lost as heat and only fluorescence in emission is observed. b) In solid state, halogen bonding between these chromophores lead to phosphorescence. c) The highly ordered crystals of aromatic bromoaldehyde shows RTP, but self-quenching due to excimer formation reduces the overall phosphorescence efficiency. d) The guest bromoaldehyde phosphor is diluted in the host (dibromo analogue of the phosphor) crystal to reduce the quenching effects while maintaining strong rigidity and external heavy-atom effect, leading to substantially high quantum efficiency (~ 18 fold increase). e) Molecular structures, f) photographs (under 365 nm UV-lamp) and g) the phosphorescence emission profiles of the chromophores studied in this work. (Reproduced with permission from Reference 16a)

Based on these two works, the field of organic phosphors have come a long way so far. Till now, most of the bright-emitting phosphors are based on the crystal-engineering of the molecules and exploit various intermolecular interactions that not only improve the rigidification

of the entire assembly, but also accelerate the ISC process as well by means of intermolecular electronic coupling between the chromophores (one example is external heavy-atom effect). In the following section, we will discuss two more significant examples of organic phosphor design for their unique organization in the solid-state that led to extraordinary photophysical properties. It must be mentioned that, both these examples are fundamentally similar to previous examples in terms of the “crystalline-induced phosphorescence” that also utilize the “intermolecular electronic coupling” in order to promote excellent intersystem crossing efficiency as well as triplet state stabilization in a crystalline assembly.

1.4.2.1.3. Stabilizing Triplet Excitons through Intermolecular Electronic Coupling

1.4.2.1.3.1. H-aggregation Induced RTP

So far, the discussion on the molecular design for efficient phosphorescence emission from metal-free organic chromophores has been primarily based on increasing spin-orbit coupling that ensure high triplet yield via fast ISC process and subsequently protecting these triplet excitons from non-radiative quenching pathways in a rigid matrix. The extent of intersystem crossing has been mainly focused on using aromatic carbonyls and heavy-atom effect. In the following example we shall see another effective way of producing high triplet density using H-aggregation between the phosphor molecules.^[17] This was first studied by Huang and co-workers in 2015, where they introduced a 4,6-diphenyl-2-carbazolyl-1,3,5-triazine (**DPhCzT**) derivative which show strong ground state H-aggregation feature in their crystal structure (the measured angle, θ , between the transition dipoles and interconnected axis was = 80.91°) (Figure 1.8a and 1.8b).^[17a] They performed detailed time-dependent density functional theory calculations to show that number of effective intersystem crossing channels were starkly different between the monomer and H-dimers (Figure 1.8c). In case of monomer, only four nearest triplet excited states were available for effective ISC transitions from lowest singlet state (S_1). On the other hand, in the H-dimer state, six such exciton transition channels were present and hence the ISC probability of the dimer was enhanced substantially.

In addition, the author also hypothesized that the intrinsically high SOC strength provided by the $n-\pi^*$ transitions promoted by the “lone” pair of the nitrogen atoms in the molecule contributes in the singlet-triplet transition via intersystem crossing. They also proposed that the H-aggregates would generate many new “stabilized” triplet state (T_n^*) which function as an energy trap and delocalize on several neighbouring molecules leading to ultralong lifetime of the phosphorescence. To validate their hypothesis, the extended their approach to a series of other

heterocyclic compounds containing N, O or P which were envisioned to promote similar $n-\pi^*$ transitions (Figure 1.8d). Moreover the planar structure of these molecules are also suitable for the parallel alignment and H-aggregation in the crystal. All these compounds were shown to exhibit ultralong phosphorescence (up to 1.35 s) with moderate quantum yield ($\sim 1.25\%$).

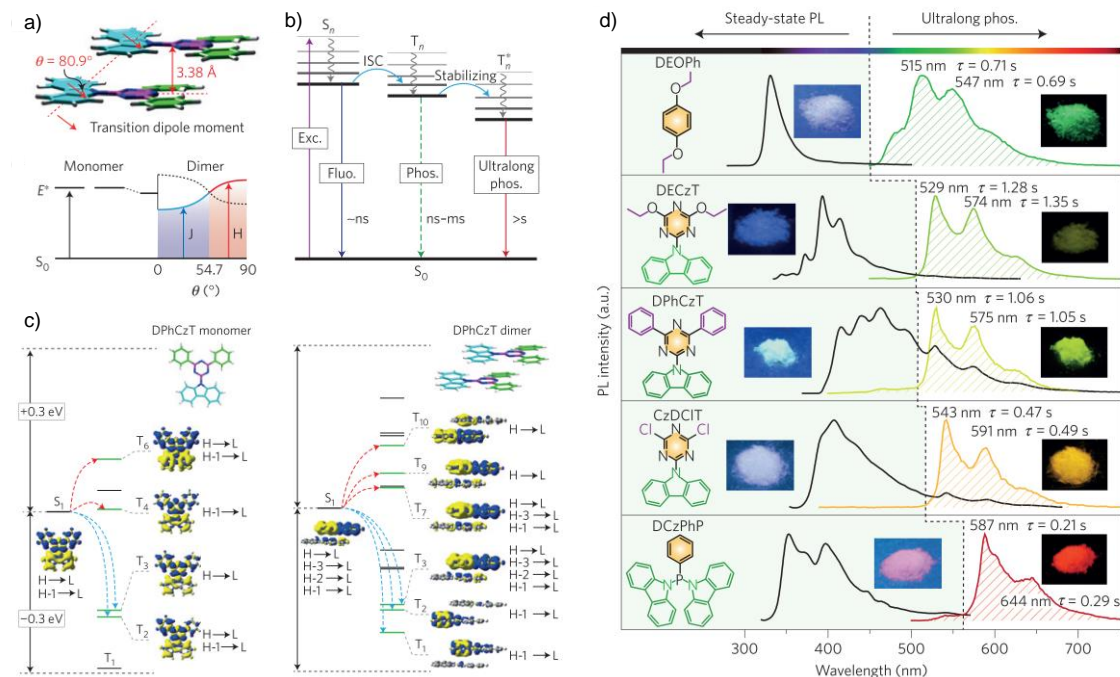


Figure 1.8. Proposed mechanism and molecular examples undergoing “H-aggregation” induced RTP. a) Crystal structure of *DPhCzT* showing H-aggregation. b) Simplified Jablonski diagram that shows the stabilization of triplet excitons (due to H-aggregation) leading to ultralong RTP. c) Schematic diagrams depicting the TD-DFT-calculated energy levels, isosurfaces and main orbital configurations of a *DPhCzT* monomer and its H-dimer at singlet (S_n) and triplet (T_n) states. d) Examples of other ambient afterglow RTP materials studied in this work showing excellent colour-tunability. (Reproduced from ref. 17a).

1.4.2.1.3.2. Intermolecular Electronic Coupling between $n-\pi^*$ and $\pi-\pi^*$ States

Bryce and co-workers, further extended the concept of intermolecular electronic coupling (IEC)^[18] between two different excited state configurations ($n-\pi^*$ and $\pi-\pi^*$) in a single molecular unit (Figure 1.9a-c). The molecular design is based on a highly twisted donor-acceptor structure that lead to such differential excited state configurations and their coupling is enhanced by an electrostatically driven intermolecular interaction in the closely-packed crystalline assembly (Figure 1.9c).^[18a] The rigid crystalline assembly not only result in high triplet stability (both from oxygen and vibrational quenching), it also ensure enhanced number of potential ISC

channels stemming from the so-called intermolecular coupling of these donor/acceptor units with partial orbital overlapping (Figure 1.9d and 1.9e). The authors also showed the mechanism work well for other n-units (sulphonyl) and same π -unit (carbazole). Detailed crystal structure analysis further provided molecular level information supporting their hypothesis as the distances between the carbazole plane and nearest carbonyl groups were very short (3.37 Å and 3.56 Å, from oxygen and carbon atom of the carbonyl group, respectively) (Figure 1.9d).

In fact, it was suggested that the stacking modes allowed the intermolecular coupling (spatial overlap) between the n and π orbitals and this packing feature is responsible for the ultralong RTP. Interestingly, introduction of heavy-halogen atom (Br) was shown to improve the phosphorescence quantum efficiency to over 5 %.

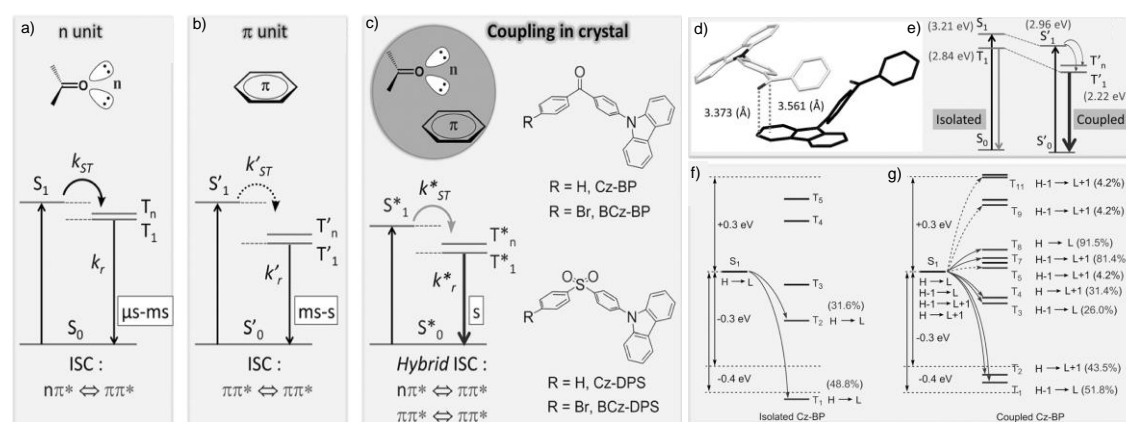


Figure 1.9. Energy level diagram of the relevant photophysical processes for the phosphorescence of organic molecules with a) $n\pi^*$ excited state configuration (i.e. containing an n unit) and b) $\pi\pi^*$ excited state configuration (i.e. containing a π unit). c) Proposed energy level diagram of the relevant photophysical processes for ultralong/afterglow phosphorescence of coupled intermolecular n and π units in organic crystals. k_r = rate of phosphorescence. k_{ST} = rate of intersystem crossing. d) Intermolecular electronic coupling of the carbonyl and Cz groups in two Cz-BP molecules that are in close proximity in a single crystal. e) Energy level diagram of the isolated and coupled Cz-BP molecule(s). Schematic representations of the TD-DFT calculated energy levels, main orbital configurations, and possible ISC channels of f) isolated Cz-BP and g) coupled Cz-BP at the singlet (S_1) and triplet (T_n) states. H and L refer to HOMO and LUMO, respectively. The plain and dashed arrows refer to the major and minor ISC channels in (c) and (d). (Reproduced from ref. 18a).

From all these examples one can understand the efficacy of crystal-engineering of certain type of organic molecules towards ambient phosphorescence emission. However, most of the reported crystalline systems suffer from the reproducibly and unpredictable emission behaviour upon subtle changes in the molecular structure. In addition, they are generally structurally complex and require multistep synthesis. Lastly, the most important factor that still remains a

formidable challenge to utilize crystalline phosphor materials for widespread practical applications, is their poor processability. In fact, in most of these classic examples outlined above, it has been pointed out that, the crystallinity of the samples must be high in order to maintain maximum efficiency which in turn, rely heavily on tedious crystallization processes. Therefore, amorphous-state and solution-processable RTP materials are next challenges in the field. It is to be noted that, solution-state ambient RTP is still rare in the literature for obvious collisional and vibrational quenching effects. Approaches to outline a universal strategy for solution state RTP would further make this exciting field of research more useful and find applications in bio-imaging and optical sensing.

1.4.2.2. Amorphous State Metal-free RTP

As has been described in the previous section, the poor solution processable nature of the organic phosphorescent crystals needed alternative strategy towards widespread applications of these materials.^[19] The approach so far has been based on increasing the SOC of the organic luminogens by introducing specific functional groups like aromatic carbonyl and dispersing them in rigid matrices. The rigid matrices can be either a glassy polymer (e. g. polyvinyl alcohol); or small molecule host like steroid (e. g. β -estradiol).

Among these different hosts, polymers have been well-explored in the recent literature including the reports from our group (George group) which will be discussed in detail in the forthcoming Chapters. Nonetheless, most widely used polymer host has been polyvinyl alcohol (PVA) for this purpose. Multiple hydrogen-bonding units from the hydroxyl groups of PVA has been shown to effectively rigidify the small organic phosphors functionalized with carboxylic acid groups. One notable and seminal example is reported by Kim and co-workers, where they utilized bromoaldehyde core, functionalized with carboxylic acid side-chains (**G1**) (Figure 1.10a). These carboxylic acid groups were shown to form strong hydrogen-bonding with the PVA chain by various control host polymers with differential hydroxyl group content. They also showed that previously studied **Br6A** molecules (without any carboxylic acid group, Figure 1.10a) shows only feeble RTP when dispersed in PVA matrix, reiterating the efficacy of hydrogen-bonding interactions that result in reduced vibrational relaxations. In addition, they were also able to show unique halogen-bonding with the neighbouring phosphor molecules organized in the host PVA (by hydroxyl-carboxylic acid hydrogen-bonding) and achieved excellent phosphorescence quantum efficiency over 24 % in air (Figure 1.10b). The authors also showed that the strength of these hydrogen-bonds can be reversibly modulated by water molecules for a unique fluorescence-to-phosphorescence switching behaviour from these polymer hybrids (Figure 1.10c).

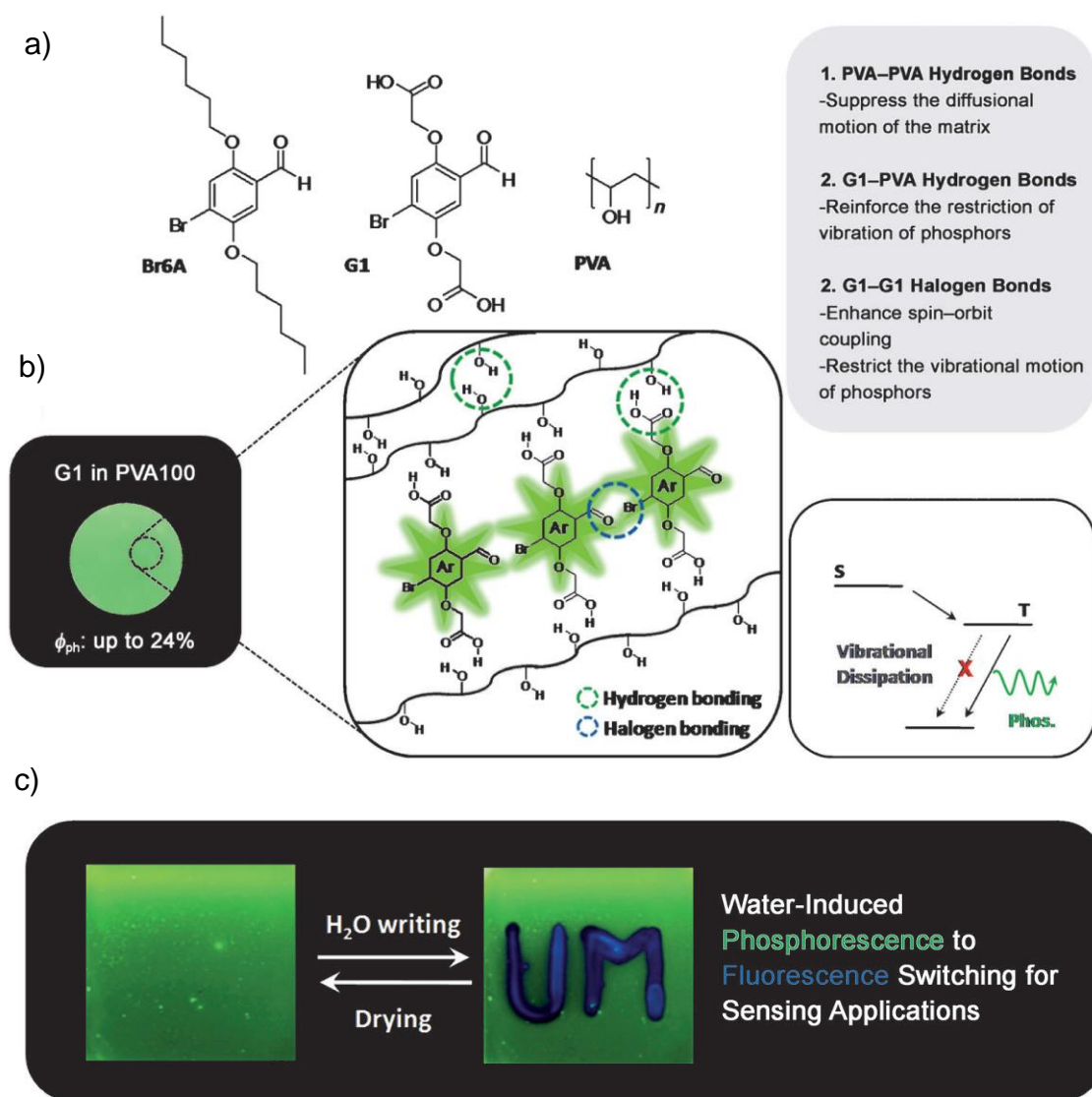


Figure 1.10. a) Chemical structures of **Br6A**, **G1**, and **PVA**. b) Photograph of phosphorescence emission (under 365 nm UV-lamp) and schematic illustration of phosphorescence processes in the **G1-PVA** hybrid film (right). c) Reversible direct writing of a fluorescent watermark on a **PVA** film embedded with **G1**. The characters “**UM**” were written with a water-soaked pen. (Reproduced with permission from Reference 16d)

Efficient RTP could also be achieved by doping organic phosphor molecules in rigid steroidal host like β -estradiol.^[20] In Figure 1.11, it can be seen that a heavily deuterated polyaromatic hydrocarbon (guest) exhibiting excellent RTP with visible afterglow feature. The authors successfully showed that the non-radiative decay pathways depend both on the non-radiative deactivation (e. g. vibrational motion) of the guest phosphors as well as diffusional quenching of the host steroidal matrix. In fact, excellent rigidity and oxygen-barrier property of the steroidal host and heavy deuteration of the guest molecules could effectively suppress both these quenching pathways. The authors studied a series of these deuterated phosphors to achieve

red-green and blue emitting ultralong/afterglow phosphors with good quantum efficiency (~10 %) and lifetime over 1 second.

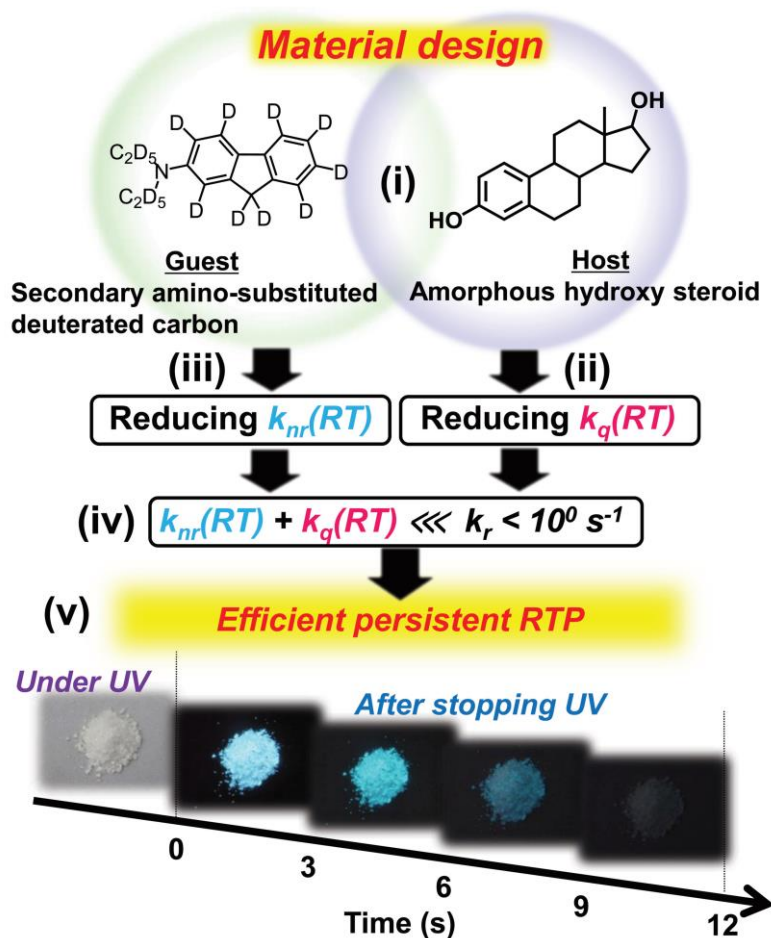


Figure 1.11. Design of a material based on a hydroxyl steroid host and a deuterated guest. (Reproduced with permission from Reference 20a)

1.4.2.3. Organic RTP in Solution State

Among all the reported RTP molecules till date, majority of the systems still rely on judicious crystal-engineering of small organic molecules in order to suppress the molecular motions. Also it has been proposed that rigid crystalline network is also effective to prevent oxygen diffusion in the matrix. On the other hand, amorphous state (e. g. doped polymer films) RTP emitters are extensively investigated for the past few years to circumvent the issues of crystal-state phosphorescence and has shown a tremendous growth in terms of efficiency and fundamental understanding. In this regard, solution state RTP from purely organic molecules still remains a daunting task and only a handful examples can be found in literature. For instance, Takeuchi and co-workers reported a brominated fluorene derivative, 7-bromo-9,9-didodecylfluorene-2-carbaldehyde (**Br-FL-CHO**), which exhibit green RTP emission at 500 nm in argon-purged CHCl_3 (Figure 1.12a-c).^[21a] Swager and co-workers developed iodo-substituted

benzo[2,1,3]thiadiazoles that showed weak red-RTP in degassed toluene.^[21b] Both these examples utilize the strong ISC efficiency of the chromophores and lack ambient triplet stability (Figure 1.12b). On the other hand, a generalized strategy based on supramolecular host-guest interactions was reported by Tian and co-workers to show unique reversible aqueous state RTP from a simple bromine-substituted isoquinoline (Figure 1.12d). The reduced vibrational and rotational motions of guest phosphor (**IQC[5]**) was shown to be minimized very efficiently inside the cavity of the cucurbit[7]uril host. More recently, Huang and co-workers have developed afterglow phosphorescence emitting organic nanoparticles for *in-vivo* bio-imaging applications (*vide infra*).^[21d] Nonetheless, there are only a handful of such examples and all of them require stringent oxygen-free conditions to produce feeble RTP emission.^[21] Needless to mention, solution state RTP holds a great promise for future development of state-of-the-art optical sensor (e. g. *in vivo* oxygen sensing) and background-free bio-imaging and hence require more focused approach. In this context, we have developed a unique organic-inorganic hybrid supramolecular assembly to show a universal strategy towards solution state RTP under fully ambient conditions. The design and photophysical properties of the system will be discussed in detail in Chapter 4.

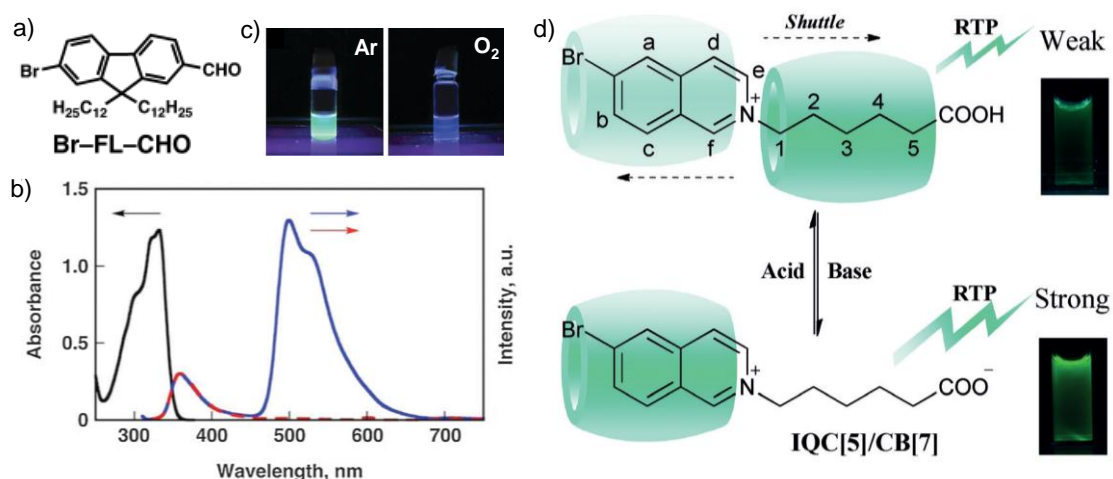


Figure 1.12. a) Molecular structure of **Br-FL-CHO** and its b) UV-Vis and emission spectra in CHCl_3 . Red line corresponds to the aerated solution whereas the blue line is Argon-purged resulting in RTP at 500 nm). c) Photographs of **Br-FL-CHO** dissolved in CHCl_3 while excited at 365 nm. d) Example of a supramolecular RTP system where reversible inclusion phenomenon of the binary **IQC[5]/CB[7]** complex is shown. (Figure 1.12.a-c and 1.12d are reproduced with permission from References 21a and 21c, respectively).

In this Thesis we majorly focus on understanding RTP mechanism and systematically underpin the design principles of these materials in crystalline state, amorphous state and even in aqueous state with minimum synthetic efforts and excellent efficiencies.

1.5. Applications of Organic Phosphors

1.5.1. Organic Light Emitting Diodes (OLEDs)

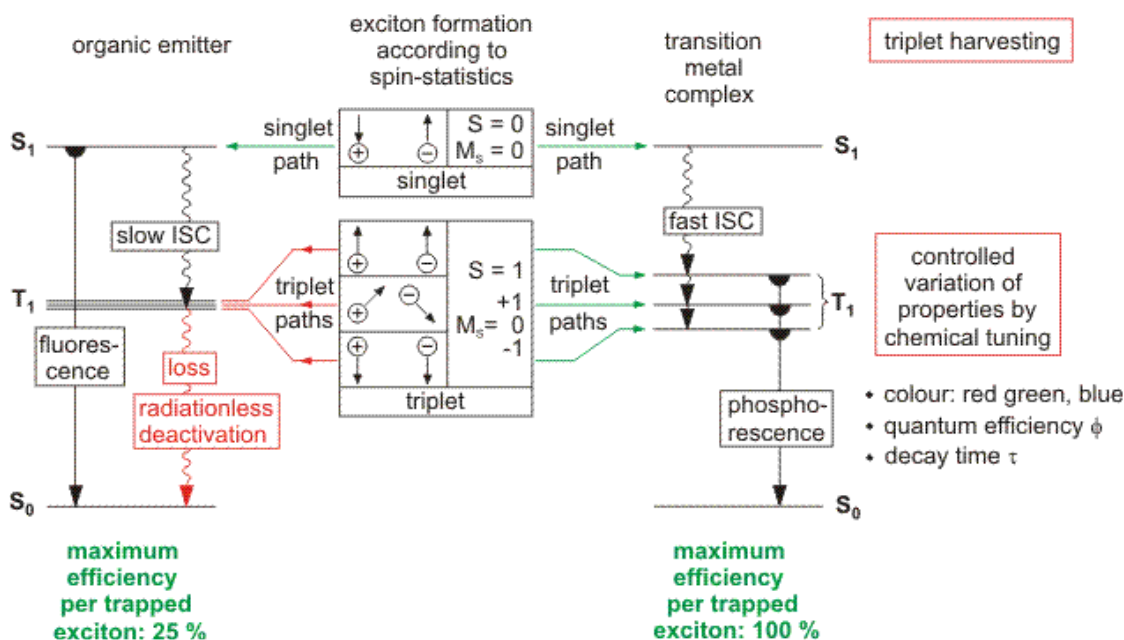


Figure 1.13. Schematic representation of spin-management in organic electroluminescent devices. (Reproduced with permission from Reference 22)

The most pre-eminent application of phosphorescent materials is in the field of organic light emitting diodes (OLEDs). It has been a paradigm shift in the electroluminescence technology since the advent of organometallic phosphorescent molecules as emitting layer in organic light-emitting diodes in late 1990s.^[9] The inherent degeneracy of triplets naturally takes a precedence over singlets in terms of exciton managements in these devices. As can be seen from Figure 1.13, the singlet and triplet excitons are formed in a 1:3 ratio (singlet: triplet) in OLEDs.^[22] For phosphorescence materials, one can achieve 100 % internal quantum efficiency (IQE) as all of the electrically generated excitons can emit as phosphorescence (all singlets goes to triplet state via ISC). On the other hand, purely organic fluorescent molecules suffer from non-radiative triplet deactivation and 75 % of the electrically generate excitons are wasted as heat, leading to maximum 25 % IQE in fluorescent OLEDs. Therefore, organometallic phosphorescent materials has been shown experimentally to be roughly 3 to 4 times higher in overall device efficiency and they were able to outperform the fluorescence based OLEDs for potential commercial applications. Since the first report of a Pt-porphyrin based phosphorescence OLED

(PhOLED),^[9a] the field has matured and gained popularity in the state-of-the-art solid state lighting technologies. In fact, they are already commercialized in many widely-used display screens (e. g. television or cellphone etc.). Examples of some of these commercial products using organometallic phosphorescent OLEDs are given in Figure 1.14.

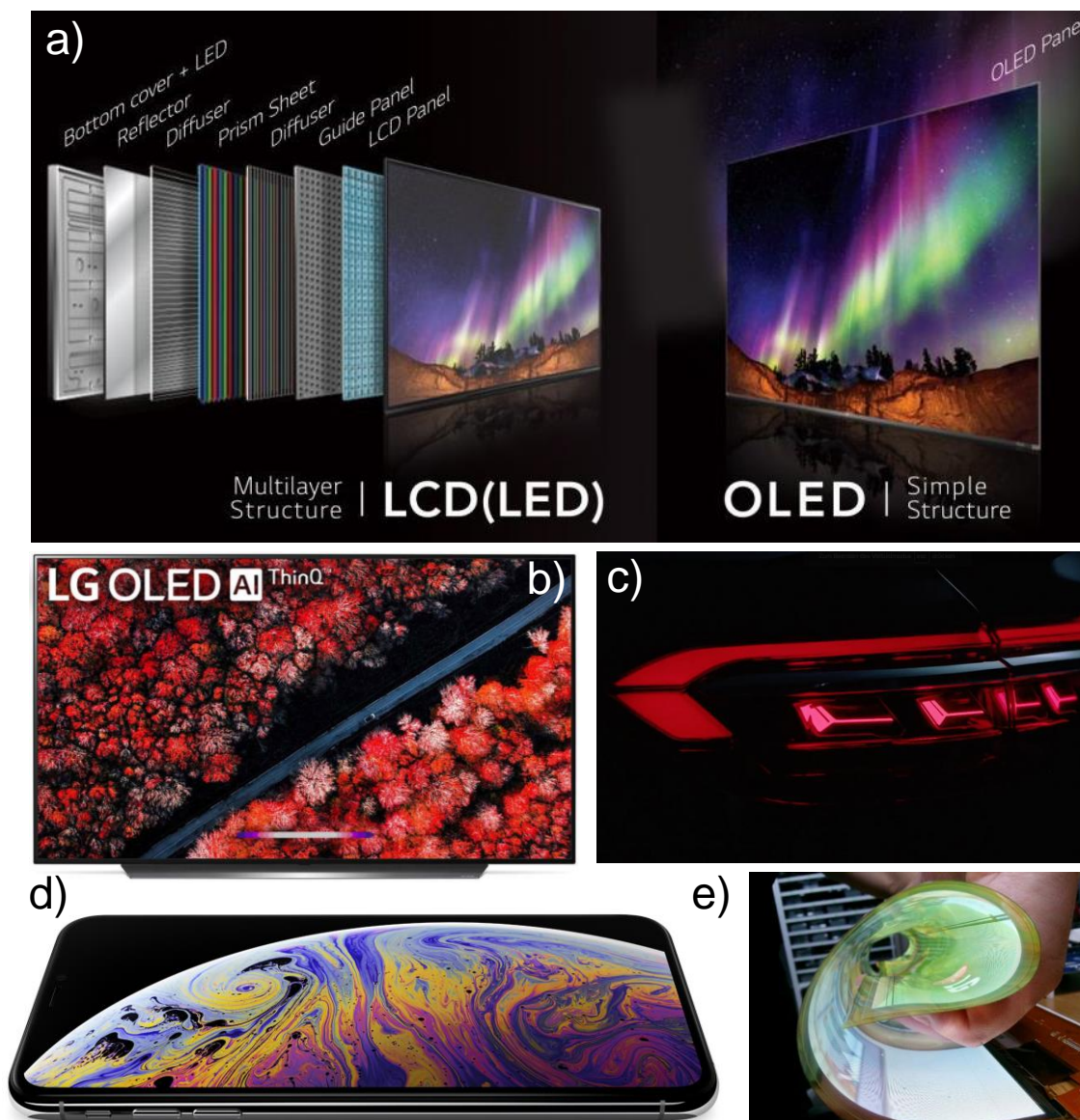


Figure 1.14. Applications of OLED devices in state-of-the-art lighting technology. a) Comparison of device structures between LCD (LED) and an OLED taking an example of modern television screens.^[23] b) LG's 55-inch Full-HD OLED TV,^[24] c) Hella's car rear-light OLED-module equipped in Audi A8,^[25] d) Apple's new iPhone XS and iPhone XS Max cellphones manufactured with OLED screen.^[26] e) LG's 18-inch flexible transparent display.^[27]

The popularity and growing acceptance of phosphorescent OLEDs over traditional inorganic ceramic based (e. g. GaN) LEDs or liquid crystal displays (LCDs) is because of its versatility in design and easy low-temperature fabrication. In addition, most widely used LCD displays needs highly energy consuming backlighting panel (made of inorganic LEDs) and therefore can never produce high-contrast (true black) images. As can be seen from Figure 1.14a, the device structure of these inorganic LED (LCD) devices is very complicated and difficult to miniaturize. On the other hand, phosphorescent OLEDs are simple in terms of device structure (Figure 1.14a and 1.15a) thus offering flexibility in device engineering and they are already being marketed as thin/flexible displays which is both aesthetic and energy-efficient. These devices do not require any backlighting and individual pixels can be illuminated upon electrical injection. This property ensures energy-efficiency and high-contrast display in an OLED. Figure 1.15a represents a simplified device structure of one such pixel. Such versatility and excellent device efficiencies have made phosphorescent OLEDs to become the frontrunner in the modern display technologies although they still suffer from suboptimal fabrication costs and device lifetimes. So far, most of the industrial and academic research on these OLEDs focused on investigating organometallic complexes (mostly Iridium) as the emissive component in the device. This in turn, require managing the cost-effectiveness, stability issues especially in the blue and UV region. Moreover, these materials are still thermally evaporated under vacuum during the device fabrication which further increases the overall cost. In addition, the purity of organometallic complexes has been an issue for a long time as trace amount of metal impurity often lead to the shortening of the device lifetime and this particular problem probably can never be solved. In addition, only a few metals (e. g. Ir) have shown promise in high-efficient phosphorescent OLEDs when chelated with suitable aromatic ligands (Figure 1.15b) and hence there is always a deficiency in material (suitable metal-ligand combination) availability to study these systems comprehensively.

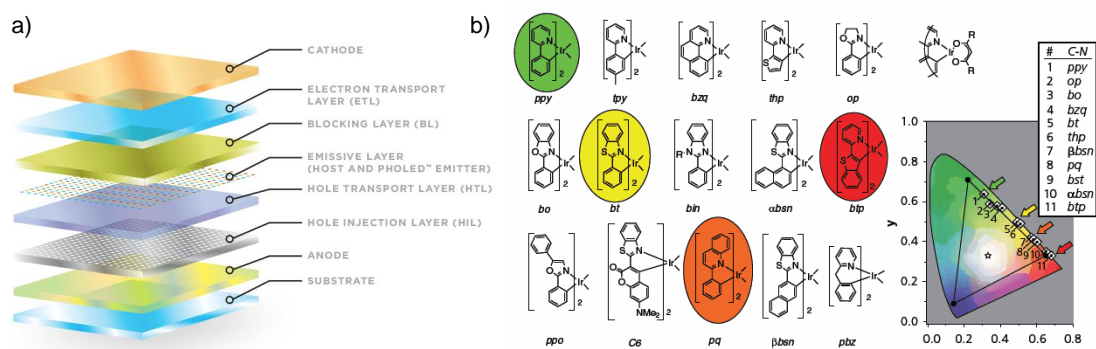


Figure 1.15. a) Simplified device architecture of an OLED device (one pixel).^[28] b) Examples of commercially available Ir-complexes used in phosphorescent OLEDs as emitting layer.^[29]

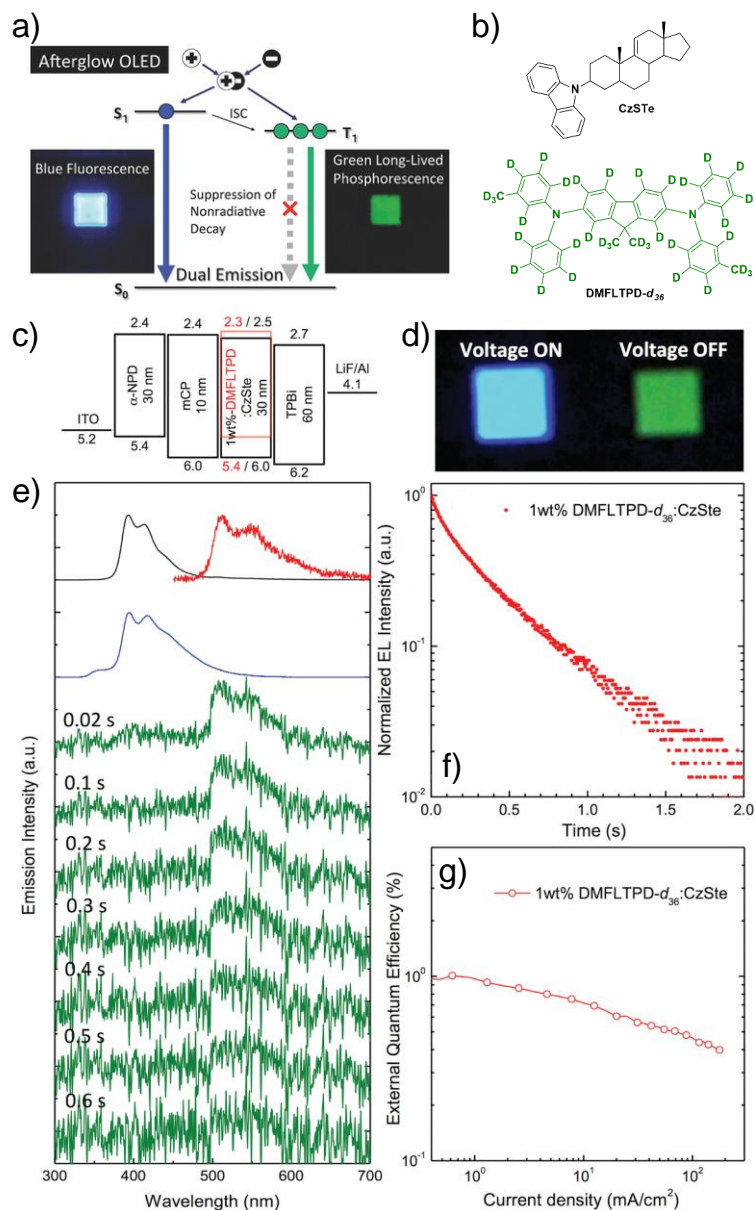


Figure 1.16. a) Schematic representation of an OLED based on metal-free organic phosphor. b) Molecular structure of the emitting layer and c) OLED device structure showing energy levels (in eV). d) Photographs of electroluminescence during (left) and after (right) electrical excitation. e) Fluorescence (black) and phosphorescence (red) spectra of a doped **CzSte** film, and electroluminescence spectra obtained for an OLED with **CzSte** as a host and **DMFLTPD-d₃₆** as dopant at different times during (blue) and after (green) electrical excitation. f) Transient electroluminescence decay curve of the device after the applied voltage was turned-off. g) EQE-current density characteristics of the OLED. (Reproduced with permission from Reference 30).

Therefore, purely organic molecules offer more flexible, low-cost alternative and they can also solve the problem of impurity as well as the scalability of the lead molecules. In fact, very recently, device prototype of “metal-free” phosphorescent OLEDs has been reported in literature although more optimizations will be required to attain the efficiency levels of organometallic phosphors (Figure 1.16).^[30] The main reason behind the poor performance of metal-free phosphorescence emitters as OLED materials stems from their typical high lifetime and low photoluminescence quantum efficiency. The first factor is especially detrimental because longer lifetime increases various non-radiative channels like triplet-triplet annihilation, triplet-singlet annihilation etc. and ultimately reducing the chance of phosphorescence decay. Nonetheless, it is very important to mention at this juncture, that thermally activated delayed fluorescence (TADF) emitters have emerged as a true competition to the organometallic phosphors and is expected to reach markets in another couple of years. We shall be discussing the exciton management of these novel TADF-emitting molecules in the next section and give a comprehensive overview of the current status and future challenges related to the design on the context of emission mechanism.

1.5.2. Optical Sensing and Bio-imaging

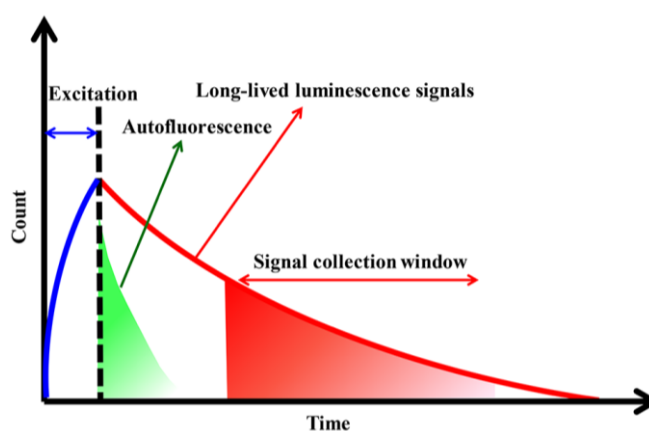


Figure 1.17. Principle of time-gated photoluminescence imaging. (Reproduced with permission from Reference 31a)

The spin-forbidden nature of phosphorescence emission renders in the huge difference in their radiative lifetime as compared to the fluorescence emission. This differential or broad lifetime range has been utilized as advanced optical sensing or bio-imaging applications. The interesting feature of such molecular probe utilize the advantage of measurements on a delayed-time scale, after the excitation source is turned off (Figure 1.17). Such unique lifetime feature has been well-exploited in bio-imaging applications where the problems of short-lived

autofluorescence of the cells can be easily countered by the long-lived emission of phosphor luminogens. In fact, the long-lived phosphorescence signals can be deconvoluted to images directly from the lifetime and hence a temporal evolution of the dynamic sensor-analyte interactions can be imaged in real time. Although majority of these molecular probes are still based on inorganic or organometallic phosphors, recent advancement in metal-free afterglow phosphor materials have shown remarkable potential to outperform the toxic metal based probes.^[31]

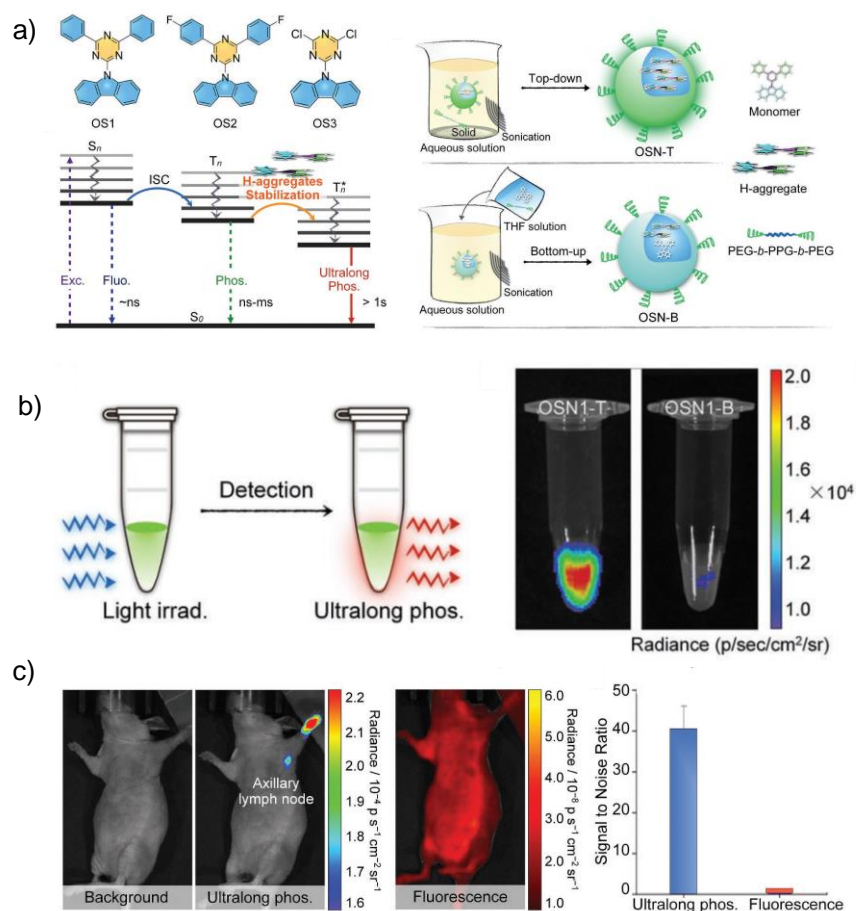


Figure 1.18. Example of *in vivo* afterglow bio-imaging. a) Molecular structures of the organic phosphors, their emission mechanism and schematic representation of nanoparticle synthesis in presence of the host polymer **PEG-b-PPG-b-PEG** both by top-down and bottom-up methodologies. b) Schematic illustration of ultraviolet activation and visible detection of ultralong phosphorescence in solution state. Nanoparticles synthesized by bottom-up methodology (**OSN1-B**) show relatively poor performance. c) Ultralong phosphorescence and fluorescence imaging of lymph node with very high signal to noise ratio in living mice 1 h after the intradermal injection of **OSN1-T** nanoparticles into the forepaw of mice. (Reproduced with permission from Reference 21d).

For instance, in 2017, Pu and co-workers have demonstrated the proof-of-concept application of a time-gated bio-imaging utilizing a metal-free afterglow phosphor as the probe.^[21d] They synthesized phosphor-encapsulated polymer nanoparticles by a top-down formulation and used the resulting afterglow nanoparticles for *in vivo* afterglow imaging in a living mice (Figure 1.18). The emission signal could be detected, seconds after the removal of incident light source with a remarkably high resolution (with signal to noise ratio of 40) by eliminating the tissue autofluorescence. This study clearly show the efficacy of afterglow phosphor materials as future biological probes and further modification in the molecular design will be very interesting to realize red/NIR afterglow emission for better penetration length and deep-imaging of live tissues.

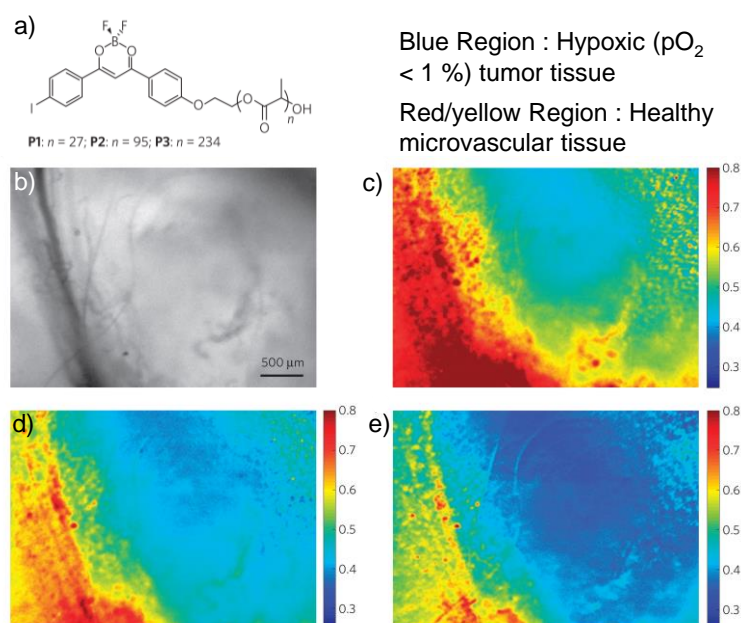


Figure 1.19. *In vivo* oxygen mapping for hypoxia imaging using phosphorescent boron nanoparticles (BNPs). a) Molecular structure of the phosphorescent polymer. *In vivo* imaging of the breast cancer 4 T1 mammary carcinoma tumour region in a mouse window chamber model showing the b) bright-field and BNP fluorescence/phosphorescence ratio while breathing c) carbogen-95 % O_2 , d) room air-21 % O_2 and e) nitrogen-0% O_2 . Dark lines in the bright-field image represent the blood vessels that run vertically quenching has been utilized to develop highly sophisticated optical-sensing materials such as *in*; More oxygenated yellow-red regions in the fluorescence/phosphorescence images undergo a detectable change in different oxygen concentration, whereas, the hypoxic tumour tissues (to the right side of the blood vessels, blue region) remain unchanged because of the low concentration of oxygen leading to low phosphorescence/fluorescence ratio. (Reproduced with permission from Reference 32).

Another important aspect of phosphorescent materials is their sensitivity towards molecular oxygen and temperature (heat). In fact, this apparent disadvantage of oxygen mediated *in vivo* oxygen mapping and developing “oxygen-sensitive” programmable luminescent tags.

Fraser and co-workers demonstrated the use of polymeric phosphorescent nanoparticles to do an *in vivo* tissue oxygen mapping (Figure 1.19).^[32] In this work the authors successfully mapped a hypoxic tumour cells which consumes the oxygen in high concentration, leaving the partial oxygen pressure below 1 % in the tissue. Utilizing the dual fluorescence and phosphorescence characteristics of their boron nanoparticles (**P2 BF₂dbm(I)PLA**) they mapped the hypoxic region (blue) and the normal (healthy) microvascular region (red/yellow) by varying the oxygen concentration in a living mouse (inhalation of gases with different oxygen concentration). In Figure 1.19c-e, the fluorescence intensity is a reference signal for the measurement of the relative intensity of phosphorescence. In this way, qualitative determination of the oxygen concentration in a particular region was done.

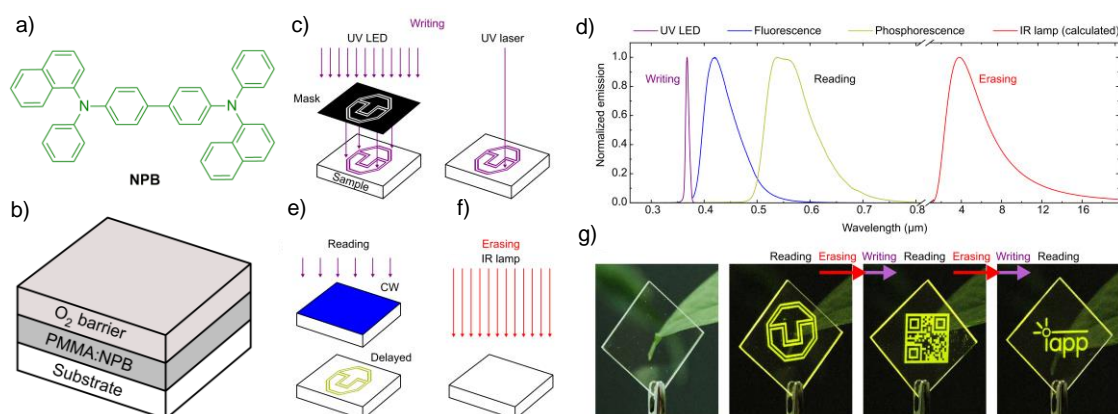


Figure 1.20. Programmable luminescent tags using amorphous state organic afterglow phosphorescence. a) Molecular structure of the phosphor and b) device structure of the system utilized for programmable labelling experiments. Overview of writing, reading and erasing procedure. c) Writing: Masked UV illumination used for the images in (g) and proposed straight laser ray writing. d) Different spectral domains used for different cycle steps. Data writing is realized with a 365-nm LED, the biluminescent NPB molecule emits at 420 nm (fluorescence) and 530 nm (phosphorescence). IR light peaking at 4 μm is used for erasing by inducing local heating. e) Reading: High luminescent contrast is achieved by phosphorescence on mask-illuminated areas in delayed emission. f) Erasing: By heating the sample through IR illumination, the programming is erased within around 1 min. g) Different phosphorescent images written successively onto the same transparent substrate. The time span between the afterglow images is about 5 min. (Reproduced with permission from Reference 33).

Very recently, Reineke and co-workers have developed unique “programmable luminescent tags” by utilizing the reversible afterglow phosphorescence emission highly sensitive to oxygen. In this work, the authors have used a commonly used hole-transporting molecule, N,N'-Bis(naphthalen-1-yl)-N,N'-bis(phenyl)benzidine or NPB and dispersed in polymethylmethacrylate.^[33] This hybrid polymer layer was then coated with an O₂-barrier layer (ethylene-vinyl alcohol copolymer). By IR-irradiation the sample temperature rises to ~100 °C and it causes an additional oxygen refilling due to the increased permeability of the top O₂-barrier layer leading to the termination of phosphorescence emission. Upon cooling down the sample to room temperature the afterglow RTP could be restored. In this way the authors could show 40 cycles of such reversible phosphorescence writing-erasing with a detectable intensity (Figure 1.20). This work describes a simple, but very powerful protocol for a state-of-the-art luminescence labelling technology using amorphous-state organic afterglow phosphorescence.

1.6. Ambient Triplet Harvesting via Thermally Activated Delayed Fluorescence (TADF)

In this section, we will discuss the TADF mechanism which has been shown to be highly promising as an alternative to organometallic phosphors to obtain high-performance OLEDs with similar efficiency. As mentioned earlier in Section 1.5.1, triplet exciton harvesting will ensure at least three time more internal quantum efficiency as compared to singlet emitting fluorescent materials (spin-statistics). The first breakthrough in the harvesting triplet excitons in an OLED device was achieved by Forrest and co-workers in 1998 using a “heavy” Pt-based porphyrin complex.^[9a] Extremely fast intersystem crossing from singlet excited state to “emissive” triplet states could be achieved by strong SOC provided by the heavy Pt-atom, for both S₁→T₁ (ISC) and T₁→S₀ (phosphorescence). This in turn, resulted in a 100 % IQE (Figure 1.21a). As we have already discussed about these organometallic phosphors in their of design and their emission mechanism, we shall now discuss the “alternative” pathway to achieve similar triplet exciton harvesting (management) *en route* to 100 % IQE in a metal-free system. The only difference here is that, the triplets are harvested somewhat “indirectly” to emit from a “singlet” excited state as “delayed fluorescence”. The delayed fluorescence mechanism^[34] can be classified mainly into three categories which are described below:

1.6.1. Triplet-triplet Annihilation Delayed Fluorescence (TTA-DF)

In this mechanism, two triplet excitons upon bimolecular collision with each other result in a high energy singlet exciton.^[35] The necessary excited state energy requirement for this process to occur, is given as: $2T_1 \geq S_1$. This means, one has to maintain a very large energy gap

between the lowest singlet and triplet excited states, so that the $2T_1$ energy is slightly above the S_1 energy (Figure 1.21b). This necessary energy requirement is not very easy to achieve and most of the TTA-DF emitters are therefore based on anthracene and related derivatives and hence the molecular design is limited. In addition, these materials cannot fully achieve a 100 % internal quantum efficiency, since, two triplet excitons are consumed in order to produce one singlet. Therefore, maximum IQE utilizing this process is $(25\% + 0.5 \times 75\% = 62.5\%)$.

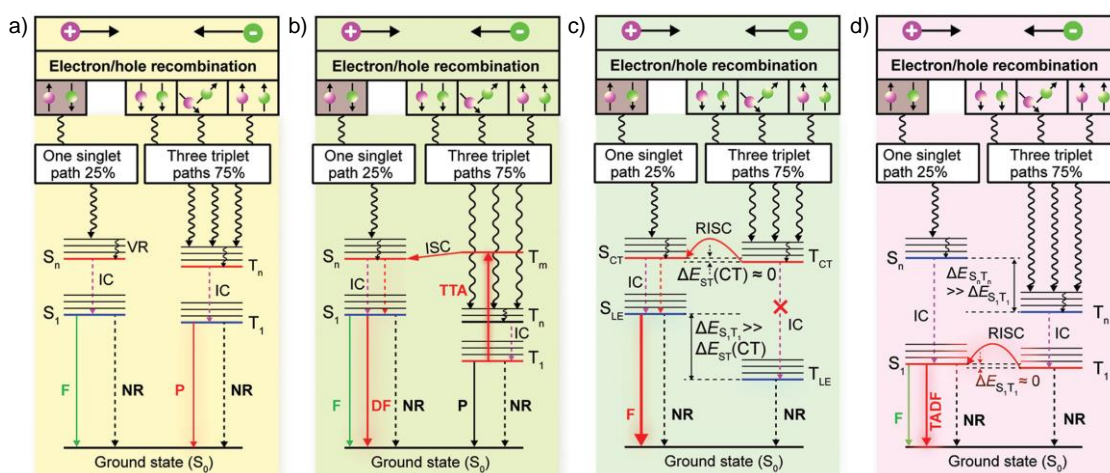


Figure 1.21. Mechanism of various triplet harvesting processes in OLED devices. a) Phosphorescence, b) Triplet–triplet annihilation delayed fluorescence (TTA-DF), c) delayed fluorescence in a hybridized local and charge-transfer (HLCT) excited state structure and d) thermally activated delayed fluorescence (TADF). F = Fluorescence, P = Phosphorescence, IC = Internal Conversion, ISC = Intersystem crossing, RISC = Reverse Intersystem Crossing, VR = Vibrational Relaxation, NR = Non-radiative relaxation and ΔE_{ST} represents the singlet-triplet energy gap. (Reproduced with permission from Reference 34d)

1.6.2. Upper Triplet Crossing

Another approach to upconvert the “non-emissive” triplet states to “emissive” singlet state is upper triplet crossing, this process is also known as a “hot exciton” delayed fluorescence.^[36] Here, the RISC takes place between higher excited triplet state (T_n , $n>1$) and singlet states (S_n , $n>1$) followed by a rapid internal conversion to lowest S_1 state and subsequent DF emission. The mechanism require two closely-lying high energy charge-transfer states (Figure 1.21c) that take part in reverse intersystem crossing and then quickly relax back to locally excited singlet state (S_1). Since, the whole process require a sequential involvement of both high energy CT excitons (hot excitons) and locally excited (cold excitons), they are synonymously called hybridized locally-excited charge transfer (HLCT) delayed fluorescence emitters.

Designing these chromophores is very challenging, because it requires a complete blockade of T_n (CT) $\rightarrow T_1$ (LE) internal conversion (violation of Kasha's rule). This is very difficult as the internal conversion is a very fast, spin-allowed, thermodynamically favourable process, in comparison to the very slow, spin-forbidden and energetically uphill RISC process. Only a few examples are available in the literature which successfully demonstrate this process and hence this field did not get much attention despite the possibility of achieving 100 % IQE in the OLEDs.

1.6.3. Thermally Activated Delayed Fluorescence (TADF)

TADF emitters have emerged as the most efficient way of harvesting triplet excitons in metal-free organic compounds which utilizes a RISC process between very close-lying T_1 and S_1 states. When the gap between S_1 and T_1 state is very low (few tens of meV), the thermal activation can facilitate this RISC process and generate delayed fluorescence ($S_1 \rightarrow S_0$) to intensify the overall luminescence of the molecule. Although, the concept of TADF phenomenon was given long back in the pioneering works of Perrin^[37] and later by Lewis/Kasha,^[11] its systematic investigation as well as practical applications have been done only during the last decade, by Adachi and co-workers.^[38] In fact, Adachi's lab first demonstrated that 100 % IQE could be achieved by very simple metal-free compounds in an OLED device. This landmark work^[38a] has been extended over the next few years to achieve equal efficiency of state-of-the-art PhOLEDs and expected to hit the market for commercial display in coming years.

The key photophysical processes in TADF include a fast prompt fluorescence (PF) and longer-lived delayed fluorescence (DF) component and they are distinguished by their differential lifetimes at the same monitoring wavelength (PF and DF usually have same spectral distribution except for few cases). In Figure 1.22, the key excited state processes are shown under optical as well as electrical excitation modes.

When a TADF molecule is excited optically (Figure 1.22a), through intersystem crossing process, triplet excited state (T_1) is populated from initially formed excited singlets (S_1). Following this, the triplet excitons up convert to the S_1 state and finally fluoresce at a longer time-scale (usually few μ s to ms) as compared to the prompt fluorescence with typical lifetimes of few ns. In this Thesis, we shall be dealing with the optically excited TADF processes (Chapters 5 and 6).

On the other hand, under electrical excitation (e. g. OLEDs), the mechanism is slightly different. The whole process is divided in four steps (Figure 1.22b). First, as per the spin-statistics (electron-hole recombination), 75 % triplets and 25 % singlets are formed. Then, these high energy excitons quickly relax to lowest excited S_1 and T_1 states (similar to a photoexcited process

that follow Kasha's Rule) via a rapid vibrational relaxation and internal conversion. Following this, the lowest excited T_1 state upconverts to S_1 state by thermal activation at the experimental temperature via RISC process. At the end, singlet excited states populated by these "extra" triplet excitons emit as delayed fluorescence (Point to note: Initially formed S_1 excitons emit quickly as prompt fluorescence in the first few nanoseconds of the electrical excitation). The PF and DF emission identified by their starkly different lifetimes as we have discussed in the previous section.

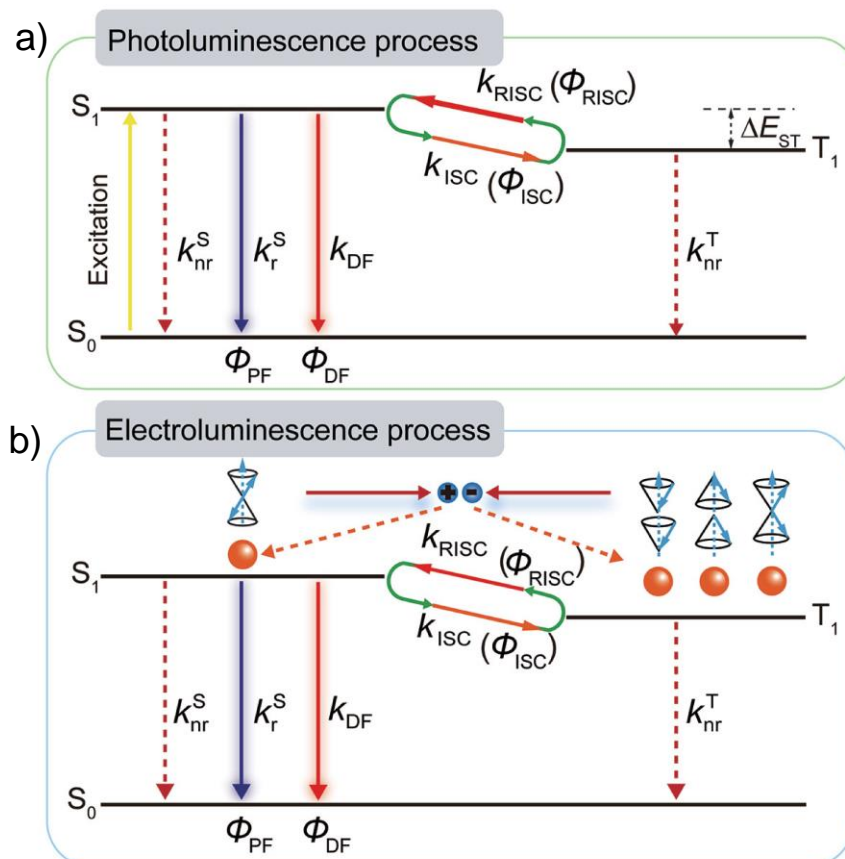


Figure 1.22. a) Photoluminescence and b) electroluminescence processes in TADF molecules. k_r^S and k_{DF} are the rate constants of PF and DF processes, respectively; k_{ISC} and k_{RISC} are the rate constants for the ISC and RISC rate constants, respectively; k_{nr}^S and k_{nr}^T are the non-radiative decay constants of S_1 and T_1 respectively; Φ_{PF} , Φ_{DF} , Φ_{RISC} , and Φ_{ISC} represent the prompt fluorescence efficiency, TADF efficiency, reverse intersystem crossing efficiency and intersystem crossing efficiency, respectively. (Reproduced with permission from Reference 34d).

Here it must be pointed out that, T_1 is always lower in energy than the S_1 state (Hund's rule of spin multiplicity). Hence, there is always a competitive ISC process which further regenerate the triplet state even after the first cycle of RISC is over. In fact, it has been seen, the

ISC rate is generally faster than the rate of RISC. Therefore, there is a balance of S_1 and T_1 exciton distribution in such TADF molecules and T_1 will have more population as it stays energetically lower. This in turn indicates that, in order to harvest “all” triplet excitons, the key parameter is maximization of the rate or extent of reverse intersystem crossing process. It has been shown that, to achieve a quantitative RISC to take place the optimum energy gap between the S_1 and T_1 states has to be below ~ 100 meV at room temperature.^[34] The design strategy to achieve such energy gap is the fundamental in any TADF molecule and in the next section we shall be describing it in more detail.

1.6.3.1. Basic Rules for Designing the TADF molecules

In the previous section we have seen that the rate of reverse intersystem crossing from $T_1 \rightarrow S_1$ state determine the efficiency of the TADF mechanism. The rate of RISC (k_{RISC}) is given in equation 1.3.

$$k_{RISC} \propto \exp\left(-\frac{\Delta E_{ST}}{k_B T}\right) \quad (1.3)$$

Here, k_B is the Boltzmann Constant and T is temperature, ΔE_{ST} is the energy gap between the lowest excited singlet and triplet states. Therefore, it is very clear that, to enhance the rate of RISC, the energy gap, ΔE_{ST} must be as low as possible (ideally few tens of meV). There are few different aspects which must be discussed to understand how one can effectively minimise this gap. First, by calculating the lowest excited singlet and triplet state (S_1 and T_1) energies which depends on three factors and expressed in equations 1.4-1.6:

- The energy gap between the HOMO and LUMO orbitals (See Figure 1.1, each electron is residing in HOMO and LUMO orbitals of S_1 and T_1 levels);
- The electron repulsion energy (K) (This is a first order Coulombic correction);
- The exchange energy (J) (This is a first order quantum mechanical correction due to electron-electron repulsion following the Pauli’s Exclusion Principle).

$$E_{S1} = E_{HOMO-LUMO} + K + J \quad (1.4)$$

$$E_{T1} = E_{HOMO-LUMO} + K - J \quad (1.5)$$

$$\Delta E_{ST} = E_{S1} - E_{T1} = 2J \quad (1.6)$$

For S_1 and T_1 states with a fixed nuclear configuration, the $E_{HOMO-LUMO}$, K and J , all contribute equally. However, because of the different spin arrangement in T_1 state, the exchange energy term (J) increases the overall energy of the S_1 state, while decreasing the energy of the T_1 state by similar extent. Therefore, despite the positive values of both J and K terms (both stems from electron-electron repulsion), there is a negative sign in equation 1.5. Further, from equation 1.6,

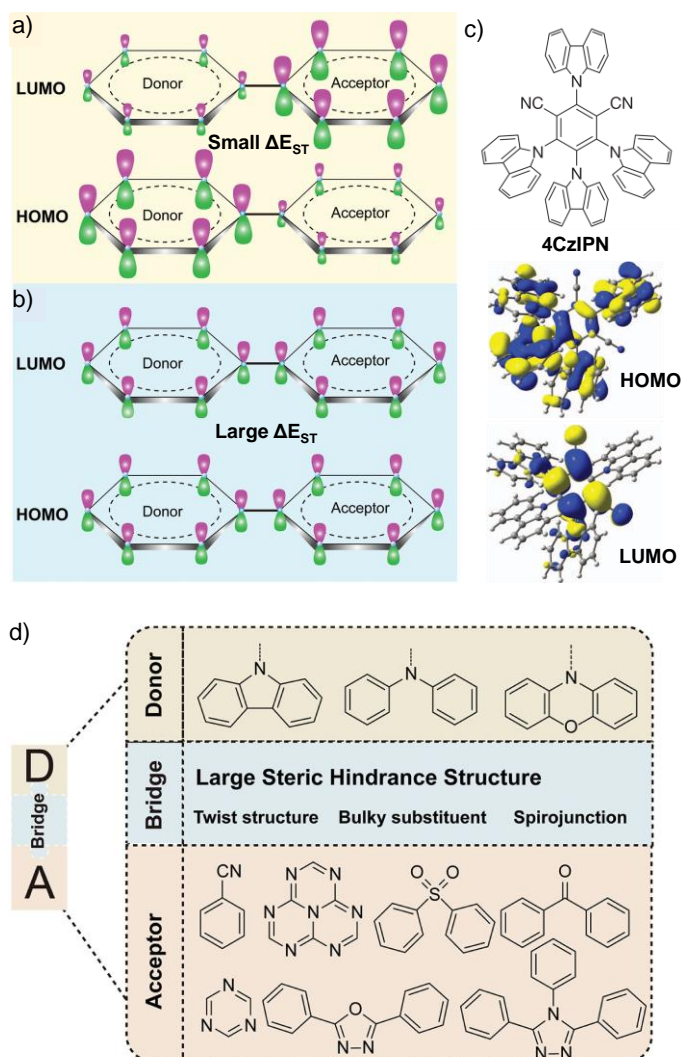


Figure 1.23. Schematic representation of the small a) and large b) overlap between HOMO and LUMO orbitals leading to small and large ΔE_{ST} , respectively. c) Molecular example of a typical donor-acceptor (D-A) type TADF molecule (**4CzIPN**) along with their spatially separated frontier molecular orbital isosurfaces. d) Schematic presentation of some of the representative intramolecular D-A type TADF molecules. (Figure 1.23a, b and d reproduced with permission from Reference 34d; Figure 1.23c reproduced with permission from Reference 38a).

we see that the energy gap between the lowest singlet and triplet excited states (ΔE_{ST}) is twice the exchange energy term ($2J$). Hence, in order to reduce this ΔE_{ST} value, one has to reduce the exchange energy between the electrons residing in HOMO and LUMO orbitals. From quantum mechanical standpoint of exchange energy, it is mathematically expresses as:

$$J = \iint \phi(r_1)\psi(r_2) \left(\frac{e^2}{r_1-r_2} \right) \phi(r_1)\psi(r_2) dr_1 dr_2 \quad (1.7)$$

Here, ϕ and ψ represent the HOMO and LUMO wavefunctions, respectively and e is electrons charge. It is assumed that the excited states under discussion (i. e. S_1 and T_1 states) are pure HOMO \rightarrow LUMO transitions. In the other cases (i. e. if the S_1 and T_1 state are combination of other transitions such as HOMO \rightarrow LUMO, HOMO-1 \rightarrow LUMO, HOMO \rightarrow LUMO+1 for instance), ϕ and ψ are replaced with the many-body electronic wavefunctions for the singlet and triplet states, respectively.^[39]

Therefore, J can be minimised by reducing the spatial overlap between the HOMO and LUMO orbitals. This is achieved by designing molecules with donor-acceptor subunits that facilitate (donor \rightarrow acceptor) electron transfer in the excited state leading to strong charge-transfer characteristics in the molecule (Figure 1.23). TADF molecules are typically donor-acceptor molecules where the subunits are covalently linked by aromatic bridges, spiro-junction or a simple sp^3 hybridized carbon (e. g. $-CH_2$ or $-CF_2$) to further reduce the spatial overlap because of a near orthogonal conformation of the donor/acceptor subunits. However, it is noteworthy to mention, a $\sim 90^\circ$ relative orientation of donor-acceptor units would completely decrease the oscillator strength (ν is proportional to J) of emission. Therefore, it is always a counterproductive situation while designing a TADF material with low ΔE_{ST} and simultaneous high oscillator strength of emission.

We shall see in this Thesis work that, there are several other factors both in terms of conformational aspect as well as relative energy levels, which also play rather pivotal role for efficient TADF emission as compared to simple minimization of ΔE_{ST} . In Chapters 5 and 6, we shall be discussing these aspects in a comprehensive manner, considering the ongoing discussion sets the basic criteria of TADF design from a purely theoretical chemistry standpoint.

1.6.3.2. Application of TADF materials

It has been well-established that TADF-emitting materials are on their way to replace the existing fluorescent (e. g. polymer LEDs) and phosphorescent OLEDs because of their cost-effective, environment-friendly and very high external quantum efficiency (EQE already reached over 36 %). Interestingly, such a high EQE can be regularly obtained in a simple OLED structures, without the need of special wave-guiding layers that improves the light outcoupling effects. Since the pioneering work of Adachi and co-workers in 2012,^[38a] these small molecule TADF systems have been exploited to achieve all colour electroluminescence with excellent efficiency (Figure 1.24). Most notably, TADF emitters have already shown promise in replacing less-efficient blue fluorescent emitters which are used for blue as well as white-emitting OLEDs, commercially. In fact, despite a rigorous investigation to develop “stable” blue emission using

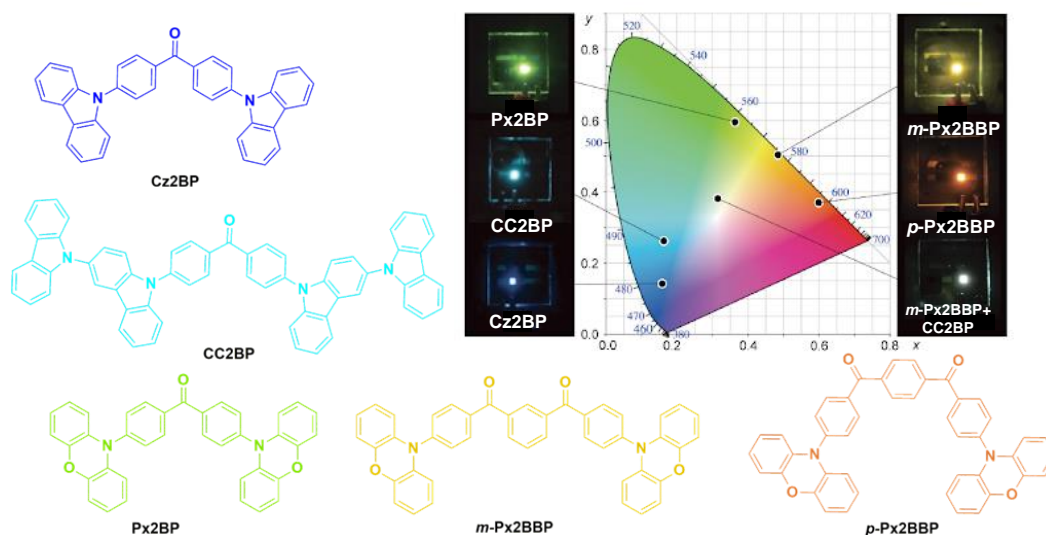


Figure 1.24. Representative examples of intramolecular D-A type TADF chromophores used in OLED devices. (Reproduced with permission from Reference 40).

the organometallic phosphors for over 20 years, there is no clear answer or roadmap for achieving this critical feat. More information about this topic can be found in reference 41. Nonetheless, there are few challenges which still need to be solved in order to get TADF more attractive than the other existing solid state lighting technologies. One of these issues is that the TADF systems suffer from is their complicated emission mechanism. Mechanism of TADF is still highly debated, especially on the involvement of locally excited triplet states in the RISC process. More insights into RISC process would plausibly overcome the problem of slow rate of charge-transfer emission (usually in the order of $\sim 10^4$ to 10^6 s $^{-1}$) which has been shown to increase the efficiency roll-off at high brightness in an OLED device. Secondly, the inherent broad emission characteristics of TADF charge-transfer emission is not desirable for colour-pure pixels in a device. To counter this problem, Adachi and co-workers have developed a unique “hyperfluorescence” methodology (Figure 1.25). In this process, Förster Resonance Energy Transfer (FRET) from charge-transfer TADF emitters to highly emitting fluorescence dopants is done in an OLED device which simultaneously improves the device colour-purity as well as operational lifetime. Very recently, WiseChip Semiconductor Inc. (in collaboration with Kyulux Inc.) has announced world's first Hyperfluorescence OLED display. This is a 2.7" monochrome yellow 128×64 passive-matrix OLED which shows high brightness (220 nits) and remarkably high operational lifetime of 50,000 hours.^[43]

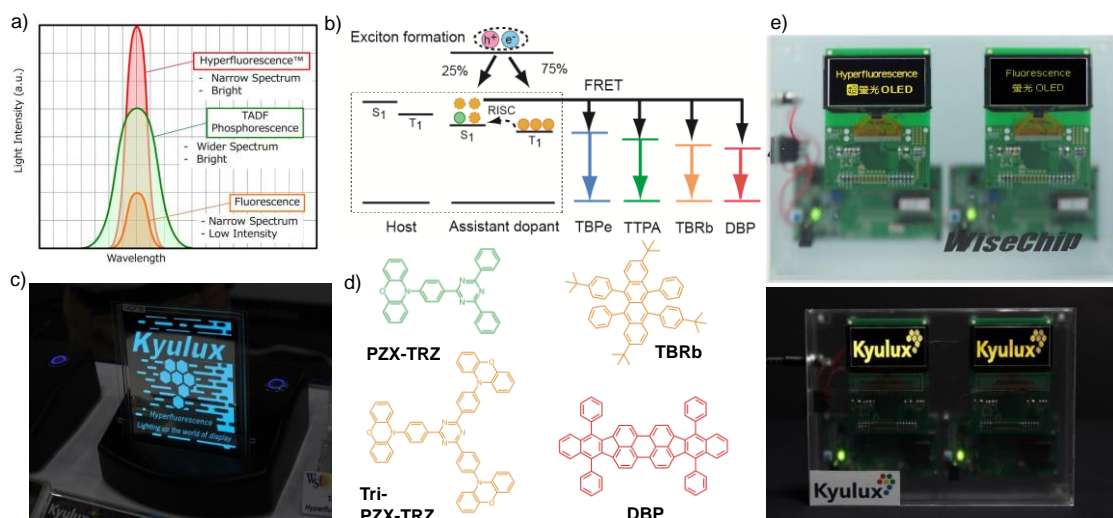


Figure 1.25. Principle and applications of Hyperfluorescent OLEDs (HF-OLEDs). a) A schematic representation of different emission mechanisms and their typical bandwidths.^[42] b) Mechanism of Hyperfluorescence involving a FRET from TADF donors to fluorescent acceptors. c) Device prototype of a blue-emitting HF-OLED manufactured by Kyulux Inc.^[42] d) Example of typical TADF (donor)-fluorescence emitter (acceptor) pairs used in HF-OLEDs. e) Commercial device prototype of HF-OLEDs that show very high operational lifetime (>50,000 hours) developed jointly by WiseChip Semiconductor Inc. and Kyulux Inc. in 2019.^[43] (Figure 1.25b and 1.25d reproduced with permission from Reference 38e).

1.7. Conclusions and Outlook

In conclusion, harvesting the triplet excitons under ambient conditions is proven to be the key criteria for maximizing the device efficiency of organic electroluminescent devices. In addition, the spin-forbidden transitions from the triplet states dramatically reduces the emission lifetime as compared to fluorescence, which in turn, offer various applications in other areas such as *in vivo* bio-imaging, oxygen mapping and data encryption-decryption technologies. The triplet excitons can be harvested as room temperature phosphorescence and the following conditions must be satisfied in order to obtain high quantum efficiency: (a) Strong spin-orbit coupling to overcome the quantum-mechanically forbidden intersystem crossing transition between the singlet and triplet states and, secondly, (b) efficient suppression of vibrational/rotational motions of the phosphor molecules (in crystalline state) and the host matrix (amorphous films). Certain functional groups such as aromatic carbonyls (or other hetero-aromatic compounds with lone pair of electrons) assisted by “heavy” halogen atoms (e. g. Br or I) are shown to be the most promising candidates for achieving high ambient RTP efficiency. It is noteworthy to mention that, despite these basic understandings and some critical breakthroughs made in recent years, there is still no

straightforward way of designing new efficient phosphors. Especially, most of the reported phosphors lack large substrate scope and therefore developing new methodologies for new and colour-tunable emitters is need of the hour. In addition, most of the organic phosphors still rely heavily on tedious crystal engineering of the chromophores and lack solution processability. In this Thesis, we specially focussed on these issues that is limiting the mass production of these materials for many unique applications and developed new universal strategies to address the same.

On the other hand, in order to obtain efficient TADF emission one needs to minimize the lowest excited singlet and triplet energy gap which is achieved by designing donor-acceptor (D-A) type charge-transfer emitters. In this case also the spin-orbit coupling is extremely important, however, more detailed investigations has to be done in order to fully understand the extent of it. Nonetheless, in past few years, TADF emitters have emerged as a viable alternative to expensive and environmentally toxic organometallic phosphorescent emitters. However, there are still some problems which must be dealt with in order to accelerate the process of commercialization. For example, there is still lack of new materials which emit efficiently in blue and red-region of the emission spectrum. It is particularly difficult to obtain pure blue because of the broad charge-transfer nature of TADF emission. On the other hand, because of the energy gap law designing red-emitters also difficult considering the fact that charge-transfer transitions are relatively slow and will have to compete with non-radiative internal conversion. In addition, the theory of thermally activated delayed fluorescence is not fully understood yet, especially the role of locally excited states in the ISC/RISC process, although there are growing number of examples that ascertains the involvement of these energy states. Therefore, more experimental evidence is required along with designing new materials that would help in understanding the mechanism more comprehensively.

1.8. References

- [1] A. Köhler, H. Bässler, *Mater. Sci. Eng. R Rep.* **2009**, *66*, 71.
- [2] J. R. Lakowicz, *Principles of Fluorescence Spectroscopy* (3rd ed.), Springer, **2011**.
- [3] We deliberately avoid the statement of $S_1 \rightarrow S_0$ transition because, there are certain exception where the molecules side-step Kasha's rule and fluorescence can be actually seen from $S_2 \rightarrow S_0$ states.
- [4] M. Kasha, *Disc. Farad. Soc.*, **1950**, *9*, 14.

- [5] a) P. W. Atkins, R. S. Friedman, *Molecular Quantum Mechanics* (Oxford University Press, New York, NY) **1997**; b) S. K. Lower, M. A. El-Sayed, *Chem. Rev.* **1966**, *66*, 199.
- [6] D. S. McClure, *J. Chem. Phys.* **1949**, *17*, 905.
- [7] M. A. El-Sayed, *J. Chem. Phys.* **1963**, *38*, 2834; b) M. A. El-Sayed, *J. Chem. Phys.* **1963**, *38*, 3032.
- [8] W. Jia, Q. Wang, H. Shi, Z. An, W. Huang, *Chem. Eur. J.* **2020**, *26*, 4437.
- [9] a) M. A. Baldo, D. F. O'Brien, Y. You, A. Shoustikov, S. Sibley, M. E. Thompson, S. R. Forrest, *Nature* **1998**, *395*, 151; b) C. Adachi, M. A. Baldo, S. R. Forrest, M. E. Thompson, *Appl. Phys. Lett.* **2000**, *77*, 904; c) B. Happ, A. Winter, M. D. Hager, U. S. Schubert, *Chem. Soc. Rev.* **2012**, *41*, 2222.
- [10] S. Schmidbauer, A. Hohenleutner, B. König, *Beilstein J. Org. Chem.* **2013**, *9*, 2088.
- [11] a) G. N. Lewis, M. Kasha *J. Am. Chem. Soc.* **1944**, *66*, 2100; b) G. N. Lewis, D. Lipkin, T. T. Magel, *J. Am. Chem. Soc.* **1941**, *63*, 3005.
- [12] a) S. Hirata, *Adv. Opt. Mater.* **2017**, *5*, 1700116; b) Kenry, C.-J. Chen, B. Liu, *Nat. Commun.* **2019**, *10*, 2111; c) S. Mukherjee, P. Thilagar, *Chem. Commun* **2015**, *51*, 10988; d) A. Forni, E. Lucenti, C. Botta, E. Cariati *J. Mater. Chem. C* **2018**, *6*, 4603.
- [13] a) M. Kiritani, T. Yoshii, N. Hirota, and M. Baba *J. Chem. Phys.* **1994**, *98*, 11265; b) M. Koyanagi, L. Goodman, *Chem. Phys. Lett.* **1971**, *9*, 636.
- [14] F. Bayrakçeken, *Spectrochim. Acta, Part A* **2008**, *71*, 603.
- [15] a) W. Z. Yuan, X. Y. Shen, H. Zhao, J. W. Y. Lam, L. Tang, P. Lu, C. Wang, Y. Liu, Z. Wang, Q. Zheng, J. Z. Sun, Y. Ma, B. Z. Tang, *J. Phys. Chem. C* **2010**, *114*, 6090; b) Y. Gong, G. Chen, Q. Peng, W. Z. Yuan, Y. Xie, S. Li, Y. Zhang, B. Z. Tang, *Adv. Mater.* **2015**, *27*, 6195; c) W. Zhao, Z. He, J. W. Y. Lam, Q. Peng, H. Ma, Z. Shuai, G. Bai, J. Hao, B. Z. Tang, *Chem* **2016**, *1*, 592; d) J. Yang, Z. Ren, B. Chen, M. Fang, Z. Zhao, B. Z. Tang, Q. Peng, Z. Li, *J. Mater. Chem. C* **2017**, *5*, 9242; e) Z. He, W. Zhao, J. W. Y. Lam, Q. Peng, H. Ma, G. Liang, Z. Shuai, B. Z. Tang, *Nat. Commun.* **2017**, *8*, 416; f) W. Zhao, T. S. Cheung, N. Jiang, W. Huang, J. W. Y. Lam, X. Zhang, Z. He, B. Z. Tang, *Nat. Commun.* **2019**, *10*, 1595; g) Y. Xiong, Z. Zhao, W. Zhao, H. Ma, Q. Peng, Z. He, X. Zhang, Y. Chen, X. He, J. W. Y. Lam, B. Z. Tang, *Angew. Chem. Int. Ed.* **2018**, *57*, 7997.
- [16] a) O. Bolton, K. Lee, H. J. Kim, K. Y. Lin, J. Kim, *Nat. Chem.* **2011**, *3*, 205; b) M. S. Kwon, Y. Yu, C. Coburn, A. W. Phillips, K. Chung, A. Shanker, J. Jung, G. Kim, K. Pipe, S. R. Forrest,

J. H. Youk, J. Gierschner, J. Kim, *Nat. Commun.* **2015**, *6*, 8947; c) D. Lee, O. Bolton, B. C. Kim, J. H. Youk, S. Takayama, J. Kim, *J. Am. Chem. Soc.* **2013**, *135*, 6325; d) M. S. Kwon, D. Lee, S. Seo, J. Jung, J. Kim, *Angew. Chem. Int. Ed.* **2014**, *53*, 11177; e) O. Bolton, D. Lee, J. Jung, J. Kim, *Chem. Mater.* **2014**, *26*, 6644.

[17] a) Z. An, C. Zheng, Y. Tao, R. Chen, H. Shi, T. Chen, Z. Wang, H. Li, R. Deng, X. Liu, W. Huang, *Nat. Mater.* **2015**, *14*, 685; b) S. Cai, H. Shi, D. Tian, H. Ma, Z. Cheng, Q. Wu, M. Gu, L. Huang, Z. An, Q. Peng, W. Huang, *Adv. Funct. Mater.* **2018**, *28*, 1705045; c) H. Shi, L. Song, H. Ma, C. Sun, K. Huang, A. Lv, W. Ye, H. Wang, S. Cai, W. Yao, Y. Zhang, R. Zheng, Z. An, W. Huang, *J. Phys. Chem. Lett.* **2019**, *10*, 595; d) S. Tian, H. Ma, X. Wang, A. Lv, H. Shi, Y. Geng, J. Li, F. Liang, Z. M. Su, Z. An, W. Huang, *Angew. Chem. Int. Ed.* **2019**, *58*, 6645; e) N. Gan, X. Wang, H. Ma, A. Lv, H. Wang, Q. Wang, M. Gu, S. Cai, Y. Zhang, L. Fu, M. Zhang, C. Dong, W. Yao, H. Shi, Z. An, W. Huang, *Angew. Chem. Int. Ed.* **2019**, *58*, 14140; f) S. Cai, H. Shi, J. Li, L. Gu, Y. Ni, Z. Cheng, S. Wang, W.-W. Xiong, L. Li, Z. An, W. Huang, *Adv. Mater.* **2017**, *29*, 1701244; g) L. Bian, H. Shi, X. Wang, K. Ling, H. Ma, M. Li, Z. Cheng, C. Ma, S. Cai, Q. Wu, N. Gan, X. Xu, Z. An, W. Huang, *J. Am. Chem. Soc.* **2018**, *140*, 10734; h) L. Gu, H. Shi, L. Bian, M. Gu, K. Ling, X. Wang, H. Ma, S. Cai, W. Ning, L. Fu, H. Wang, S. Wang, Y. Gao, W. Yao, F. Huo, Y. Tao, Z. An, X. Liu, W. Huang, *Nat. Photonics* **2019**, *13*, 406; i) L. Gu, H. Shi, M. Gu, K. Ling, H. Ma, S. Cai, L. Song, C. Ma, H. Li, G. Xing, X. Hang, J. Li, Y. Gao, W. Yao, Z. Shuai, Z. An, X. Liu, W. Huang, *Angew. Chem. Int. Ed.* **2018**, *57*, 8425; j) E. Lucenti, A. Forni, C. Botta, L. Carlucci, C. Giannini, D. Marinotto, A. Previtali, S. Righetto, E. Cariati, *J. Phys. Chem. Lett.* **2017**, *8*, 1894; k) Z. Cheng, H. Shi, H. Ma, L. Bian, Q. Wu, L. Gu, S. Cai, X. Wang, W. W. Xiong, Z. An, W. Huang, *Angew. Chem. Int. Ed.* **2018**, *57*, 678.

[18] a) Z. Yang, Z. Mao, X. Zhang, D. Ou, Y. Mu, Y. Zhang, C. Zhao, S. Liu, Z. Chi, J. Xu, Y. C. Wu, P. Y. Lu, A. Lien, M. R. Bryce, *Angew. Chem. Int. Ed.* **2016**, *55*, 2181; b) L. Xu, G. Li, T. Xu, W. Zhang, S. Zhang, S. Yin, Z. An, G. He, *Chem. Commun.* **2018**, *54*, 9226; c) Z. He, H. Gao, S. Zhang, S. Zheng, Y. Wang, Z. Zhao, D. Ding, B. Yang, Y. Zhang, W. Z. Yuan, *Adv. Mater.* **2019**, *31*, 1807222; d) S. Pan, Z. Chen, X. Zheng, D. Wu, G. Chen, J. Xu, H. Feng, Z. Qian, *J. Phys. Chem. Lett.* **2018**, *14*, 3939; e) Y. Wang, J. Yang, Y. Tian, M. Fang, Q. Liao, L. Wang, W. Hu, B. Z. Tang, Z. Li, *Chem. Sci.* **2020**, *11*, 833.

[19] N. Gan, H. Shi, Z. An, W. Huang, *Adv. Funct. Mater.* **2018**, *28*, 1802657.

[20] a) S. Hirata, K. Totani, J. Zhang, T. Yamashita, H. Kaji, S. R. Marder, T. Watanabe, C. Adachi, *Adv. Funct. Mater.* **2013**, *23*, 3386; b) S. Hirata, M. Vacha, *Adv. Opt. Mater.* **2017**, *5*,

1600996; c) S. Hirata, K. Totani, H. Kaji, M. Vacha, T. Watanabe, C. Adachi, *Adv. Opt. Mater.* **2013**, *1*, 438.

[21] a) J. Xu, A. Takai, Y. Kobayashi, M. Takeuchi, *Chem. Commun.* **2013**, *49*, 8447; b) G. D. Gutierrez, G. T. Sazama, T. Wu, M. A. Baldo, T. M. Swager, *J. Org. Chem.* **2016**, *81*, 4789; c) Y. Gong, H. Chen, X. Ma, H. Tian, *ChemPhysChem* **2016**, *17*, 1934; d) X. Zhen, Y. Tao, Z. An, P. Chen, C. Xu, R. Chen, W. Huang, K. Pu, *Adv. Mater.* **2017**, *29*, 1606665; e) Y. Yu, M. S. Kwon, J. Jung, Y. Zeng, M. Kim, K. Chung, J. Gierschner, J. H. Youk, S. M. Borisov, J. Kim, *Angew. Chem. Int. Ed.* **2017**, *56*, 16207; f) S. Kuila, K. V. Rao, S. Garain, P. K. Samanta, S. Das, S. K. Pati, M. Eswaramoorthy, S. J. George, *Angew. Chem. Int. Ed.* **2018**, *57*, 17115; g) S. Kuila, S. Garain, M. Eswaramoorthy, S. J. George, *Mat. Res. Exp.* **2019**, *6*, 124003; h) H. Chen, X. Ma, S. Wu, H. Tian, *Angew. Chem. Int. Ed.* **2014**, *53*, 14149.

[22] H. Yersin, *Top. Curr. Chem.* **2004**, *241*, 1.

[23] <https://lgindiablog.com/compare-oled-tv-vs-led-tv-how-oled-is-a-different-technology-with-superior-picture-quality/>

[24] <https://www.lg.com/in/tvs/lg-OLED55C9PTA#none>

[25] <https://www.eenewsautomotive.com/news/audi-picks-hella-oled-rear-lights>

[26] <https://www.oled-info.com/apple-oled>

[27] <https://www.extremetech.com/computing/186241-lgs-flexible-and-transparent-oled-displays-are-the-beginning-of-the-e-paper-revolution>

[28] <https://oled.com/oleds/>

[29] <https://www.sigmaaldrich.com/technical-documents/articles/material-matters/achieving-high-efficiency.html>

[30] R. Kabe, N. Notsuka, K. Yoshida, C. Adachi, *Adv. Mater.* **2016**, *28*, 655.

[31] a) K. Y. Zhang, Q. Yu, H. Wei, S. Liu, Q. Zhao, W. Huang, *Chem. Rev.* **2018**, *118*, 1770; b) H. Xu, R. Chen, Q. Sun, W. Lai, Q. Su, W. Huang, X. Liu, *Chem. Soc. Rev.* **2014**, *43*, 3259.

[32] G. Zhang, G. M. Palmer, M. W. Dewhirst, C. L. Fraser, *Nat. Mater.* **2009**, *8*, 747.

[33] M. Gmelch, H. Thomas, F. Fries, S. Reineke, *Sci. Adv.* **2019**, *5*, eaau7310.

[34] a) Z. Yang, Z. Mao, Z. Xie, Y. Zhang, S. Liu, J. Zhao, J. Xu, Z. Chi, M. P. Aldred, *Chem. Soc. Rev.* **2017**, *46*, 915; b) P. L. Santos, M. K. Etherington, A. P. Monkman, *J. Mater. Chemistry*

C **2018**, *6*, 4842; c) M. Y. Wong, E. Zysman-Colman, *Adv. Mater.* **2017**, *29*, 1605444; d) Y. Tao, K. Yuan, T. Chen, P. Xu, H. Li, R. Chen, C. Zheng, L. Zhang, W. Huang, *Adv. Mater.* **2014**, *26*, 7931.

[35] a) C. J. Chiang, A. Kimyonok, M. K. Etherington, G. C. Griffiths, V. Jankus, F. Turksoy, A. P. Monkman, *Adv. Funct. Mater.* **2013**, *23*, 739; b) B. H. Wallikewitz, D. Kabra, S. Gelinas, R. H. Friend, *Phys. Rev. B* **2012**, *85*, 45209; c) D. Di, L. Yang, J. M. Richter, L. Meraldi, R. M. Altamimi, A. Y. Alyamani, D. Credginton, K. P. Musselman, J. L. MacManus-Driscoll, R. H. Friend, *Adv. Mater.* **2017**, *29*, 1605987.

[36] a) W. Li, D. Liu, F. Shen, D. Ma, Z. Wang, T. Feng, Y. Xu, B. Yang, Y. Ma, *Adv. Funct. Mater.* **2012**, *22*, 2797; b) W. Li, Y. Pan, R. Xiao, Q. Peng, S. Zhang, D. Ma, F. Li, F. Shen, Y. Wang, B. Yang, Y. Ma, *Adv. Funct. Mater.* **2014**, *24*, 1609; c) Y. Pan, W. Li, S. Zhang, L. Yao, C. Gu, H. Xu, B. Yang, Y. Ma, *Adv. Opt. Mater.* **2014**, *2*, 510; d) L. Yao, S. Zhang, R. Wang, W. Li, F. Shen, B. Yang, Y. Ma, *Angew. Chem. Int. Ed.* **2014**, *53*, 2119.

[37] F. Perrin, F. La Fluorescence des Solutions, *Ann. Phys.* **1929**, *12*, 169.

[38] a) H. Uoyama, K. Goushi, K. Shizu, H. Nomura, C. Adachi, *Nature* **2012**, *492*, 234; b) Q. Zhang, B. Li, S. Huang, H. Nomura, H. Tanaka, C. Adachi, *Nat. Photonics* **2014**, *8*, 326; c) Q. Zhang, J. Li, K. Shizu, S. Huang, S. Hirata, H. Miyazaki, C. Adachi, *J. Am. Chem. Soc.* **2012**, *134*, 14706; d) S. Y. Lee, T. Yasuda, H. Komiyama, J. Lee, C. Adachi, *Adv. Mater.* **2016**, *28*, 4019; e) H. Nakanotani, T. Higuchi, T. Furukawa, K. Masui, K. Morimoto, M. Numata, H. Tanaka, Y. Sagara, T. Yasuda, C. Adachi, *Nat. Commun.* **2014**, *5*, 4016; f) H. Noda, X.-K. Chen, H. Nakanotani, T. Hosokai, M. Miyajima, N. Notsuka, Y. Kashima, J.-L. Brédas, C. Adachi, *Nat. Mater.* **2019**, *18*, 1084.

[39] F. B. Dias, T. J. Penfold, A. P. Monkman, *Methods Appl. Fluoresc.* **2017**, *5*, 012001.

[40] N. Aizawa, I. S. Park, T. Yasuda, *AAPPS Bull.* **2016**, *26*, 9.

[41] X. Cai, S.-J. Su, *Adv. Funct. Mater.* **2018**, *28*, 1802558.

[42] <https://www.kyulux.com/category/tadf/page/2/>

[43] <https://www.oled-info.com/wisechip-launches-worlds-first-hyperfluorescence-oled-display-27-yellow-pmoled>

Part A

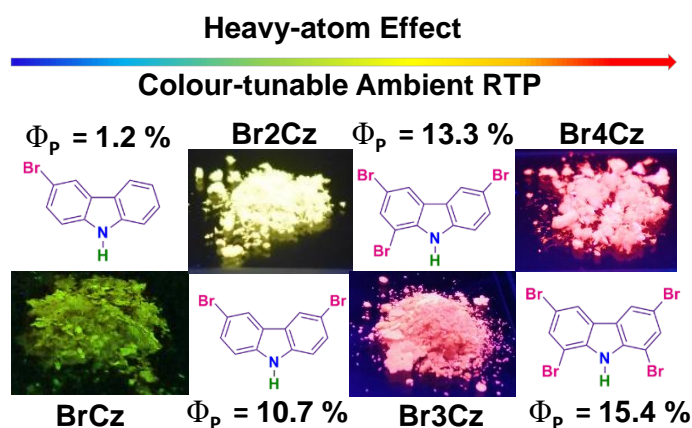
Room Temperature Phosphorescence

CHAPTER 2

Ambient Room Temperature Phosphorescence in Heavy-atom Substituted Crystalline Carbazole Derivatives with Simple Molecular Design*

Abstract

Development of RTP material from easily available organic molecules is a challenging task. In this chapter, we showed a simple heavy-atom substitution strategy to develop colour-tunable (greenish-yellow to deep-red) RTP from commercially available Carbazole derivatives. Carbazole has been known to show weak RTP for decades, although a systematic investigation to improve the RTP quantum efficiency (Φ_P) has not been done so far. In this work, with detailed theoretical and single crystal structure analysis we elucidated the importance of intra- and intermolecular heavy-atom interactions that lead to highly efficient red-emitting RTP ($\Phi_P = 15.4$ %) under fully ambient conditions.



*Manuscript based on this work is under revision.

2.1. Introduction

Metal-free small organic molecules exhibiting room temperature phosphorescence (RTP) has attracted great attention in recent years because of their potential applications in bio-imaging, organic light-emitting diodes (OLEDs) and optical sensing.^[1] Molecular design of purely organic room temperature phosphors often require heavy-atoms (such as Br or I) and non-bonding lone pair containing heteroatoms (nitrogen, oxygen, sulphur or phosphorous), which are capable of inducing efficient spin-orbit coupling (SOC) between excited $n-\pi^*$ and $\pi-\pi^*$ states (El-Sayed's rule).^[2-3] Further, ambient triplet harvesting also requires restricted molecular motion of the phosphors to minimize the vibrational dissipation of triplet states and hence efficient RTP is often observed in crystalline networks of phosphors or while they are embedded in rigid amorphous host matrices.^[4-8] Nevertheless, majority of RTP emitters with appreciable photoluminescence efficiency also requires effective intermolecular interactions via H-aggregation^[6], halogen bonding^[7], carbonyl- π interactions^[8] etc. in order to amplify the SOC strength and intersystem crossing (ISC) efficiency in conjunction with enhanced molecular rigidity. However, most ambient organic phosphors have complex molecular designs which require multi-step synthesis and also have only limited substrate scope due to unpredictable. In this respect small hetero-aromatic molecules such as, carbazole would be of great interest with the possibility of a structure-property investigation by synthetically artless systematic functionalization with heavy-atoms. It is worthwhile to mention that, carbazole (Cz) was one of the model molecular system for the seminal work on organic triplet excitons, by Lewis and Kasha.^[9] Carbazole substructure has been recently explored as the donor component in the charge-transfer molecular designs for thermally activated delayed fluorescence (TADF) for the harvesting of triplets via reverse ISC process.^[10a] However, surprisingly despite having good triplet yields, carbazole or its substituted derivatives are not yet investigated in detail for the ambient triplet harvesting and RTP.^[10] In this chapter, we have performed a structure-property study of simple carbazole derivatives (**BrCz**, **Br2Cz**, **Br3Cz** and **Br4Cz**) by a systematic variation of core-substitution with heavy atoms to realize greenish-yellow and red emissive ambient RTP phosphors in crystalline state with high efficiency (Figure 2.1). Comprehensive spectroscopic, theoretical and X-ray diffraction studies unveil the crucial role of heavy-atom effect and multiple non-covalent intermolecular interactions in the crystal state to enhance the ISC efficiency and to minimize molecular motions to facilitate the ambient RTP with tunable emission wavelengths. While the mono-bromo substituted carbazole derivative, **BrCz**, displays a long-persistent greenish- yellow RTP ($\Phi_P = 1.2\%$, $\tau_{avg.} = 182$ ms), the tetra-Br-substituted

carbazole molecule, **Br4Cz**, shows red-emissive RTP with excellent phosphorescence quantum yield over 15 % ($\tau_{\text{avg.}} = 3.1$ ms) in air, signifying the crucial role of heavy-atoms.

2.2. Design Strategy and Synthesis

Systematic bromination of commercially available carbazole and the consequent heavy-atom effect on the RTP intensity is the basic design rule we follow in this chapter. All the brominated derivatives (**BrCz**, **Br2Cz**, **Br3Cz** and **Br4Cz**) studied here, were synthesized by one-step bromination of **Cz**, using different equivalents of N-Bromosuccinimide (NBS) with excellent yields (50 % - 80 %). These molecules were characterized by ^1H and ^{13}C NMR spectroscopy, mass spectrometry and single crystal X-ray diffraction analysis (see Experimental Section).

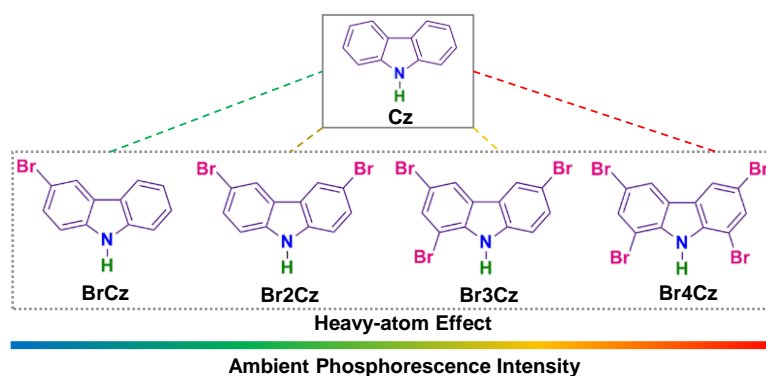


Figure 2.1. Chemical structures of the brominated carbazoles and the arrow indicate the heavy-atom induced phosphorescence enhancement.

2.3. Spectroscopic Studies in Solution-state

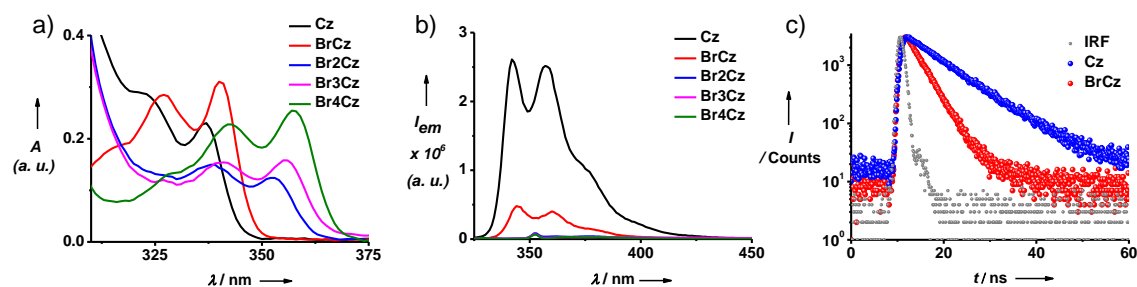


Figure 2.2. a) Absorption and b) fluorescence spectra ($\lambda_{\text{exc.}} = 320$ nm) of 0.01 mM solutions of **Cz**, **BrCz**, **Br2Cz**, **Br3Cz** and **Br4Cz** in THF. c) Fluorescence decays of 0.01 mM **Cz** ($\tau_{\text{avg.}} = 7.9$ ns) and **BrCz** ($\tau_{\text{avg.}} = 3.2$ ns) in THF, monitored at 380 nm ($\lambda_{\text{exc.}} = 340$ nm). Absorption at 275-320 nm region corresponds to $S_0 \rightarrow S_2$ ($^1\pi-\pi^*$ transition).^[11]

In solution state ($c = 0.01$ mM, THF), all the derivatives show characteristic $S_0 \rightarrow S_1$ ($^1\pi-\pi^*$) absorption features of carbazole in the 300-370 nm region (Figure 2.2a).^[11] The control molecule Cz, (nascent carbazole), exhibits strong fluorescence in the 350-450 nm range with an average lifetime of 7.9 ns (Figure 2.2b). **BrCz** with one Br-atom at the core showed a decreased fluorescence intensity and lifetime ($\tau_{\text{avg.}} = 3.2$ ns, Figure 2.2b and 2.2c). Increasing the number of Br atoms at the carbazole core (i. e. **Br2Cz**, **Br3Cz** and **Br4Cz**) result in further decrease in fluorescence intensity although no RTP could be observed in the solution phase due to rapid vibrational and collisional quenching (Figure 2.2b). These changes in fluorescence features of the Br-substituted carbazole derivatives compared to the nascent Cz, hint towards an increase in SOC efficiency with the increase in number of heavy atoms at the carbazole core, which activates the competitive ISC process to depopulate the singlet excitons.

2.4. Time-dependent Density Functional Theory (TDDFT) Calculations

To get more insight into the ISC efficiency of these carbazole derivatives upon heavy-atom substitution, time-dependent density functional theory (TDDFT) was performed using B3LYP exchange-correlation functional with 6-31+g(d) basis set for all atoms except Br, for which LANL2DZ basis set along with the corresponding effective core potential (ECP) was used (see Experimental Section).

Interestingly, multiple triplet excited states (T_n) were lying closely to the lowest excited singlet level (S_1), which is ideal for thermodynamically allowed ISC transitions. Next, the extent of SOC efficiency was determined quantitatively by examining the spin-orbit coupling matrix element (SOCME) between neighbouring S_1 - T_n states for all molecules. In case of **BrCz** (4.40 cm^{-1}) and **Br2Cz** (7.76 cm^{-1}), the magnitude of SOCME between S_1 and T_3 states were higher than the nascent **Cz** (0.54 cm^{-1}) (Figure 2.3 a-c). Interestingly, the magnitude of SOCME increased significantly in the case of **Br3Cz** ($S_1 \rightarrow T_3$ transition, 54.1 cm^{-1}) and **Br4Cz** ($S_1 \rightarrow T_5$ transition, 70 cm^{-1}) owing to further enhancement of internal heavy-atom perturbation in addition to the change in molecular orbital configurations in T_3 state of **Br3Cz** and T_5 of **Br4Cz** (Figure 2.3d, 2.3e and Figure 2.4). Increasing SOCME with gradual insertion of Br-atoms in the core not only facilitates ISC to result in high triplet yields, but it also helps in activating spin-forbidden $T_1 \rightarrow S_0$ radiative transition for efficient RTP, when other non-radiative decay channels are efficiently minimized.

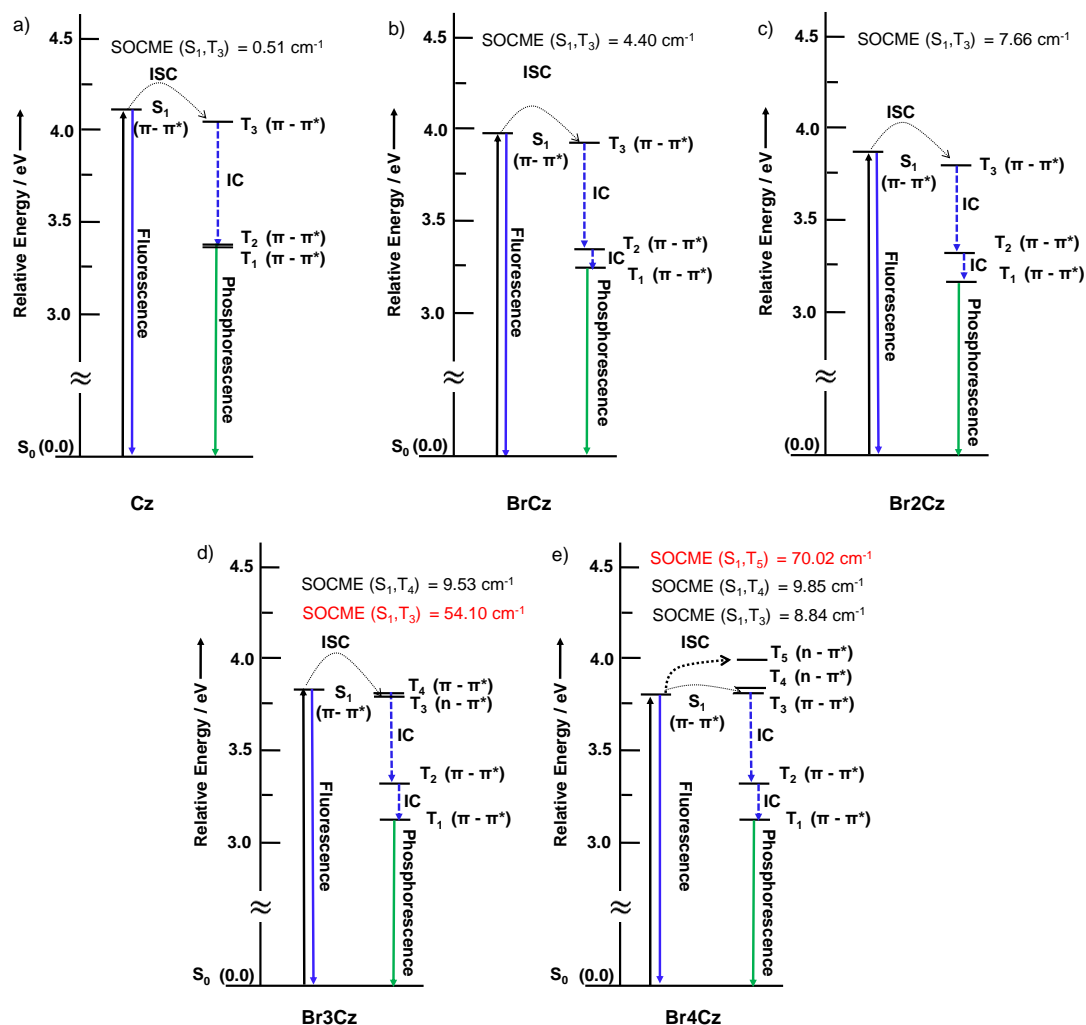


Figure 2.3. Jablonski diagram for (a) Cz, (b) BrCz, (c) Br2Cz, (d) Br3Cz and (e) Br4Cz (T_1 , T_2 , T_3 , T_4 - and T_5 level of theory). Corresponding S_1 - T_n SOCME values are also denoted in each case. Highest SOC values for Br3Cz and Br4Cz are highlighted in red which also enable the most efficient ISC pathways.

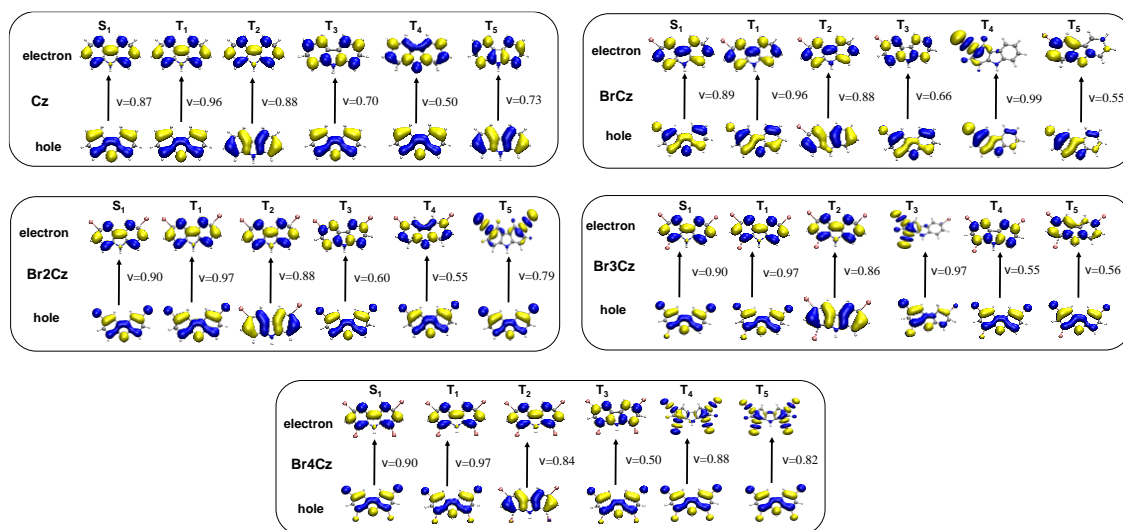


Figure 2.4. Natural transition orbitals of different excited states for Cz, BrCz, Br2Cz, Br3Cz and Br4Cz calculated using TD-B3LYP/6-31+g(d)/LANL2DZ level of theory. Hole and electron wavefunctions with the largest weight (v) provided for each transition.

2.5. Ambient RTP in Crystalline State

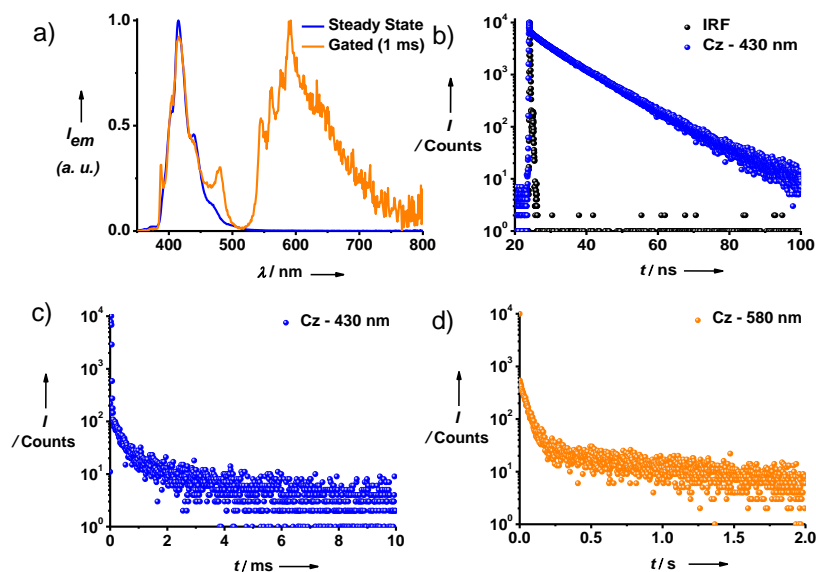


Figure 2.5. Photophysical studies of the nascent carbazole (Cz) crystals under ambient conditions: a) Normalized steady state and gated emission spectra of Cz-crystals excited at 340 nm (delay time = 1 ms). Time resolved decay profiles of the Cz-crystals, showing b) fluorescence ($\lambda_{exc.} = 373$ nm, $\lambda_{monitored} = 430$ nm, $\tau_{avg.} = 10.01$ ns), c) delayed fluorescence ($\lambda_{exc.} = 340$ nm, $\lambda_{monitored} = 430$ nm, $\tau_{avg.} = 1.13$ ms) and d) phosphorescence ($\lambda_{exc.} = 340$ nm, $\lambda_{monitored} = 580$ nm, $\tau_{avg.} = 762.3$ ms) at room temperature. Phosphorescence intensity was too weak for quantum yield measurements.

Since RTP could not be observed in the solution state due to non-radiative vibrational dissipation of triplets, we further explored the crystalline phases of heavy-atom substituted carbazole derivatives along with the nascent Cz, in an attempt to minimize the molecular motions. First, single crystals of **Cz**, **BrCz**, **Br2Cz**, **Br3Cz** and **Br4Cz** were grown from saturated chloroform: methanol (1:2 v/v) solvent mixtures by slow evaporation over 12 h to 4 days. **Cz** crystals exhibited strong fluorescence ($\Phi_F = 53.7\%$) in the 370-500 nm region while exciting at 340 nm with lifetime of 10.01 ns (Figure 2.5). Further, time-gated emission spectrum (delay time = 1 ms) also revealed a weak delayed fluorescence ($\tau_{avg.} = 1.13$ ms) component along with a red-shifted yellow-emissive afterglow phosphorescence band with a maximum at 586 nm ($\tau_{avg.} = 762.3$ ms), characteristic of carbazole chromophores in the crystalline state (Figure 2.5a, Video 2.1).^[10c] Phosphorescence characteristics of the bromo-substituted carbazole derivatives are summarized in Table 2.1. Monobromo substituted **BrCz** crystals showed a significantly reduced fluorescence intensity ($\Phi_F = 2.4\%$) compared to **Cz**, along with an increase in RTP intensity ($\Phi_P = 1.2\%$) as expected. The average lifetime of RTP band was 182 ms which is also reflected in the afterglow characteristics of **BrCz** under UV-excitation (Fig. 2.6a, 2.6e and Video 2.2). Remarkably, with increasing number of Br in **Cz** core, RTP quantum efficiency increased gradually, which is expected based on the increasing heavy-atom effect (Fig. 2.6b-d).^[4a] **Br2Cz** crystals showed very weak fluorescence with strong greenish-yellow RTP ($\Phi_P = 10.7\%$) and an average lifetime of $\tau_{avg.} = 0.12$ ms as evident from the steady-state and time-gated emission spectrum (delay time = 0.15 ms, Fig. 2.6b and 2.6f). Crystals of **Br3Cz** show strong orange-red emitting RTP (550-800 nm region, $\lambda_{max.} = 588$ nm) with comparatively higher phosphorescence quantum efficiency ($\Phi_P = 13.3\%$) and average lifetime of 3.1 ms (Fig. 2.6c and 2.6g). Tetrabromo substituted **Br4Cz** crystals exhibited further bathochromic shift in the phosphorescence band with a maximum at 602 nm with concomitant enhancement in the RTP intensity ($\Phi_P = 15.4\%$, $\tau_{avg.} = 3.7$ ms, Fig. 2.6d and 2.6h). It is worth noting that, **Br3Cz** and **Br4Cz** crystals exhibit strong ambient RTP in the orange and red-emitting region with high quantum efficiency (13.3% and 15.4%, respectively) compared to the crystals of **Cz**, **BrCz** and **Br2Cz**, in agreement with the gradual increase in heavy-atom effect discussed earlier (*vide infra*). Such strong ambient-stable RTP are among the best reported red-phosphors known till date (Table 2.2, Scheme 2.1).^[1b,4b]

Table 2.1. RTP features of brominated carbazoles in crystals.

Phosphor	λ_{em} (nm)	Φ_P	$\tau_{avg.}$ ($\lambda_{monitored}$)
BrCz	558, 604, 672	1.2 %	182 ms (570 nm)
Br2Cz	466, 532, 582	10.7 %	0.12 ms (580 nm)
Br3Cz	588, 636	13.3 %	3.1 ms (590 nm)
Br4Cz	602, 648	15.4 %	3.7 ms (610 nm)

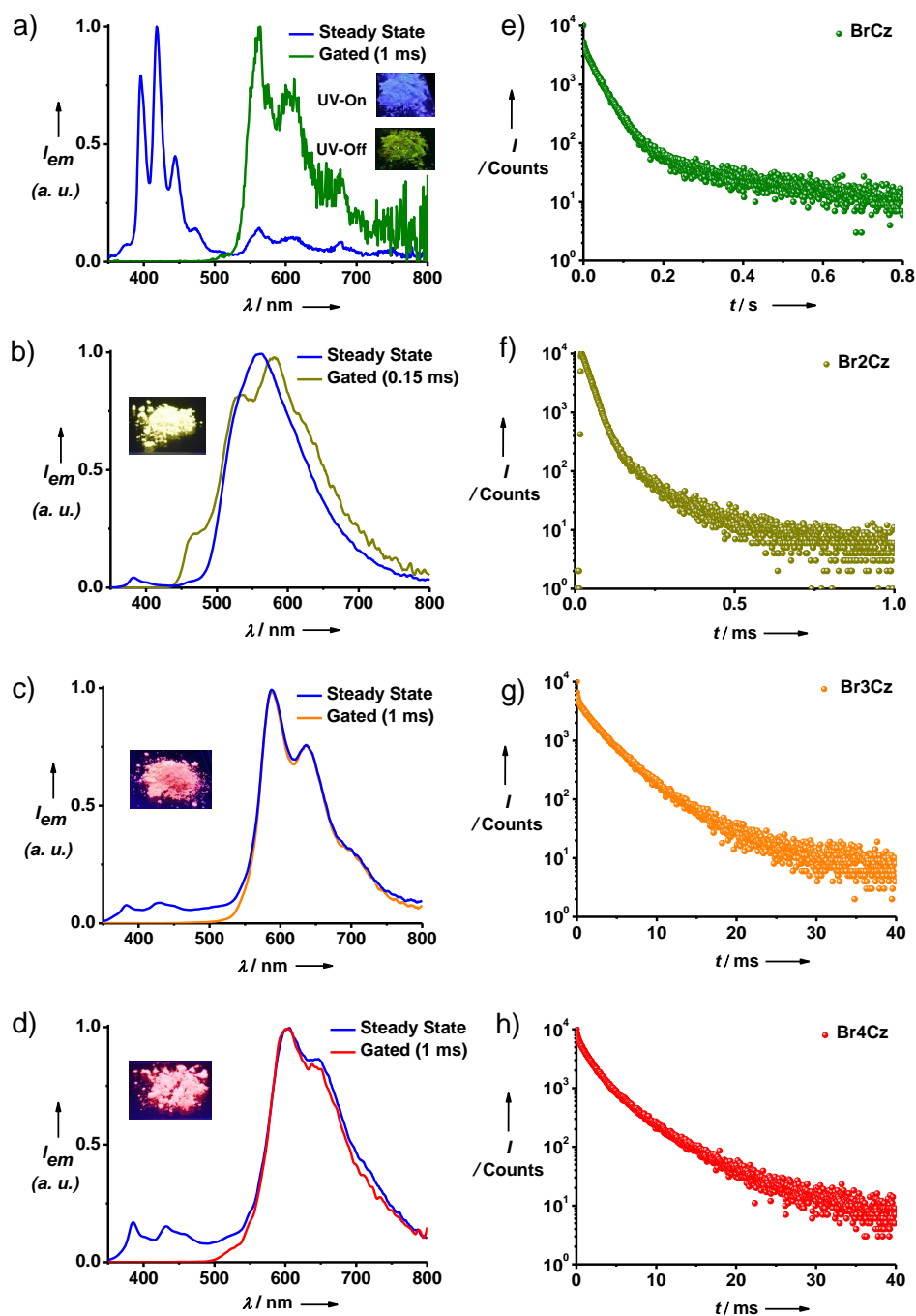


Figure 2.6. Steady-state and gated emission spectra of the crystalline samples of (a) **BrCz**, (b) **Br2Cz**, (c) **Br3Cz** and (d) **Br4Cz** under ambient conditions (Inset of each figure is the corresponding photographs of the phosphorescent crystals under 365 nm UV-excitation). Corresponding phosphorescence decays of (e) **BrCz** ($\lambda_{\text{monitored}} = 570 \text{ nm}$), (f) **Br2Cz** ($\lambda_{\text{monitored}} = 580 \text{ nm}$), (g) **Br3Cz** ($\lambda_{\text{monitored}} = 590 \text{ nm}$) and (h) **Br4Cz** ($\lambda_{\text{monitored}} = 610 \text{ nm}$) crystals when excited at 340 nm.

2.6. Single-Crystal X-Ray Diffraction Studies

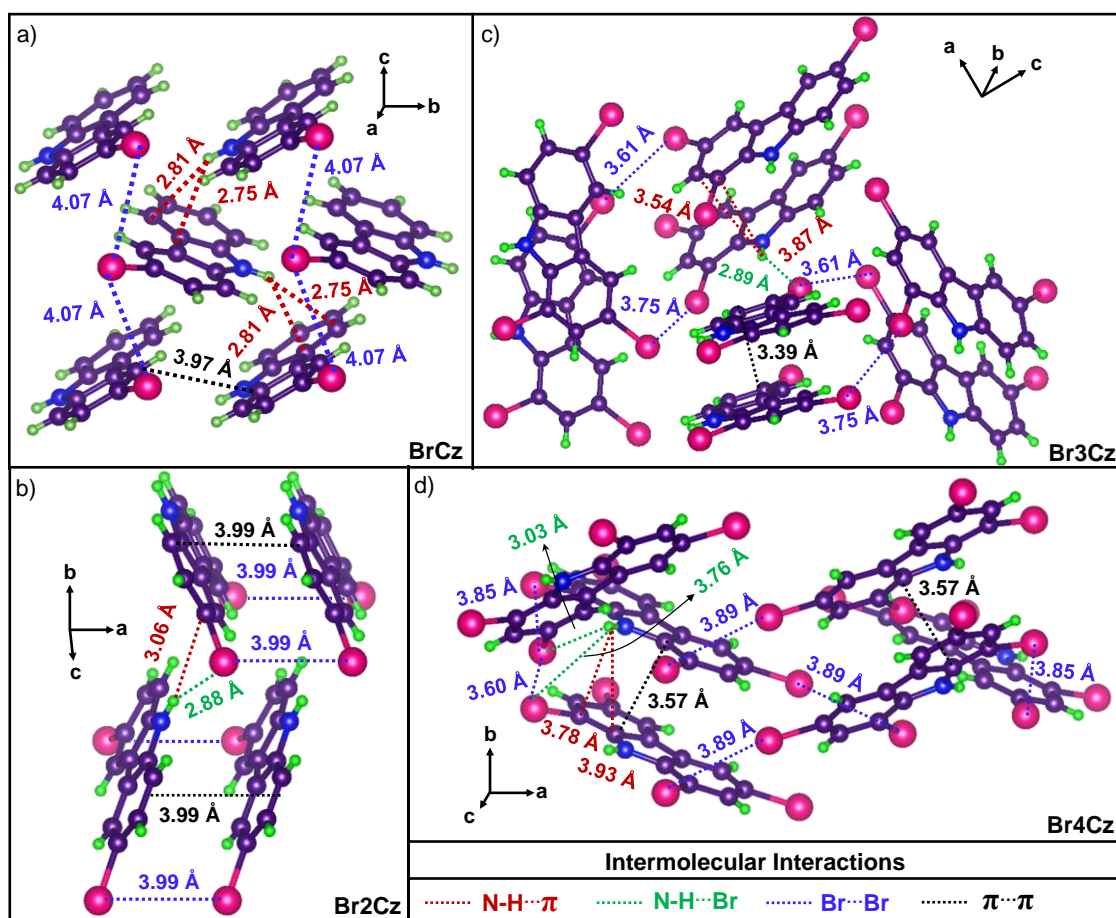


Figure 2.7. Single-crystal structures and molecular packing models of a) **BrCz**, b) **Br2Cz**, c) **Br3Cz** and d) **Br4Cz** with denoted intermolecular interactions. Various types of intermolecular interactions are shown in different coloured dotted lines along with the corresponding distances.

To get further molecular insights into the intense RTP from the crystals of bromine-substituted Cz-derivatives, molecular organization of the phosphors was investigated using single crystal X-ray diffraction analyses (Fig. 3). In Fig. 3a, stacking of **BrCz** in its crystal is shown, where the central **BrCz** molecule is surrounded by four other molecules with multiple non-covalent intermolecular interactions such as N-H \cdots π (2.75 Å and 2.81 Å), Br \cdots Br (4.07 Å) and a weak parallel displaced π – π stacking (3.97 Å). On the other hand, **Br2Cz** forms more number of such intermolecular interactions, namely, N-H \cdots π (3.06 Å), Br \cdots Br (3.99 Å) and N-H \cdots Br (2.88 Å), which are evident along with a partial co-facial π – π stacking (3.99 Å) interactions (Fig. 3b). We envision that, more number of interactions among the **Br2Cz** leads to more densely-packed crystalline assembly with lesser vibrational motions compared to **BrCz**, resulting in crystalline

assembly with lesser vibrational motions compared to **BrCz**, resulting in substantially higher quantum efficiency. Further we envisage that, the π -stacking interactions present between the molecules in **Br2Cz** compared to **BrCz** would be responsible for its red-shifted RTP maximum. Similarly in **Br3Cz** crystals, several intermolecular interactions such as N-H \cdots π (3.54 Å and 3.87 Å), Br \cdots Br (3.61 Å and 3.75 Å), N-H \cdots Br (2.89 Å) and π - π (3.39 Å) interactions were observed (Fig. 2.7c). **Br4Cz** also show these N-H \cdots π (3.78 Å and 3.93 Å), Br \cdots Br (3.60 Å, 3.85 Å and 3.89 Å), N-H \cdots Br (3.03 and 3.76 Å) and π - π (3.57 Å) non-covalent intermolecular interactions with neighbouring molecules (Fig. 2.7d). Hence, in general, it is evident that multiple short-contacts between the brominated molecules through various intermolecular interactions lead to densely-packed crystalline lattices in **Br2Cz**, **Br3Cz** and **Br4Cz** which is essential for minimizing non-radiative deactivation pathways to result in efficient RTP, compared to relatively loosely-packed crystals of **BrCz** or **Cz** (Figure 2.7, 2.8 and Table 2.2).^[10c] In addition, we envision that many Br \cdots Br interactions present in the crystalline samples of these molecules would also lead to an external heavy-atom effect, generally considered to be a contributing factor for efficient RTP emission in metal-free organic phosphors.^[12] Further, the red-shifted orange and red ambient RTP with significant quantum yield ($\Phi_P > \sim 15\%$), could be attributed to the very strong π -stacking interactions present as evident from the stacking distances of 3.4-3.6 Å.

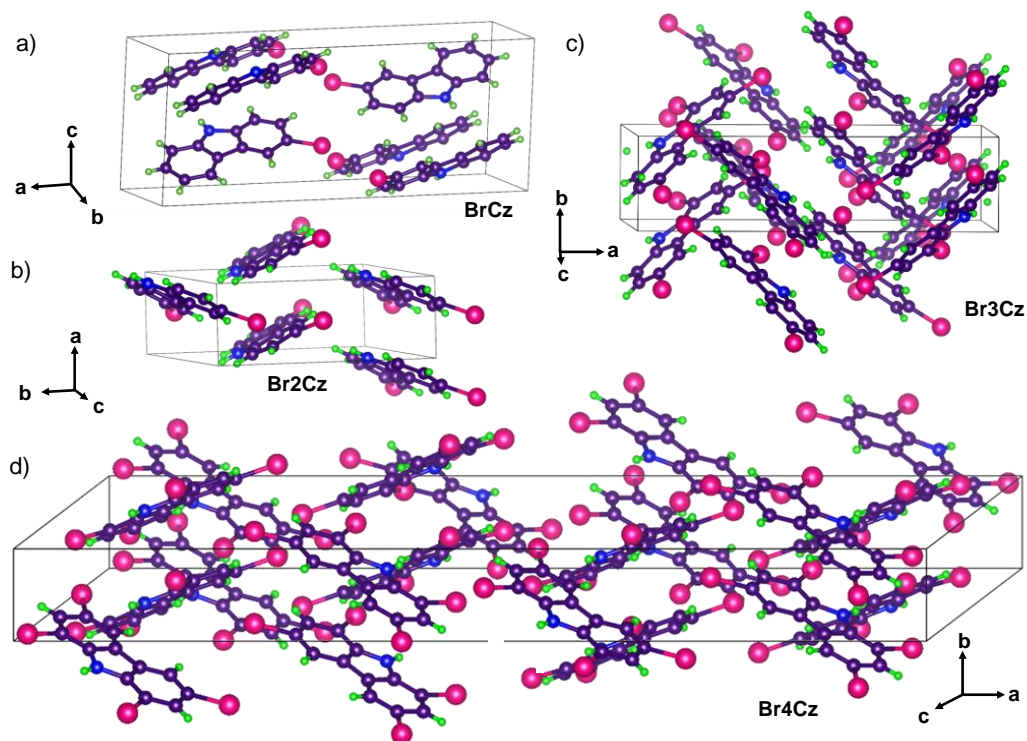


Figure 2.8. Single-crystal unit cells of a) **BrCz**, b) **Br2Cz**, c) **Br3Cz** and d) **Br4Cz**.

Table 2.2. Crystal data and structure refinement for **BrCz**, **Br2Cz**, **Br3Cz** and **Br4Cz**.

Sample	BrCz	Br2Cz	Br3Cz	Br4Cz
Empirical formula	C ₁₂ H ₈ BrN	C ₁₂ H ₇ Br ₂ N	C ₁₂ H ₆ Br ₃ N	C ₁₂ H ₅ Br ₄ N
Formula weight	246.10	325.01	403.91	482.81
Temperature	273.15 K	273.15 K	296.15 K	296.15 K
Wavelength	0.71073 Å	0.71073 Å	0.71073 Å	0.71073 Å
Crystal system	Monoclinic	Monoclinic	Orthorhombic	Monoclinic
Space group	<i>P</i> 2 ₁ / <i>c</i>	<i>P</i> 2 ₁	<i>Pna</i> 2 ₁	<i>C</i> 2/ <i>c</i>
Unit cell dimensions	<i>a</i> = 20.381(3) Å, <i>b</i> = 5.8483(7) Å, <i>c</i> = 7.9296(10) Å, β = 91.435(7)°	<i>a</i> = 3.9879(2) Å, <i>b</i> = 11.0867(6) Å, <i>c</i> = 11.8903(6) Å, β = 90.853(2)°	<i>a</i> = 17.4721(11) Å, <i>b</i> = 4.5809(3) Å, <i>c</i> = 15.0216(9) Å,	<i>a</i> = 38.831(2) Å, <i>b</i> = 3.9995(2) Å, <i>c</i> = 16.9741(10) Å, β = 103.898(5)°
Volume	944.9(2) Å ³	525.64(5) Å ³	1202.30(13) Å ³	2559.0(3) Å ³
Z	4	2	4	8
Density (calculated)	1.730 g/cm ³	2.053 g/cm ³	2.231 g/cm ³	2.506 g/cm ³
Absorption coefficient	4.302 mm ⁻¹	7.671 mm ⁻¹	10.035 mm ⁻¹	12.555 mm ⁻¹
F(000)	488	310	760	1792
Crystal size	0.24 x 0.16 x 0.04 mm ³	0.24 x 0.16 x 0.04 mm ³	0.18 x 0.04 x 0.02 mm ³	0.3 x 0.12 x 0.04 mm ³
θ range for data collection	2.999 to 26.386°	2.512 to 26.359°	2.331 to 26.399°	2.927 to 28.272°
Index ranges	-25 <= <i>h</i> <= 25, -7 <= <i>k</i> <= 7, -9 <= <i>l</i> <= 9	-4 <= <i>h</i> <= 4, -13 <= <i>k</i> <= 13, -14 <= <i>l</i> <= 14	-21 <= <i>h</i> <= 21, -5 <= <i>k</i> <= 5, -18 <= <i>l</i> <= 18	-50 <= <i>h</i> <= 50, -5 <= <i>k</i> <= 5, -22 <= <i>l</i> <= 22
Reflections collected	8574	11613	24150	35328
Independent reflections	1859 [<i>R</i> _{int} = 0.0770]	2123 [<i>R</i> _{int} = 0.0531]	2449 [<i>R</i> _{int} = 0.1267]	3163 [<i>R</i> _{int} = 0.1111]
Completeness to θ = 25.242°	96.4% ^a	99.9%	99.7%	99.7%
Refinement method	Full-matrix least-squares on <i>F</i> ²	Full-matrix least-squares on <i>F</i> ²	Full-matrix least-squares on <i>F</i> ²	Full-matrix least-squares on <i>F</i> ²
Data / restraints / parameters	1859 / 6 / 127	2123 / 7 / 136	2449 / 7 / 145	3163 / 0 / 154
Goodness-of-fit	1.161	1.059	1.081	1.052
Final <i>R</i> indices [<i>I</i> > 2 σ (<i>I</i>)]	<i>R</i> _{obs} = 0.0961, ^a <i>wR</i> _{obs} = 0.2532	<i>R</i> _{obs} = 0.0289, <i>wR</i> _{obs} = 0.0699	<i>R</i> _{obs} = 0.0553, <i>wR</i> _{obs} = 0.1191	<i>R</i> _{obs} = 0.0444, <i>wR</i> _{obs} = 0.1165

R indices [all data]	$R_{\text{all}} = 0.1173$, $wR_{\text{all}} = 0.2666$	$R_{\text{all}} = 0.0318$, $wR_{\text{all}} = 0.0713$	$R_{\text{all}} = 0.0874$, $wR_{\text{all}} = 0.1323$	$R_{\text{all}} = 0.0755$, $wR_{\text{all}} = 0.1372$
Largest diff. peak and hole	1.773 and -1.484 $e \cdot \text{\AA}^{-3}$	0.527 and -0.744 $e \cdot \text{\AA}^{-3}$	1.159 and -0.659 $e \cdot \text{\AA}^{-3}$	0.965 and -0.822 $e \cdot \text{\AA}^{-3}$

$R = \Sigma ||F_o| - |F_c|| / \Sigma |F_o|$, $wR = \{ \Sigma [w(|F_o|^2 - |F_c|^2)^2] / \Sigma [w(|F_o|^4)] \}^{1/2}$ and $w = 1 / [\sigma^2(F_o^2) + (0.0903P)^2 + 17.4887P]$ where $P = (F_o^2 + 2F_c^2) / 3$.

a: The refinement parameters (Completeness and R index) for **BrCz** is deviate slightly from ideal values due to the poor quality and weak diffraction of the single crystals.

2.7. Origin of the Phosphorescence in Crystals

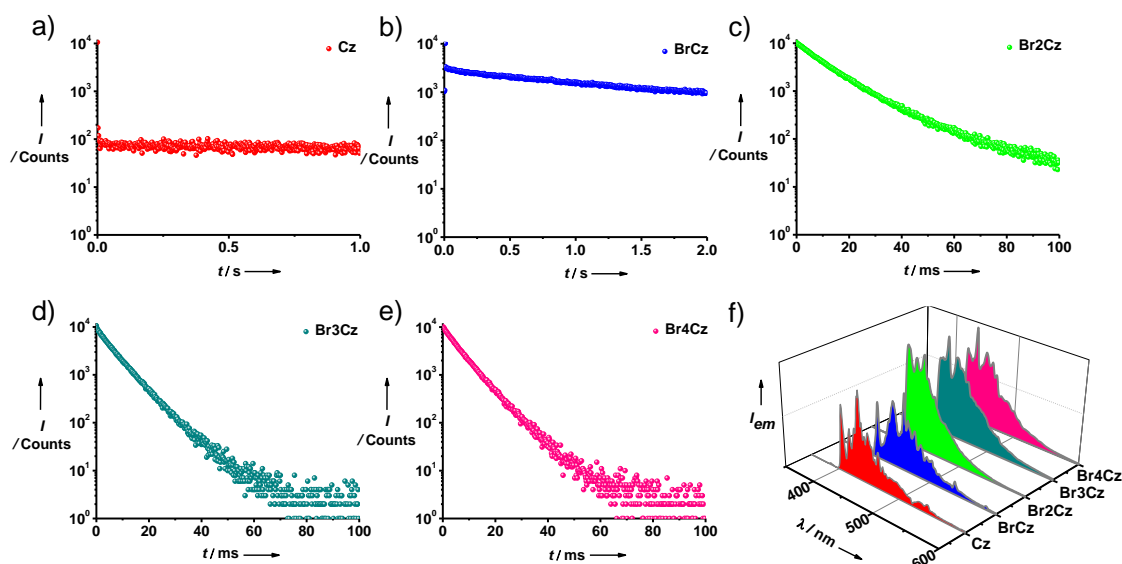


Figure 2.9. Phosphorescence lifetimes of 0.01 mM THF solution of (a) **Cz** ($\tau_{\text{avg.}} = 5.7$ s), (b) **BrCz** ($\tau_{\text{avg.}} = 1.27$ s), (c) **Br2Cz** ($\tau_{\text{avg.}} = 13.31$ ms), (d) **Br3Cz** ($\tau_{\text{avg.}} = 6.9$ ms) and (e) **Br4Cz** ($\tau_{\text{avg.}} = 6.7$ ms) at 77 K. In all cases $\lambda_{\text{exc.}} = 320$ nm and $\lambda_{\text{monitored}} = 430$ nm. f) Gated emission (phosphorescence) spectra of 0.01 mM THF solution of **Cz**, **BrCz**, **Br2Cz**, **Br3Cz** and **Br4Cz** at 77 K ($\lambda_{\text{exc.}} = 320$ nm, delay time = 5 ms).

In the solution state, the triplet excitons of brominated carbazole derivatives are readily quenched by various non-radiative decay pathways, mainly because of intermolecular collisions and intra-molecular vibrational or rotational motions leading to nearly non-emissive nature of the samples (Figure 2.2). However, crystallization rigidifies the molecular conformations efficiently which in turn prevents the intra/intermolecular quenching pathways arising from strong supramolecular interactions between the phosphor molecules to result in excellent RTP, even in air (Figure 2.5- Figure 2.7). Notably, such rigidification is traditionally achieved under cryogenic

conditions where phosphorescence is activated in glassy solvent matrices.^[13] Interestingly, diluted THF (0.01 mM) solutions of both nascent and Br-substituted carbazole samples when frozen at 77 K (Figure 2.9a) showed very weak phosphorescence in the blue region (400 nm-550 nm) (Fig. 2.9b). This indicates that the monomeric triplet energy state of all these molecules are much higher compared to the crystalline samples. From the excitation spectra in crystalline state (Figure 2.10), it is evident that red-shifted bands appearing beyond 360 nm suggest that the phosphorescence of brominated derivatives (or fluorescence of **Cz**) are aggregated or forming excimers in the solid state.^[14] Hence, crystallization not only improves the RTP intensity compared to cryogenic conditions, but also helps in the pre-organization of phosphors towards an excimer or aggregation-induced, red-shifted phosphorescence emission.^[14] Understanding the origin of phosphorescence band is extremely important in order to designate the energy levels accurately, which in turn provide an important aspect to elucidate other triplet emission mechanisms such as thermally activated delayed fluorescence.^[15] More discussions regarding these experiments will be discussed at length in Chapters 5 and 6.

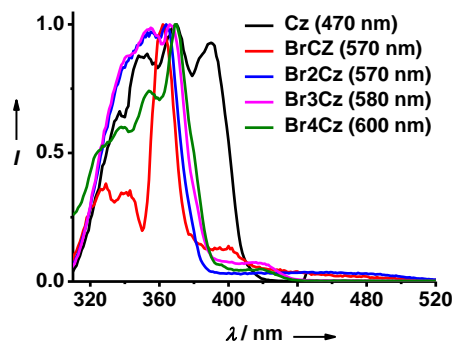


Figure 2.10. Excitation spectra of **Cz**, **BrCz**, **Br₂Cz**, **Br₃Cz** and **Br₄Cz** crystals monitored at different wavelengths.

2.8. Conclusions

In summary, a series of structurally simple, bromine-substituted carbazole phosphors have been synthesized, which show excellent RTP under fully ambient conditions in crystalline state. Structural and organization differences in terms of number of heavy-atoms and various non-covalent and π -stacking interactions allowed to harness efficient RTP, with tunable colour and triplet lifetime in air, from the crystalline samples of these novel derivatives. Since, carbazole is a central molecular substructure in designing state-of-the-art TADF emitters and also as host molecules for energy-efficient OLEDs, the present carbazole derivatives with more efficient triplet yields are expected to pave the way for exciting molecular designs with better performance.^[10,12] Lastly, we envision that the simple halogenation approach reported here to

activate the RTP in carbazole derivatives, will encourage to revisit other commercially available aromatic heterocyclics such as phenothiazine, thianthrene, etc. for ambient triplet harvesting.

2.9. Experimental Section

2.9.1. General Methods

NMR Measurements: ^1H and ^{13}C NMR spectra were recorded on a BRUKER AVANCE-400 Fourier transformation spectrometer with 400 and 100 MHz, respectively. The spectra are calibrated with respect to the residual solvent peaks. The chemical shifts are reported in parts per million (ppm) with respect to TMS. Short notations used are, s for singlet, d for doublet, t for triplet, q for quartet and m for multiplet.

Optical Measurements: Electronic absorption spectra were recorded on a Perkin Elmer Lambda 900 UV-Vis-NIR Spectrometer and emission spectra were recorded at FLSP920 spectrometer, Edinburgh Instruments.

Lifetime measurements and quantum yield: Solid state fluorescence lifetime was performed on a Horiba DeltaFlex time-correlated single-photon-counting (TCSPC) instrument. A 373 nm nano-LED with a pulse repetition rate of 1 MHz was used as the light source. Phosphorescence lifetime ($\lambda_{exc.} = 380$ nm) and gated emission was measured on FLSP920 spectrometer, Edinburgh Instruments equipped with a micro flash lamp ($\mu\text{F}2$) set-up. Solution state fluorescence lifetimes were performed on this instrument using a 340 nm LED source with a pulse repetition rate of 1 MHz. The instrument response function (IRF) was collected by using a scatterer (Ludox AS40 colloidal silica, Sigma-Aldrich). Quantum yield was measured using an integrated sphere using the same FLSP920 spectrometer.

High Resolution Mass Spectroscopy (HRMS): HR-MS was carried out using Agilent Technologies 6538 UHD Accurate-Mass Q-TOFLC/MS.

Computational Details: All the molecules were optimized in their ground state using Density Functional Theory (DFT) with B3LYP^{S1} functional and 6-31+g(d) basis set for all atoms except Br, for which LANL2DZ basis set along with the corresponding effective core potential (ECP) was used. The excited singlet and triplet state energies were calculated using time-dependent DFT (TDDFT) method. Tamm-Dancoff approximation (TDA)^{S2} was considered for the calculation for triplet energies to overcome the triplet instability issue. Nature of the excited states was described using natural transition orbital (NTO) analysis to describe the nature of excitation.^{S3} All the DFT/TDDFT calculations were performed using Gaussian 09 software (G09RevE.01).^{S4} Spin-orbit couplings between the singlet and triplet excited states were

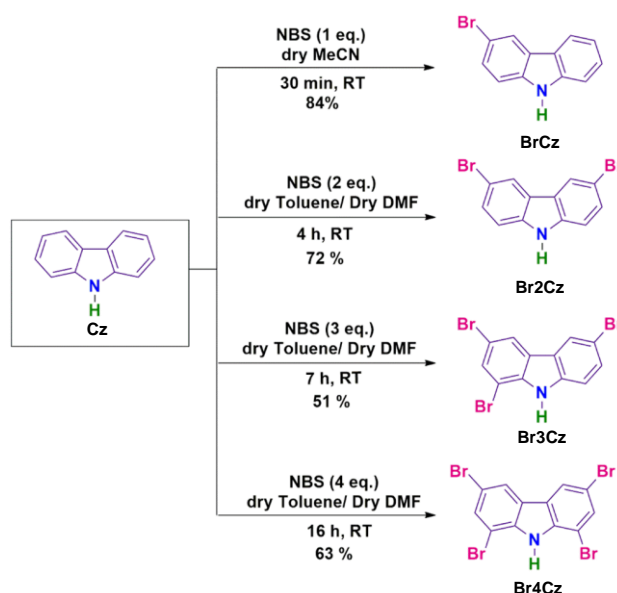
calculated based on Breit-Pauli Spin-orbit Hamiltonian with an effective charge approximation as implemented in the PySOC code.^{S5}

Single crystal X-ray diffraction (SCXRD): The single crystal samples of **BrCz**, **Br2Cz**, **Br3Cz** and **Br4Cz** were mounted on a thin glass fibre with commercially available super glue. SCXRD data of these samples were collected on a Bruker D8 Venture diffractometer (Photon CMOS detector) equipped with a microfocus sealed tube X-ray source operating at 50 kV and 1 mA, with ω scan mode. Mo- α ($\lambda = 0.71073 \text{ \AA}$) and Cu- α ($\lambda = 1.5406 \text{ \AA}$) radiation was used to collect the data. The program, SAINT^{S6} was used for the integration of diffraction profiles followed by the absorption corrections using the SADABS program.^{S7} The structures were solved by dual space methods/intrinsic phasing followed by successive Fourier and difference Fourier syntheses. All the non-hydrogen atoms were refined anisotropically. Calculations were performed using SIR-92,^{S8} SHELXT,^{S9} SHELXL-2014,^{S10} SHELXL 97,^{S11} PLATON,^{S12} WinGX system,^{S13} version 2014 and Olex2.^{S14} The Cambridge Crystallographic Data Centre (CCDC) reference numbers for **BrCz**, **Br2Cz**, **Br3Cz** and **Br4Cz** are 1992307, 1992306, 1992308 and 1992309, respectively.

2.9.2. Synthetic Schemes and Procedures

The synthesis of **BrCz**, **Br2Cz**, **Br3Cz** and **Br4Cz** is shown in Scheme 2.1.

Materials: Carbazole and N-bromosuccinimide (NBS) were purchased from Alfa Aeser and used without further purification.



Scheme 2.1. Synthetic scheme for **BrCz**, **Br2Cz**, **Br3Cz** and **Br4Cz**.

Synthetic Procedures

Commercially available **Cz** (> 97 % purity, Alfa Aeser) was crystallized from saturated CHCl_3 : MeOH (1:2, v/v) solutions by slow evaporation over 12 hours to be used for photophysical studies.

Cz (White crystalline solid): ^1H NMR (400 MHz, $\text{DMSO-}d_6$, ppm): δ_H 11.2 (s, 1H), 8.1 (d, $J = 8$ Hz, 2H), 7.4 (d, $J = 8$ Hz, 2H), 7.3 (t, $J = 8$ Hz, 2H), 7.1 (t, $J = 8$ Hz, 4H); ^{13}C NMR (100 MHz, $\text{DMSO-}d_6$, ppm): δ_C 139.6, 125.4, 122.3, 120.0, 118.4, 110.8.

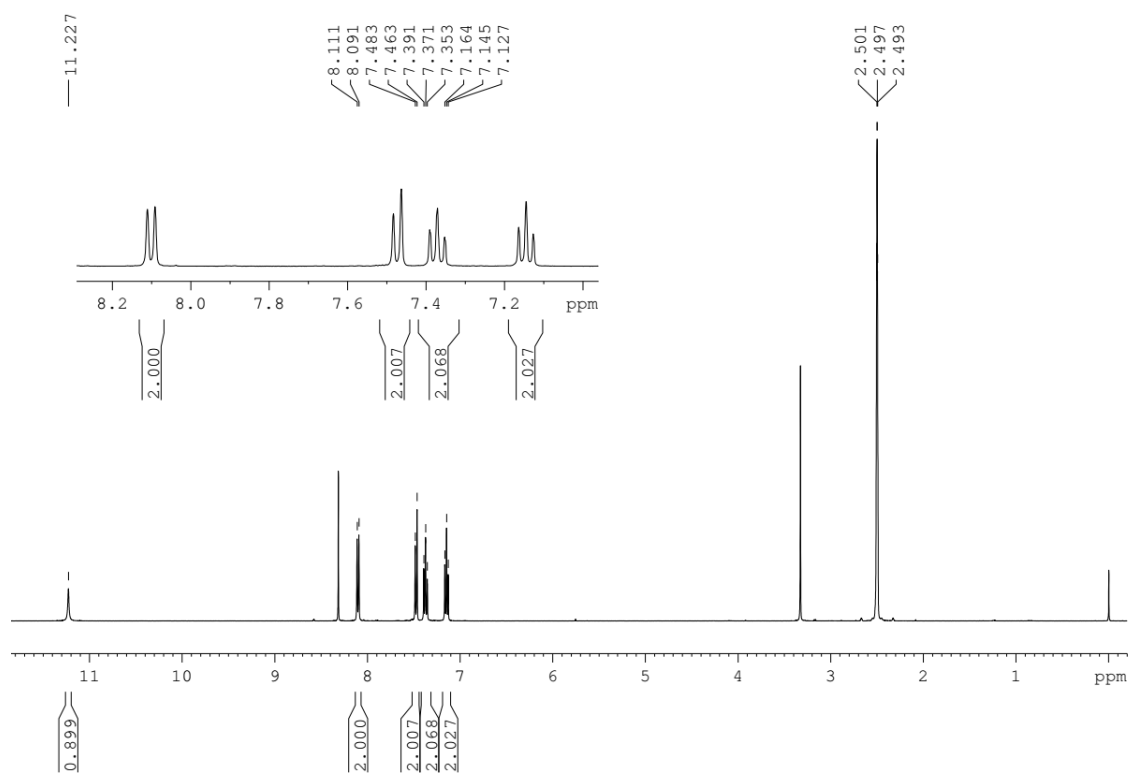


Figure 2.11. ^1H NMR spectrum of **Cz** in $\text{DMSO-}d_6$.

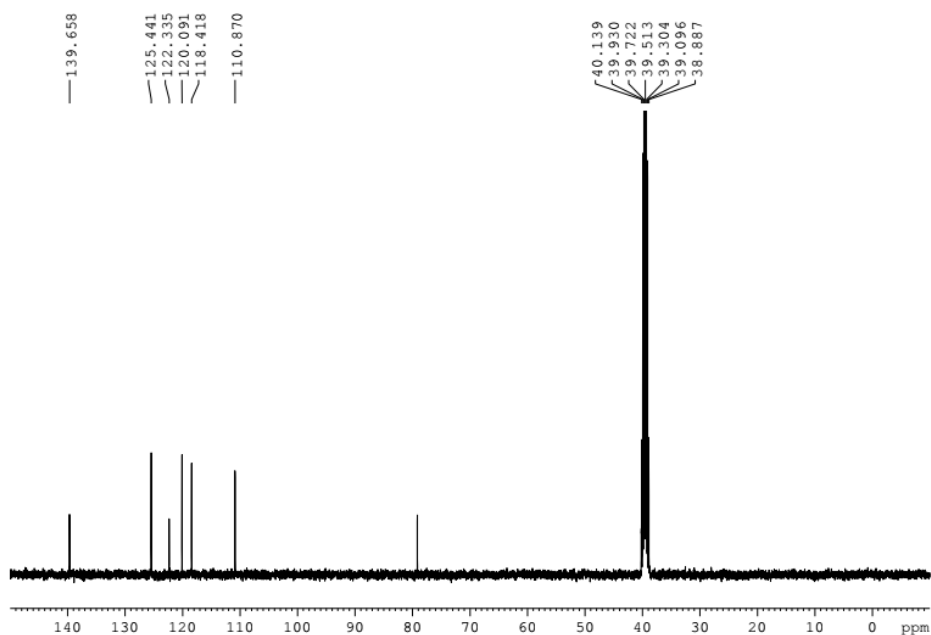


Figure 2.12. ^{13}C NMR spectrum of Cz in $\text{DMSO-}d_6$.

Synthesis of BrCz: N-bromosuccinimide (NBS) (1.05 g, 5.9 mmol, 1.0 eq.) was dissolved in dry acetonitrile and drop wise added to a solution of carbazole (1.05 g, 5.9 mmol, 1.0 eq.) taken in a 100 ml RB flask at $0\text{ }^\circ\text{C}$. This reaction mixture was stirred at the same temperature for 30 minutes before pouring into cold water to get a white precipitate. The precipitate was then filtered off, dried under vacuum at $50\text{ }^\circ\text{C}$ for 4 hours and then recrystallized from saturated CHCl_3 :MeOH (1:2, v/v) solutions by slow evaporation over 24 hours.

BrCz: white crystalline solid (1.23 g, 84 % yield).

^1H NMR (400 MHz, $\text{DMSO-}d_6$, ppm): δ_{H} 11.4 (s, 1H), 8.3 (d, $J = 1.6$ Hz, 1H), 8.1 (d, $J = 7.6$ Hz, 1H), 7.5-7.4 (m, 4H), 7.1 (t, $J = 7.2$ Hz, 1H). ^{13}C NMR (100 MHz, $\text{DMSO-}d_6$, ppm): δ_{C} 140.1, 138.3, 127.8, 126.2, 124.3, 122.6, 121.4, 120.6, 118.8, 112.8, 111.1, 110.5. HRMS (ESI, negative mode): m/z calculated for $\text{C}_{12}\text{H}_8\text{BrN}$: 243.9840: observed 243.9756 $[\text{M-H}]^-$.

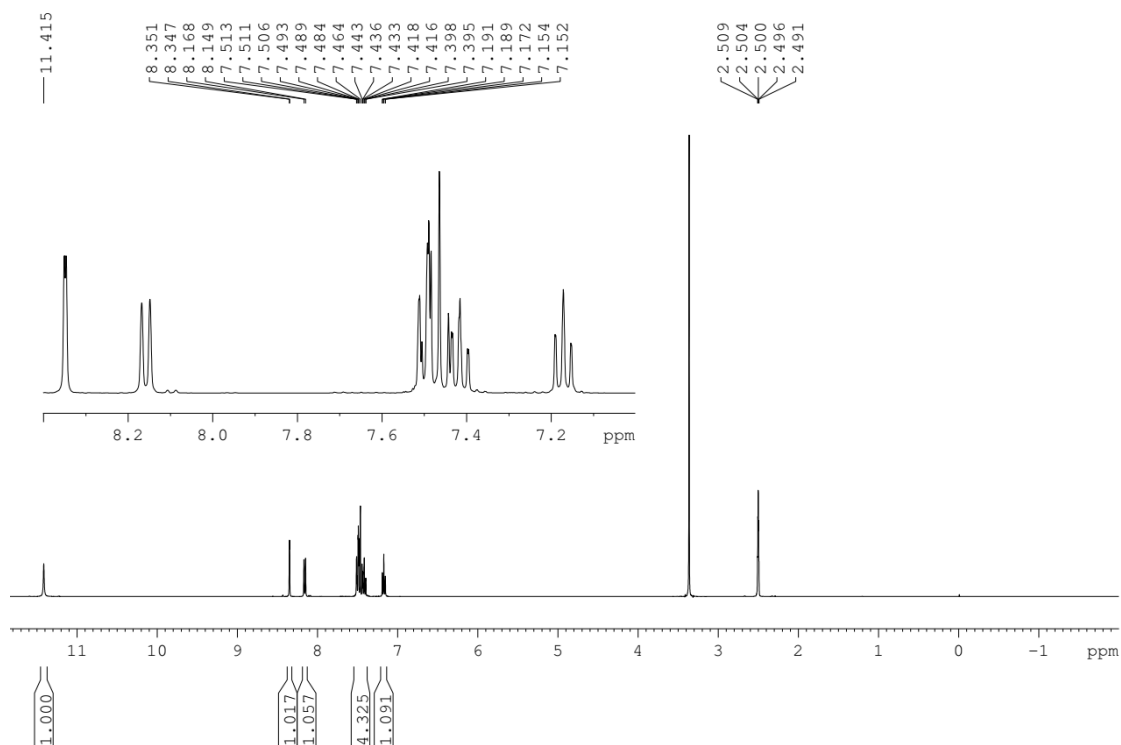


Figure 2.13. ^1H NMR spectrum of **BrCz** in $\text{DMSO-}d_6$.

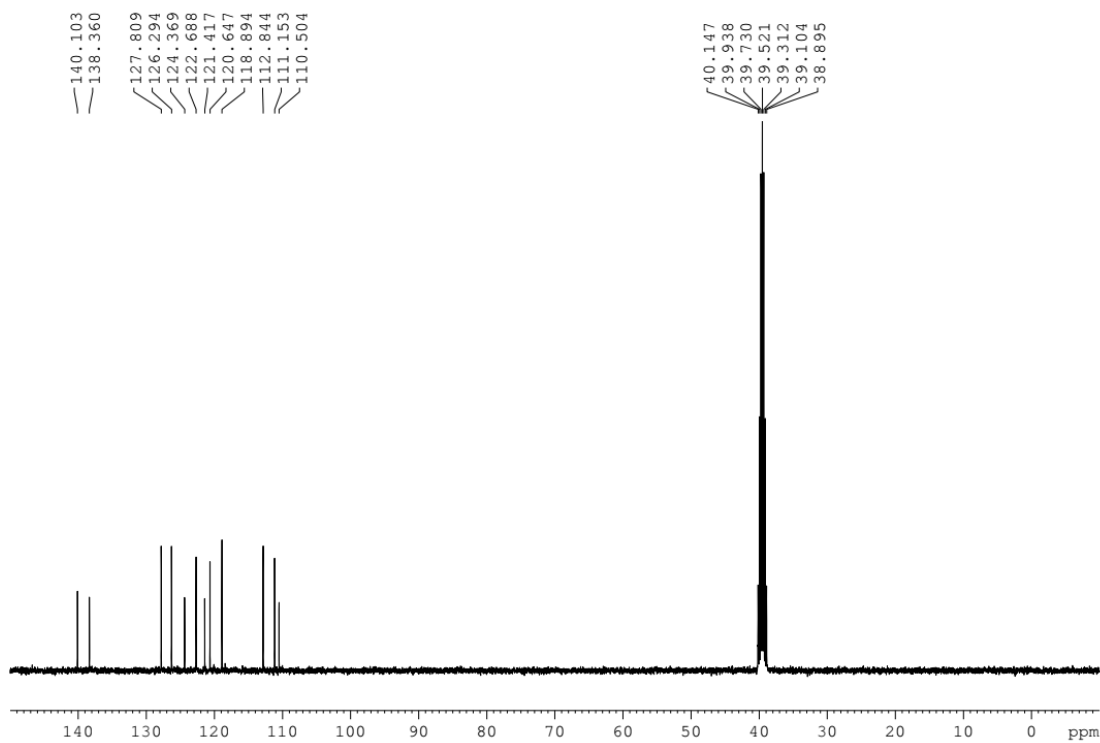


Figure 2.14. ^{13}C NMR spectrum of **BrCz** in $\text{DMSO-}d_6$.

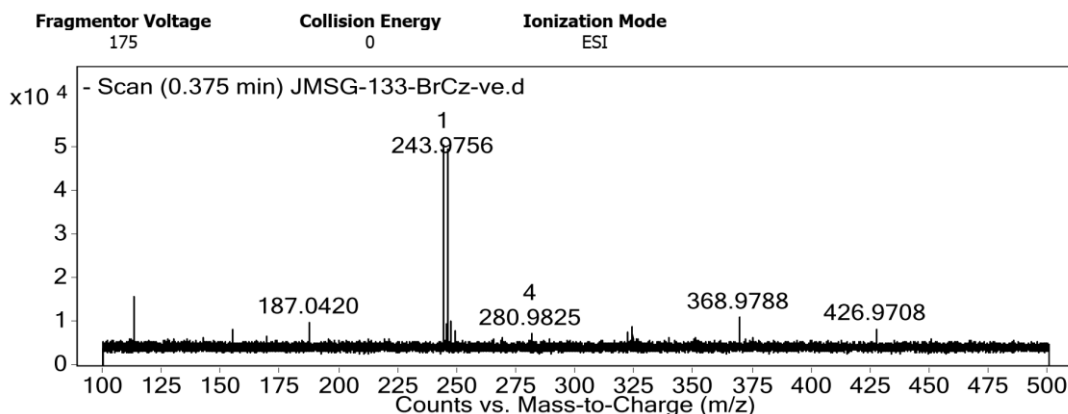


Figure 2.15. ESI-HRMS of **BrCz** in negative mode.

Synthesis of Br2Cz: Carbazole (1.0 g, 5.9 mmol) was taken in a 100 ml RB flask and then dissolved in dry toluene. This solution was cooled down to 0 °C in an ice-bath followed by the drop wise addition of N-bromosuccinimide (NBS) (2.1 g, 11.8 mmol, 2.0 eq.) dissolved in dry DMF. After stirring this solution for 4 h at RT, it was poured into cold water (50 ml) to obtain the white precipitate. This was filtered, washed repeatedly with cold methanol (50 ml) and then dried under vacuum oven at 50 °C for 4 hours. This white solid was then purified by silica-gel column chromatography (Chloroform: Hexane = 1: 10). The white **Br2Cz** amorphous solid was further recrystallized from saturated CHCl₃: MeOH (1:2 v/v) solutions by slow evaporation over 4 days.

Br2Cz: white crystalline solid (1.4 g, 72 % yield).

¹H NMR (400 MHz, DMSO-*d*₆, ppm): δ_H 11.5 (s, 2H), 8.4 (d, J = 1.6 Hz, 2H), 7.5 (dd, J = 8.4 Hz, 4H). ¹³C NMR (100 MHz, DMSO-*d*₆, ppm): δ_C 138.7, 128.6, 123.3, 1123.2, 113.1, 110.9. HRMS (ESI, negative mode): *m/z* calculated for C₁₂H₇Br₂N: 324.8925; observed 323.8854 [M-H]⁻.

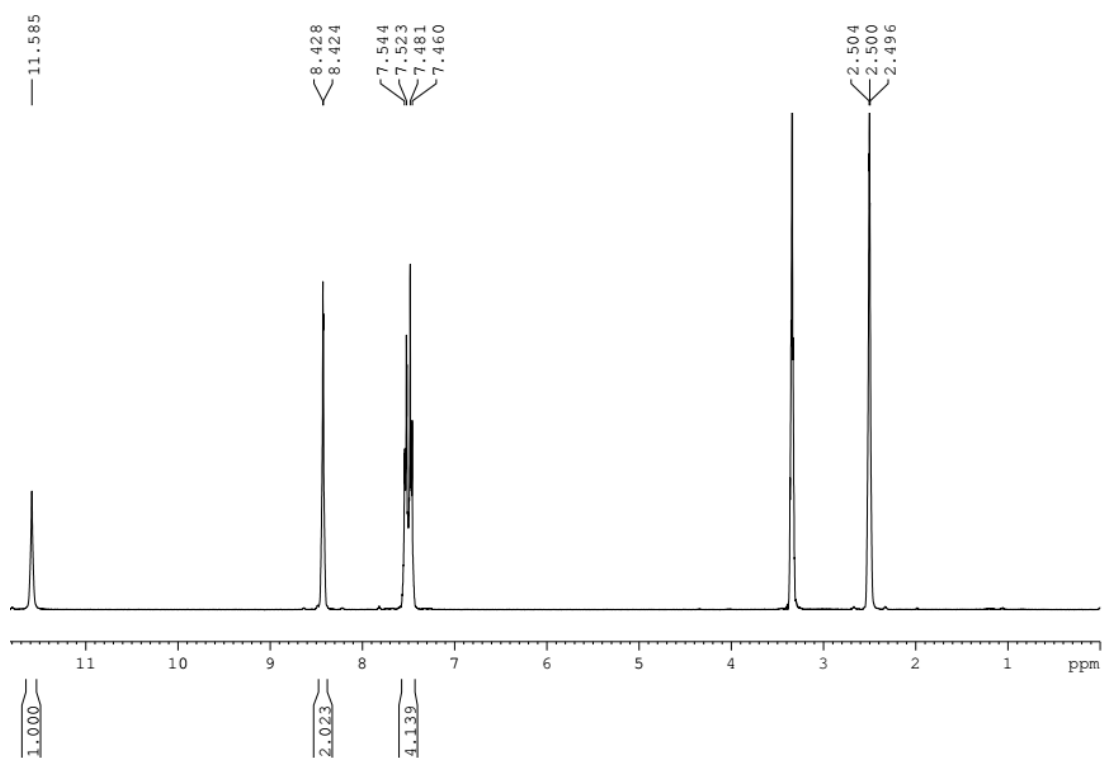


Figure 2.16. ^1H NMR spectrum of **Br2Cz** in $\text{DMSO-}d_6$.

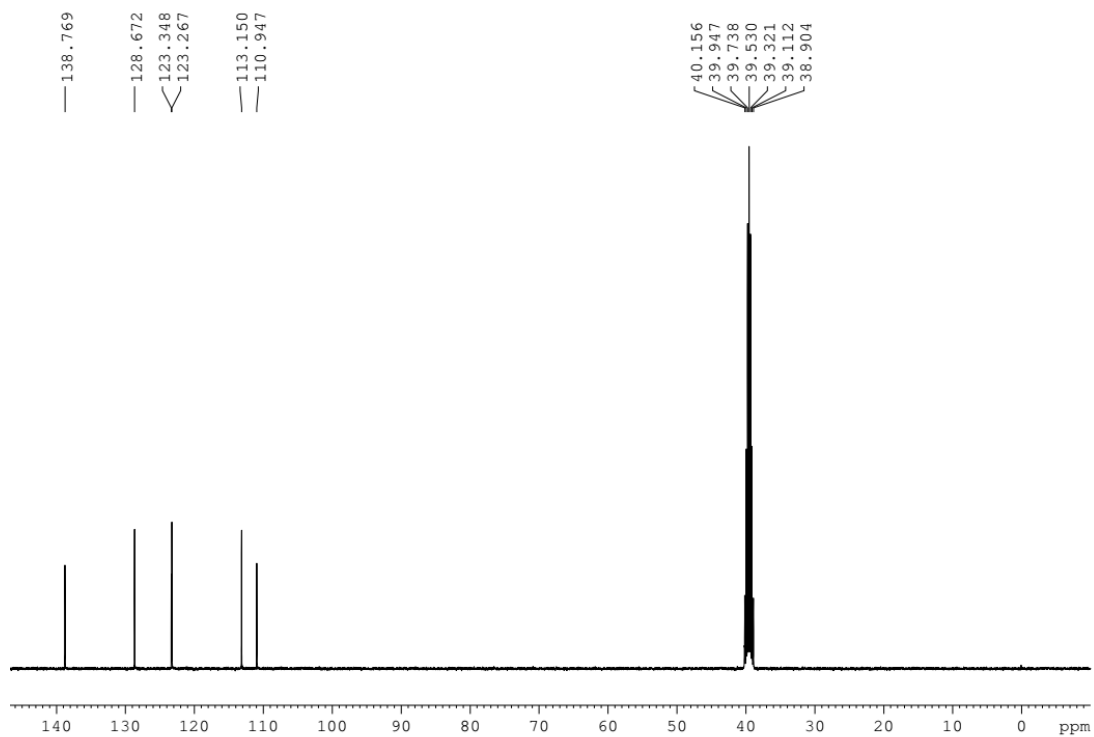


Figure 2.17. ^{13}C NMR spectrum of **Br2Cz** in $\text{DMSO-}d_6$.

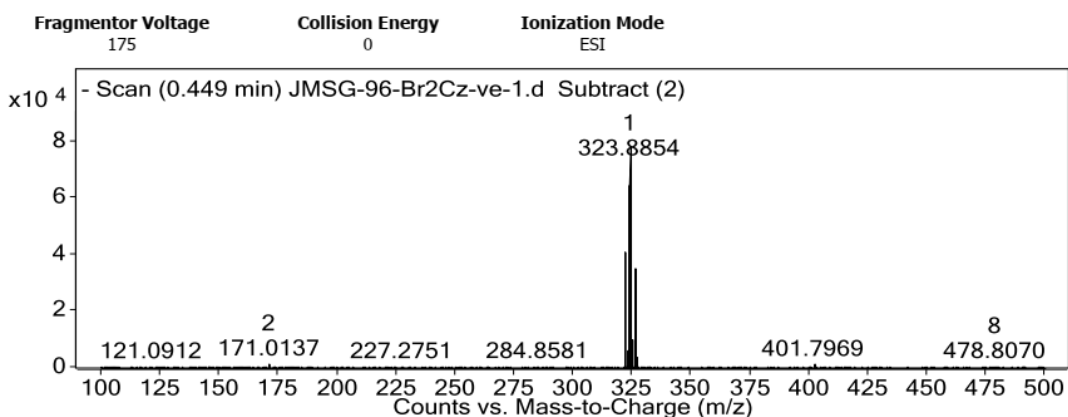


Figure 2.18. ESI-HRMS spectrum of **Br2Cz** in negative mode.

Synthesis of Br3Cz: This compound was synthesized and recrystallized by a similar method to that of **Br2Cz**, using carbazole (1.0 g, 5.9 mmol) and N-bromosuccinimide (NBS) (3.1 g, 17.7 mmol, 3.0 eq.).

Br3Cz: White crystalline solid (1.24 g, 51 % yield).

^1H NMR (400 MHz, DMSO- d_6 , ppm): δ_{H} 11.7 (s, 1H), 8.4 (d, $J = 7.2$ Hz, 2H), 7.8 (d, $J = 1.2$ Hz, 1H), 7.6-7.5 (m, 2H). ^{13}C NMR (100 MHz, DMSO- d_6 , ppm): δ_{C} 138.9, 137.4, 130.0, 129.5, 124.4, 123.8, 123.5, 122.8, 113.7, 111.7, 110.8, 104.4. HRMS (ESI, negative mode): m/z calculated for $\text{C}_{12}\text{H}_6\text{Br}_3\text{N}$: 403.8009; observed 403.7939 [$\text{M}-\text{H}$] $^-$.

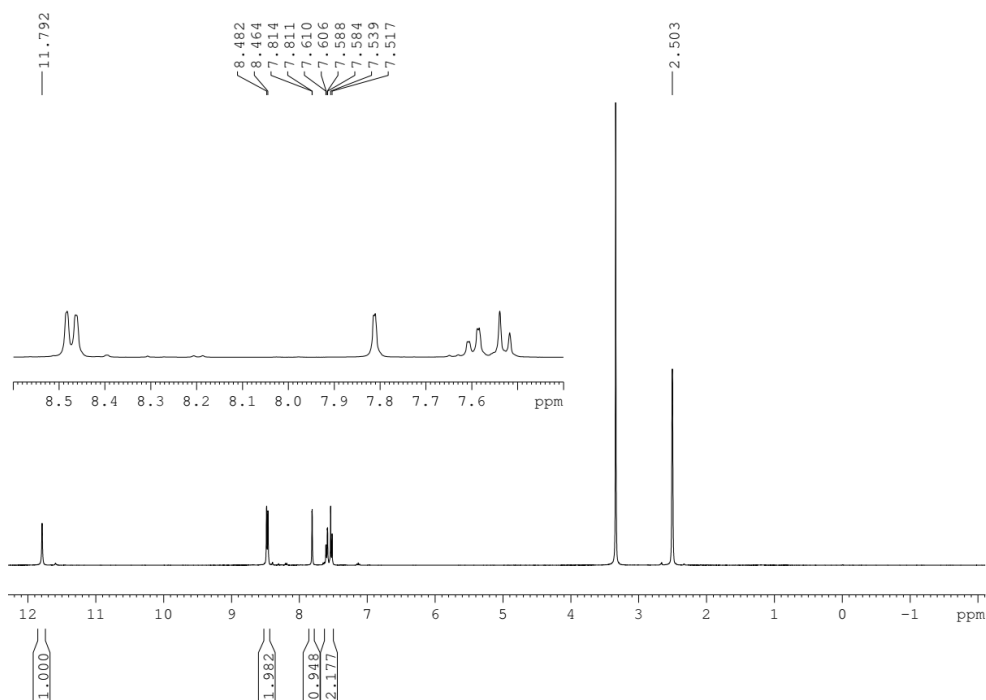


Figure 2.19. ^1H NMR spectrum of **Br3Cz** in DMSO- d_6 .

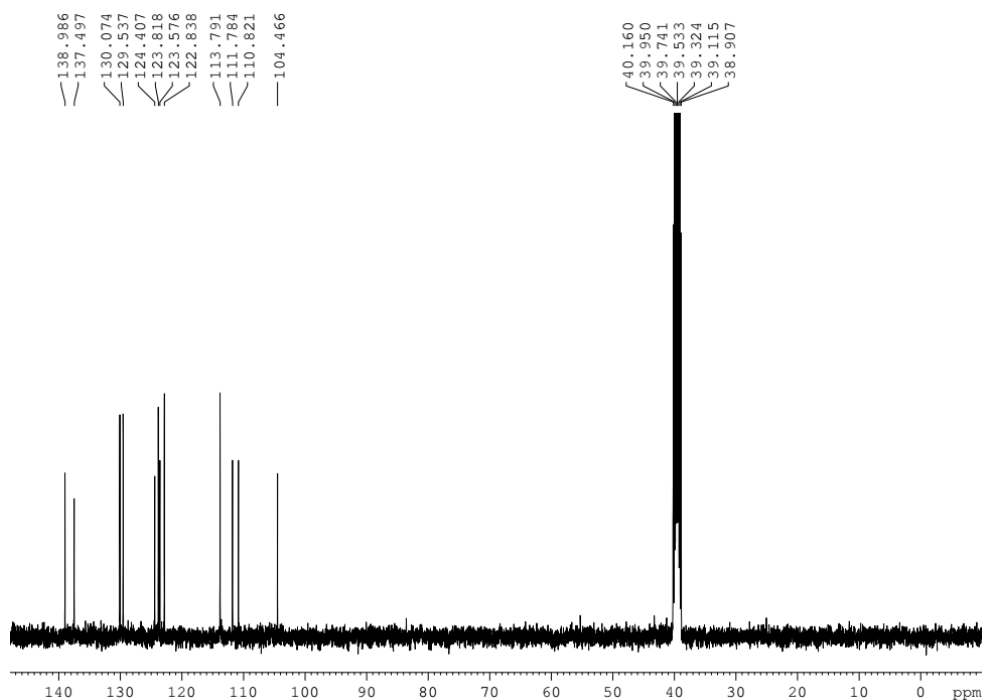


Figure 2.20. ^{13}C NMR spectrum of **Br3Cz** in $\text{DMSO-}d_6$.

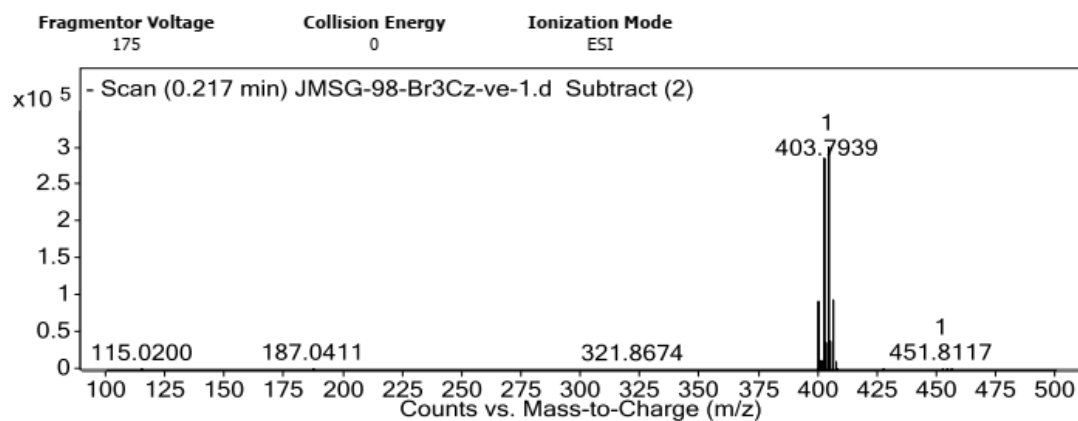


Figure 2.21. ESI-HRMS spectrum of **Br3Cz** in negative mode.

Synthesis of Br4Cz: This compound was synthesized and recrystallized by a similar method to that of **Br2Cz**, using carbazole (1.0 g, 5.9 mmol) and N-bromosuccinimide (NBS) (4.2 g, 23.6 mmol, 4.0 eq.).

Br4Cz: White Crystalline solid (1.8 g, 63 % yield).

^1H NMR (400 MHz, $\text{DMSO-}d_6$, ppm): δ_H 11.6 (s, 1H), 8.5 (d, $J = 2.0$ Hz, 2H), 7.8 (d, $J = 1.6$ Hz, 2H). ^{13}C NMR (100 MHz, $\text{DMSO-}d_6$, ppm): δ_C 137.9, 131.5, 125.0, 123.1, 111.9, 105.1. HRMS (ESI, negative mode): m/z calculated for $\text{C}_{12}\text{H}_5\text{Br}_4\text{N}$: 482.7115 : observed 481.7045 $[\text{M-H}]^-$.

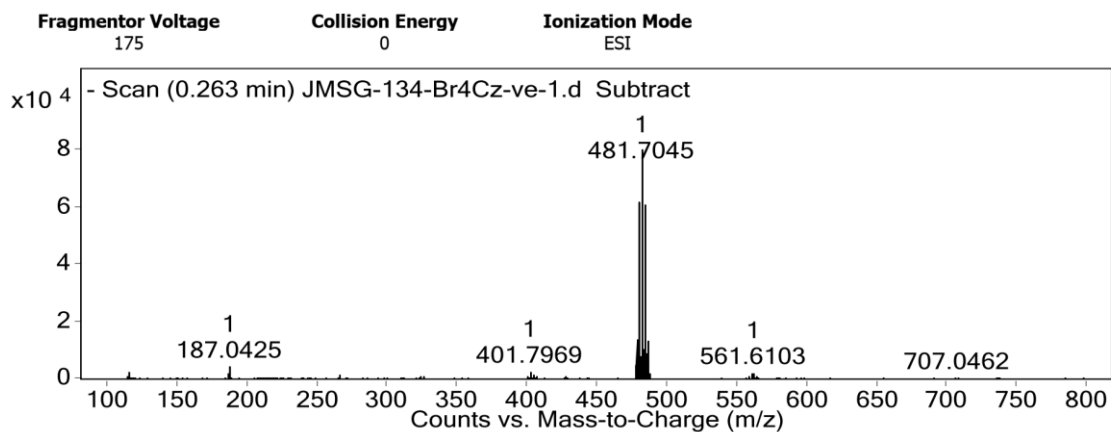


Figure 2.22. ESI-HRMS spectrum of **Br4Cz** in negative mode.

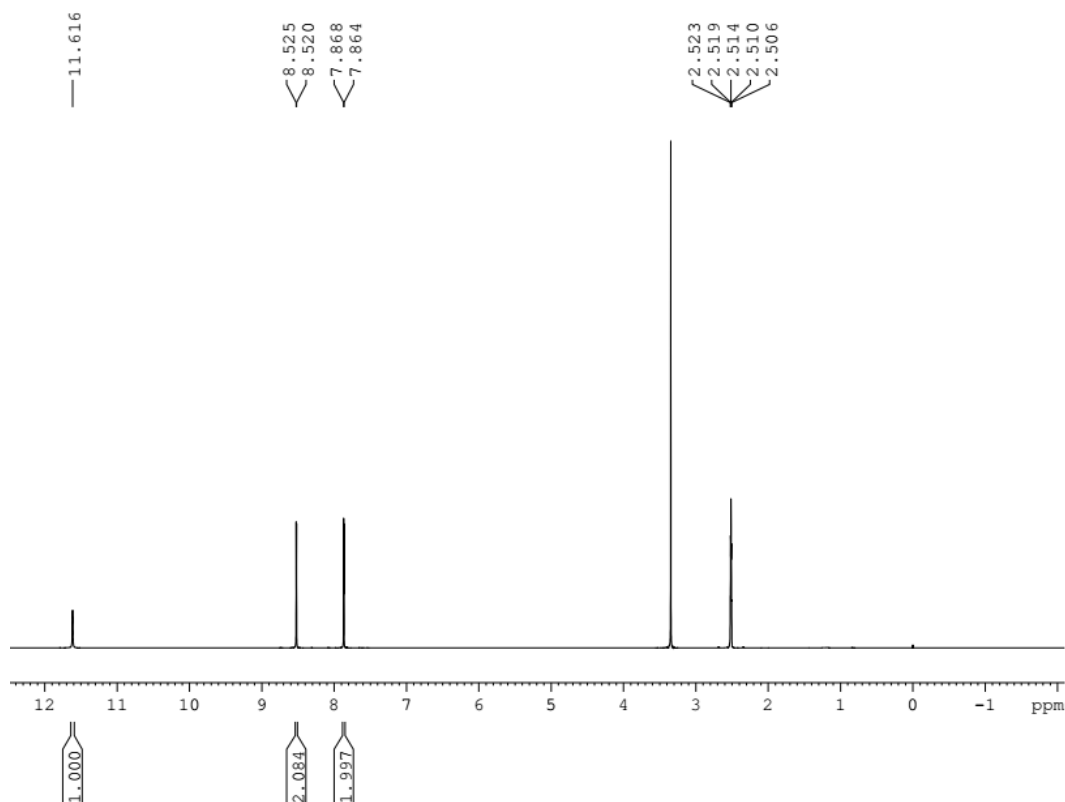


Figure 2.23. ^1H NMR spectrum of **Br4Cz** in $\text{DMSO-}d_6$.

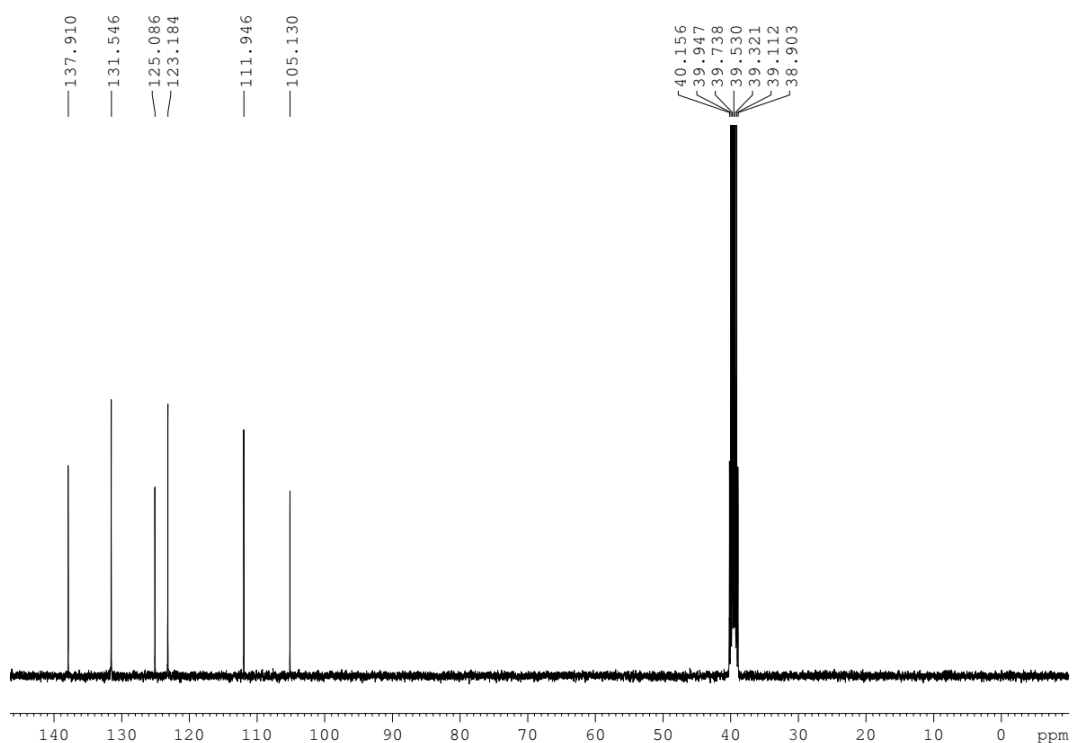


Figure 2.24. ^{13}C NMR spectrum of Br_3Cz in $\text{DMSO}-d_6$.

2.10. References

[1] a) M. Baroncini, G. Bergamini, P. Ceroni, *Chem. Commun.* **2017**, 53, 2081; b) Kenry, C. Chen, B. Liu, *Nat. Commun.* **2019**, 10, 2111; c) A. Forni, E. Lucenti, C. Botta, E. Cariati, *J. Mater. Chem. C* **2018**, 6, 4603; d) Y. Yu, M. S. Kwon, J. Jung; Y. Zeng, M. Kim, K. Chung, J. Gierschner, J. H. Youk, S. Borisov, J. Kim, *Angew. Chem. Int. Ed.* **2017**, 56, 16207; e) S. Mukherjee, P. Thilagar, *Chem. Commun.* **2015**, 51, 10988; f) N. Gan, H. Shi, Z. An, W. Huang, *Adv. Funct. Mater.* **2018**, 28, 1802657; g) X. Zhen, Y. Tao, Z. An, P. Chen, C. Xu, R. Chen, W. Huang, K. Pu, *Adv. Mater.* **2017**, 29, 160666.

[2] N. J. Turro, *Modern Molecular Photochemistry*, University Science Books, Sausalito, **1991**, pp. 99-100.

[3] a) S. K. Lower, M. El-Sayed, *Chem. Rev.* **1966**, 66, 199; b) M. A. El-Sayed, *J. Chem. Phys.* **1963**, 38, 2834; c) G. Baryshnikov, B. Minaev, H. Ågren, *Chem. Rev.* **2017**, 117, 6500.

[4] a) Y. Gong, G. Chen, Q. Peng, W. Z. Yuan, Y. Xie, S. Li, Y. Zhang, B. Z. Tang, *Adv. Mater.* **2015**, 27, 6195; (b) S. Hirata, *Adv. Opt. Mater.* **2017**, 5, 1700116; c) J. Xu, A. Takai, Y. Kobayashi, M. Takeuchi, *Chem. Commun.* **2013**, 49, 8447; d) S. Kuila, A. Ghorai, P. K. Samanta,

R. B. K. Siram, S. K. Pati, K. S. Narayan, S. J. George *Chem. Eur. J.* **2019**, *25*, 16007; e) S. Kuila, K. V. Rao, S. Garain, P. K. Samanta, S. Das, S. K. Pati, M. Eswaramoorthy, S. J. George, *Angew. Chem. Int. Ed.* **2018**, *57*, 17115; f) Z. He, W. Zhao, J. W. Y. Lam, Q. Peng, H. Ma, G. Liang, Z. Shuai, B. Z. Tang, *Nat. Commun.* **2017**, *8*, 416; g) Goudappagouda, A. Manthanath, V. C. Wakchaure, K. C. Ranjeesh, T. Das, K. Vanka, T. Nakanishi, S. S. Babu, *Angew. Chem. Int. Ed.* **2019**, *58*, 2284; h) W. Z. Yuan, X. Y. Shen, H. Zhao, J. W. Y. Lam, L. Tang, P. Lu, C. Wang, Y. Liu, Z. Wang, Q. Zheng, J. Z. Sun, Y. Ma, B. Z. Tang, *J. Phys. Chem. C* **2010**, *114*, 6090; i) S. Kuila, S. J. George, *Angew. Chem. Int. Ed.* **2020**, *59*, 9393.

[5] a) S. Hirata, K. Totani, J. Zhang, T. Yamashita, H. Kaji, S. R. Marder, T. Watanabe and C. Adachi, *Adv. Funct. Mater.* **2013**, *23*, 3386; b) R. Kabe, N. Notsuka, K. Yoshida, C. Adachi, *Adv. Mater.* **2016**, *28*, 655; (c) L. Gu, H. Wu, H. Ma, W. Ye, W. Jia, H. Wang, H. Chen, N. Zhang, D. Wang, C. Qian, Z. An, W. Huang, Y. L. Zhao, *Nat. Commun.* **2020**, *11*, 944; d) D. Lee, O. Bolton, B. C. Kim, J. H. Youk, S. Takayama, J. Kim, *J. Am. Chem. Soc.* **2013**, *135*, 6325; e) Y. Katsurada, S. Hirata, K. Totani, T. Watanabe, M. Vacha, *Adv. Opt. Mater.* **2015**, *3*, 1726; f) S. Hirata, M. Vacha, *Adv. Opt. Mater.* **2017**, *5*, 1600996.

[6] a) Z. An, C. Zheng, Y. Tao, R. Chen, H. Shi, T. Chen, Z. Wang, H. Li, R. Deng, X. Liu, W. Huang, *Nat. Mater.* **2015**, *14*, 685; b) W. Gao, Y. Su, Z. Wang, Y. Zhang, D. Zhang, P. Jia, C. Yang, Y. Li, R. Ganguly, Y. L. Zhao, *ACS Appl. Mater. Interfaces* **2019**, *11*, 47162; c) S. Xu, R. Chen, C. Zheng, W. Huang, *Adv. Mater.* **2016**, *28*, 9920.

[7] a) O. Bolton, K. Lee, H.-J. Kim, K. Y. Lin, J. Kim, *Nat. Chem.* **2011**, *3*, 205; b) M. S. Kwon, D. Lee, S. Seo, J. Jung, J. Kim, *Angew. Chem. Int. Ed.* **2014**, *53*, 11177; c) M. A. Niyas, R. Ramakrishnan, V. Vijay, E. Sebastian, M. Hariharan, *J. Am. Chem. Soc.* **2019**, *141*, 4536.

[8] a) Z. Yang, Z. Mao, X. Zhang, D. Ou, Y. Mu, Y. Zhang, C. Zhao, S. Liu, Z. Chi, J. Xu, Y. C. Wu, P. Y. Lu, A. Lien, M. R. Bryce, *Angew. Chem. Int. Ed.* **2016**, *55*, 2181; b) S. M. A. Fatemina, Z. Mao, S. Xu, Z. Yang, Z. Chi and B. Liu, *Angew. Chem. Int. Ed.* **2017**, *56*, 12160; c) Goudappagouda, K. Asokan, R. Nayak, R. Krishnan, S. S. Babu, *Dyes Pigm.* **2020**, *173*, 107931; d) V. C. Wakchaure, K. C. Rajneesh, Goudappagouda, T. Das, K. Vanka, R. Gonnade, S. S. Babu, *Chem. Commun.* **2018**, *54*, 6028.

[9] a) G. N. Lewis, M. Kasha, *J. Am. Chem. Soc.* **1944**, *66*, 2100; b) G. N. Lewis, D. Lipkin, T. T. Magel, *J. Am. Chem. Soc.* **1941**, *63*, 3005.

[10] a) H. Uoyama, K. Goushi, K. Shizu, H. Nomura, C. Adachi, *Nature* **2012**, *492*, 234; b) B. Wex, B. R. Kaafarani, *J. Mater. Chem. C* **2017**, *5*, 8622; c) C. Sun, X. Ran, X. Wang, Z. Cheng,

Q. Wu, S. Cai, L. Gu, N. Gan, H. Shi, Z. An, H. Shi, W. Huang, *J. Phys. Chem. Lett.* **2018**, *9*, 335; d) H. Y. Gao, Q. J. Shen, X. R. Zhao, X. Q. Yan, X. Pang, W. J. Jin, *J. Mater. Chem.* **2012**, *22*, 5336; e) C. S. Bilen, N. Harrison, D. J. Morantz, *Nature* **1978**, *271*, 235.

[11] N. Siraj, S. Das, F. Hasan, C. Lu, L. W. Kiruri, K. E. S. Gall, I. M. Warner, *RSC Adv.* **2015**, *5*, 9939.

[12] a) H. Shi, Z. An, P. Li, J. Yin, G. Xing, T. He, H. Chen, J. Wang, H. Sun, W. Huang and Y. L. Zhao, *Cryst. Growth Des.* **2016**, *16*, 808; b) S. Cai, H. Shi, D. Tian, H. Ma, Z. Cheng, Q. Wu, M. Gu, L. Huang, Z. An, Q. Peng, W. Huang, *Adv. Funct. Mater.* **2018**, *28*, 1705045.

[13] D. S. McClure, *J. Chem. Phys.* **1949**, *17*, 905.

[14] a) K. Tani, Y. Tohda, H. Takemura, H. Ohkita, S. Itoh, M. Yamamoto, *Chem. Commun.* **2001**, *19*, 1914; b) Y. Wang, J. Yang, Y. Tian, M. Fang, Q. Liao, L. Wang, W. Hu, B. Z. Tang, Z. Li, *Chem. Sci.* **2020**, *11*, 833; c) H. Benten, J. Guo, H. Ohkita, S. Ito, M. Yamamoto, N. Sakumoto, K. Hori, Y. Tohda, K. Tani, *J. Phys. Chem. B* **2007**, *111*, 10905; d) S. T. Hoffmann, P. Schrogel, M. Rothmann, R. Q. Albuquerque, P. Strohhriegl, A. Kohler, *J. Phys. Chem. B* **2011**, *115*, 414.

[15] a) J. Gibson, A. P. Monkman, T. J. Penfold, *ChemPhysChem* **2016**, *17*, 2956; b) M. K. Etherington, J. Gibson, H. Higginbotham, T. J. Penfold, A. P. Monkman, *Nat. Commun.* **2016**, *7*, 13680; c) H. Noda, X.-K. Chen, H. Nakanotani, T. Hosokai, M. Miyajima, N. Notsuka, Y. Kashima, J.-L. Brédas, C. Adachi, *Nat. Mater.* **2019**, *18*, 1084; d) J. U. Kim, I. S. Park, C.-Y. Chan, M. Tanaka, Y. Tsuchiya, H. Nakanotani, C. Adachi, *Nat. Commun.* **2020**, *11*, 1765; d) S. Kuila, A. Ghorai, P. K. Samanta, R. B. K. Siram, S. K. Pati, K. S. Narayan and S. J. George, *Chem. Eur. J.* **2019**, *25*, 16007.

Chapter 3

Organic Long Persistent Luminescence in Solution Processable Amorphous Films

Chapter 3.1. Long Persistent Phosphorescence from Functionalized Coronenes

Chapter 3.2. *Activating “Afterglow Delayed Fluorescence” via Phosphorescence Energy Transfer*

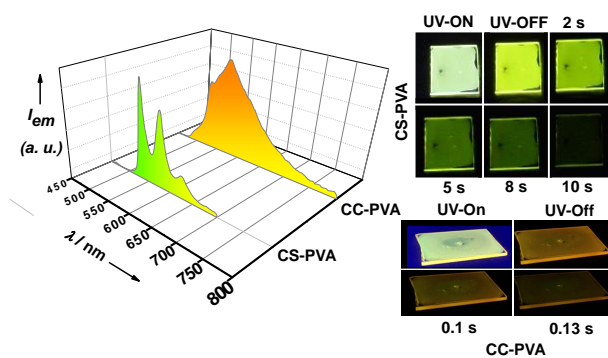
Chapter 3.2. *Temporally-pure White Afterglow Using Complementary Blue and Greenish Yellow Ultralong Room Temperature Phosphors*

CHAPTER 3.1

Long Persistent Phosphorescence from Functionalized Coronenes *

Abstract

In this section, we studied two water-soluble coronene derivatives to achieve amorphous state afterglow/ultralong room temperature phosphorescence in PVA films. Effective isolation of the coronene molecules (phosphors) in the PVA matrix simultaneously reduces the molecular motions and protects the triplets from oxygen-mediated quenching. Excellent aqueous processability of these systems with high phosphorescence efficiency (with quantum yield over 20 % and lifetime over 2 seconds) proves the efficacy of supramolecular self-assembly between the host PVA and guest phosphors. This strategy has been extended for novel molecular designs for afterglow emission in the forthcoming chapters.



*Manuscript based on this work is under preparation.

3.1.1. Introduction

There are two main factors primarily considered for the design of ambient purely organic phosphors: a) activation of efficient intersystem crossing for both $S_1 \rightarrow T_1$ and $T_1 \rightarrow S_0$ transitions and b) minimization of non-radiative deactivation pathways (e. g. vibrational motions and oxygen-mediated quenching) for bright phosphorescence emission under ambient conditions. So far, the most effective approach that satisfy these conditions is crystallization of the organic phosphor molecules.^[1] However, the main drawbacks of crystalline phosphor materials are their poor processability and critical growth conditions, which often result in reproducibility issues related to materials synthesis and luminescence performance.^[2] In addition, it is always difficult to produce long-lived phosphor materials without the control of molecular organization that promote intermolecular electronic coupling between the chromophores in aggregated state.^[3] This criteria is particularly detrimental for most organic molecules due to aggregation induced quenching phenomena. Nonetheless, certain crystalline organic chromophores with high lifetime (in the order of seconds) have been studied for their potential applications in bio-imaging and information storage applications.^[4] Therefore, purely organic phosphor materials are worth investigating in order to replace existing rare-earth elements based inorganic phosphors.^[5] In that regard, solution-processable and amorphous phase ultralong RTP (or afterglow phosphorescent) materials have attracted a lot of attention in past few years and likely to outperform state-of-the-art crystalline URTP emitters for aforementioned applications.^[6] In order to develop such materials, remarkably simple design principles are taken into account. First, the chromophores are generally functionalized with carbonyls groups or with lone-pair containing heteroatoms like N, P or S, to enhance the spin-orbit coupling efficiency (El-Sayed's Rule).^[7] Secondly, immobilization of these chromophores in a rigid amorphous host matrix (typically a polymer or a cage-like host) by non-covalent host-guest interactions (e. g. electrostatic and hydrogen-bonding interactions).^[8] Among various host-guest systems developed for amorphous phase URTP systems, phosphor-doped polymer hybrids have emerged as the best alternative because of their easy, cheap and scalable preparation conditions. In addition, in most of these cases the guest chromophores are effectively isolated in the polymer matrix leading to predictable phosphorescence emission wavelengths (from monomer state). One of the most utilized polymer utilized for this purpose is polyvinyl alcohol (**PVA**), developed by Monkman and co-workers.^[9] They studied RTP properties of a series of commercially available water-soluble conjugated polymers functionalized with carboxylate, sulphonate and quaternary ammonium side-groups which form strong hydrogen-bonding and ion-dipole interactions with the polar hydroxyl groups of host **PVA**. They showed **PVA** could effectively isolate and suppress the molecular motions of these highly fluorescent conjugated polymers to result in phosphorescence under vacuum. The

isolation of phosphor molecules offer a possibility of colour-tuning by designing phosphors with known monomer triplet energy. In this chapter (3.1), we studied two water-soluble coronene molecules functionalized with carboxylate and quaternary ammonium groups (Figure 3.1.1a) in line with the original design studied by Monkman and co-workers. We envisioned that the known afterglow phosphorescence feature of unsubstituted coronene molecules under cryogenic conditions^[10] as well as in rigid zeolite framework,^[11] would provide us an ideal system to develop fully water-processable, amorphous URTP polymer hybrids in air.

3.1.2. Design Strategy

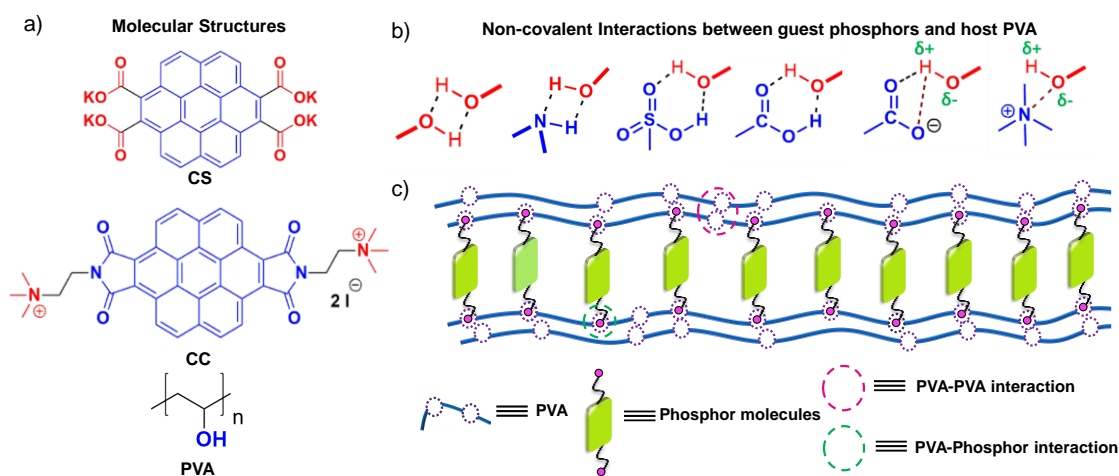


Figure 3.1.1. a) Molecular structures of the phosphors (guest) and polymer matrix (host). b) Example of non-covalent hydrogen-bonding and ion-dipole interactions possible between PVA and guest molecules. c) Schematic representation of a PVA-phosphor assembly.

In this chapter we discuss the phosphorescence properties of two water-soluble coronene derivatives, coronene tetracarboxylate (CS) and dicationic coronenebisimide (CC) (Figure 3.1.1a). Both these compounds consist of multiple carbonyl groups in the backbone and as has been discussed earlier, they are expected to produce high triplet density by following the El-Sayed's rule. In addition, CS is functionalized with four carboxylate groups and expected to exhibit ion-dipole interaction with polar hydroxyl groups of PVA host. In a similar manner, the pendant quaternary ammonium groups of CC are also envisioned to interact with PVA which in turn would result in effective suppression of the molecular motions of the guest molecules, ultimately leading to strong RTP in air. Here it is also very important to note the efficacy of PVA as host because of its salient properties, especially useful for triplet harvesting. There is a plethora of functional groups (such as sulphonates, amines, carboxylic, sulphonic, and phosphoric acids etc.) which can undergo supramolecular self-assembly with host PVA through various non-covalent interactions such as hydrogen-bonding and ion-dipole interactions. Therefore,

molecular design utilizing these functional groups would render an efficient minimization of the non-radiative decay processes (Figure 3.1.1b). Interestingly, **PVA** is known for forming strong intermolecular H-bonding network between the polymer chains which helps in reducing the vibrational/diffusional motion of itself (as the host matrix) and lowers the oxygen permeability to a great extent (Figure 3.1.1c). Both these properties are extremely detrimental for triplet stability.

3.1.3. Ambient Triplet Harvesting from CS

3.1.3.1. Solution-state Photophysical Properties of CS

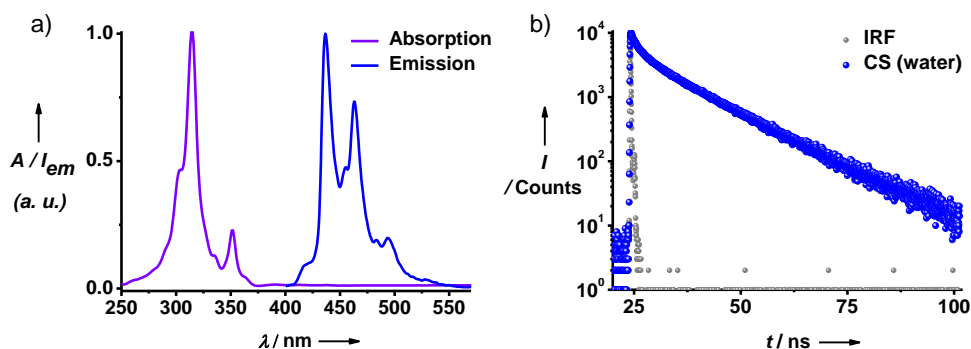


Figure 3.1.2. a) Normalized absorption and fluorescence spectra of CS in water ($\lambda_{exc.} = 350$ nm, $[CS] = 0.1$ mM). b) Fluorescence decays of CS in water ($[CS] = 0.1$ mM, $\lambda_{exc.} = 373$ nm, $\lambda_{monitored} = 440$ nm, $\tau_{avg.} = 10.54$ ns). IRF = instrument response function.

CS (0.1 mM) shows characteristic absorption bands at 250-450 nm region in its UV-Vis spectrum suggesting its molecularly dissolved nature in water (Figure 3.1.2a). The corresponding emission spectra also show strong vibronic feature of fluorescence at 400-500 nm region (at $\lambda_{exc.} = 350$ nm) (Figure 3.1.2a). The fluorescence nature of the emission was confirmed by the corresponding lifetime profile with average lifetime of 10.5 ns ($\lambda_{exc.} = 373$ nm, $\lambda_{monitored} = 440$ nm) (Figure 3.1.2b). However, due to fast vibrational relaxations no phosphorescence can be observed in the solution state. In general the vibrational motions are effectively reduced in solid films or crystals. In the next section we will study the emission properties of CS in both neat films as well as by dispersing the molecules in amorphous **PVA** matrix.

3.1.3.2. Ultralong Room Temperature Phosphorescence (Afterglow) of CS-PVA hybrids

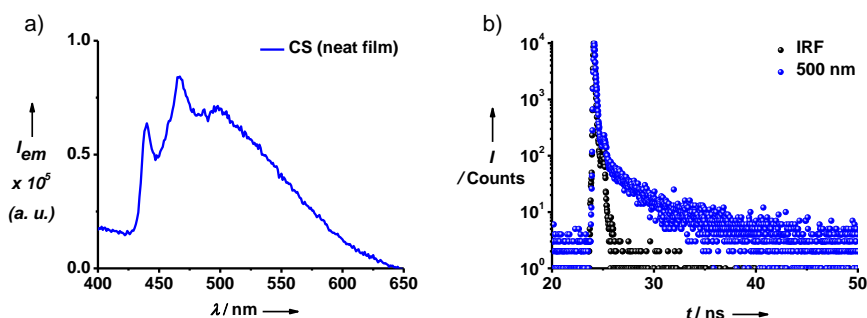


Figure 3.1.3. a) Emission spectrum ($\lambda_{exc.} = 350 \text{ nm}$) and b) corresponding fluorescence decay ($\lambda_{exc.} = 373 \text{ nm}$, $\lambda_{monitored} = 500 \text{ nm}$) profile of CS in neat film. IRF = instrument response function.

CS in its neat thin film state does not show any phosphorescence, however a broad peak (at 500-550 nm region, $\Phi_F < 0.1 \%$, $\lambda_{exc.} = 350 \text{ nm}$) is observed suggesting the strong aggregate formation with excimer-like emission characteristics, observed previously for unsubstituted coronene (Figure 3.1.3a). The emission intensity, though, was very weak and no reliable lifetime could be measured from the neat films (Figure 3.1.3b). Interestingly, PVA effectively isolates the CS molecules resulting in better luminescence efficiency. CS-PVA films obtained by dispersing the 2 wt. % of chromophores in the PVA matrix showed an intense greenish-yellow emission band at 500-700 nm region in addition to characteristic blue fluorescence of CS (Figure 3.1.4). Sharp vibrational features in the absorption spectrum of CS in the PVA matrix, compared to that of neat CS film reiterates the molecularly dispersed organization of the chromophores in the film (Figure 3.1.5). Interestingly, a gated spectrum of these films showed a strong delayed emission in the 500-700 nm range with a weak blue fluorescence component (Figure 3.1.4).

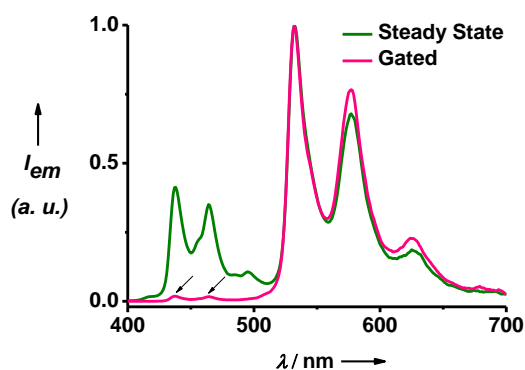


Figure 3.1.4. Steady-state and gated emission spectra of 2 wt. % CS-PVA film ($\lambda_{exc.} = 350 \text{ nm}$, delay time = 5 ms). Arrows indicate the thermally activated delayed fluorescence peaks.

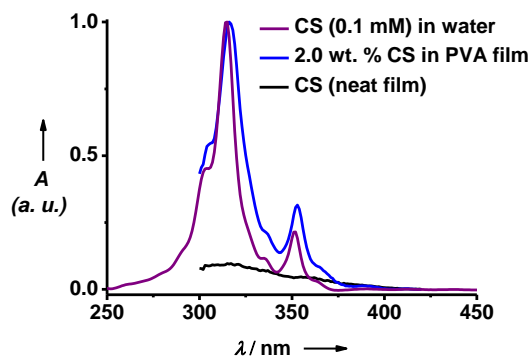


Figure 3.1.5. Absorption spectra of CS in water (0.1 mM), in PVA matrix (2 wt. %) and as neat film suggesting the aggregation of CS molecules in the film state and molecularly dissolved nature in the PVA matrix and in water.

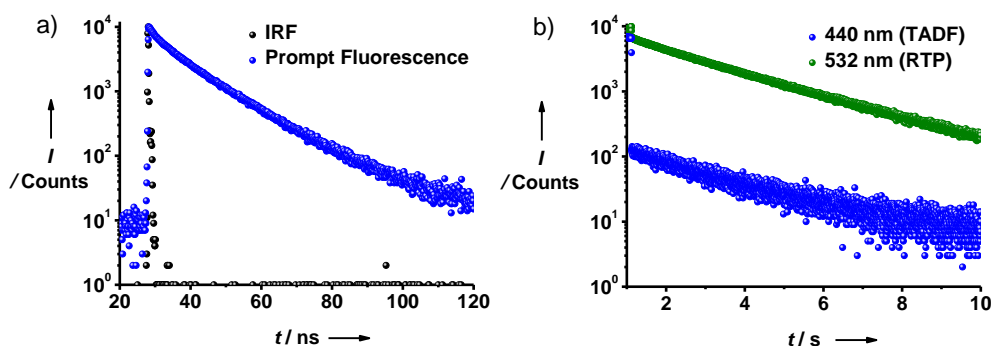


Figure 3.1.6. Time-resolved emission decay profiles of the 2 wt. % CS-PVA film showing a) prompt fluorescence ($\lambda_{exc.} = 373$ nm, $\lambda_{monitored} = 440$ nm, $\tau_{avg.} = 11.23$ ns), b) thermally activated delayed fluorescence ($\lambda_{exc.} = 355$ nm, $\lambda_{monitored} = 440$ nm, $\tau_{avg.} = 2.27$ s) and room temperature phosphorescence ($\lambda_{exc.} = 355$ nm, $\lambda_{monitored} = 532$ nm, $\tau_{avg.} = 2.46$ s). IRF = instrument response function.

Time-resolved lifetime experiments were further performed to understand the nature of these two distinct emission bands. Interestingly, on monitoring the fluorescence at 440 nm, CS-PVA hybrid film showed a prompt as well as delayed fluorescence feature with an average lifetime of 11.2 ns ($\lambda_{exc.} = 373$ nm) and 2.27 s ($\lambda_{exc.} = 355$ nm), respectively (Figure 3.1.6).

Fluence dependent emission measurements, further revealed a linear increase (slope = 0.7) of the emission intensity with increasing excitation intensity suggesting the thermally activated delayed fluorescence nature of the DF emission. However, the overall fluorescence quantum yield was found to be weak ($\Phi_F = 2.2$ %), hinting towards a competing pathway for the depopulation of singlet states. In fact, the long-wavelength emission band (500-700 nm region) showed a very high average lifetime of 2.46 s in air, suggesting its room temperature phosphorescence (RTP) nature (Figure 3.1.6b). Remarkable ambient stability and greenish-yellow afterglow with high quantum yield ($\Phi_P = 23.4$ %) of these CS-PVA films are evident

from the photographs of the films under 365 nm UV-excitation (Figure 3.1.8 and Video 3.1.1). However, at very high weight percentages of CS (50 wt. %) in PVA, the phosphorescence intensity decreases due to the semi-crystalline to amorphous phase transformation of the PVA matrix which would facilitate triplet quenching via enhanced vibrational dissipation (Figure 3.1.9 and Figure 3.1.10). It is worthwhile to mention here, for all the subsequent PVA based studies we shall see, the maximum quantum efficiency of phosphorescence is achieved only by diluting the chromophores in large amount of PVA. Typical composition for best performing materials is 1-2 wt. % dye dispersion in PVA.

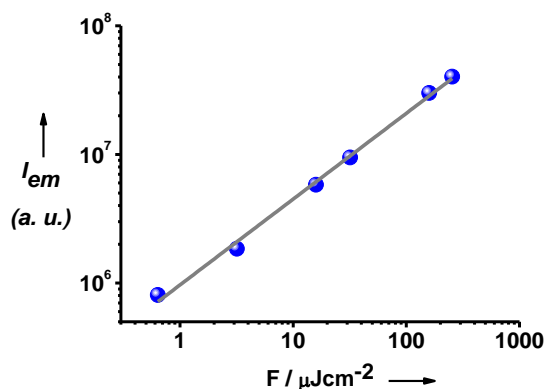


Figure 3.1.7. Dependence of the emission intensity of 2 wt. % CS-PVA hybrid film on excitation power intensity.

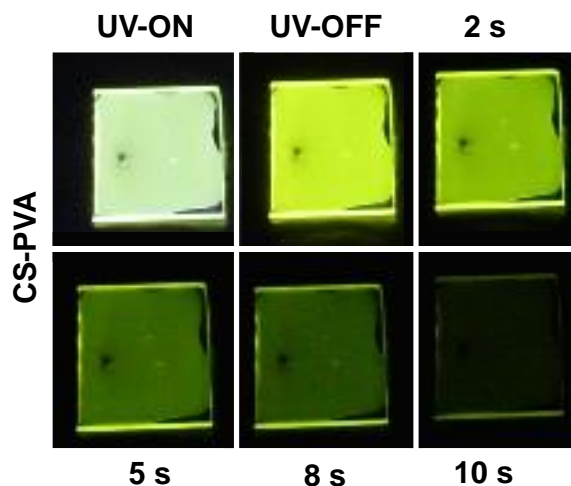


Figure 3.1.8. Photographs of 2 wt. % CS-PVA film under 365 nm excitation and long afterglow when the source is turned off.

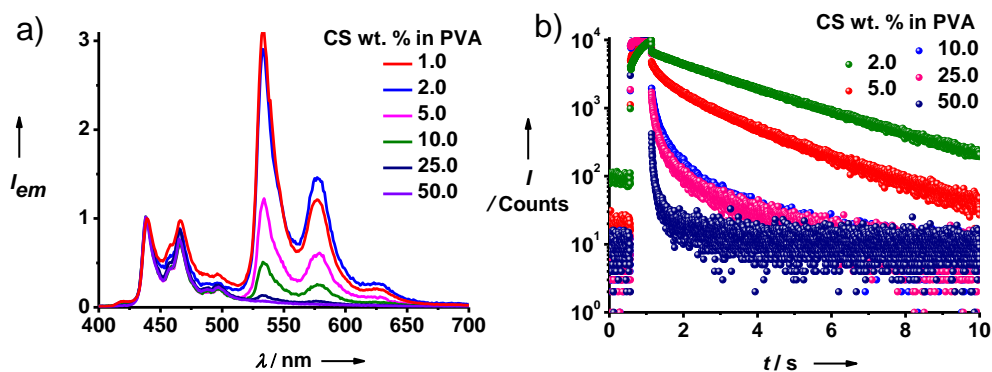


Figure 3.1.9. Composition dependent studies of CS-PVA hybrids. a) Emission spectra ($\lambda_{exc.} = 350$ nm), b) corresponding phosphorescence lifetime ($\lambda_{exc.} = 355$ nm; $\lambda_{monitored} = 532$ nm).

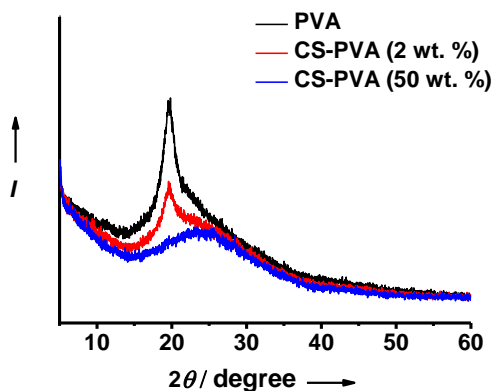


Figure 3.1.10. Powder XRD pattern CS-PVA hybrids of varying composition.

3.1.4. Orange-emitting Phosphorescence Afterglow of CC-PVA hybrids

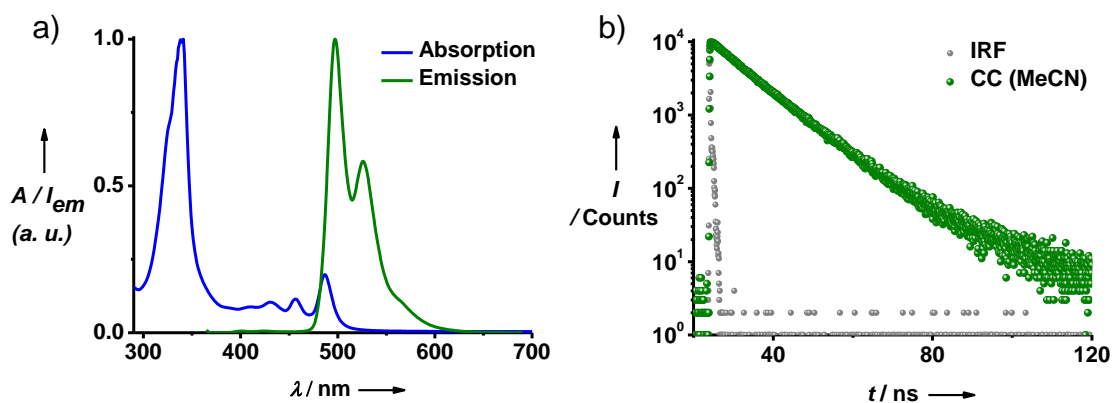


Figure 3.1.11. a) Normalized absorption and fluorescence spectra of CC in acetonitrile ($\lambda_{exc.} = 340$ nm, $[CC] = 0.05$ mM). b) Fluorescence decay profile of CC in acetonitrile ($[CC] = 0.05$ mM, $\lambda_{exc.} = 373$ nm, $\lambda_{monitored} = 510$ nm). IRF = instrument response function.

Having a comprehensive understanding on the triplet emission properties of **CS-PVA** hybrids, we next investigated the photophysical properties of the cationic coronene derivative, **CC**. First, we performed the absorption and emission measurements in solution state followed by elucidation of the RTP characteristics in solid film state.

Unlike the **CS**, the dicationic derivative, **CC** is known to form non-emissive H-aggregates in water.^[12] Therefore, in order to understand the monomer state emission profile of **CC**, it was dissolved in acetonitrile in low concentration (0.05 mM). In acetonitrile, it shows characteristic absorption peaks at 340 nm and 490 nm (Figure 3.1.11a). On the other hand, it showed strong green fluorescence in the emission profile ($\lambda_{exc.} = 340$ nm), although no triplet contribution was observed (Figure 3.1.11a). The average fluorescence lifetime of **CC** in acetonitrile was measured to be 10.25 ns ($\lambda_{exc.} = 373$ nm, $\lambda_{monitored} = 510$ nm) (Figure 3.1.11b).

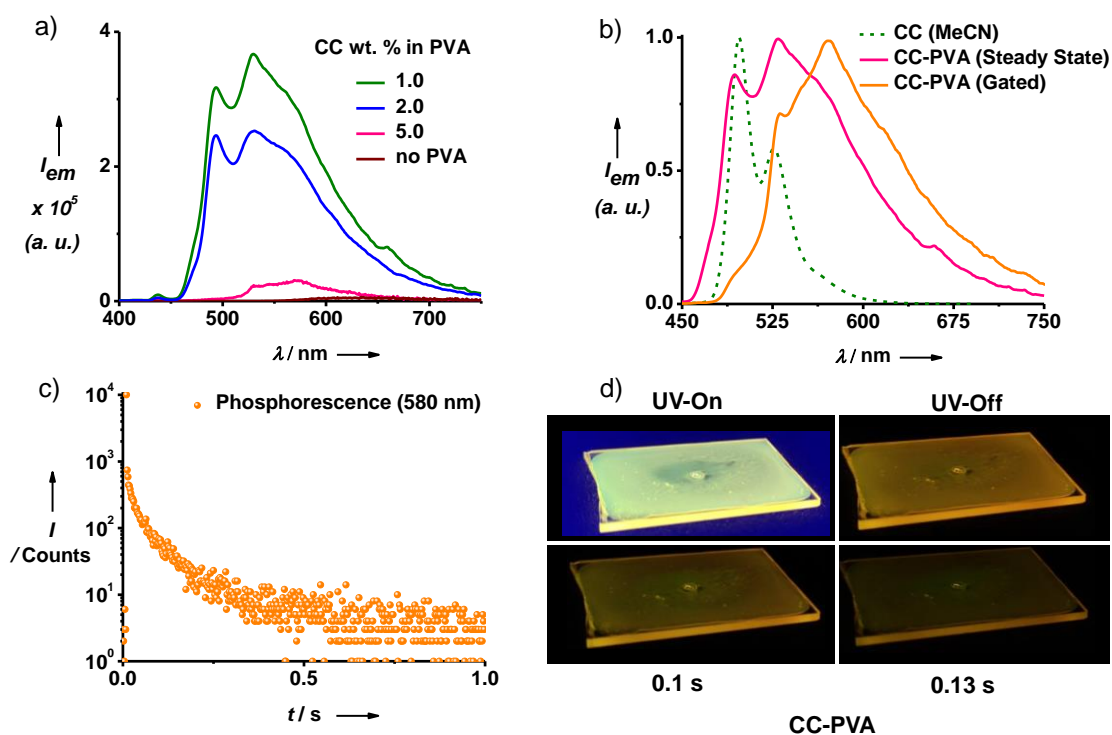


Figure 3.1.12. a) Composition dependent emission profile of **CC-PVA** hybrids ($\lambda_{exc.} = 340$ nm). b) Steady-state and gated emission spectra of 1 wt. % **CC-PVA** film ($\lambda_{exc.} = 340$ nm, delay time = 1 ms). The dotted plot is molecularly dissolved fluorescence of 0.05 mM **CC** in MeCN. c) Time-resolved emission decay profiles of the 1 wt. % **CC-PVA** film showing ultralong RTP emission ($\lambda_{exc.} = 340$ nm, $\lambda_{monitored} = 580$ nm). d) Photographs of 1 wt. % **CC-PVA** film under 365 nm excitation and long afterglow when the source is turned off.

On the other hand, in neat film state, **CC** forms strong aggregation and the intensity could only be improved upon dispersion in **PVA** at very low concentration (1 wt. % **CC** in **PVA**) (Figure 3.1.12a). Interestingly, the gated emission (delay time = 1 ms) of the 1 wt. % **CC-PVA** hybrid film showed an orange-emitting phosphorescence band with average lifetime of 52.3 ms ($\lambda_{\text{exc.}} = 340$ nm, $\lambda_{\text{monitored}} = 580$ nm) (Figure 3.1.12b and 3.1.12c). Such a high phosphorescence lifetime was also evident from visible orange-emitting afterglow upon cessation of the UV-source ($\lambda_{\text{exc.}} = 365$ nm, Figure 3.1.12d and Video 3.1.2). Here, it is worth mentioning that, the steady-state emission of **CC-PVA** overlaps with the fluorescence band when dissolved in acetonitrile (Figure 3.1.11a). This suggests towards effective isolation of the **CC** molecules in **PVA** which lead to strong RTP as has been seen in case of **CS**. Nonetheless, the phosphorescence intensity of **CC-PVA** was substantially weaker ($\Phi_{\text{total}} = 13.6$ %) than **CS-PVA** hybrids, which is rationalized by the flexible ethylene chains present in the **CC**. Therefore, in the subsequent chapters we shall use **CS-PVA** system for further exploration of amorphous phosphorescence hybrids instead of **CC-PVA**.

3.1.5. Conclusions

In summary, we have studied two water-soluble phosphors (**CS** and **CC**) that show excellent ultralong RTP or phosphorescence afterglow in air. Such simple but efficient protocol for air-stable, transparent, solution-processed ultralong RTP with excellent triplet harvesting properties (maximum $\Phi_{\text{P}} \sim 25$ % and $\tau_{\text{avg.}} > 2.4$ s) are rarely reported in literature. This ambient stability is envisioned to be a result of multiple carbonyl groups present in the chromophores, which impart sufficient spin-orbit coupling to facilitate ISC and the resulting triplet excitons are further stabilized by the rigid **PVA** host. Remarkably, both phosphors show monomeric feature in the emission spectra suggesting the excellent templating effect of **PVA** to reduce the aggregation induced quenching and this particularly important feature will be exploited in the forthcoming chapters for new molecular design and understanding their excited state properties comprehensively.

3.1.6. Experimental Section

3.1.6a. General Methods

Optical measurements: Electronic absorption spectra were recorded on a Perkin Elmer Lambda 900 UV-Vis-NIR Spectrometer and emission spectra were recorded on Edinburgh FLS1000 spectrometer. UV-Vis and emission spectra were recorded in 1 mm path length cuvette. Fluorescence spectra of films were recorded in front-face geometry to avoid self-absorption at high concentrations.

Lifetime and quantum yield measurements: Fluorescence lifetimes were performed on a Horiba Delta Flex time-correlated single-photon-counting (TCSPC) instrument. A 373 nm LED laser diode with a pulse repetition rate of 1 MHz was used as the light source. The instrument response function (IRF) was collected using a scatterer (Ludox AS40 colloidal silica, Sigma-Aldrich). Phosphorescence lifetime was obtained in the same instrument using 355 nm LED laser diode (spectraLED). Gated emission was measured on FLS1000 spectrometer, Edinburgh Instruments equipped with a micro flash-lamp (μF_2) set-up. Quantum yield was measured using an integrated sphere in the same instrument.

3.1.6b. Materials

$\text{CS}^{[13]}$ and $\text{CC}^{[12]}$ was synthesized according to literature procedures.

3.1.6c. Protocol for Dye-polymer Hybrids Sample Preparation: First a stock solution of **PVA** was prepared by heating 0.5 g of the polymer in 10 ml of distilled water for 3 hours under stirring conditions. **CS-PVA** (or **CC-PVA**) hybrids were prepared by adding appropriate amount of **CS** (or **CC**) to 1 ml of **PVA** stock solutions (for example, for 2 wt. % **CS/CC-PVA**, 1 mg of **CS/CC** is used) followed by sonication and heating the solution 60 °C for 5 minutes to get a clear solution. All these samples were then drop-casted on a clean glass substrate followed by drying under vacuum at 60 °C to make the corresponding hybrid films.

3.1.7. References

- [1] a) O. Bolton, K. Lee, H. J. Kim, K. Y. Lin, J. Kim, *Nat. Chem.* **2011**, 3, 205; b) O. Bolton, D. Lee, J. Jung, J. Kim, *Chem. Mater.* **2014**, 26, 6644; c) W. Z. Yuan, X. Y. Shen, H. Zhao, J. W. Y. Lam, L. Tang, P. Lu, C. Wang, Y. Liu, Z. Wang, Q. Zheng, J. Z. Sun, Y. Ma, B. Z. Tang, *J. Phys. Chem. C* **2010**, 114, 6090; d) Y. Gong, G. Chen, Q. Peng, W. Z. Yuan, Y. Xie, S. Li, Y. Zhang, B. Z. Tang, *Adv. Mater.* **2015**, 27, 6195.
- [2] X. Ma, J. Wang, H. Tian, *Acc. Chem. Res.* **2019**, 52, 738.
- [3] a) Z. Yang, Z. Mao, X. Zhang, D. Ou, Y. Mu, Y. Zhang, C. Zhao, S. Liu, Z. Chi, J. Xu, Y. C. Wu, P. Y. Lu, A. Lien, M. R. Bryce, *Angew. Chem. Int. Ed.* **2016**, 55, 2181; b) Z. An, C. Zheng, Y. Tao, R. Chen, H. Shi, T. Chen, Z. Wang, H. Li, R. Deng, X. Liu, W. Huang, *Nat. Mater.* **2015**, 14, 685.
- [4] a) S. Hirata, *Adv. Opt. Mater.* **2017**, 5, 1700116; b) Kenry, C.-J. Chen, B. Liu, *Nat. Commun.* **2019**, 10, 2111; c) S. Mukherjee, P. Thilagar, *Chem. Commun* **2015**, 51, 10988; d) A. Forni, E. Lucenti, C. Botta, E. Cariati *J. Mater. Chem. C* **2018**, 6, 4603; e) M. Gmelch, H.

Thomas, F. Fries, S. Reineke, *Sci. Adv.* **2019**, *5*, eaau7310; f) X. Zhen, Y. Tao, Z. An, P. Chen, C. Xu, R. Chen, W. Huang, K. Pu, *Adv. Mater.* **2017**, *29*, 1606665.

[5] T. Matsuzawa, Y. Aoki, N. Takeuchi, Y. Murayama, *J. Electrochem. Soc.* **1996**, *143*, 2670.

[6] N. Gan, H. Shi, Z. An, W. Huang, *Adv. Funct. Mater.* **2018**, *28*, 1802657.

[7] a) M. Kiritani, T. Yoshii, N. Hirota, and M. Baba *J. Chem. Phys.* **1994**, *98*, 11265; b) M. Koyanagi, L. Goodman, *Chem. Phys. Lett.* **1971**, *9*, 636; c) H. Wu, W. Chi, Z. Chen, G. Liu, L. Gu, A. K. Bindra, G. Yang, X. Liu, Y. L. Zhao, *Adv. Funct. Mater.* **2019**, *29*, 1807243

[8] a) Y. Gong, H. Chen, X. Ma, H. Tian, *ChemPhysChem* **2016**, *17*, 1934; b) H. Chen, X. Ma, S. Wu, H. Tian, *Angew. Chem. Int. Ed.* **2014**, *53*, 14149; c) Z. He, H. Gao, S. Zhang, S. Zheng, Y. Wang, Z. Zhao, D. Ding, B. Yang, Y. Zhang, W. Z. Yuan, *Adv. Mater.* **2019**, *31*, 1807222.

[9] H. A. Al-Attar, A. P. Monkman, *Adv. Funct. Mater.* **2012**, *22*, 3824.

[10] J. L. Kropp, W. R. Dawson, *J. Phys. Chem.* **1967**, *71*, 4499.

[11] H. Mieno, R. Kabe, N. Notsuka, M. D. Allendorf, C. Adachi, *Adv. Opt. Mater.* **2016**, *4*, 1015.

[12] a) S. A-Fouet, I. Seguy, J.-F. Bobo, P. Destruel, H. Bock, *Chem. Eur. J.* **2007**, *13*, 1746; b) K. V. Rao, *Supramolecular Synthesis of Novel Organic and Hybrid Materials of π -Systems for Optoelectronic Functions* (PhD thesis), Bangalore, JNCASR, **2013**, pp. 173.

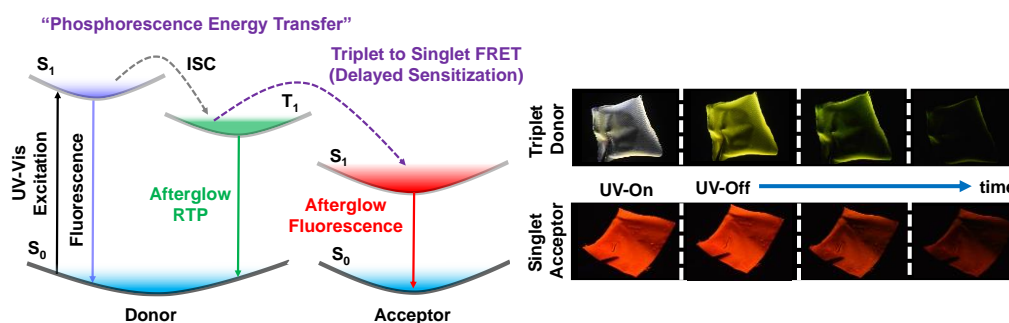
[13] A. Ghosh, K. V. Rao, S. J. George, C. N. R. Rao, *Chem. Eur. J.* **2010**, *16*, 2.

CHAPTER 3.2

Activating “Afterglow Delayed Fluorescence” via Phosphorescence Energy Transfer*

Abstract

In the present study, a delayed sensitization of the singlet state of organic dyes via phosphorescence energy transfer from organic phosphors is proposed as an alternative strategy to realize “afterglow fluorescence”. This concept is demonstrated with a long-lived phosphor as the energy donor and commercially available fluorescent dyes as the energy acceptor. Triplet to singlet Förster resonance energy transfer (TS-FRET) between donor and acceptor chromophores, which are co-organized in an amorphous polymer-matrix, results in tunable yellow and red afterglow from the fluorescent acceptors. Moreover, these afterglow fluorescent hybrids are highly solution-processable and show excellent air-stability with good quantum yields (over 50 %).



*Manuscript based on this work has been published in *Angew. Chem. Int. Ed.* **2020**, *59*, 9393.

3.2.1. Introduction

Purely organic systems with long-persistent luminescence (afterglow) have gained increasing interest due to their great potential in optical sensing, light-emitting diodes and imaging probes as well as a viable alternative to well-studied inorganic phosphors containing toxic, rare and expensive elements.^[1] Organic phosphor equivalents displaying afterglow emission have been realized mainly by enhancing the spin-orbit coupling with heavy-atom designs and by minimizing the vibrational dissipation within crystalline phases.^[2] The ambient afterglow from solution-processable organic phosphors has also been achieved in a few systems, by incorporating them in polymeric matrices or micro-environments with good oxygen barrier performance.^[3] However, high quantum yield and tunable afterglow emission, particularly in the red region, still remains as a challenge in organic afterglow phosphors.^[4] Although thermally activated delayed fluorescence (TADF) emitters are promising for good colour-tunability and high quantum yields, their lifetimes are only in the μs to ms timescale and hence specially designed exciplex TADF systems are required to exhibit afterglow.^[5] Thus, alternative and generalized strategies are essential to realize tunable afterglow emission from purely organic chromophores under ambient and solution-processable conditions.

Förster resonance energy transfer (FRET) between singlet states of chromophores have been extensively investigated in multi-chromophoric assemblies to attain tunable fluorescent materials.^[6] Herein, we envisage that, energy transfer from long-lived singlet or triplet state of donor molecules to singlet state of fluorescent acceptors, would provide an attractive strategy to extract afterglow fluorescence from acceptors via a delayed sensitization process.^[7] Further this approach would circumvent the tedious molecular engineering required to extract afterglow fluorescence via the TADF process and moreover the delayed emission can be tuned by the suitable choice of common dye molecules. Recently, singlet-singlet energy transfer from TADF chromophores has been demonstrated to get a wide-range of fluorescent materials with tunable, afterglow features under inert atmosphere.^[8] On the contrary, analogous triplet- to-singlet energy transfer (TS-FRET) process from purely organic phosphorescence materials to induce delayed fluorescence is less explored regardless of its successful demonstration in organometallic molecular systems.^[9] In this context, herein we report phosphorescence energy transfer (via TS-FRET) process in purely organic donor and acceptor multi-chromophoric assemblies to render unprecedented air-stable and water-processable afterglow fluorescent materials via a delayed sensitization process (Figure 3.2.1a). More importantly, the wavelength of afterglow could be tuned by the TS-FRET process to various fluorescent dye molecules of interest having a spectral overlap with the phosphor emission, to yield yellow and red afterglow fluorescence under

ambient conditions. Further the remarkable ambient afterglow and the solution processability of these materials have been demonstrated with self-standing, flexible films and inks.

3.2.2. Design Strategy and Prerequisites for Triplet-to-singlet FRET

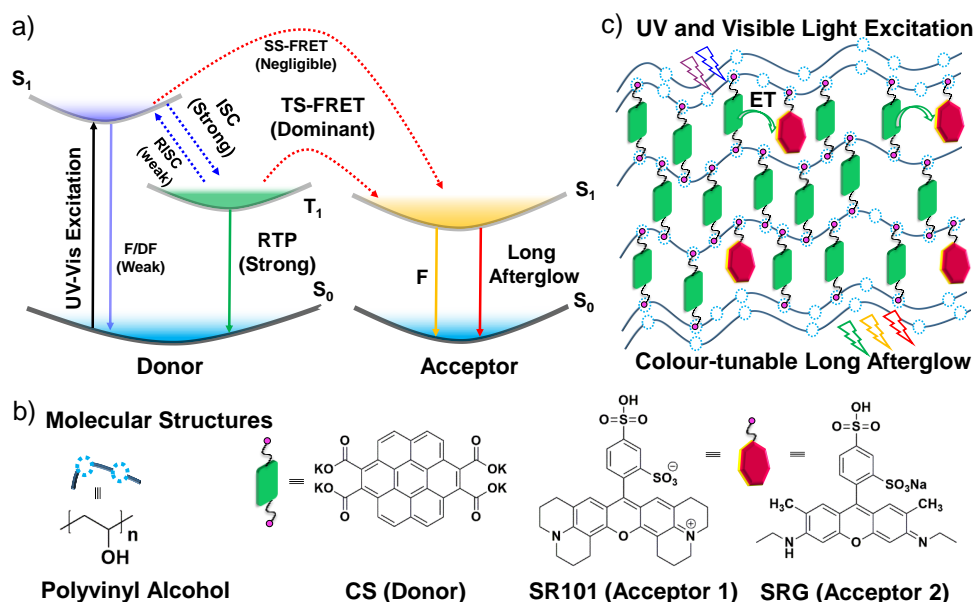


Figure 3.2.1. a) Simplified Jablonski diagram to explain the phosphorescence energy transfer and other photophysical process in the present study. (F = Fluorescence, DF = Delayed Fluorescence, ISC = Intersystem Crossing, $RISC$ = Reverse Intersystem Crossing, RTP = Room Temperature Phosphorescence, $SS-FRET$ = Singlet to Singlet Förster Resonance Energy Transfer, $TS-FRET$ = Triplet to Singlet Förster Resonance Energy Transfer). b) Molecular structures of various components used in the present study. c) Schematic representation of the **PVA** scaffold with anchored donor and acceptor chromophores. (ET = Energy Transfer).

We have used poly(vinylalcohol) (**PVA**) as the matrix to host the chromophores, because of its high tensile strength, flexibility and resistance of oxygen which would minimize the vibrational and oxygen quenching of the triplet of donor phosphors.^[3d] Further we envisage that the pendant hydroxyl functional groups of the **PVA** polymer chains makes it an attractive supramolecular scaffold to anchor and organize both donor and acceptor chromophores appropriately functionalized with hydrogen-bonding groups, through weak secondary interactions.^[3c, d] In the present study we have used coronene tetracarboxylate salt (**CS**) as a long-persistent triplet energy donor, which exhibits greenish-yellow, ambient afterglow when incorporated into the **PVA** matrix. Further, commercially available, highly fluorescent dyes Sulpharhodamine 101 (**SR101**) and Sulpharhodamine G (**SRG**) with good spectral overlap with the **CS** phosphor emission are used as the acceptor chromophores to demonstrate the concept of

phosphorescence energy transfer (Figure 3.2.1b). Both donor (**CS**) and acceptor molecules (**SR101** and **SRG**) are water-soluble dyes with ionic/hydroxyl side-groups (carboxylates, sulphonates and sulphonic acid) which facilitates supramolecular self-assembly with the host **PVA** via ion-dipole and hydrogen-bonding interactions, thereby reducing the molecular motions to minimize the non-radiative decay processes (Figure 3.2.1b-c).

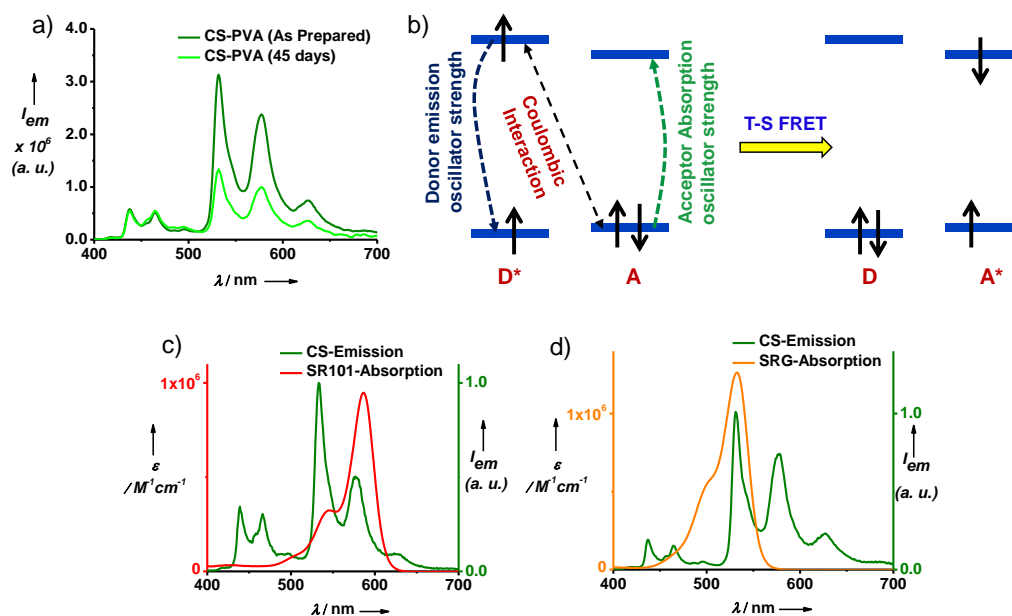


Figure 3.2.2. a) Emission spectrum of 2 wt. % CS in PVA showing considerable RTP intensity even after 45 days compared to the freshly prepared samples ($\lambda_{exc.} = 350 \text{ nm}$) in air. b) Schematic representation of TS-FRET mechanism. Spectral overlap of CS RTP with the absorption of c) SR101 and d) SRG. $[\text{SR101}] = [\text{SRG}] = 10^{-5} \text{ M}$ in water ($\lambda_{exc.} = 350 \text{ nm}$).

Strong phosphorescence emission of **CS-PVA** hybrids in the air ($\Phi_P = 23.4 \%$) along with excellent air-stability even after a month suggests strong oscillator strength of $T_1 \rightarrow S_0$ transition in the present case (Figure 3.2.2a). We envisage that the efficient RTP in the present system is an indication of strong spin-orbit coupling process due to similar the $n-\pi^*$ transitions in the conventional phosphors containing aromatic carbonyl groups, according to El-Sayed's rule.^[2a] Strong spin-orbit coupling and consequent RTP intensity is particularly significant as the oscillator strength of donor emission (i. e. phosphorescence in the present case) is a pre-requisite for the dipole-dipole coupling between the excited donor and ground-state acceptor molecules to facilitate the FRET process (Figure 3.2.2b).^[7a, c] Thus, we envision that, doping **CS-PVA** hybrids with appropriate fluorescent acceptor molecules with overlapping absorption with the RTP emission of **CS** can facilitate a triplet to singlet Förster-type Resonance Energy Transfer (TS-FRET) process. Further, TS-FRET process from afterglow phosphorescent donor can result in a

persistent “delayed fluorescence” from the otherwise short-lived acceptor singlet states, by a delayed sensitization process. The persistent delayed fluorescence is envisioned to be a result of slow phosphorescence decay. As can be seen from Table 3.2.1, the radiative rate of fluorescence (k_F^r) is 10 times slower than the rate of intersystem crossing (k_{ISC}) leading to major deactivation of singlet excitons. This could also be a plausible reason for inefficient typical FRET between singlet states, in the present systems (*vide infra*). More importantly, the radiative rate of phosphorescence (k_P^r) is extremely slow ($\sim 0.1 \text{ s}^{-1}$) as a result of extremely slow lifetime over a few seconds. Since, the rate of energy transfer is inversely proportional to the lifetime of the donor emission, we expect a slow and long-range energy transfer to the acceptors which are dispersed in the polymer matrix to result in afterglow delayed emission via energy transfer.^[10]

Table 3.2.1. Summary of emission characteristics of 2 wt. % CS-PVA film.^[11]

$\langle\tau_F\rangle$ (ns)	Φ_F	k_F^r (s^{-1})	$\langle\tau_P\rangle$ (s)	Φ_P	k_P^r (s^{-1})	k_{ISC} (s^{-1})
11.23	0.022	1.9×10^6	2.46	0.234	9.5×10^{-2}	20.8×10^6

$$k_F^r = \Phi_F / \langle\tau\rangle_F; k_P^r (\text{s}^{-1}) = \Phi_P / \langle\tau\rangle_P; k_{ISC} = \Phi_P / \langle\tau\rangle_F$$

Broad RTP emission of **CS-PVA** hybrids allows the choice of various acceptors for colour-tuneable and narrow bandwidth emission. Rhodamine dyes, **SR101** ($\lambda_{\text{abs.}} = 520\text{-}600 \text{ nm}$, $\lambda_{\text{max.}} = 610 \text{ nm}$) and **SRG** ($\lambda_{\text{abs.}} = 450\text{-}550 \text{ nm}$, $\lambda_{\text{max.}} = 560 \text{ nm}$) show excellent spectral overlap with the phosphorescence band of **CS** (Figure 3.2.2c and 3.2.2d), prerequisite for TS-FRET. Further the specific secondary interactions between the chromophores and the **PVA** matrix are expected to promote an efficient co-assembly to maintain a close donor-acceptor distance in the resulting hybrids for the efficient energy transfer process (Figure 3.2.1).

3.2.3. Red-emitting Ambient Afterglow Fluorescence in CS-SR101-PVA Hybrid Films

First, transparent films of **SR101** (1 wt. % to 10 wt. % with respect to the amount of **CS**) doped **CS-PVA** (**CS** is 2 wt. % with respect to **PVA**) hybrids were prepared by drop-casting corresponding aqueous solutions with appropriate ratio of the components on to glass substrates followed by complete drying under vacuum (see experimental section). Emission spectra of **SR101** doped **CS-PVA** films ($\lambda_{\text{exc.}} = 350 \text{ nm}$) showed a gradual decrease of the **CS** phosphorescence emission centred at 532 nm and a concomitant enhancement of **SR101** fluorescence at 600-700 nm region, with increasing doping of **SR101**, which hint towards an efficient energy transfer process from the triplet state of donor to the acceptor molecules (Figure 3.2.3a). In addition, a significant red-shift in the normalized gated emission spectra (with a delay

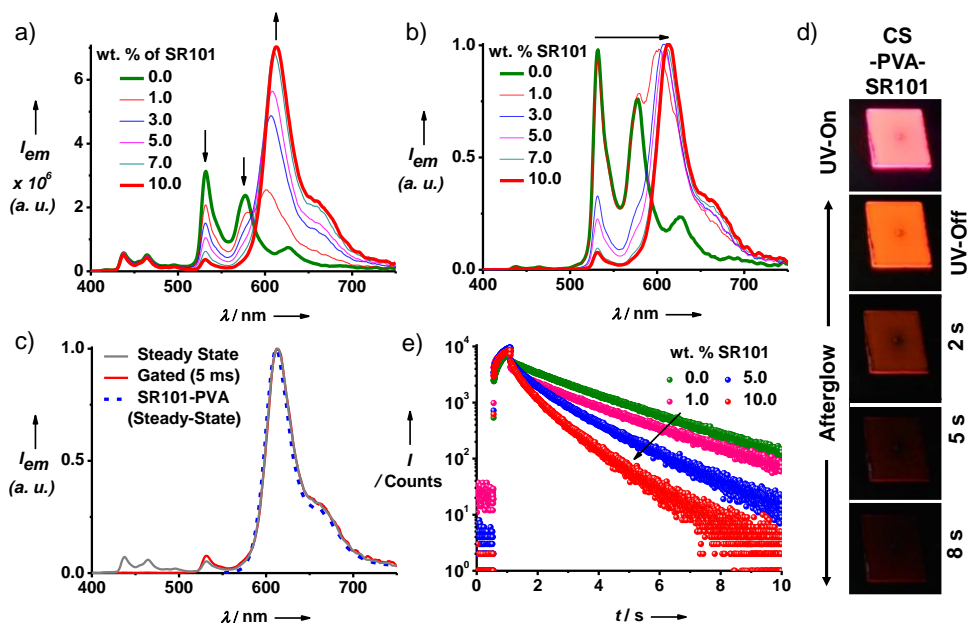


Figure 3.2.3. Phosphorescence energy transfer (CS to SR101): a) Normalized steady-state and ($\lambda_{exc.} = 350$ nm) b) gated emission ($\lambda_{exc.} = 350$ nm, delay time = 5 ms) of CS-PVA hybrid films with different wt. % of SR101, which clearly shows the delayed emission component from the SR101 with the quenching of CS phosphorescence emission. c) Steady-state and gated emission spectra of CS-PVA film with 10 wt. % SR101 doped in CS-PVA ($\lambda_{exc.} = 350$ nm, delay time = 5 ms) along with steady-state fluorescence spectrum of a 0.2 wt. % SR101-PVA film ($\lambda_{exc.} = 545$ nm) without the donor CS, confirming the singlet fluorescence origin of the delayed emission. d) Photographs of CS-SR101-PVA hybrid films (with 10 wt. % of the SR101), showing afterglow emission over 5 seconds when the excitation with 365 nm UV-lamp is turned off. e) Time-resolved emission decay profiles of CS-PVA hybrid films with different wt. % of SR101 showing a quenching of the CS triplet lifetime with an increasing percentage of the SR101 ($\lambda_{exc.} = 355$ nm, $\lambda_{monitored} = 532$ nm).

time of 5 ms) of these films, with respect to that of the phosphorescence emission from pure CS-PVA hybrids, further indicates the long-lived character of the acceptor emission (Figure 3.2.3b). Remarkably, the gated emission of SR101 doped CS-PVA film match with that of the fluorescence spectrum of pure SR101 anchored PVA films which clearly indicated the delayed fluorescence nature of the acceptor emission (Figure 3.2.3c). The gated emission from the acceptor in the hybrid films is also evident from the visible afterglow colour change from greenish-yellow (pure CS phosphorescence) to deep-red (pure SR101 fluorescence) region of the visible spectrum (Figure 3.1.2d and Figure 3.2.3d and Video 3.1.1). Furthermore, time-resolved emission lifetime analyses of CS phosphorescence monitored at 532 nm ($\lambda_{exc.} = 355$ nm), showed a gradual decrease of the average lifetime ($\tau_{avg.}$) from 2.46 s to 1.33 s in 5 wt. % CS-SR101-PVA

film, which further reduces to 0.86 s with higher **SR101** content (10 wt. % with respect to **CS**) (Figure 3.2.3e).

These decay profiles clearly suggest the presence of an efficient non-radiative FRET from the triplet state of **CS** donors to the singlet states of the acceptor in the hybrid films (TS-FRET), thus ruling out the possibility of a trivial energy transfer (emission-reabsorption process) where no change in donor lifetime is expected. Singlet-singlet FRET process is unlikely in the present case due to the weak **CS** fluorescence contribution (probably due to highly efficient intersystem crossing) and smaller spectral overlap integral (Figure 3.2.2c and Table 3.2.1).

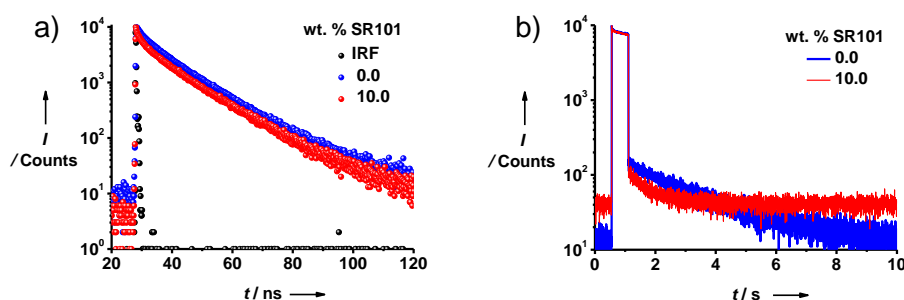


Figure 3.2.4. a) Fluorescence decay ($\lambda_{exc.} = 373$ nm) and b) delayed fluorescence decay of **CS-PVA** hybrid films with and without the acceptor doping ($\lambda_{exc.} = 355$ nm, $\lambda_{monitored} = 440$ nm). In both these cases 10 wt. % **SR101** (with respect to **CS**) was used as acceptor dopant. IRF = instrument response function.

In order to elucidate the singlet-singlet FRET comprehensively, time-resolved decay experiments were performed (Figure 3.2.4). Average fluorescence lifetime of **CS-PVA** (2 wt. % with respect to **PVA**) 11.23 ns reduces negligibly to 11.06 ns (in presence of 10 wt. % **SR101**); whereas significant decrease of average delayed fluorescence lifetime ($\lambda_{exc.} = 355$ nm, $\lambda_{monitored} = 440$ nm, $\tau_{avg.} = 2.27$ s to 0.83 s) suggests efficient consumption of triplets via T-S energy transfer (TS-FRET). This observation clearly suggests that triplet state of **CS** (phosphorescence) is predominantly the energy donor manifold in the present system. As a control, the gated emission of the **CS-SR101-PVA** films were compared with that of direct excitation of the acceptor **SR101** ($\lambda_{exc.} = 545$ nm) in the hybrid films and in the **SR101** anchored **PVA** films without the **CS**. In both cases no delayed emission component were observed (Figure 3.2.5a and 3.2.5b, blue and black curves). The absence of delayed fluorescence in the **SR101-PVA** samples without **CS** is also reiterated from the only normal (prompt) fluorescence lifetime profile of **SR101** with an average lifetime of 5.4 ns (Figure 3.2.5c). In addition, we also observed a substantial blue-shift and sharper emission in the presence of **PVA** suggests that **SR101** interacts well with **PVA** and are well-dispersed in the matrix leading to minimum optical losses due to aggregation, in line

with our design strategy (*vide infra*) (Figure 3.2.5d). Hence, it is evident that the long-lived triplet excitons of donor **CS** molecules are the only source of the delayed population of the singlet state of acceptor **SR101** via an efficient TS-FRET mechanism to result in “persistent delayed fluorescence”.

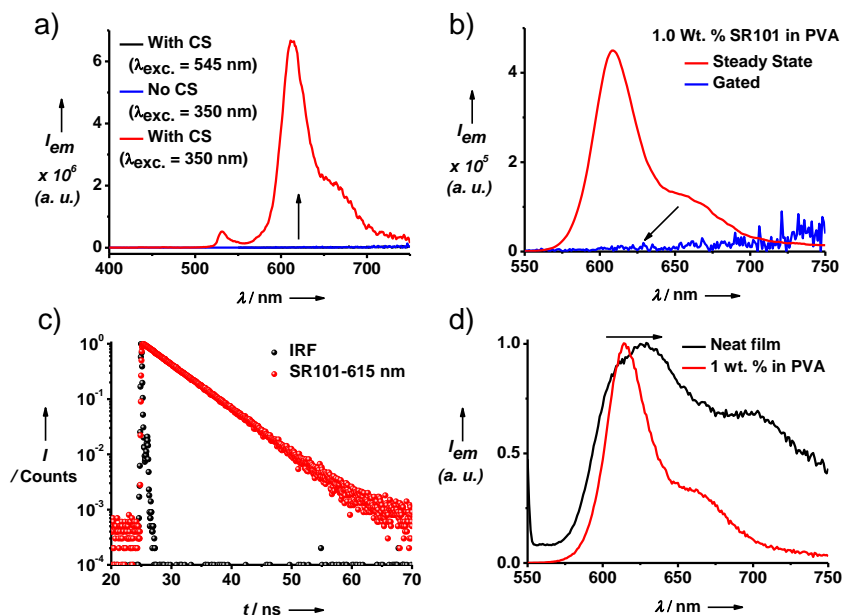


Figure 3.2.5. a) Gated emission spectra (delay time = 1 ms) of pure 0.2 wt. % **SR101-PVA** (with respect to the amount of **PVA**) hybrid films ($\lambda_{exc.} = 350$ nm) and **CS-PVA** hybrid films doped with 10 wt. % of **SR101** (with respect to the amount of **CS**) upon direct ($\lambda_{exc.} = 545$ nm) and indirect excitation ($\lambda_{exc.} = 350$ nm) of the acceptor, to reiterate the necessity of energy transfer process to extract delayed fluorescence from the **SR101** dye molecules. b) Steady state and gated (1 ms delay time) emission spectra of 0.2 wt. % **SR101-PVA** hybrid film ($\lambda_{exc.} = 540$ nm). c) Fluorescence decay of 0.2 wt. % **SR101-PVA** hybrid film monitored at 615 nm ($\lambda_{exc.} = 532$ nm). IRF = instrument response function. d) Normalized emission spectra of 0.2 wt. % **SR101-PVA** hybrid film without donor along with its neat film state showing reduced aggregation in **PVA** film ($\lambda_{exc.} = 540$ nm).

3.2.4. Yellow Afterglow Fluorescence Using **SRG** dye as FRET-acceptor

TS-FRET induced long-persistent (afterglow) delayed fluorescence could also be extended to yellow-emitting **SRG** acceptor, having a good spectral overlap with the triplet emission of **CS** (Figure 3.2.6 and 3.2.7). As evident from Figure 3.2.6a, increasing the amount of **SRG** (acceptor) in the **CS-PVA** hybrid films results in a gradual decrease in phosphorescence emission of **CS** at 532 nm, with a concomitant enhancement of **SRG** emission at 550-570 nm

region. In addition, substantial red-shift in gated emission spectra (delay time = 5 ms) along with a visible afterglow colour change of these films from green (CS phosphorescence) to yellow (SRG fluorescence), clearly indicates an energy transfer process from donor triplet excited state of CS to the singlet state of SRG (Figure 3.2.6b and 3.2.6c and Video 3.1.1). The delayed afterglow fluorescence origin was also evident from the identical gated emission profile of SRG doped CS-PVA film with that of pure SR101 doped PVA films (Figure 3.2.6d). Further, similar to the SR101 case, phosphorescence lifetime of CS phosphorescence (monitored at 532 nm), gradually decrease from $\tau_{\text{avg.}} = 2.46$ s to 0.8 s in 10 wt. % CS-SRG-PVA film (Figure 3.2.6e). The T-S FRET mechanism behind the afterglow delayed fluorescence of SRG molecules was further proved unequivocally by the detailed gated emission and time-resolved fluorescence experiments as explained previously, in the case of SR101 (Figure 3.2.7).

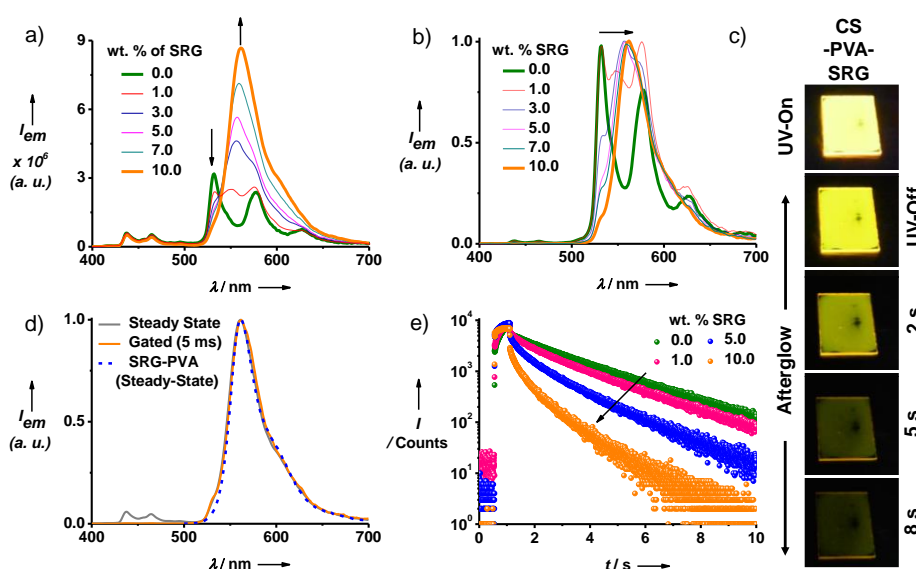


Figure 3.2.6. Phosphorescence energy transfer (CS to SRG): a) Steady-state and ($\lambda_{\text{exc.}} = 350$ nm) b) normalized gated emission ($\lambda_{\text{exc.}} = 350$ nm, delay time = 5 ms) of CS-PVA hybrid films with different wt. % of SRG, which clearly shows the delayed emission component from the SRG with the quenching of CS phosphorescence emission. c) Photographs of CS-SRG-PVA hybrid films (with 10 wt. % of the SRG), showing afterglow emission over 5 seconds when the excitation with 365 nm UV-lamp is turned off. d) Steady-state and gated emission spectra of CS-PVA film with 10 wt. % SRG doped in CS-PVA ($\lambda_{\text{exc.}} = 350$ nm, delay time = 5 ms) showing the delayed fluorescence from SRG, along with steady-state fluorescence spectrum ($\lambda_{\text{exc.}} = 490$ nm) of a 0.2 wt. % SRG-PVA film without the donor CS. e) Time-resolved emission decay profiles of CS-PVA hybrid films with different wt. % of SRG showing a quenching of the CS triplet lifetime with increasing percentage of the SRG ($\lambda_{\text{exc.}} = 355$ nm, $\lambda_{\text{monitored}} = 532$ nm).

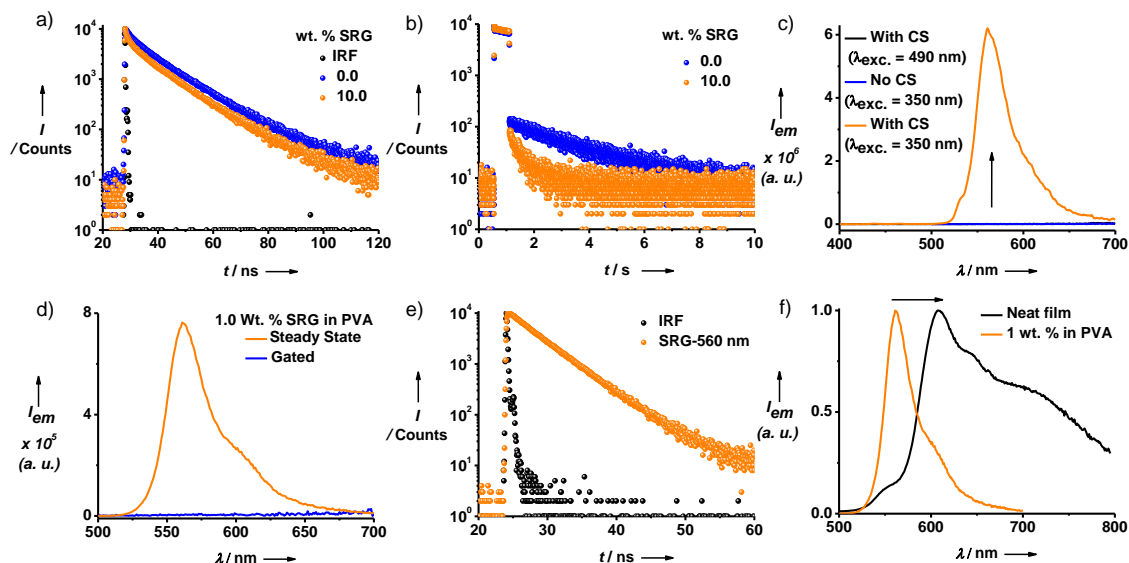


Figure 3.2.7. a) Fluorescence decay ($\lambda_{exc.} = 373 \text{ nm}$, $\lambda_{monitored} = 440 \text{ nm}$, $\tau_{avg.}$ of donor changes from 11.23 ns (pure CS) to 10.39 ns (doped with SRG)) and b) delayed fluorescence decay ($\lambda_{exc.} = 355 \text{ nm}$, $\lambda_{monitored} = 440 \text{ nm}$, $\tau_{avg.}$ of donor changes from 2.27 s (pure CS) to 0.75 s (doped with SRG)) of CS-PVA hybrid film with and without the SRG doping. In both cases, 10 wt. % SRG (with respect to CS) was used as the acceptor dopant. c) Gated emission spectra (delay time = 1 ms) of pure 0.2 wt. % SRG-PVA (with respect to the amount of PVA) hybrid films ($\lambda_{exc.} = 350 \text{ nm}$) and CS-PVA hybrid films doped with 10 wt. % of SRG (with respect to the amount of CS) upon direct ($\lambda_{exc.} = 545 \text{ nm}$) and indirect excitation ($\lambda_{exc.} = 350 \text{ nm}$) of the acceptor. d) Steady state and gated (1 ms delay time) emission spectra of 0.2 wt. % SRG-PVA hybrid film ($\lambda_{exc.} = 490 \text{ nm}$) showing no delayed component. e) Fluorescence decay profile of 0.2 wt. % SRG-PVA hybrid film at 560 nm ($\lambda_{exc.} = 480 \text{ nm}$, $\tau_{avg.} = 4.3 \text{ ns}$). IRF = instrument response function. f) Normalized emission spectra of 0.2 wt. % SRG-PVA hybrid film without donor along with its neat film state showing reduced aggregation in PVA film ($\lambda_{exc.} = 490 \text{ nm}$).

The predominance of the TS-FRET mechanism in the present study is further reiterated from the calculated Förster radius of both SS-FRET and TS-FRET pathways. In Table 3.2.2, energy transfer parameters are summarized. The smaller Förster radius for singlet-singlet FRET i. e. $R_F(S-S)$ is a direct manifestation of poor quantum yield of the fluorescence and smaller overlap integral. The physical significance of such observation can be explained in terms of relative FRET efficiencies. From the calculated FRET radii of both the competing processes, the S-S FRET efficiency will be poor especially when the distance between donor-acceptor is high and randomly oriented in the polymer matrix (such as our present system). Thus, we have observed the triplet to singlet energy transfer from the CS phosphorescence to two fluorescent acceptor dyes, SRG and SR101, with good efficiency (> 65 % in both cases with 10 wt. % of

acceptor loading), resulting in unprecedented long-persistent red and yellow delayed fluorescence, respectively, under ambient conditions.

Table 3.2.2. Förster Radius Calculation.

Acceptor	J^λ (S-S) $\text{nm}^4\text{M}^{-1}\text{cm}^{-1}$	J^λ (T-S) $\text{nm}^4\text{M}^{-1}\text{cm}^{-1}$	R_F (S-S) Å	R_F (T-S) Å
SRG	1.48×10^{15}	3.12×10^{16}	25.6	60.5
SR101	2.54×10^{14}	3.03×10^{16}	19.0	42.2

The Förster Radius (R_F) is calculated according to equation 3.2.^[10]

$$R_F = 0.211 \times \sqrt[6]{\kappa^2 n^{-4} \Phi_D J^\lambda} \quad (\text{in } \text{Å}) \quad (3.2)$$

In equation 3.2, κ represents the orientation factor of a molecular dipole, Φ_D is quantum yield of the donor, n is the refractive index of the polymer host (**PVA**) in the wavelength range of interest (400-700 nm), and J^λ is the overlap integral between donor emission and acceptor absorption. J^λ is calculated from the normalized emission spectrum of the donor with a molar extinction co-efficient (ϵ) of the acceptors. Here, Φ_D (Phosphorescence) = 0.234, Φ_D (Fluorescence) = 0.022, $\kappa = 0.476$ (randomly oriented and well-separated dipoles during the transition), $n = 1.48$, J^λ were calculated from a|e 1.2 FluorTools software.^[12]

3.2.5. Afterglow Hybrids as Encryption Materials

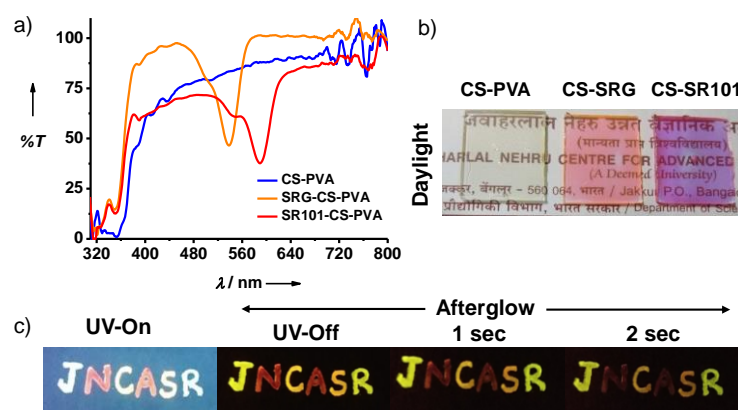


Figure 3.2.8. a) Transmittance spectra and b) corresponding photographs (taken under daylight) of **CS-PVA** (2 wt. % with respect to **PVA**), 10 wt. % **SRG-CS-PVA**, 10 wt. % **SR101-CS-PVA** (10 wt. % **SRG** or **SR101** with respect to **CS**) dropcasted thin films, displaying their highly transparent nature. c) Demonstration of afterglow ink with unique ambient stability and solution-processability: Letters “**JNCASR**” (Institute Name) written using the viscous liquids of the hybrids on a plain paper under UV excitation (365 nm) and subsequent afterglow upon removing the light source. **CS-PVA** (letters **J** and **R**), **CS-SRG-PVA** (letters **C** and **S**) and **CS-SR101-PVA** (letters **N** and **A**).

These multi-chromophoric assemblies anchored to **PVA** films are excellent with respect to their high transmittance, colour-tunability and ambient afterglow characteristics which are stable for months (Figure 3.2.8 and 3.2.9). The viscous nature of the chromophore-**PVA** hybrids facilitates the drop-casting as well as its use as inks to coat or write on various substrates such as glass and paper, which upon drying can be used for encryption purposes. In order to demonstrate this unique ambient-stability and solution processability features of these afterglow hybrids, six letters of “JNCASR” (institute name) were written on plain paper. The letters were written with different afterglow hybrid solutions; **CS-PVA** (letters J and R), **CS-SR101-PVA** (letters N and A) and **CS-SRG-PVA** (letters C and S). Upon excitation with 365 nm UV light, the letters J, N, C, A, S and R exhibited white (due to blue fluorescent background and weak blue fluorescence of **CS**), red, yellow, red, yellow and white luminescence, respectively. When the light source was switched off, a clear visible afterglow emission appeared from these letters with a differential lifetime depending on its phosphorescence or delayed fluorescence origin (Figure 3.2.8c, Video 3.2.1).

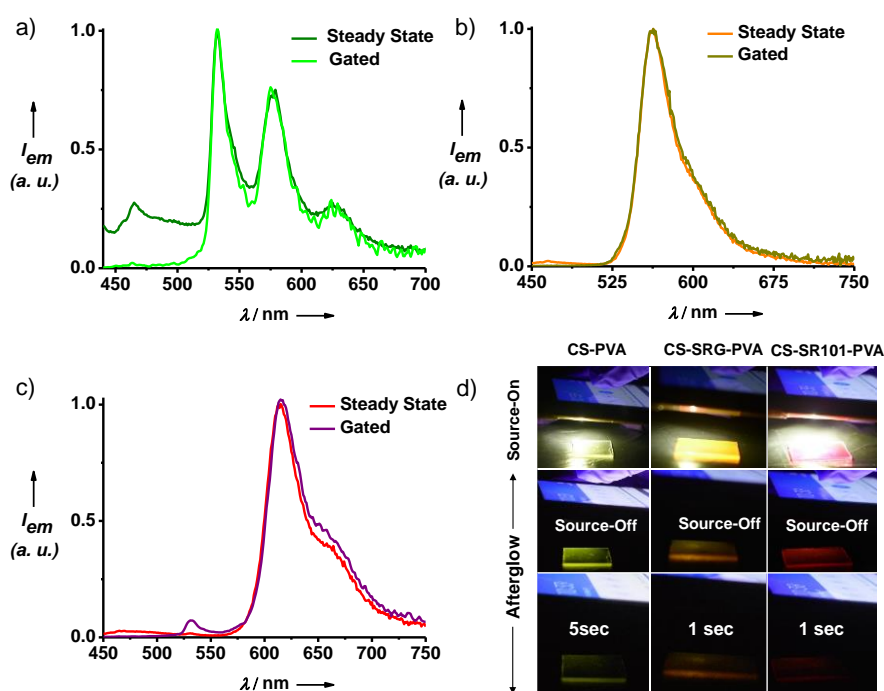


Figure 3.2.9. Normalized steady state and gated spectra of a) **CS-PVA** (2 wt. % with respect to **PVA**), b) 10 wt. % **SRG-CS-PVA** and c) 10 wt. % **SR101-CS-PVA** (10 wt. % **SRG** or **SR101** with respect to **CS**) films shown in Figure S15b, when excited at the visible wavelength ($\lambda_{exc.} = 430$ nm and delay time = 5 ms in all cases); d) photographs of afterglow emission from these films is obtained by the visible light excitation using a cell phone flashlight.

Interestingly, since CS absorbs in the visible range (400–450 nm), afterglow emission could also be observed with excitation by low-intensity sources like common cell phone flashlights as demonstrated with the glass slides drop-casted with these hybrids (Figure 3.2.9 and Video 3.2.2). Such visible light excited afterglow is rare in purely organic systems and potentially useful for various applications.^[13] Further the donor molecules could be easily synthesized in gram scales and hence practically suitable for large-area coating on various substrates. Thin films (6 cm x 6 cm) of these afterglow hybrids are even self-standing and flexible as demonstrated in Figure 3.2.10. Remarkably, stretching or folding of these self-standing films hardly affected the afterglow emission (Video 3.2.3) and are stable for months even in air. To the best of our knowledge, such kind of ambient and solution-processable materials from purely organic systems is unprecedented.

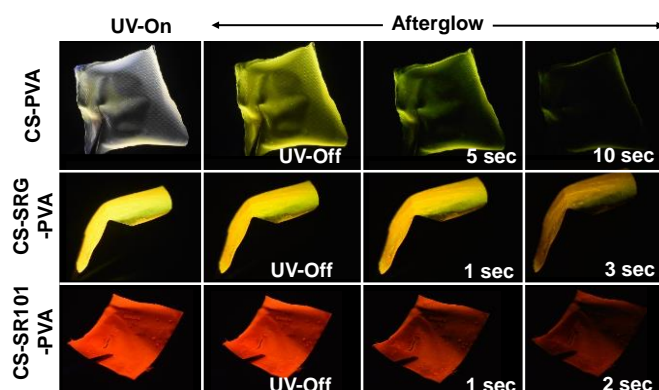


Figure 3.2.10. Demonstrations of the solution processability, self-standing and ambient afterglow properties from SRG/SR101 doped CS-PVA hybrid films ($\lambda_{exc.} = 365$ nm).

3.2.6. Conclusions

In conclusion, we have demonstrated colour tunable organic afterglow fluorescence from the metal-free organic systems by an unprecedented triplet-singlet Förster-type energy transfer (TS-FRET) process. TS-FRET from a long-lived organic phosphor to fluorescent acceptor by their co-assembly in the polymer matrix, results in delayed sensitization of the acceptor singlet to realize the persistent fluorescence, the wavelength of which could be tuned by the appropriate choice of acceptor dyes. The unique solution processability and ambient stability of these afterglow hybrids have been displayed by the drop-casting on the glass substrates, writing/painting on the paper surfaces and by the self-standing nature of the dye-doped polymer films. Furthermore, the red-emitting afterglow/long-persistent delayed fluorescence achieved here is relatively unexplored and offers a lot of potential applications as NIR-emitting afterglow materials in bio-imaging and lighting devices. As a perspective, the phosphorescence energy

transfer and consequent delayed fluorescence presented here provide great opportunities to achieve tunable long-persistent fluorescent from well-known dyes without tedious molecular engineering and synthetic efforts.

3.2.7. Experimental Section

3.2.7a. General Methods

Optical measurements: Electronic absorption spectra were recorded on a Perkin Elmer Lambda 900 UV-Vis-NIR Spectrometer and emission spectra were recorded on Edinburgh FLS1000 spectrometer. UV-Vis and emission spectra were recorded in 1 mm path length cuvette. Fluorescence spectra of films were recorded in front-face geometry to avoid self-absorption at high concentrations.

Lifetime and quantum yield measurements: Fluorescence lifetimes were performed on a Horiba Delta Flex time-correlated single-photon-counting (TCSPC) instrument. A 373 nm LED laser diode with a pulse repetition rate of 1 MHz was used as the light source. The instrument response function (IRF) was collected using a scatterer (Ludox AS40 colloidal silica, Sigma-Aldrich). Phosphorescence lifetime was obtained in the same instrument using 355 nm LED laser diode (spectraLED). Gated emission was measured on FLS1000 spectrometer, Edinburgh Instruments equipped with a micro flash-lamp (μF_2) set-up. Quantum yield was measured using an integrated sphere in the same instrument.

3.2.7b. Materials: **SRG** and **SR101** were purchased from Sigma-Aldrich. Polyvinylalcohol (MW = ~85,000-1,24,000 ~90 % hydrolysed) was obtained from SDFCL, India.

3.2.7c. Protocol for Dye-polymer Hybrids Sample Preparation: First a stock solution of **PVA** was prepared by heating 0.5 g of the polymer in 10 ml of distilled water for 3 hours under stirring conditions. **CS-PVA** hybrids were prepared by adding appropriate amount of **CS** to 1 ml of **PVA** stock solutions (for example, for 2 wt. % **CS-PVA** 1 mg of **CS** is used) followed by sonication and heating the solution 60 °C for 5 minutes to get a clear solution. For samples to study energy transfer, appropriate amount of either **SR101/SRG** aqueous solutions was added to 2 wt. % **CS-PVA** hybrid solutions and heated at 60 °C for few minutes until it becomes a transparent solution. All these samples were then drop-casted on a clean glass substrate followed by drying under vacuum at 60 °C to make the corresponding hybrid films.

3.2.8. References

- [1] a) S. Hirata, *Adv. Opt. Mater.* **2017**, *5*, 1700116; b) X. Zhen, Y. Tao, Z. An, P. Chen, C. Xu, R. Chen, W. Huang, K. Pu, *Adv. Mater.* **2017**, *29*, 1606665; c) T. Matsuzawa, Y. Aoki, N. Takeuchi, Y. Murayama, *J. Electrochem. Soc.* **1996**, *143*, 2670; d) H. Xu, R. Chen, Q. Sun, W. Lai, Q. Su, W. Huang, X. Liu, *Chem. Soc. Rev.* **2014**, *43*, 3259; e) S. Xu, R. Chen, C. Zheng, W. Huang, *Adv. Mater.* **2016**, *28*, 9920; f) R. Kabe, N. Notsuka, K. Yoshida, C. Adachi, *Adv. Mater.* **2016**, *28*, 655.
- [2] a) O. Bolton, K. Lee, H. J. Kim, K. Y. Lin, J. Kim, *Nat. Chem.* **2011**, *3*, 205; b) Z. An, C. Zheng, Y. Tao, R. Chen, H. Shi, T. Chen, Z. Wang, H. Li, R. Deng, X. Liu, W. Huang, *Nat. Mater.* **2015**, *14*, 685; c) Y. Gong, G. Chen, Q. Peng, W. Z. Yuan, Y. Xie, S. Li, Y. Zhang, B. Z. Tang, *Adv. Mater.* **2015**, *27*, 6195; d) Y. Xiong, Z. Zhao, W. Zhao, H. Ma, Q. Peng, Z. He, X. Zhang, Y. Chen, X. He, J. W. Y. Lam, B. Z. Tang, *Angew. Chem. Int. Ed.* **2018**, *57*, 7997; e) Y. Shoji, Y. Iwabata, Q. Wang, D. Nemoto, A. Sakamoto, N. Tanaka, J. Seino, H. Nakai, T. Fukushima, *J. Am. Chem. Soc.* **2017**, *139*, 2728.
- [3] a) H. Wu, W. Chi, Z. Chen, G. Liu, L. Gu, A. K. Bindra, G. Yang, X. Liu, Y. L. Zhao, *Adv. Funct. Mater.* **2019**, *29*, 1807243; b) Y. Su, Y. Zhang, Z. Wang, W. Gao, P. Jia, D. Zhang, C. Yang, Y. Li, Y. L. Zhao, *Angew. Chem. Int. Ed.* **2019**, 10.1002/anie.201912102; c) N. Gan, H. Shi, Z. An, W. Huang, *Adv. Funct. Mater.* **2018**, *28*, 1802657; d) H. A. Al-Attar, A. P. Monkman, *Adv. Funct. Mater.* **2012**, *22*, 3824; e) Y. Su, S. Z. F. Phua, Y. Li, X. Zhou, D. Jana, G. Liu, W. Q. Lim, W. K. Ong, C. Yang, Y. L. Zhao, *Sci. Adv.* **2018**, *4*, eaas9732. f) Goudappagouda, A. Manthanath, V. C. Wakchaure, K. C. Ranjeesh, T. Das, K. Vanka, T. Nakanishi, S. S. Babu, *Angew. Chem. Int. Ed.* **2019**, *58*, 2284.
- [4] a) W. Jia, Q. Wang, H. Shi, Z. An, W. Huang, *Chem. Eur. J.* **2020**, 10.1002/chem.201904500; b) Kenry, C.-J. Chen, B. Liu, *Nat. Commun.* **2019**, *10*, 2111.
- [5] R. Kabe, C. Adachi, *Nature* **2017**, *550*, 384.
- [6] a) F. Würthner, S. Ahmed, C. Thalacker, T. Debaerdemaeker, *Chem. Eur. J.* **2002**, *8*, 4742; b) A. Ajayaghosh, V. K. Praveen, C. Vijayakumar, *Chem. Soc. Rev.* **2008**, *37*, 109; c) J. A. H. P. Sol, V. Dehm, R. Hecht, F. Würthner, A. P. H. J. Schenning, M. G. Debije, *Angew. Chem. Int. Ed.* **2018**, *57*, 1030; d) A. Ajayaghosh, V. K. Praveen, C. Vijayakumar, S. J. George, *Angew. Chem. Int. Ed.* **2007**, *46*, 6260; e) C. Vijayakumar, V. K. Praveen, A. Ajayaghosh, *Adv. Mater.* **2009**, *21*, 2059; f) K. V. Rao, K. K. R. Datta, M. Eswaramoorthy, S. J. George, *Adv. Mater.* **2013**, *25*, 1713; g) A. Ajayaghosh, C. Vijayakumar, V. K. Praveen, S. S. Babu, R. Varghese, *J. Am. Chem. Soc.* **2006**, *128*, 7174; h) F. J. M. Hoeben, L. M.

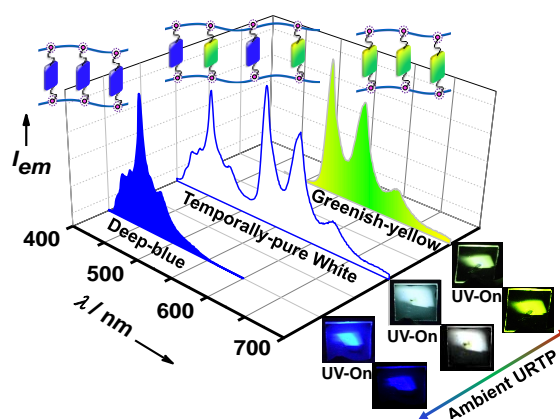
- Herz, C. Daniel, P. Jonkheijm, A. P. H. J. Schenning, C. Silva, S. C. J. Meskers, D. Beljonne, R. T. Phillips, R. H. Friend, E. W. Meijer, *Angew. Chem. Int. Ed.* **2004**, *43*, 1976.
- [7] a) A. Cravencoco, M. Hertzog, C. Ye, M. N. Iqbal, U. Mueller, L. Eriksson, K. Börjesson, *Sci. Adv.* **2019**, *5*, eaaw5978; b) A. Kirch, M. Gmelch, S. Reineke, *J. Phys. Chem. Lett.* **2019**, *10*, 310; c) D. Wasserberg, S. C. J. Meskers, R. A. J. Janssen, *J. Phys. Chem. A* **2007**, *111*, 1381; d) G. D. Scholes, *Annu. Rev. Phys. Chem.* **2003**, *54*, 57.
- [8] K. Jinnai, R. Kabe, C. Adachi, *Adv. Mater.* **2018**, *30*, 1800365.
- [9] a) M. A. Baldo, M. E. Thompson, S. R. Forrest, *Nature* **2000**, *403*, 750; b) Y. Sun, N. Giebink, H. Kanno, B. Ma, M. Thompson and S. Forrest, *Nature* **2006**, *440*, 908; c) Z. Li, Y. Han, F. Wang, *Nat. Commun.* **2019**, *10*, 3735; d) B. W. D'Andrade, M. A. Baldo, C. Adachi, J. Brooks, M. E. Thompson, S. R. Forrest, *Appl. Phys. Lett.* **2001**, *79*, 1045; e) M. Planells, E. Klampaftis, M. Congiu, R. Shivanna, K. V. Rao, O. Chepelin, A. C. Jones, B. S. Richards, S. J. George, K. S. Narayan, N. Robertson, *Eur. J. Inorg. Chem.* **2014**, 3095.
- [10] J. R. Lakowicz, *Principles of Fluorescence Spectroscopy (3rd ed.)*, Springer, **2011**, pp. 442.
- [11] Y. Gong, G. Chen, Q. Peng, W. Z. Yuan, Y. Xie, S. Li, Y. Zhang, B. Z. Tang, *Adv. Mater.* **2015**, *27*, 6195.
- [12] a/e - UV-Vis-IR Spectral Software 1.2, FluorTools, <http://www.fluortools.com>.
- [13] a) S. Cai, H. Shi, J. Li, L. Gu, Y. Ni, Z. Cheng, S. Wang, W. W. Xiong, L. Li, Z. An, W. Huang, *Adv. Mater.* **2017**, *29*, 1701244; b) L. Gu, H. Shi, L. Bian, M. Gu, K. Ling, X. Wang, H. Ma, S. Cai, W. Ning, L. Fu, H. Wang, S. Wang, Y. Gao, W. Yao, F. Huo, Y. Tao, Z. An, X. Liu, W. Huang, *Nat. Photonics* **2019**, *13*, 406.

CHAPTER 3.3

Temporally-pure White Afterglow Using Complementary Blue and Greenish-Yellow Ultralong Room Temperature Phosphors*

Abstract

In this Chapter, we show an unprecedented ambient white afterglow phosphorescence emission with colour purity during the entire period of delayed emission, after the cessation of excitation source. Such temporal-purity from organic materials has not been achieved previously, due to the different excited state lifetimes of constituting primary or complementary components. Here, we demonstrate a remarkable, ambient “temporally pure white afterglow”, which lasts for over 7 seconds, by co-organizing complementary blue and greenish-yellow organic room temperature phosphors with similar ultralong lifetimes and efficiency, in an amorphous polymer film. We also report, one of the most efficient amorphous state deep-blue afterglow emitting room temperature phosphor, with ultralong lifetime up to 2.26 s and maximum quantum efficiency of 17.5 %, from purely organic triazatruxene (TAT) molecule en route to the realization of this white afterglow. Further, broad and complementary absorption features of the co-organized phosphors in the visible region facilitates an excitation dependent dynamic colour-tuning of the afterglow from sky-blue to greenish-yellow.



*Manuscript based on this work has been published in *Adv. Funct. Mater.* **2020**, 30, 2003693.

3.3.1. Introduction

Luminescence afterglow from ultralong-lived excited states generates emission for a longer duration of seconds to hours, even after the termination of excitation process. This fascinating emission phenomenon has great potential in unique applications such as in night-vision lighting, signage or displays as a sustainable energy source, in bio-imaging to eliminate autofluorescence from cell components and in security protection.^[1-4] However, until recently, the afterglow emission could be realized only with rare-earth element doped inorganic phosphors which suffers from heavy-metal toxicity and poor processability.^[5] In this respect, the recent success with organic phosphors exhibiting ultralong room temperature phosphorescence (URTP or afterglow RTP) provides a promising alternative with solution processability, versatile structural design for tunable emission and low cost.^[6] However, design of highly efficient organic URTP emitters under ambient conditions, still remains as a grand challenge due to its weak spin-orbit coupling (SOC) efficiency and the non-radiative dissipation of triplets via vibrational and oxygen quenching, which limits the generation of long-lived triplet states.^[7] Ambient afterglow phosphorescence has been achieved in organic molecules via the restriction of the molecular motions by the crystallization of phosphors^[8a] or by embedding the phosphors in amorphous polymer matrices^[8b-c] or in the cavities/inter-layer galleries of host molecules/materials.^[8d] Very recently, new molecular designs and photophysical processes have also been proposed to achieve organic afterglow such as donor-acceptor thermally activated delayed fluorescence (TADF) exciplexes,^[9] and by the delayed sensitization of singlets via phosphorescence energy transfer process (Shown in Chapter 3.2).^[10] Yet, most of the URTP organics reported till date, exhibit only green and yellow afterglow emission and blue, red or white long-persistent emission are seldom reported.^[3a,6a,8a]

White-light emitting organic materials have attracted continued attention for many practical applications including panel displays and lighting devices.^[11] Molecular designs for all organic white-light fluorescent materials are well established, using multi-component systems/assemblies with either two complementary colours (blue and yellow) or three primary colours (red, green and blue).^[11,12] However, equivalent white-light emitting organic phosphors and especially afterglow materials are very difficult to accomplish as it would require multiple phosphors with either complementary or primary emission colours with ultralong lifetime which is challenging for a field in its infancy.^[1a,8a] Another problem with this multi-component approach would be the different delayed emission lifetimes of the individual components, that can cause the change in the colour of white afterglow with delay time. In this respect, Vacha and co-workers have attempted white -afterglow, using a single component emitter with dual long-lived

emission features from its triplet state (red emissive) and singlet state (cyan emissive) exhibiting ultralong TADF.^[13] However, a rational molecular design of TADF emitters with dual emission features having similar long lifetime and high efficiency would require fine modulation of singlet-triplet gap and hence would be a daunting task.^[14] Similarly, Tang and co-workers have attempted white RTP with single component exhibiting dual phosphorescence emission by exploiting a high-lying triplet (T_2) emission along with the phosphorescence from T_1 states.^[15] However, the fast decay of T_2 states ($\tau_{avg.} = 0.41$ ms) hampered the white colour purity during the time phase of afterglow to result in a yellow afterglow exclusively from the T_1 state ($\tau_{avg.} = 123.4$ ms). In this work, we proposed that ambient white afterglow with temporal colour purity can be obtained by a multi-component assembly of multiple URTP-emitting phosphors with similar lifetime and quantum yield. Though very recently, Zhao and co-workers have elegantly demonstrated an excitation wavelength dependent multi-colour afterglow by conjugating ultralong lived multiple phosphors into a co-polymer, white afterglow could not be accomplished.^[16] In this Chapter, we show an unprecedented ambient white afterglow with exceptional temporal colour purity. In addition, exploiting the complementary absorption profiles of these **CS-TAT-PVA** hybrids, we have further demonstrated an excitation-dependent multi-colour afterglow emission.^[16]

3.3.2. Design Strategy and Synthesis

We exploited two afterglow emitters with complementary colours (blue and greenish-yellow) that exhibit monomer state room temperature phosphorescence when anchored to polyvinylalcohol (**PVA**) host matrix to obtain white afterglow (Figure 3.3.1). Previously studied coronene tetracarboxylate (**CS**)-**PVA** hybrids act as the greenish-yellow emitting component with high phosphorescence quantum efficiency ($\sim 25\%$) and long-lifetime (~ 2.5 s) in air. On the other hand, a new heteroatom (nitrogen) containing rigid polyaromatic hydrocarbon, triazatruxene (**TAT**) was used as the complementary blue component. Amorphous **PVA** films of **TAT** exhibit deep-blue-emitting afterglow ($\tau_{avg.} = 2.26$ s) with Commission International de l'Éclairage (CIE) colour co-ordinates of (0.15, 0.06). It is worth mentioning that, **TAT-PVA** hybrid is one of the most efficient amorphous state, deep-blue emitting phosphorescent system known till date with a phosphorescence quantum yield (Φ_P) of 17.5%.^[16-18] Having shown a successful demonstration of efficient deep-blue afterglow, we later prepared multi-component amorphous **PVA** hybrid films of **TAT** and **CS**, to achieve “temporally-pure” ambient white-emitting afterglow with the CIE colour co-ordinates of (0.29, 0.33) (Figure 3.3.1).

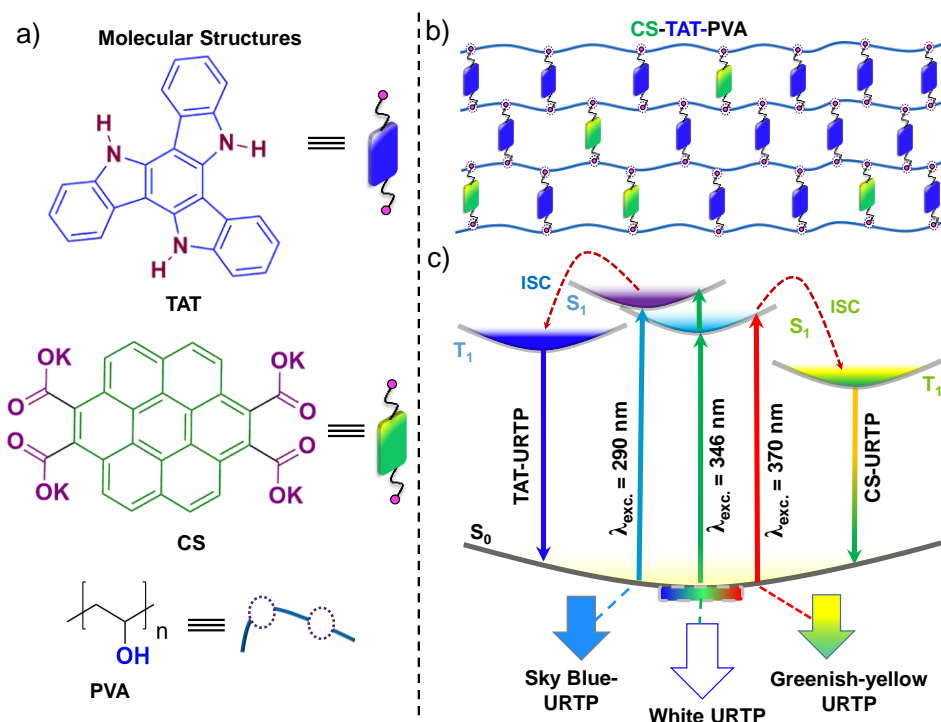


Figure 3.3.1. a) Molecular structures of organic phosphors (*TAT* and *CS*) and the polymer host (*PVA*) studied in this work. b) Schematic representation of multi-component *PVA* hybrids non-covalently anchored with blue and greenish-yellow phosphor molecules. c) Proposed Jablonski diagram for white phosphorescence and excitation-dependent URTP under ambient conditions. *TAT* and *CS* undergo deep-blue and greenish-yellow ultralong room temperature phosphorescence (URTP) in air when anchored to *PVA* individually. On the other hand their co-organized films show temporally-pure white emission while excited at 346 nm along with a dynamic multi-color afterglow from sky-blue to greenish-yellow while excited at 290 nm and 370 nm, respectively.

We envisaged that triazatruxene (*TAT*) molecule with its planar structure and with three -NH groups from its carbazole substructure and having a high triplet energy (2.85 eV) would be an ideal system to harvest deep-blue phosphorescence.^[19] The heteroatoms in carbazole moiety are shown to promote intersystem crossing (ISC) via activating $n-\pi^*$ transitions in the classical works of Lewis and Kasha to yield blue phosphorescence under cryogenic conditions,^[20] and more recently its ambient triplet harvesting has been achieved by Zhao and co-workers via H-bonding induced diluted confinement of carbazole derivatives in *PVA* matrix.^[17c] Although, twisted donor-acceptor derivatives with *TAT* core, were exploited recently for TADF molecular design, *TAT* or its derivatives are hitherto un-explored for the URTP under ambient conditions.^[19] In this chapter, *TAT-PVA* hybrids are first investigated for realizing ambient blue

phosphorescence. **TAT** is expected to exhibit non-covalent interactions with the pendant hydroxyl groups of **PVA** host via H-bonding interactions to minimize vibrational dissipation of the triplets in the resulting processable hybrids.^[21] **TAT** was synthesized in gram scale from oxindole in moderate yields and was characterized by ^1H , ^{13}C NMR spectroscopy and high resolution mass spectrometry (see experimental section).

3.3.3. Deep-blue Phosphorescence from TAT

3.3.3.1. Photophysical Properties of TAT in Solution-state

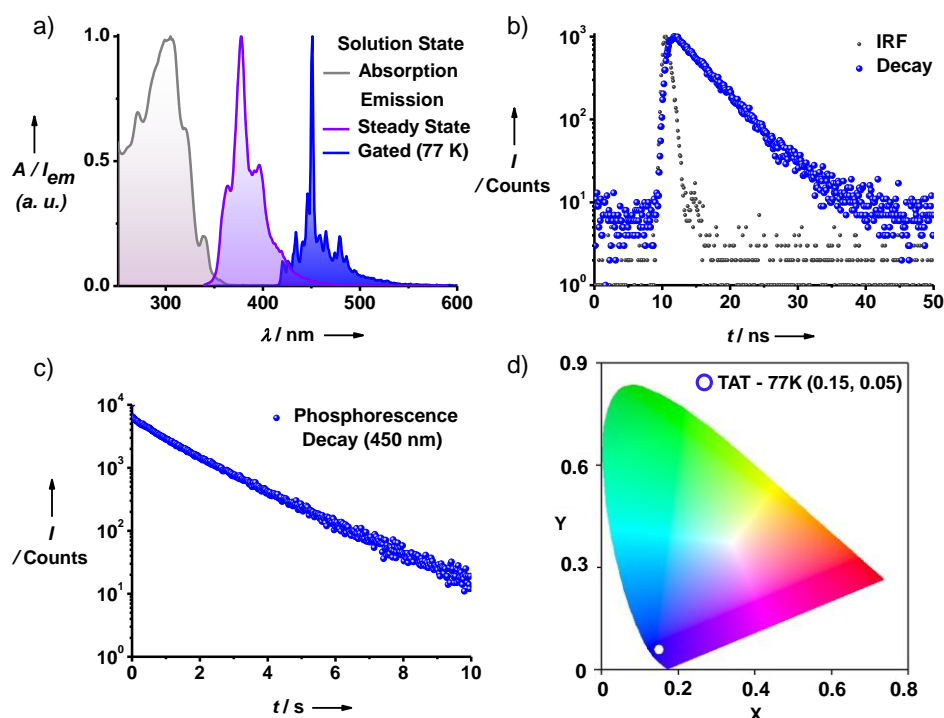


Figure 3.3.2. a) Normalized absorption, steady-state (room temperature) and gated emission (phosphorescence, 77 K) spectra of 0.05 mM **TAT** dissolved in MeOH ($\lambda_{exc.} = 330 \text{ nm}$, delay time = 5 ms). Time-resolved b) fluorescence (at room temperature, $\lambda_{exc.} = 340 \text{ nm}$, $\lambda_{monitored} = 380 \text{ nm}$, $\tau_{avg.} = 4.8 \text{ ns}$) and c) phosphorescence (at 77 K, $\lambda_{exc.} = 330 \text{ nm}$, $\lambda_{monitored} = 450 \text{ nm}$, $\tau_{avg.} = 1.52 \text{ s}$) decay profiles of 0.05 mM **TAT** in MeOH. d) Commission Internationale de l'Eclairage (CIE) colour co-ordinates of **TAT** phosphorescence in MeOH at 77 K ($[\text{TAT}] = 0.05 \text{ mM}$).

TAT is molecularly dissolved in methanol solvent (0.05 mM), as evident from its emission spectrum exhibiting strong fluorescence ($\lambda_{exc.} = 330 \text{ nm}$, $\lambda_{max.} = 378 \text{ nm}$, Figure 3.3.2a) with sharp vibrational features with an average lifetime of 4.8 ns ($\lambda_{exc.} = 340 \text{ nm}$, $\lambda_{monitored} = 380 \text{ nm}$, Figure 3.3.2b). As expected, **TAT** in methanol solution did not show any phosphorescence at room temperature due to the fast vibrational and rotational quenching of the triplet states.

However, glassy matrix of the same solution at 77 K showed promising ultra-long blue phosphorescence with an average lifetime of 1.52 s and with afterglow characteristics ($\lambda_{exc.} = 330$ nm, $\lambda_{monitored} = 450$ nm, Figure 3.3.2a-c). Further, the sharp vibrational features of the time-gated emission spectrum (delay time = 5 ms) at low concentration (0.05 mM) reiterates the monomeric origin of phosphorescence in the deep-blue region of the visible spectrum with Commission International de l'Eclairage (CIE) color co-ordinates of (0.15, 0.05) (Figure 3.3.2d). The calculated lowest excited singlet (S_1) – triplet (T_1) energy gap of **TAT** was reasonably low (0.36 eV), to assist an efficient ISC and subsequent phosphorescence emission if the vibrational quenching of triplet is minimized in rigid environments (Figure 3.3.2a).

3.3.3.2. Deep-blue Emitting TAT-PVA Afterglow Hybrids at Room Temperature

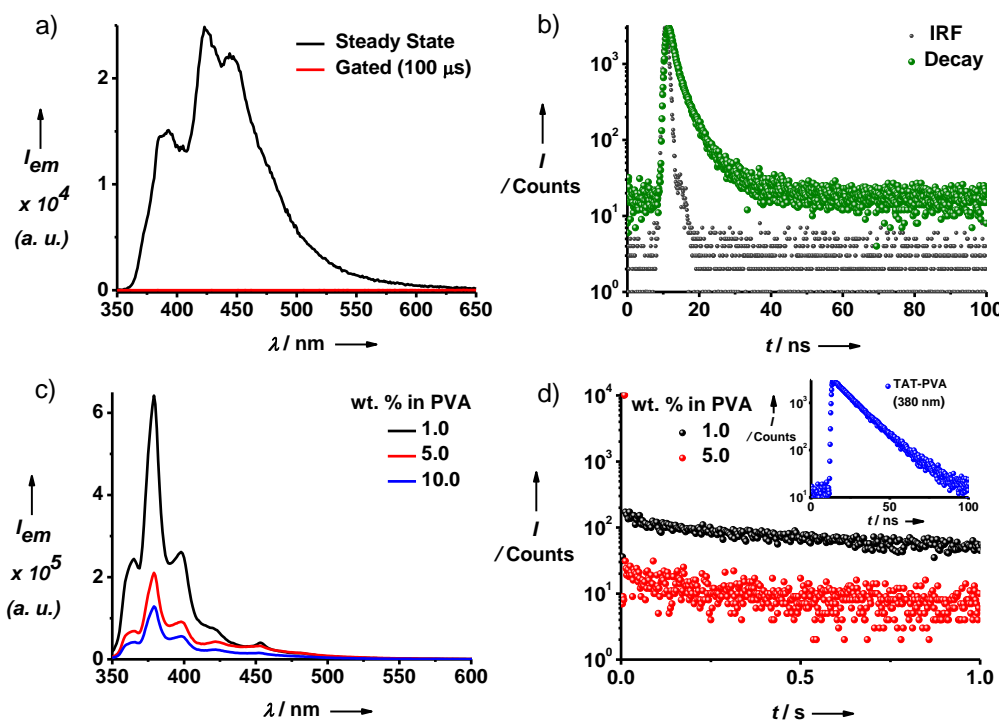


Figure 3.3.3. a) Steady-state and gated emission spectra of **TAT** in neat film state ($\lambda_{exc.} = 330$ nm, delay time = 100 μ s). b) Fluorescence decay profile of **TAT** in neat film state monitored at 430 nm ($\lambda_{exc.} = 340$ nm, $\tau_{avg.} = 3.16$ ns). c) Emission spectra ($\lambda_{exc.} = 330$ nm) and d) phosphorescence decay profile of **TAT-PVA** hybrids with varying composition showing decreasing intensity with increasing dye component in the **PVA** matrix. ($\lambda_{exc.} = 340$ nm, $\lambda_{monitored} = 450$ nm, $\tau_{avg.} = 2.26$ s and 0.27 s for 1 wt. % and 5 wt. % **TAT-PVA** compositions, respectively). Inset of 3.3.3d shows fluorescence decay profile of 1 wt. % **TAT-PVA** hybrid film monitored at 380 nm ($\lambda_{exc.} = 340$ nm, $\tau_{avg.} = 13.3$ ns).

At first we attempted to stabilize the room temperature phosphorescence (RTP) from **TAT** by minimizing the vibrational dissipation in neat solid films. However it was not successful, due to aggregation induced emission quenching of excited states as expected from large π -conjugated molecules (Figure 3.3.3a and 3.3.3b). Thus, next we attempted the rigidification of **TAT** chromophores in its isolated or dispersed state by the H-bonding directed anchoring to the pendant hydroxyl groups of the **PVA** chains, which would spatially separate the chromophores and will also minimize the vibrational dissipation of the triplets. Thus **TAT-PVA** hybrid films with different weight percentages of **TAT** (wt. %) with respect to **PVA** (1-10 wt. %) were prepared by adding appropriate volumes of a methanol solution of **TAT** (x mg/ml) to aqueous solution of **PVA** (100 mg/ml), followed by drop-casting on glass substrate and drying under vacuum at 60 °C. We have used 1 wt. % **TAT-PVA** film to perform detailed photophysical measurements as higher wt. % of **TAT** has resulted in emission quenching probably due to the inter-chromophoric interactions (Figure 3.3.3c and 3.3.3d).

1 wt. % **TAT-PVA** hybrid film showed sharp absorption and steady state emission (fluorescence; $\lambda_{\text{exc.}} = 330$ nm, $\lambda_{\text{max.}} = 380$ nm) spectral features with vibrational peaks similar to that of molecularly dissolved chromophores in dilute methanol solution (Figure 3.3.4a, Figure 3.3.3d, inset). In addition, hybrid films exhibited enhanced fluorescence quantum yield ($\Phi_{\text{F}} = 35.3$ %) compared to the negligible emission in neat films. These observations suggest towards the spatial isolation of **TAT** chromophores in **PVA** matrix which is envisaged to be due to the scaffolding of molecules via strong hydrogen-bonding interaction between the -NH (**TAT**) and -OH (**PVA**) groups.^[17,21] Remarkably, upon ceasing the excitation source (330 nm UV lamp), an intense deep-blue emission persisted over 10 seconds from **TAT-PVA** hybrid films, under aerated conditions suggesting ambient, ultra-long room temperature phosphorescence (Figure 3.3.4b, Video 3.3.1). This is further evident from the time-gated (delay time = 5 ms) emission profile which shows pure-blue phosphorescence ($\Phi_{\text{P}} = 17.5$ %) with CIE colour co-ordinates of (0.15, 0.06) and a visible afterglow with an average lifetime of 2.26 s ($\lambda_{\text{exc.}} = 330$ nm, $\lambda_{\text{monitored}} = 450$ nm) (Figure 3.3.4c and 3.3.4d). Again, the spectral similarity of this amorphous state phosphorescence with that of the isolated monomers in glassy matrix (77 K) suggests the monomeric origin of afterglow **TAT** triplet emission.

Ambient blue afterglow phosphorescence is considered as the holy grail in organic lighting materials and to the best of our knowledge, **TAT-PVA** hybrid in the present study is among the most efficient deep-blue emitting amorphous state ultralong room temperature phosphor ($\Phi_{\text{P}} = 17.5$ %). Most notable reports of amorphous phosphors include carbazole and polyphosphazene derivatives in **PVA** matrix ($\Phi_{\text{P}} = 16$ -29%).^[17] On the other hand, blue-emitting

URTP molecules in crystalline state have been reported by Huang's group with 2,4,6-trimethoxy-1,3,5-triazine ($\Phi_P = 31.2\%$)^[18b] and Tang's group with benzophenone derivatives ($\Phi_P = 39.7\%$).^[7a] It is worthwhile to mention that, unlike the crystalline phosphors exhibiting URTP through the intermolecular excitonic coupling between stacked chromophores, which simultaneously accelerate the ISC rate and reduce vibrational motions, the **TAT-PVA** phosphor presented here exhibit afterglow in its monomeric state and in an amorphous phase, thus not very sensitive to the molecular organization.^[3a,10a,18b,21] Moreover, these derivatives can be synthesized with simple synthetic procedures and in large quantities and hence we envisage great potential for the triazatruxene-based blue phosphors in solution-processable lighting devices.

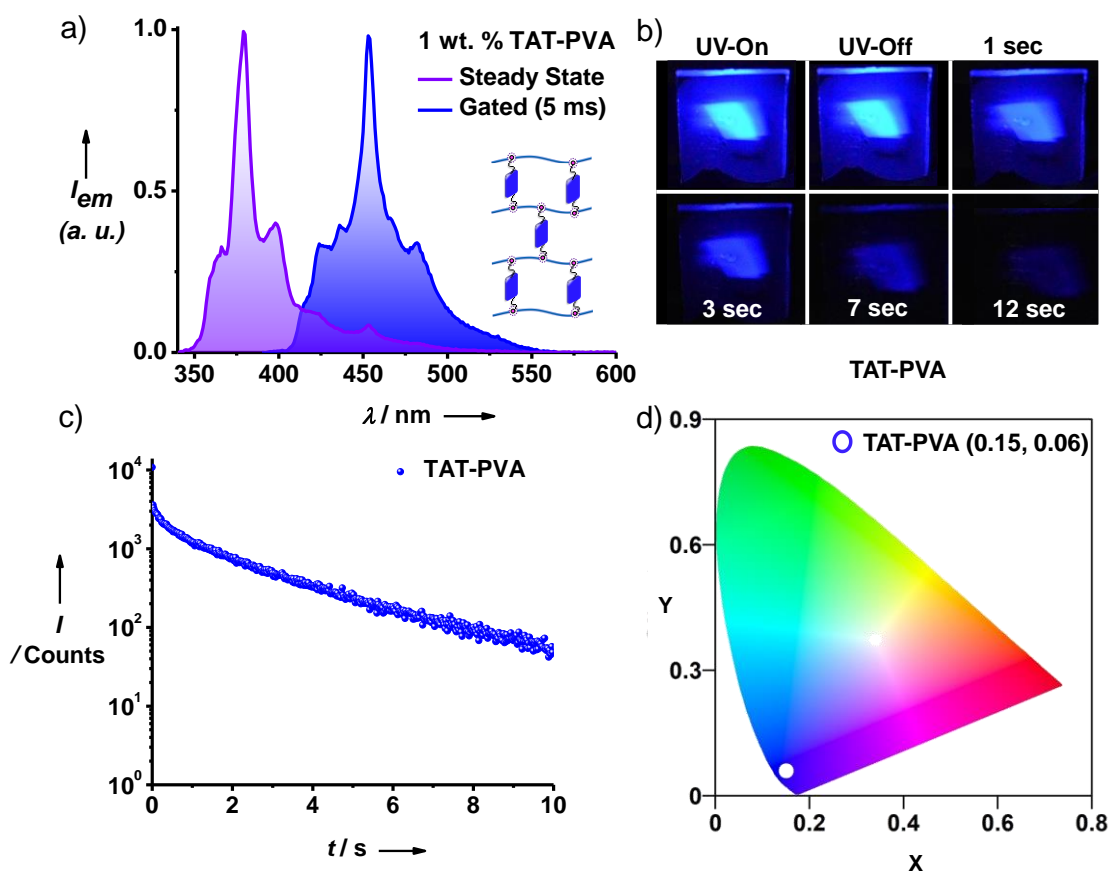


Figure 3.3.4. a) Normalized steady-state and gated emission spectra (delay time = 5 ms) of 1 wt. % **TAT-PVA** hybrid film excited at 330 nm (Inset: schematic illustration of **TAT** anchored **PVA** scaffold) and b) corresponding time-dependent photographs of blue afterglow phosphorescence (330 nm UV-excitation). c) Phosphorescence decay profile of the 1 wt. % **TAT-PVA** ($\lambda_{exc.} = 330$ nm) monitored at 450 nm. d) Commission International de l'Eclairage (CIE) colour co-ordinates of blue-emitting phosphorescence exhibited by **TAT-PVA** hybrid films at room temperature.

3.3.4. Temporally-pure White Afterglow

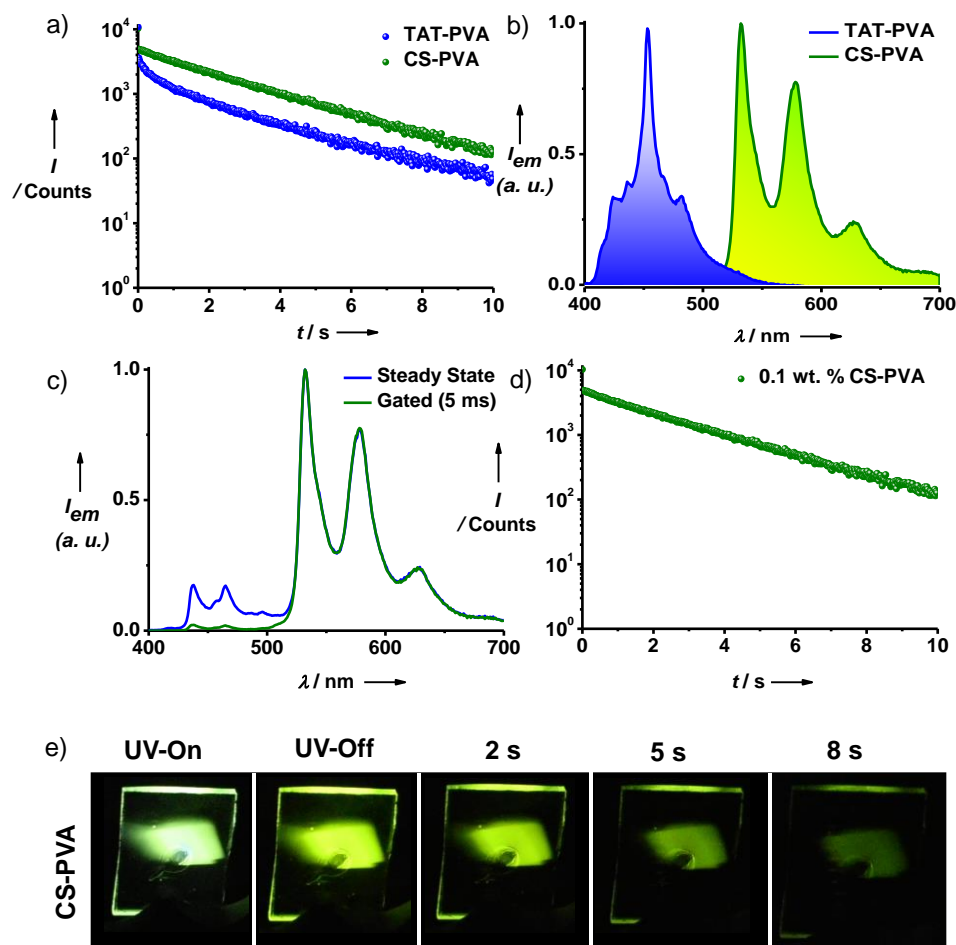


Figure 3.3.5. a) Phosphorescence decay profile of 1 wt. % TAT-PVA (blue phosphor, $\lambda_{exc.} = 330$ nm, $\lambda_{monitored} = 450$ nm, $\tau_{avg.} = 2.26$ s) and 0.1 wt. % CS-PVA (greenish-yellow phosphor, $\lambda_{exc.} = 340$ nm, $\lambda_{monitored} = 530$ nm, $\tau_{avg.} = 2.6$ s) hybrid films showing similar average lifetimes. b) Gated phosphorescence spectra of 1 wt. % TAT-PVA (blue phosphor, $\lambda_{exc.} = 330$ nm, delay time = 5 ms) and 0.1 wt. % CS-PVA hybrid films (greenish-yellow phosphor, $\lambda_{exc.} = 340$ nm, delay time = 5 ms). Inset: Schematic illustration of CS-anchored PVA scaffold. c) Normalized steady-state, gated emission spectra ($\lambda_{exc.} = 340$ nm, delay time = 5 ms) and d) phosphorescence decay profile of 0.1 wt. % CS-PVA hybrid film ($\lambda_{exc.} = 340$ nm, $\lambda_{monitored} = 532$ nm, $\tau_{avg.} = 2.6$ s). e) Photographs of 0.1 wt. % CS-PVA hybrid film upon 340 nm UV-excitation and its greenish-yellow emitting long persistent emission when the source is turned off. Phosphorescence quantum efficiency of 0.1 wt. % CS-PVA was observed to be 20.7 %, very similar in range as compared to 1 wt. % TAT-PVA (17.5 %).

After demonstrating, ambient blue-emitting afterglow from solution-processable amorphous **TAT-PVA** hybrids, we further attempted the ambient white-afterglow phosphorescence, by co-assembling the **TAT** blue phosphor with a complementary greenish-yellow phosphor in amorphous **PVA** matrix. An efficient white-afterglow would require similar triplet lifetime of both phosphors as different delayed emission lifetime of the components in the multi-phosphor hybrids would lead to temporal change in the afterglow emission wavelength, thus deviating from the pure white-light emission during the time-range of afterglow. Hence, the design of white afterglow materials with temporal colour purity has been a great challenge and are seldom reported.^[13] In that regard, previously studied ambient greenish-yellow afterglow phosphorescence from **CS-PVA** hybrid was envisaged to be an ideal complementary colour-component for **TAT-PVA** blue phosphor (phosphorescence spectral range 400-550 nm), as **CS** covers both green and red wavelengths of the visible spectrum with excellent phosphorescence intensity and high lifetime (phosphorescence spectral range 500-700 nm, $\Phi_P \sim 25\%$, $\tau_{\text{avg.}} \sim 2.5$ s) (Figure 3.3.5a and 3.3.5b).^[10a] Notably, the combination of **CS** and **TAT** embedded in **PVA** matrix is an ideal choice in order to obtain temporally-pure white-light afterglow considering their similar persistent phosphorescence lifetime and quantum efficiency (Figure 3.3.5a-e and Video 3.3.2).

First, a titration experiment was performed with varying amount of doped **CS** in 1 wt. % of **TAT-PVA** hybrid to identify the right composition of phosphors to extract afterglow (see experimental section) (Figure 3.3.6). Interestingly, **TAT-PVA** films doped with 10 wt. % **CS** with respect to the concentration of **TAT** component when excited with 346 nm light, showed white-light emitting phosphorescence with excellent quantum efficiency ($\Phi_P = 15.8\%$) and CIE colour co-ordinates of (0.29, 0.33) (Figure 3.3.7a-c, Video 3.3.3). Further, these films exhibited clear white afterglow features persisting over 7 seconds upon removing the excitation source. Time resolved emission spectra of the hybrid film recorded at different delay times showed similar phosphorescence spectral features suggesting an unprecedented “temporal colour-purity” of the white afterglow due to the similar phosphorescence lifetime possessed by its two complementary phosphors (**CS** and **TAT**) (Figure 3.3.7c and Figure 3.3.8). Remarkable ambient white afterglow without temporal changes in emission wavelength is evident from the constant CIE colour co-ordinates at different time intervals during the afterglow (Figure 3.3.7d). Previous attempts to achieve white afterglow in pure organic systems was based on single component phosphors by harvesting additional high energy, long-lived excited state emission such as TADF^[13] or higher lying triplet (T_2) emission in combination with the triplet (T_1) phosphorescence.^[15] However, different lifetime of these long-lived states and interdependency

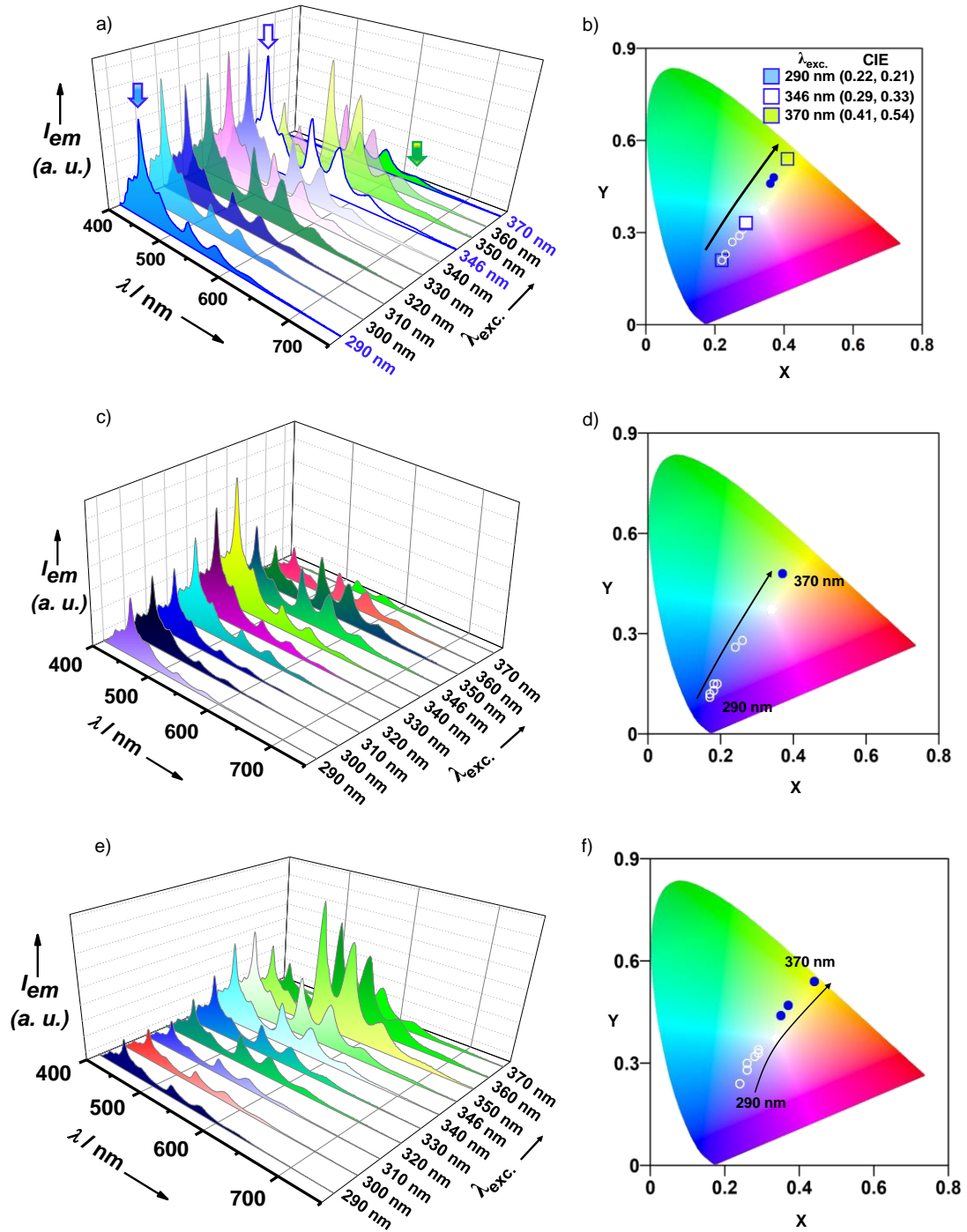


Figure 3.3.6. Excitation dependent ultralong phosphorescence profile and corresponding Commission International de l'Eclairage (CIE) colour co-ordinates of *TAT-PVA* hybrid films doped with (a, b) 10 wt. %, (c, d) 1 wt. % and (e, f) 20 wt. % CS (amount of CS is with respect to *TAT*) showing the linear trajectory of the colour modulation. In all cases 5 ms delay time was used. Arrows in figure 3.3.6a, indicate the phosphorescence spectra corresponding to sky-blue, white and greenish-yellow emission when excited at 290 nm, 346 nm and 370 nm, respectively.

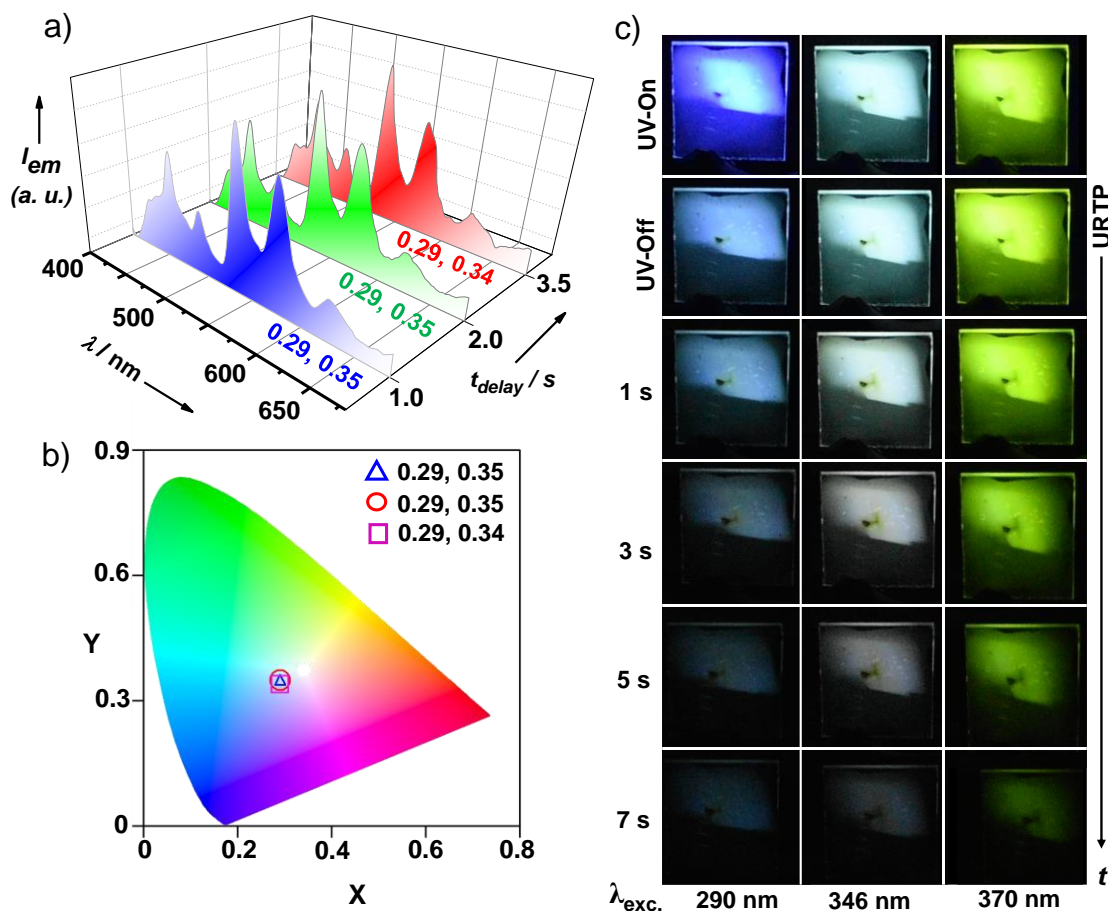


Figure 3.3.7. a) Time dependent emission spectra (delay time = 1s, 2s and 3.5 s) during afterglow time period and b) corresponding CIE colour co-ordinates of CS doped TAT-PVA hybrid showing a “temporal purity” of white afterglow phosphorescence after the excitation source at 346 nm is turned-off. c) Photographs of CS-TAT-PVA hybrid film (with 10 wt. % CS doping) under different excitation wavelengths ($\lambda_{exc.}$ = 290 nm, 346 nm and 370 nm) showing clear color-tunable afterglow upon turning-off the source including the temporally-pure white-afterglow phosphorescence emission (middle column).

of the photo-physical processes from excited electronic landscape of single system would lead to differential decay of the two afterglow emission to result in changes in the afterglow colour with time. Hence, we demonstrate that temporal colour purity of white URTP from organic systems can be maintained during the entire time period of afterglow using two complementary long-lived phosphors with similar lifetime and quantum efficiency (Figure 3.3.4 and Figure 3.3.5). This unprecedented white afterglow system is also benefited from the absence of any Förster Resonance Energy Transfer (FRET) process between the two phosphors, due to the minimal spectral overlap between them.

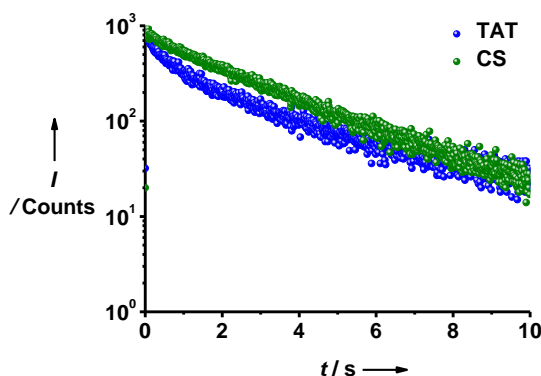


Figure 3.3.8. Phosphorescence decay profile of 10 wt. % CS doped TAT-PVA film monitored at 450 nm and 530 nm ($\lambda_{exc.} = 346$ nm). Average lifetime of TAT (2.2 s) and CS (2.48 s) in this hybrid is observed to be of similar magnitude.

3.3.5. Excitation Dependent Colour-tunable Afterglow

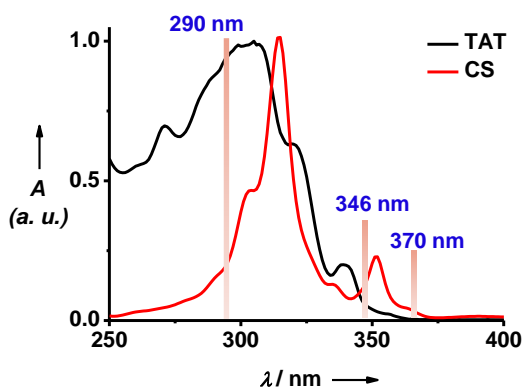


Figure 3.3.9. Normalized absorption spectra of 0.05 mM TAT (in MeOH) and 0.1 mM PVA (in water). The indicated wavelengths are showing differential absorption co-efficient of these two chromophores.

Since the absorption profiles of the two constituting phosphors, **CS** and **TAT**, in the multi-component **PVA** hybrid show clear differences in the 250-400 nm region, we further envision the realization of a tunable persistent phosphorescence from these hybrids with multiple excitation wavelengths (Figure 3.3.9). Apart from the white afterglow obtained from the excitation at 346 nm, where both phosphors have significant optical density, excitation at 290 nm where **CS** has weaker absorption as compared to **TAT**, resulted in sky-blue emitting afterglow (Figure 3.3.7c and 3.3.6a). The clear visible sky-blue afterglow with a CIE colour co-ordinates of (0.22, 0.21) persists over 7s after the removal of light-source ($\lambda_{exc.} = 290$ nm, delay time = 5 ms) (Figure 3.3.7c, left column, Figure 3.3.6b and Video 3.3.4). On the other hand, the ambient long-lived phosphorescence changed to greenish-yellow when the excitation wavelength of >350

nm is used, where **TAT** has negligible absorption (Figure 3.3.7c and 3.3.6a). The greenish-yellow phosphorescence with CIE colour co-ordinates of (0.41, 0.54) ($\lambda_{exc.} = 370$ nm, delay time = 5 ms) (Figure 3.3.7c, right column, 3.3.6b and Video 3.3.5) exhibited an afterglow for 7s upon removal of the light-source. The excitation dependent nature of the afterglow in these hybrids is clearer from the corresponding phosphorescence spectra recorded under ambient conditions (Figure 3.3.6). Variation of excitation wavelength from 290 to 370 nm, showed clear change in the emission contributions from different components moving from blue to green. Further the remarkable colour variation of the afterglow from **CS-TAT-PVA** hybrids is very evident from the CIE coordinates, which revealed a gradual linear change from blue to greenish-yellow upon changing the excitation from 290 nm to 370 nm (Figure 3.3.6b). Excitation dependent afterglow could also be tuned by modulating the composition of the components in the hybrid films (Figure 3.3.6c and 3.3.6d).

3.3.6. Conclusions

In summary, we have demonstrated an ambient white ultralong phosphorescence in amorphous phase, by the co-anchoring of complementary blue and greenish-yellow room temperature organic phosphors into a polymer matrix. The resultant white afterglow with the CIE co-ordinates of (0.29, 0.33) exhibited an unprecedented temporal colour purity as evident from the time-resolved emission spectra and constant CIE co-ordinates with various delay times, which is achieved by the similar ultralong lifetimes and quantum efficiencies of both phosphor components. White afterglow with temporal colour purity was made possible by the design of blue-URTP materials from structurally simple triazatruxene (**TAT**) doped in amorphous **PVA** films, to result in one of the most efficient organic deep-blue emitting afterglow phosphors in air, with maximum quantum efficiency of 17.5 % and long lifetime over 2.2 s, reported till date under similar experimental conditions. An aromatic coronene derivative (**CS**) with carboxylate functional groups, recently reported from our group, has been used at the complementary greenish-yellow URTP phosphor. The hydrogen-bonding as well as ion-dipole interaction with the polar hydroxyl groups of **PVA**, successfully isolate and rigidify these phosphor molecules and result in narrow-bandwidth monomer triplet emission. Further an excitation wavelength dependent dynamic multi-colour afterglow could also be demonstrated from these multi-component amorphous films, by exploiting the differential absorption profiles of **TAT** and **CS**. Afterglow materials presented here are envisioned to find applications in state-of-the art bio-imaging, anti-counterfeiting, information storage or multicolor display because of their unique processability, ambient stability and scalable synthesis.

3.3.7. Experimental Section

3.3.7a. General Methods

NMR Measurements: ^1H and ^{13}C NMR spectra were recorded on a BRUKER AVANCE-400 fourier transformation spectrometer with 400 and 100 MHz, respectively. The spectra are calibrated with respect to the residual solvent peaks. The chemical shifts are reported in parts per million (ppm) with respect to TMS. Short notations used are, s for singlet, d for doublet, t for triplet, q for quartet and m for multiplet.

Optical Measurements: Electronic absorption spectra were recorded on a Perkin Elmer Lambda 900 UV-Vis-NIR spectrometer and emission spectra were recorded at FLS1000 spectrometer, Edinburgh Instruments. UV-Vis and emission spectra were recorded in 10 mm path length cuvette. Fluorescence spectra of the films were recorded in front-face geometry to avoid self-absorption at high concentrations.

Lifetime and quantum yield measurements: Fluorescence lifetimes were performed on a FLS1000 spectrometer, Edinburgh Instruments by time-correlated single-photon-counting (TCSPC) method. A 340 nm LED with a pulse repetition rate of 1 MHz was used as the light source. The instrument response function (IRF) was collected by using a scatterer (Ludox AS40 colloidal silica, Sigma-Aldrich). Phosphorescence lifetime and gated emission was measured on FLS1000 spectrometer, Edinburgh Instruments equipped with a micro flash lamp ($\mu\text{F}2$) set-up. Quantum yield was measured using an integrated sphere equipped with the same instrument. Time-resolved emission spectra was measured between 400-680 nm emission wavelength region, using a micro-flash lamp by exciting the thin film at 346 nm. The data obtained here was deconvoluted in the same FLS1000 spectrometer in order to obtain the delay times of 1-3.5 s.

High Resolution Mass Spectrometry (HRMS): HR-MS was carried out using Agilent Technologies 6538 UHD Accurate-Mass Q-TOFLC/MS.

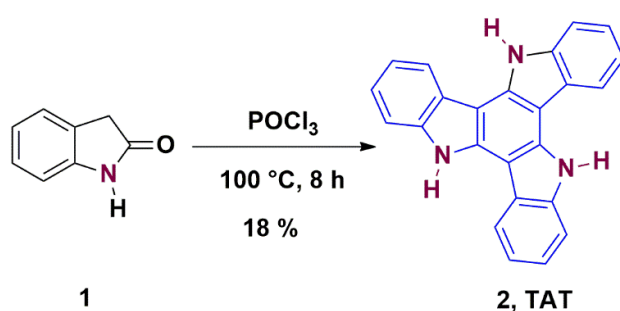
3.3.7b. Protocol for Dye-polymer Hybrids Sample Preparation: First, a stock solution of **PVA** was prepared by heating 0.5 g of the polymer in 10 ml of distilled water for 3 hours under stirring conditions. a) **TAT-PVA** hybrids were prepared by adding appropriate amount of **TAT** (dissolved in MeOH) to 1 ml of **PVA** stock solutions (for example, for 1 wt. % **TAT-PVA** 0.5 mg of **TAT** is used) followed by sonication and heating the solution at 60 °C for 5 minutes to get a semi-transparent solution. b) For samples to study excitation dependent URTP, appropriate amount of **CS** aqueous solutions were added to 1 wt. % **TAT-PVA** hybrid solutions and heated at 60 °C for few minutes until it becomes a homogeneous suspension. All these samples were

then drop-casted on a clean glass substrate followed by drying under vacuum at 60 °C to make the corresponding hybrid films.

3.3.7c. Synthetic Schemes and Procedures

Materials: Oxindole, phosphorous oxychloride, methyl iodide, potassium carbonate and solvents were purchased from Spectrochem; tetrabutylammonium iodide (TBAI), 2-Chloro-N,N-dimethyl ethylamine hydrochloride and sodium hydride were purchased from Sigma-aldrich and used without further purification.

Synthetic Scheme:



Scheme 3.3.1. Synthetic scheme for **TAT**.

Synthetic Procedure:

CS was synthesized according to literature procedure.^[22] **TAT** was synthesized according to literature procedure with some modifications.^[23]

Synthesis of TAT: A mixture of 2-oxindole (3 g, 22.55 mmol) and phosphoryl chloride (15 mL, 65 mmol) were taken in 100 mL round bottom (RB) flask under N₂ atmosphere. The reaction mixture was then stirred at 100 °C for 8 hours to obtain a dark brown suspension. The resulting suspension was poured into ice-water and stirred at room temperature for additional 12 hours. The dark green suspension was then slowly (highly exothermic reaction) neutralized completely with 10 % aqueous NaOH and filtered. The obtained green residue was dried under vacuum oven at 70 °C and further purified by 100-200 mesh silica-gel column chromatography by using mixture of solvent 30 % ethyl acetate in hexane. The obtained pale brown solid was recrystallized in 20 mL of acetone to get crystalline off-white solid as a desired compound (triazatruxene, TAT).

TAT: Off-white solid (yield: 18 %); ¹H NMR (400 MHz, DMSO-*d*₆, ppm): δ_H 11.86 (s, 3H), 8.67 (d, 3H, J = 7.6 Hz), 7.72 (d, 3H, J = 7.6 Hz), 7.41-7.31 (m, 6H); ¹³C NMR (100 MHz, DMSO-*d*₆,

ppm): δ_C 138.5, 133.7, 122.4, 122.2, 119.8, 119.0, 110.9, 100.5; HRMS (APCI): m/z calculated for $C_{24}H_{15}N_3$: 345.1266: observed 346.1427 $[M+H]^+$.

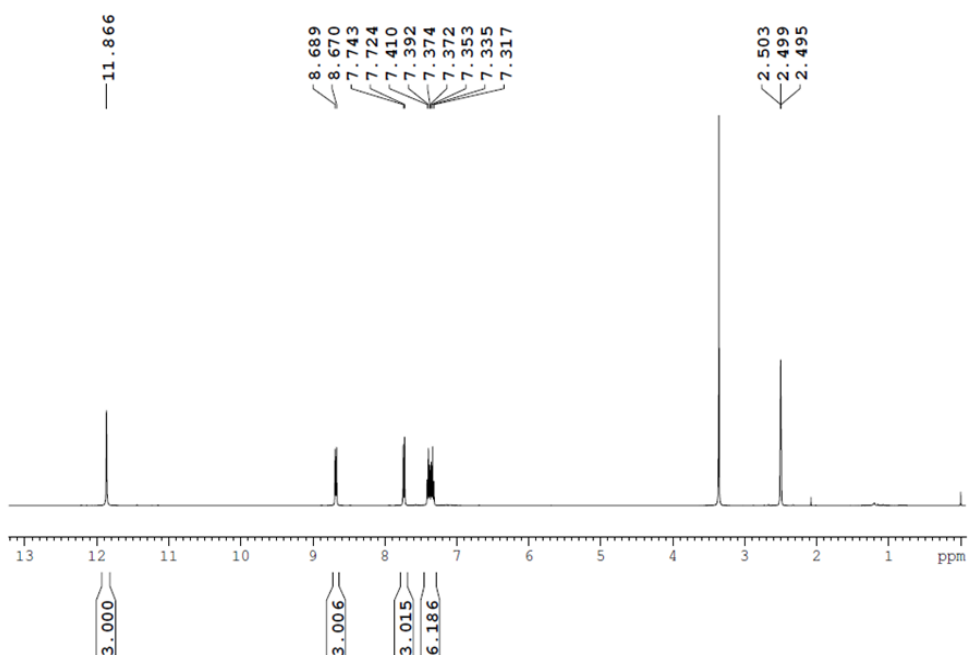


Figure 3.3.10. 1H NMR spectrum of *TAT* in $DMSO-d_6$.

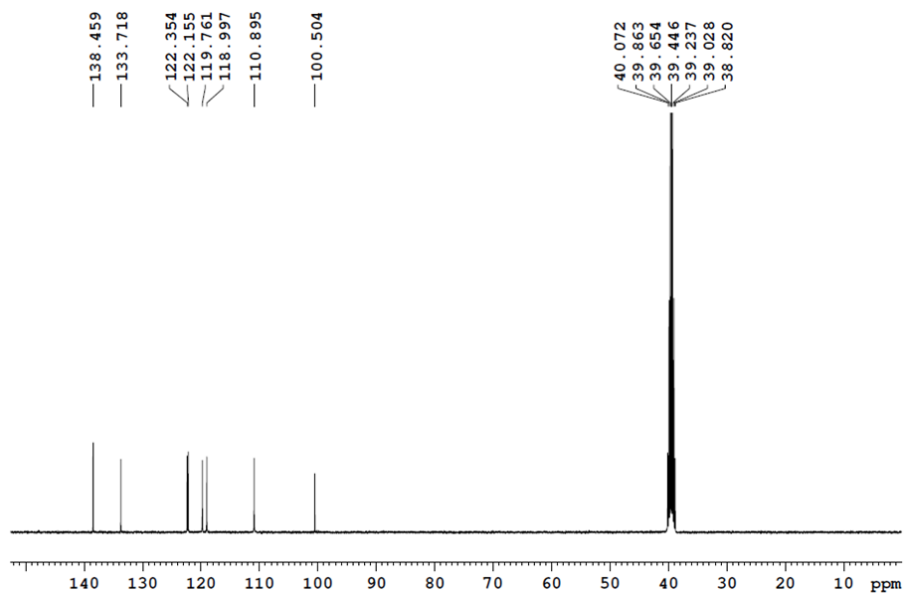


Figure 3.3.11. ^{13}C NMR spectrum of *TAT* in $DMSO-d_6$.

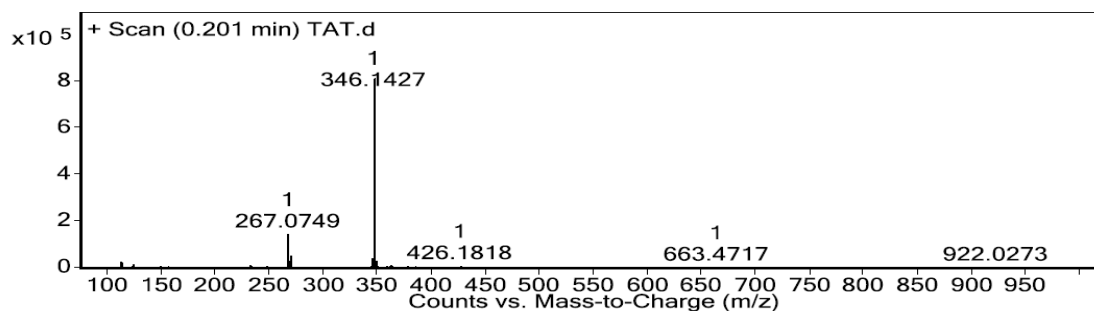


Figure 3.3.12. APCI-HRMS spectrum of TAT.

3.3.8. References

- [1] a) S. Xu, R. Chen, C. Zheng, W. Huang, *Adv. Mater.* **2016**, *28*, 9920; b) R. Kabe, N. Notsuka, K. Yoshida, C. Adachi, *Adv. Mater.* **2016**, *28*, 655; c) Z. Pan, Y. Lu, F. Liu, *Nat. Mater.* **2012**, *11*, 58.
- [2] T. Maldiney, A. Bessi re, J. Seguin, E. Teston, S. K. Sharma, B. Viana, A. J. J. Bos, P. Dorenbos, M. Bessodes, D. Gourier, D. Scherman, C. Richard, *Nat. Mater.* **2014**, *13*, 418-426; b) G. Zhang, G. M. Palmer, M. Dewhirst, C. L. Fraser, *Nat. Mater.* **2009**, *8*, 747.
- [3] a) Z. An, C. Zheng, Y. Tao, R. Chen, H. Shi, T. Chen, Z. Wang, H. Li, R. Deng, X. Liu, W. Huang, *Nat. Mater.* **2015**, *14*, 685; b) M. Gmelch, H. Thomas, F. Fries, S. Reineke, *Sci. Adv.* **2019**, *5*, eaau7310.
- [4] Z. He, H. Gao, S. Zhang, S. Zheng, Y. Wang, Z. Zhao, D. Ding, B. Yang, Y. Zhang, W. Z. Yuan, *Adv. Mater.* **2019**, *31*, 1807222.
- [5] T. Matsuzawa, Y. Aoki, N. Takeuchi, Y. Murayama, *J. Electrochem. Soc.* **1996**, *143*, 2670.
- [6] a) S. Hirata, *Adv. Optical Mater.* **2017**, *5*, 1700116; b) N. Gan, H. Shi, Z. An, W. Huang, *Adv. Funct. Mater.* **2018**, *28*, 1802657; c) Y. Xie, Y. Ge, Q. Peng, C. Li, Q. Li, Z. Li, *Adv. Mater.* **2017**, *29*, 1606829.
- [7] a) W. Z. Yuan, X. Y. Shen, H. Zhao, J. W. Y. Lam, L. Tang, P. Lu, C. Wang, Y. Liu, Z. Wang, Q. Zheng, J. Z. Sun, Y. Ma, B. Z. Tang, *J. Phys. Chem. C* **2010**, *114*, 6090; b) O. Bolton, K. Lee, H. J. Kim, K. Y. Lin, J. Kim, *Nat. Chem.* **2011**, *3*, 205; c) S. Kuila, K. V. Rao, S. Garain, P. K. Samanta, S. Das, S. K. Pati, M. Eswaramoorthy, S. J. George, *Angew. Chem. Int. Ed.* **2018**, *57*, 17115; *Angew. Chem.* **2018**, *130*, 17361.
- [8] a) Kenry, C.-J. Chen, B. Liu, *Nat. Commun.* **2019**, *10*, 2111; b) S. Hirata, K. Totani, J. Zhang, T. Yamashita, H. Kaji, S. R. Marder, T. Watanabe, C. Adachi, *Adv. Funct. Mater.* **2013**, *23*, 3386; c) M. Louis, H. Thomas, M. Gmelch, A. Haft, F. Fries, S. Reineke, *Adv. Mater.* **2019**, *31*, 1807887; d) H. Mieno, R. Kabe, N. Notsuka, M. D. Allendorf, C. Adachi, *Adv. Optical Mater.* **2016**, *4*, 1015.

- [9] a) R. Kabe, C. Adachi, *Nature* **2017**, *550*, 384-387; b) K. Jinnai, R. Kabe, C. Adachi, *Adv. Mater.* **2018**, *30*, 1800365.
- [10] a) S. Kuila, S. J. George, *Angew. Chem. Int. Ed.* **2020**, DOI: 10.1002/anie.202002555; b) A. Kirch, M. Gmelch, S. Reineke, *J. Phys. Chem. Lett.* **2019**, *10*, 310; c) Y. Mu, B. Xu, Z. Yang, S. K. B. Mane, J. Zhao, Y. Zhang, Z. Chi, B. Z. Tang, *ACS Appl. Mater. Interfaces* **2020**, *12*, 5073.
- [11] V. K. Praveen, C. Ranjith, N. Armaroli, *Angew. Chem. Int. Ed.* **2014**, *53*, 365.
- [12] a) S. Das, N. Okamura, S. Yagi, A. Ajayaghosh, *J. Am. Chem. Soc.* **2019**, *141*, 5635; b) C. Vijayakumar, V. K. Praveen, A. Ajayaghosh, *Adv. Mater.* **2009**, *21*, 2059; c) S. S. Babu, V. K. Praveen, A. Ajayaghosh, *Chem. Rev.* **2014**, *114*, 1973; d) S. S. Babu, J. Aimi, H. Ozawa, N. Shirahata, A. Saeki, S. Seki, A. Ajayaghosh, H. Möhwald, T. Nakanishi, *Angew. Chem. Int. Ed.* **2012**, *51*, 3391; e) J. Wang, X. Gu, H. Ma, Q. Peng, X. Huang, X. Zheng, S. H. Sung, G. Shan, J. W. Lam, Z. Shuai, B. Z. Tang, *Nat. Commun.* **2018**, *9*, 2963; f) K. V. Rao, K. K. R. Datta, M. Eswaramoorthy, S. J. George, *Adv. Mater.* **2013**, *25*, 1713-1718; g) R. Abbel, C. Grenier, M. J. Pouderoijen, J. W. Stouwdam, P. E. L. G. Leclere, R. P. Sijbesma, E. W. Meijer, A. P. H. J. Schenning, *J. Am. Chem. Soc.* **2009**, *131*, 833; h) X. Zhang, S. Rehm, M. M. Safont-Sempere, F. Würthner, *Nat. Chem.* **2009**, *1*, 623-629; i) X. Zhang, D. Görl, F. Würthner, *Chem. Commun.* **2013**, *49*, 8178-8180; j) S. Park, J. E. Kwon, S. H. Kim, J. Seo, K. Chung, S. Y. Park, D. J. Jang, B. M. Medina, J. Gierschner, S. Y. Park, *J. Am. Chem. Soc.* **2009**, *131*, 14043; k) K. T. Kamtekar, A. P. Monkman, M. R. Bryce, *Adv. Mater.* **2010**, *22*, 572.
- [13] S. Hirata, M. Vacha, *Adv. Opt. Mater.* **2017**, *5*, 1600996.
- [14] Y. Tao, K. Yuan, T. Chen, P. Xu, H. Li, R. Chen, C. Zheng, L. Zhang, W. Huang, *Adv. Mater.* **2014**, *26*, 7931.
- [15] Z. He, W. Zhao, J. W. Y. Lam, Q. Peng, H. Ma, G. Liang, Z. Shuai, B. Z. Tang, *Nat. Commun.* **2017**, *8*, 416.
- [16] L. Gu, H. Wu, H. Ma, W. Ye, W. Jia, H. Wang, H. Chen, N. Zhang, D. Wang, C. Qian, Z. An, W. Huang, Y. Zhao, *Nat. Commun.* **2020**, DOI: 10.1038/s41467-020-14792-1.
- [17] a) Y. Su, Y. Zhang, Z. Wang, W. Gao, P. Jia, D. Zhang, C. Yang, Y. Li, Y. L. Zhao, *Angew. Chem. Int. Ed.* **2019**, DOI: 10.1002/anie.201912102; b) Z. Wang, Y. Zhang, C. Wang, X. Zheng, Y. Zheng, L. Gao, C. Yang, Y. Li, L. Qu, Y. Zhao, *Adv. Mater.* **2020**, *32*, 1907355; c) H. Wu, W. Chi, Z. Chen, G. Liu, L. Gu, A. K. Bindra, G. Yang, X. Liu, Y. L. Zhao, *Adv. Funct. Mater.* **2019**, *29*, 1807243; d) Y. Su, S. Z. F. Phua, Y. Li, X. Zhou, D. Jana, G. Liu, W. Q. Lim, W. K. Ong, C. Yang, Y. L. Zhao, *Sci. Adv.* **2018**, *4*, eaas9732.

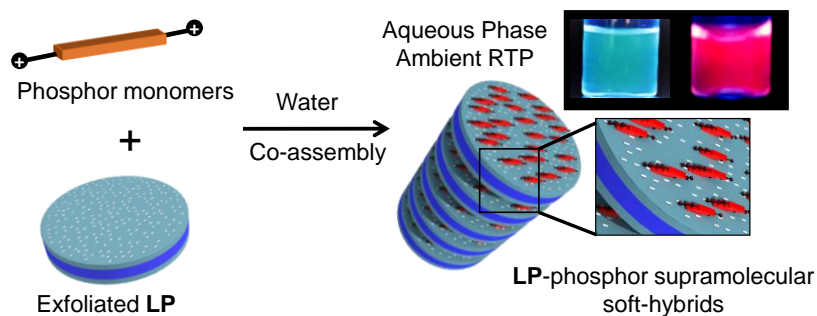
- [18] a) H. Thomas, D. L. Pastoetter, M. Gmelch, T. Achenbach, A. Schlögl, M. Louis, X. Feng, S. Reineke, *Adv. Mater.* **2020**, DOI: 10.1002/adma.202000880; b) L. Gu, H. Shi, L. Bian, M. Gu, K. Ling, X. Wang, H. Ma, S. Cai, W. Ning, L. Fu, H. Wang, S. Wang, Y. Gao, W. Yao, F. Huo, Y. Tao, Z. An, X. Liu, W. Huang, *Nat. Photonics* **2019**, *13*, 406.
- [19] P. L. dos Santos, J. S. Ward, D. G. Congrave, A. S. Batsanov, J. Eng, J. E. Stacey, T. J. Penfold, A. P. Monkman, M. R. Bryce, *Adv. Sci.* **2018**, *5*, 1700989.
- [20] G. N. Lewis, M. Kasha, *J. Am. Chem. Soc.* **1944**, *66*, 2100.
- [21] H. A. Al-Attar, A. P. Monkman, *Adv. Funct. Mater.* **2012**, *22*, 3824.
- [22] A. Ghosh, K. V. Rao, S. J. George, C. N. R. Rao, *Chem. Eur. J.* **2010**, *16*, 2.
- [23] F. Wang, X.-C. Li, W.-Y. Lai, Y. Chen, W. Huang, F. Wudl, *Org. Lett.* **2014**, *16*, 2942.

CHAPTER 4

Aqueous Phase and Ambient Room Temperature Phosphorescence via Supramolecular Self-assembly*

Abstract

Solution state room temperature phosphorescence (RTP) from purely organic chromophores is rarely achieved. In this Chapter, we showed remarkable stabilization of triplet excitons to obtain aqueous phase green and deep-red phosphorescence under fully ambient conditions by a unique supramolecular hybrid assembly between inorganic laponite (LP) clay and bromine (heavy-atom) containing aromatic carbonyl compounds. Structural rigidity and oxygen tolerance of the inorganic template along with controlled molecular organization via supramolecular scaffolding are envisaged to alleviate this unprecedented aqueous phase phosphorescence.



*Manuscripts based on this work have been published in *Angew. Chem. Int. Ed.* **2018**, 57, 17115 (hot paper) and *Mat. Res. Exp.* **2019**, 6, 124003.

4.1. Introduction

Room temperature phosphorescent materials based on purely organic molecules have attracted much attention recently as an alternative to expensive, rare and toxic metal based organometallic phosphors.^[1] However, most of the organic systems are not efficient phosphors as they are susceptible to vibrational and oxygen-mediated quenching of their triplets.^[2] This point thus also explains the fact that most efficient organic RTP have been reported in crystal state which minimizes the non-radiative quenching of triplet excitons by providing a rigid network and a barrier for oxygen diffusion.^[3] However it poses concerns over the solution processability of these phosphorescent materials for applications in display devices and sensors. In this respect, solution-processable organic RTP materials are more advantageous mainly because they generally do not need any specific molecular packing unlike the crystalline systems.^[4] With this objective, amorphous organic RTP materials have been recently designed by the incorporation of triplet-emitting phosphors into polymeric^[5] and cage-like hosts.^[6] In fact, in past couple of years, there has been a significant development in the area of solution-processed amorphous RTP materials and their successful translation into various optical sensing^[7] and even electroluminescent devices^[8] is particularly noteworthy. However, despite various examples of RTP in the crystalline and amorphous state, purely organic compounds showing RTP in solution state are still extremely rare^[9] mainly because of unmanageable vibrational and collisional quenching pathways available for the triplet deactivation.

A supramolecular scaffolding approach,^[10] with controlled and rigid organization of organic phosphors can be envisaged to be an efficient, alternative approach for the design of solution state RTP materials. In this respect, co-assembly of organic phosphors with an inorganic silicate template would be advantageous as latter's structural rigidity and nanoscale periodicity can lead to well-organized chromophores with limited diffusional motion of both the components to minimize the vibrational quenching of triplets in solution state.^[11] Further, oxygen tolerance of the inter-layer galleries of such organic-inorganic hybrids would be an added benefit to harvest phosphorescence even in presence of dissolved oxygen in the solvent.^[12] We envision that a supramolecular hybrid co-assembly approach between soluble organic and inorganic components in solution would also render soft-hybrids with processable or amorphous nature.^[13]

In this chapter, we showed an ambient red phosphorescence from a core-substituted naphthalene diimide (NDI) derivative (**BrNDI**, Figure 4.1), using a unique organic-inorganic supramolecular scaffolding approach. It is worthwhile to mention, our core-substituted naphthalene diimide (**BrNDI**) design is in line with previously studied organic phosphors having multiple carbonyl groups and heavy-atom (Br) substitution in their π -conjugated backbone, to

generate high triplet density by efficient intersystem crossing (ISC). In fact, an electrostatically driven co-assembly of **BrNDI** phosphor with a water soluble inorganic silicate based nanoplate (Laponite, **LP**) gives RTP both in solution and solution-processed, transparent thin films. Remarkably, by virtue of the oxygen barrier characteristics of the microenvironments in these supramolecular assemblies, an unprecedented stabilization of phosphorescence in aqueous solution is observed. Our preliminary studies on unsubstituted naphthalene diimides (**pNDI**) also helped us understanding the self-assembly process as well as the importance of the heavy-atom effect in order to obtain such remarkable ambient stable RTP from the brominated naphthalene diimide (**BrNDI**). Such a simple self-assembly strategy require more substrate scope to validate its extension to other molecular systems and promising for the development of novel “aqueous phase” optical sensors and bio-imaging probes with limited synthetic efforts.^[1c, 9c, 9d] Keeping this aspect in mind, we have also studied and successfully demonstrated a green-emitting aqueous phase RTP system (**BrPhS**) from a model bromoaldehyde compound, which has been already investigated in great detail as crystalline and amorphous state RTP emitter previously.^[3a, 14]

4.2. Design Strategy and Synthesis

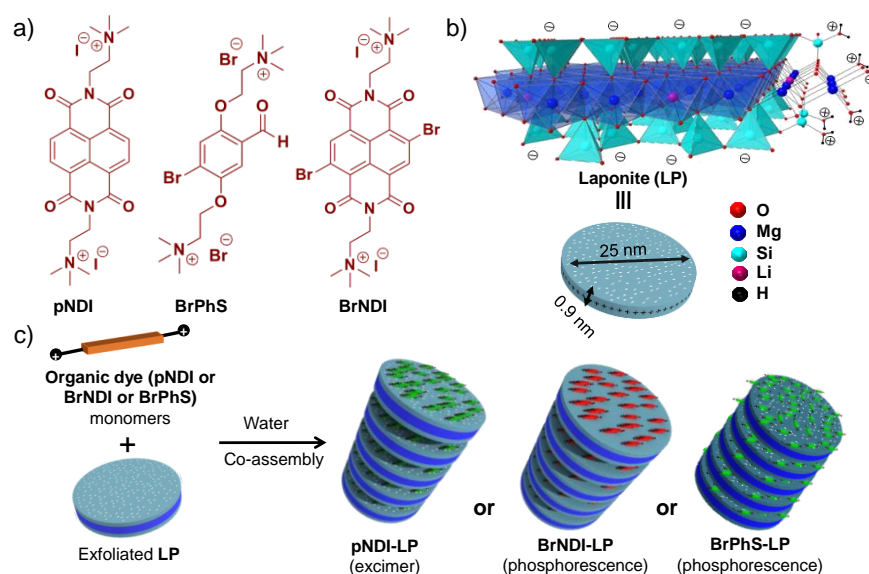


Figure 4.1. a) Molecular structures of **pNDI**, **BrPhS** and **BrNDI** and b) schematic diagram of Laponite (**LP**) structure. c) Schematic of the proposed ionic hybrid self-assembly of exfoliated **LP** nanoplates (by the wrapping of anionic polymer shown in blue color along the edges) and cationic chromophores in water.

The schematic representation and molecular structures of **LP** nanoparticles and the organic dyes are shown in Figure 4.1. In this work, we have used water soluble **LP** clay nanoplates as the inorganic scaffold, with monodisperse dimensions of 25 nm diameter and 0.9 nm thickness.^[15] These inorganic particles have a unique structure with orthogonally charged surfaces and edges, having negative and positive charges, respectively (Figure 4.1b). **LP** particles can be exfoliated in aqueous solutions by neutralizing the positively charged edges with anionic polymer such as sodium polyacrylate, which prevent the electrostatically driven “House of Cards” packing of LP particles.^[16] As a result, the negatively charged surface of **LP** can be used further for the electrostatic anchoring and co-assembly of complementary positively charged chromophores (Figure 4.1c).^[17] Hence in order to promote an ionic self-assembly both the phosphors (**BrNDI** and **BrPhS**) were functionalized with quaternary ammonium cation groups and synthesized in good yields (see Experimental Section). Another important feature of these chromophores include the presence of aromatic carbonyl groups and Br-atoms in the core which were envisioned to promote efficient ISC. It is worthwhile to mention that, NDI and its core-substituted derivatives have been well-studied for their remarkable fluorescence properties, their phosphorescence properties are rarely explored despite good ISC efficiencies in some derivatives.^[18] In this Chapter, we have also revisited the unsubstituted (parent) NDI derivative (studied previously in our group), **pNDI** and used as a model cationic system to investigate the hybrid co-assembly, whereas core-heavy atom (Br) substituted **BrNDI-LP** is designed to promote ISC and the subsequent stabilization of the triplets. On the other hand, the **BrPhS** has been studied to show the efficacy of our hybrid self-assembly approach as a generalized methodology for the development of future aqueous phase RTP systems.

4.3. Previous Work on **pNDI-LP** Self-assembly

4.3.1. Solution-state Self-assembly

Preliminary investigations on the hybrid co-assembly between **pNDI** and **LP** nanoplates and the resultant modulations in the molecular organization of NDI chromophores using spectroscopic and light scattering experiments were done previously, by Rao *et al.* in our laboratory.^[19] Detailed titrations were performed in water by increasing the concentration of **pNDI** from 0.1 mM to 5.0 mM at a constant weight percentage of **LP** (2.25 wt.%). With increasing concentration, a decrease in the intensity of **pNDI** monomer emission ($\lambda_{\text{max.}} = 430$ nm) with concomitant appearance of new broad emission centered at 510 nm is observed (Figure 4.2a). Time-resolved fluorescence decay profiles of this new emission showed a major long-lived component with a lifetime of 28.9 ns, characteristic of excimer formation between NDI chromophores (Figure 4.2b).^[20] Further, the excitation spectra collected at 510 nm showed a 20

nm red-shifted peak at 398 nm with respect to the monomer absorption ($\lambda_{\max} = 378$ nm), suggesting that excimer-like emission is originated from the assembled chromophores in the ground state (Figure 4.2a and 4.2c).^[21] These results indicate the pre-organization of NDI chromophores in a J-type slipped manner templated by the inorganic LP scaffold. Zeta potential and Dynamic Light Scattering (DLS) studies showed that, negative charge on LP particles decreases along with simultaneous increase in the hydrodynamic radius, when the concentration of pNDI is increased in the hybrids (Figure 4.2d), signifying an extended hybrid co-assembly of LP and chromophores directed by electrostatic interactions. Formation of extended assembly is further evident from the hydrogel formation at high concentrations (>3.0 mM, inset, Figure 4.2a).

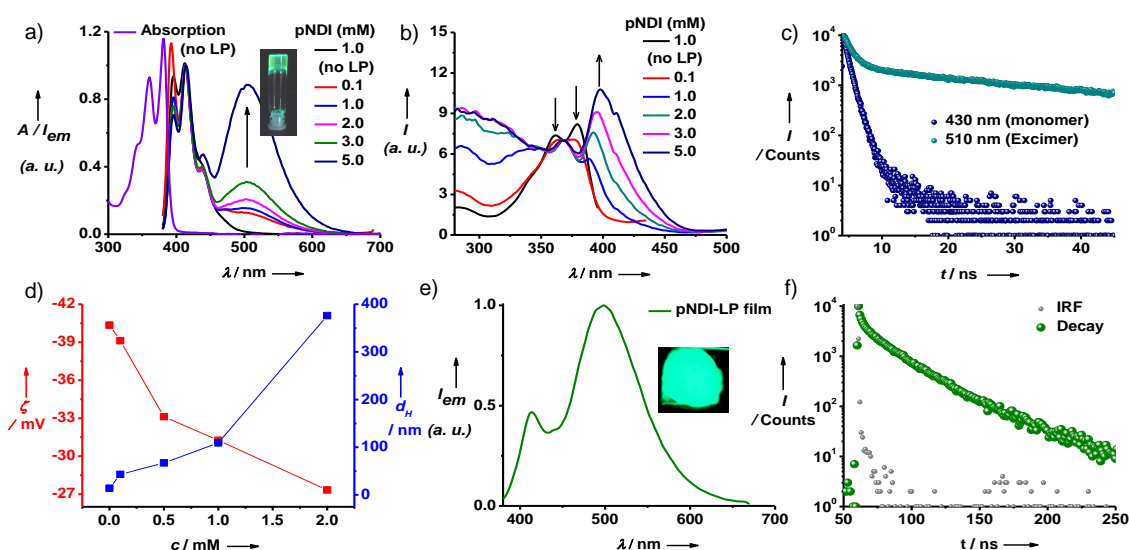


Figure 4.2. Normalized a) absorption, emission and b) excitation spectra of pNDI-LP hybrids (LP = 2.25 wt. %, $\lambda_{exc.} = 365$ nm) in solution. c) Fluorescence lifetime profiles of pNDI-LP hybrids monitored at monomer (430 nm) and excimer wavelengths (510 nm) in water ($[pNDI] = 1.0$ mM, LP = 2.25 wt. %, $\lambda_{exc.} = 373$ nm). d) Zeta potential and DLS measurements of pNDI-LP hybrids in water during the titration (LP = 2.25 wt. %). e) Normalized emission ($\lambda_{exc.} = 365$ nm) and f) corresponding fluorescence decays ($\lambda_{exc.} = 405$ nm, $\lambda_{monitored} = 500$ nm) in film state. Inset of a) and e) shows the photographs of pNDI-LP hybrids in the gel state and film state, respectively, under 365 nm UV irradiation ($[pNDI] = 5.0$ mM).

4.3.2. Excimer Fluorescence in Solid-state Thin-films

Solutions and hydrogels of pNDI-LP hybrids could also be transferred onto glass substrates without affecting the molecular organization as evident from the J-aggregated spectral features and excimer emission retained in the film state. The emission spectrum of film made

from **pNDI-LP** hybrid hydrogel (5.0 mM-**pNDI**) showed major amount of excimer emission at 500 nm with a lifetime of 25.3 ns (Figure 4.2e and 4.2f). These films are highly transparent and showed more than 99 % transmittance above 550 nm where these dyes do not have an absorbance (Figure 4.3a). This validates the efficient supramolecular scaffolding of the chromophores by the **LP** templates and also the excellent solution processability of these hybrids with homogeneous organization.

4.3.3. Morphology Studies

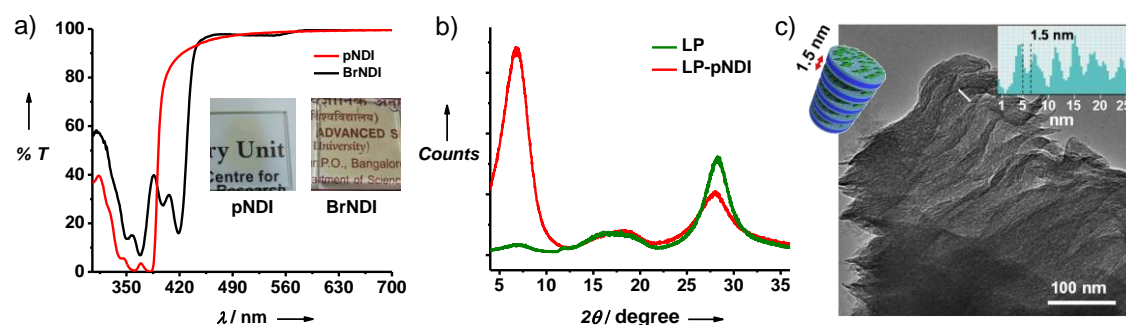


Figure 4.3. a) Transmittance spectra of **pNDI** and **BrNDI-LP**-hybrid thin films. Inset: Photographs of thin films under daylight. ($[pNDI] = 5.0 \text{ mM}$, $[BrNDI] = 1.0 \text{ mM}$, 2.25 wt. % **LP**). b) PXRD pattern of films made from 5.0 mM **pNDI-LP** hybrids along with blank **LP** (**LP** = 2.25 wt. %). c) TEM image of **pNDI-LP** xerogels ($[pNDI] = 5.0 \text{ mM}$, **LP** = 2.25 wt. %) and inset shows the electron density profile of the white line.

Powder X-ray diffraction (PXRD) pattern of the **LP** film showed two peaks at 17° and 28° characteristic of the crystalline lattice planes of **LP** particle. Absence of any peak at the low angle region in the PXRD pattern ruled out the stacking of **LP** particles at this concentration. Remarkably, a strong low angle peak ($2\theta = 6.4^\circ$) corresponding to a d-spacing of $\sim 1.4 \text{ nm}$ was observed for the **pNDI-LP** hybrid films suggesting an extended organization by the alternating co-assembly of **LP** templates and **pNDI** linkers via electrostatic interactions (Figure 4.3b). Since the observed d-spacing is less than that expected from **pNDI** with a molecular dimension of 1.48 nm and **LP** particles with 0.9 nm thickness, we envisage a tilted slipped stacking of the chromophores in the interlayer galleries. The extended organization is further supported by transmission electron microscopy (TEM) of the corresponding hybrid xerogels, which showed nanoscale striations with alternating bright and dark contrasts due to the organic-inorganic layered co-stacking (Figure 4.3c).

4.4. Time-dependent Density Functional Theory Calculations to Understand the Implication of Heavy-atom Effect

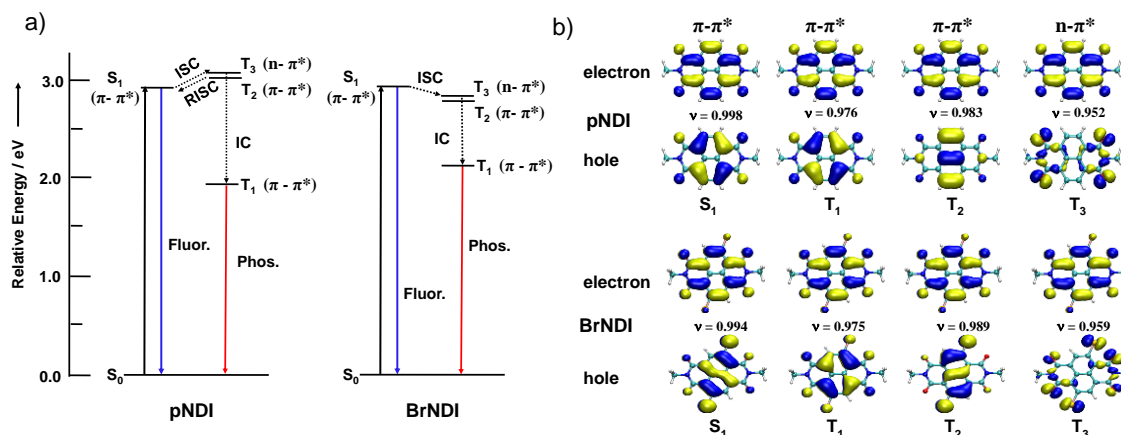


Figure 4.4. a) Jablonski diagram for **pNDI** and **BrNDI** (T_1 -, T_2 - and T_3 -state energies are calculated using T_1 -state optimized geometry) and b) natural transition orbitals (NTOs) calculated using TD-B3LYP/6-31+g(d) level of theory.

Inspired by the organization of **pNDI** chromophores by the the LP nanoplates, we have further attempted the triplet state stabilization using similar approach. However, to harness triplet excitons, an efficient ISC is crucial and internal heavy atom effect is considered to be the most viable strategy to achieve the same.^[1,3a,4a] Hence **pNDI** design is modified to **BrNDI**, with two Br as the heavy atoms substituted at the core. Time-dependent density functional theory (TDDFT) calculations using B3LYP exchange-correlation functional were performed to get a qualitative understanding on the ISC efficiency of **pNDI** and **BrNDI** molecules (Figures 4.4). The ISC rate is determined by the spin-orbit coupling (SOC) strength, whose quantitative estimate can be obtained by calculating the SOC matrix element (SOCME) between S_1 and T_n states. The main contributing channel for ISC is found to be S_1 (π - π^*) to T_3 (n - π^*) in both the molecules and this corroborates with the El Sayed's rule, which forbids SOC between S_1 (π - π^*) and T_1 (π - π^*)/ T_2 (π - π^*) states.^[22] Accordingly, for **BrNDI** (**pNDI**) the SOCME between T_1 and T_2 with S_1 are found to be 0.12 (0.00) cm^{-1} and 0.06 (0.01) cm^{-1} , respectively. The SOCME between T_3 and S_1 is higher in **BrNDI** (21.03 cm^{-1}) compared to **pNDI** (0.15 cm^{-1}) owing to the presence of heavy Br atoms in the former. Strong SOC in **BrNDI** not only leads to faster ISC to improve the triplet yield, but also allows the spin-forbidden $T_1 \rightarrow S_0$ transition to facilitate room temperature phosphorescence, provided other non-radiative pathways are minimized.

4.5. Aqueous and Amorphous Phase RTP from BrNDI-LP hybrids

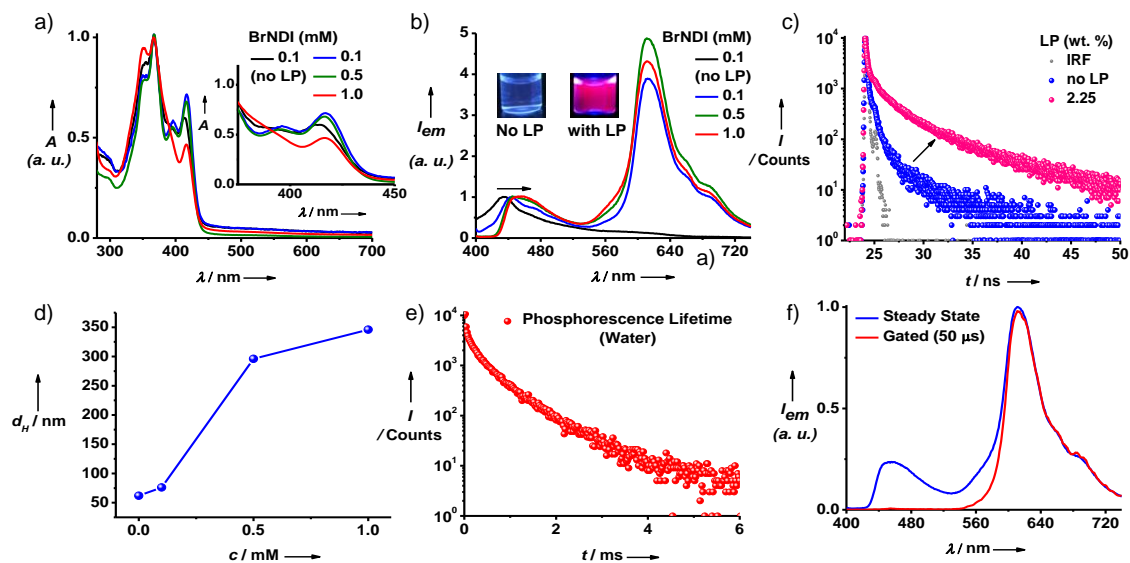


Figure 4.5. Aqueous Phase RTP from **BrNDI-LP** hybrids. a) Normalized absorption and b) emission spectra of different concentrations of **BrNDI-LP** hybrids in water ($\lambda_{exc} = 380$ nm, **LP** = 2.25 wt. %). Inset of (a) shows zoomed version showing the red-shift in **LP**-hybrid samples. Inset of (b) shows the photographs of **BrNDI-LP** hybrids under 365 nm UV irradiation. c) Fluorescence decay profiles of **BrNDI** with different wt. % of **LP** ($[BrNDI] = 0.1$ mM, $\lambda_{monitored} = 437$ nm for sample without **LP** and $\lambda_{monitored} = 475$ nm for **LP**-hybrids in water, $\lambda_{exc.} = 373$ nm) showing gradual increase in fluorescence lifetime suggesting J-aggregation. d) DLS profile of different concentrations of **BrNDI** hybrids with 2.25 wt. % **LP** in water. e) Phosphorescence lifetime profile, f) steady state and gated emission spectra of **BrNDI-LP** hybrids in water ($[BrNDI] = 1.0$ mM, **LP** = 2.25 wt. %, $\lambda_{exc.} = 380$ nm, $\lambda_{monitored} = 615$ nm, delay time = 50 μ s).

In an attempt to harness the triplets of **BrNDI** as ambient phosphorescence, supramolecular hybrids with **LP** was synthesized similar to **pNDI** (*vide supra*). Owing to the increased hydrophobicity of Br substituted NDI core, the solubility of **BrNDI** decreases and hence its photophysical properties could not be explored beyond 1.0 mM concentration. Red-shift in the absorption (411 nm to 418 nm) and fluorescence (437 nm to 445 nm) spectra with increased fluorescence lifetime of **BrNDI** on interaction with **LP** suggests the J-aggregation of chromophores similar to **pNDI** molecules (Figure 4.5 a-c). Corresponding increase in the DLS signifies the extended hybrid co-assembly (Figure 4.5 d). Interestingly, a new emission band with a maximum at 613 nm was observed in these **BrNDI-LP** hybrid assemblies (**LP** = 2.25 wt. %) (Figure 4.5b). Average lifetime of the new red-shifted emission was found to be 347 μ s compared to the short lifetime of 0.34 ns corresponding to the monomer fluorescence, suggesting the phosphorescence nature of the emission (Figure 4.5c, 4.5e and 4.5f). We envisage that reduced

vibrational motions and less oxygen content provided by the supramolecular microenvironments in the organic-inorganic hybrid galleries facilitate the triplet emission even in water. To the best of our knowledge this is the first report of an aqueous state stabilized RT red phosphorescence under ambient conditions with high lifetime.^[23] Remarkably, corresponding solution processed hybrid films showed enhanced room temperature phosphorescence emission ($\Phi_P = 3.5\%$) with a lifetime of 523 μs and corresponding fluorescence emission is significantly quenched as evident from the gated spectrum with a time delay of 50 μs (Figures 4.6a and 4.6b). Increased phosphorescence intensity with enhanced lifetime under vacuum and at lower temperatures further proves the triplet character of the emission (Figure 4.6c and 4.6d).

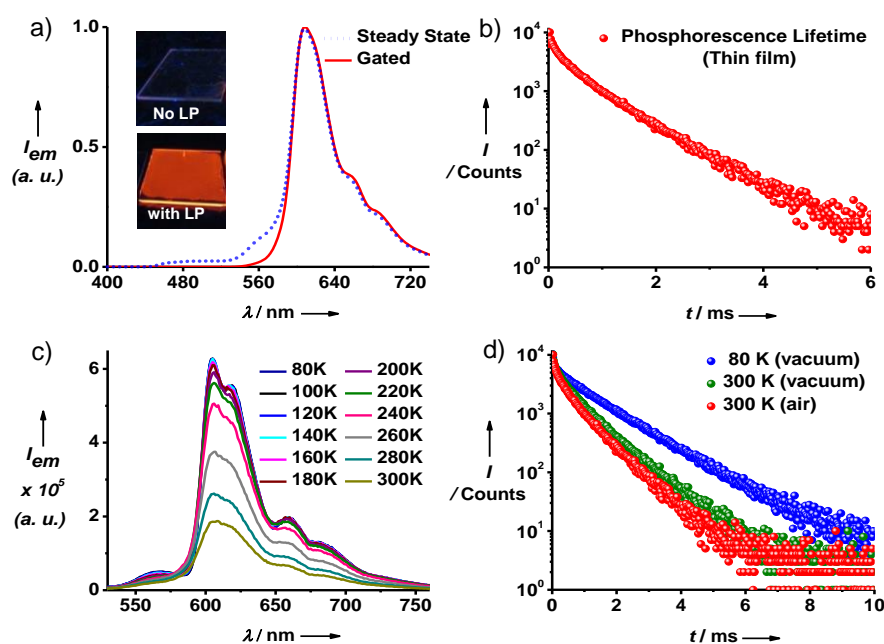


Figure 4.6. Amorphous state RTP emission from **BrNDI-LP** hybrid films. a) Steady state and gated emission spectra (delay time = 50 μs). Inset: Photograph of the corresponding neat and **BrNDI-LP** hybrid films under 365 nm UV-lamp. b) Phosphorescence decay spectra of the **BrNDI-LP** hybrid film in air. Temperature dependent c) emission and d) phosphorescence decay profile of **BrNDI-LP** hybrid film showing increased intensity at low temperature and under vacuum. (In all cases, [**BrNDI**] = 1.0 mM, **LP** = 2.25 wt. %, $\lambda_{exc.} = 380\text{ nm}$, $\lambda_{monitored} = 615\text{ nm}$).

4.6. Role of Anion- π Charge-transfer States on the ISC Process

In order to explain the remarkable stabilization of triplets in aqueous and ambient conditions by the supramolecular scaffolding strategy we further investigated the spectroscopic properties in detail. A closer look at the absorption spectra of the **BrNDI** and **BrNDI-LP** hybrids in solution showed a weak, broad absorption in the 450-580 nm range apart from the high energy locally excited transitions (inset, Figure 4.5a and Figure 4.7a).^[24] These spectral features are

characteristic of the charge-transfer (CT) interaction between iodide counter anion and NDI core, as reported for anion- π complexes of electron deficient NDIs with externally introduced anions.^[25] Interestingly, selective excitation of this red-shifted absorption band at 480 nm of both **BrNDI** and its **LP** hybrids show an emission with maxima at 580 nm (Figure 4.7b-e). High lifetime (4.75 ns) of this new emission band and the excitation spectra (collected at 625 nm) hints towards an anion- π induced CT emission,^[26] although it is rarely explored in NDI systems (Figure 4.7f and Figure 4.8b). Presence of CT interaction between NDI core and the counter iodide ions is further supported by TDDFT calculations where NTO (natural transition orbital) analysis

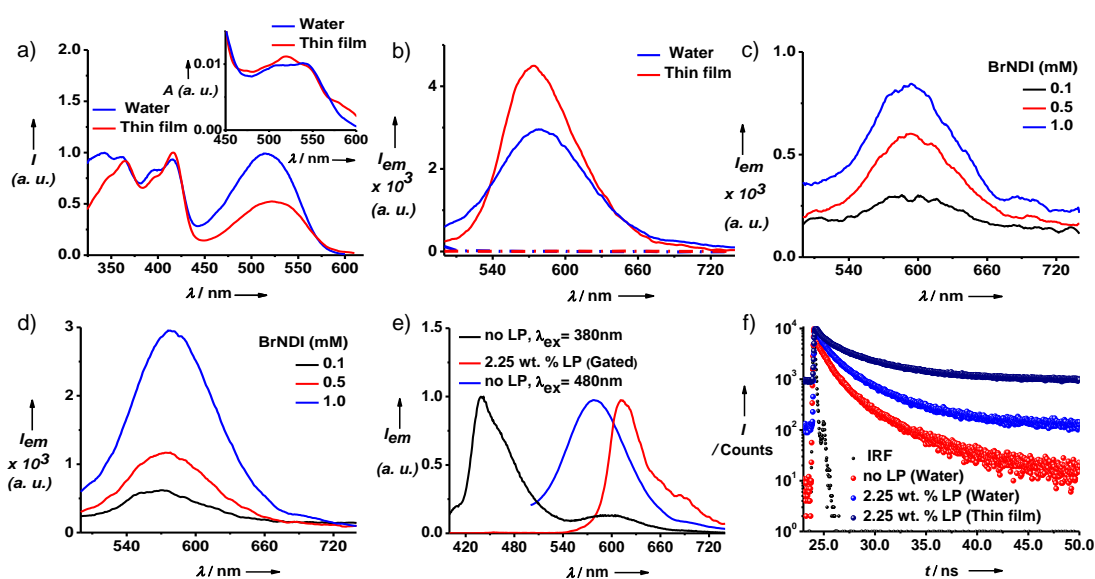


Figure 4.7. Anion- π charge-transfer (CT) emission. a) Excitation spectra (monitored at 625 nm) of **BrNDI-LP** hybrids in water and thin film ($[\text{BrNDI}] = 1.0 \text{ mM}$, **LP** = 2.25 wt. %). Inset : Corresponding absorption spectra showing anion- π CT absorption. b) Steady state emission spectra of **BrNDI-LP** hybrids in water and thin film by exciting at the CT band and dotted lines shows corresponding gated emission spectra, suggesting no phosphorescence component ($[\text{BrNDI}] = 1.0 \text{ mM}$, **LP** = 2.25 wt. %, $\lambda_{\text{exc.}} = 480 \text{ nm}$, delay time = 50 μs). Emission spectra of different concentrations of **BrNDI** c) without and d) with 2.25 wt. % **LP** while excited at CT absorption wavelength ($\lambda_{\text{exc.}} = 480 \text{ nm}$). e) Overlaying normalized emission spectra depicting three different types of emission in **BrNDI**: Locally excited fluorescence ($\lambda_{\text{exc.}} = 380 \text{ nm}$, black curve, a tail at 540-680 nm region corresponds to the anion- π charge-transfer emission), charge-transfer fluorescence ($\lambda_{\text{exc.}} = 480 \text{ nm}$, blue curve) and phosphorescence ($\lambda_{\text{exc.}} = 380 \text{ nm}$, red curve, this gated emission (delay time = 50 μs) differentiates between all fluorescence bands. ($[\text{BrNDI}] = 1.0 \text{ mM}$, **LP** = 2.25 wt. %). d) Lifetime spectra of CT emission in **BrNDI** and **BrNDI-LP** hybrids in water and thin film ($\lambda_{\text{exc.}} = 373 \text{ nm}$,^[27] $\lambda_{\text{monitored}} = 580 \text{ nm}$, ($[\text{BrNDI}] = 1.0 \text{ mM}$, **LP** = 2.25 wt. %).

shows a CT transition between counter anion (donor) and NDI core (acceptor) (Figure 4.8a). Since CT states are known to play important role in promoting the ISC process we further explored this aspect.^[26, 28] In order to resolve the contributions of overlapping anion- π mediated CT and phosphorescence emissions, we have performed gated excitation spectra at 625 nm (Figures 4.7e and 4.8c). Although steady state excitation spectra of the hybrids collected at 625 nm in solution and film states showed a strong band corresponding to this CT absorption in the 450-580 nm range, a gated excitation spectra (50 μ s delay-time) did not show any CT absorption; instead showed only peaks corresponding to the locally excited NDI absorption (Figure 4.7a, 4.8b and 4.8c). In addition, no phosphorescence emission was observed when the CT band is selectively excited at 480 nm, thus ruling out a CT mediated ISC (Figure 4.7b). Moreover, exchanging the iodide counter anions with BF_4^- does not affect the phosphorescence of the resulting **BrNDI-BF₄-LP** hybrids, further suggesting the absence of external heavy atom effect from the counter ions and CT mediated triplet emission in our system (Figure 4.8d-f). On the

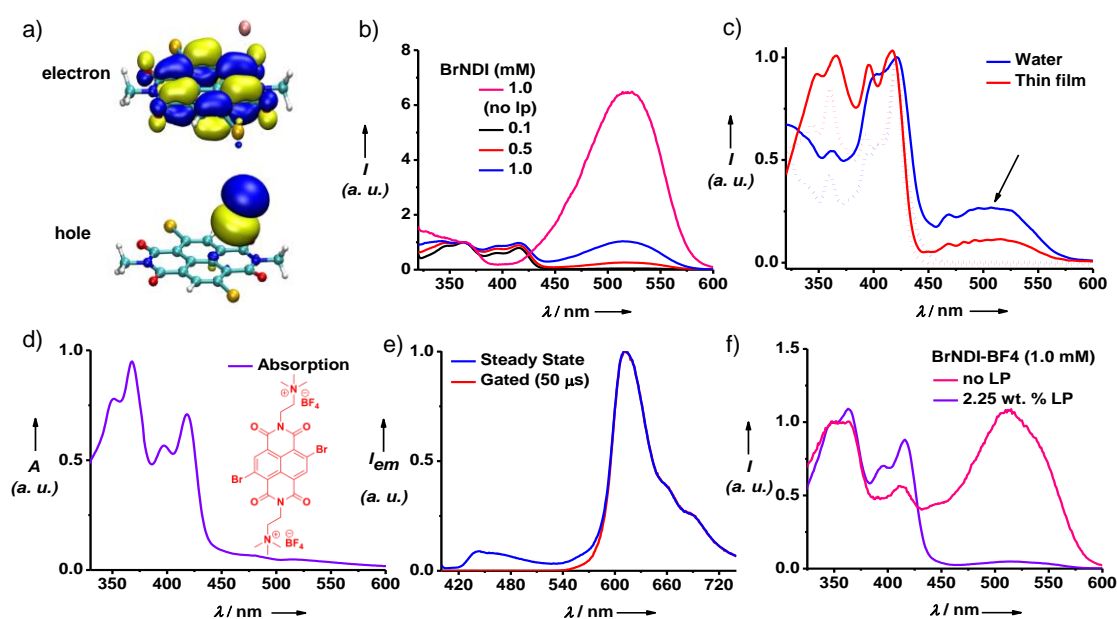


Figure 4.8. a) Natural transition orbitals (NTOs) of dibromo NDI and iodide complex, calculated using TD-CAM-B3LYP/6-31+g(d) level of theory. Effect of CT-states on the ISC process. b) Normalized excitation spectra of different concentrations of **BrNDI** (LP = 2.25 wt. %, $\lambda_{monitored}$ = 625 nm) in water. c) Normalized steady state and corresponding gated excitation spectra (showed in dotted lines) of **BrNDI-LP** hybrids in water and thin film (LP = 2.25 wt. %, $\lambda_{monitored}$ = 625 nm, delay time = 50 μ s). Control experiments on **BrNDI-BF₄** with LP: d) Absorption, e) normalized steady state and gated emission (λ_{exc} = 380 nm, delay time = 50 μ s), c) excitation ($\lambda_{monitored}$ = 625 nm) spectra of 0.1 mM **BrNDI-BF₄-LP** hybrids. (LP = 2.25 wt. %). Inset of (d) shows the molecular structure of **BrNDI-BF₄**.

other hand, titration of **BrNDI** (0.1 mM) with **LP** showed an increased aggregation of the chromophore with concomitant increase in the phosphorescence intensity, which hints toward the role of aggregation in fostering ISC efficiency and phosphorescence, as shown previously in the case of H-aggregated RTP crystals (Figure 4.9).^[3c,f]

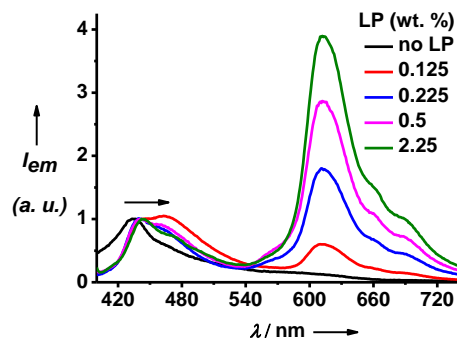


Figure 4.9. Emission spectra of **BrNDI** with increasing wt. % of **LP** in water. ($[\text{BrNDI}] = 1.0 \text{ mM}$, $\lambda_{\text{exc.}} = 380 \text{ nm}$).

The unique features of the supramolecular RTP system as outlined above, is highlighted by its excellent air-stability, easy-scalability and the robustness. However, more examples are needed to validate the versatility of this approach. With this objective in mind, in the next section we studied a very simple bromoaldehyde derivative, **BrPhS** (Figure 4.1). As has been explained in Chapter 1, bromoaldehyde functionalized chromophores are considered as the simplest design for ambient RTP materials, because of the presence of a carbonyl group (envisaged to produce excited state molecular orbital configurations that follow El-Sayed's rule) and an additional bromine group that would accelerate the ISC further. In fact, the initial breakthroughs on ambient RTP systems pioneered by Kim *et al.*^[3a, 14] as well as Tang *et al.*^[3a,3d], were in principle, utilized this scaffold and therefore envisioned as highly suitable for our current objective. However, we modified the side-chain of a previously studied molecules by Kim *et al.*^[3a, 14], to make the system water-soluble for the ionic co-assembly with the host laponite (**LP**). The detailed photophysical studies and a successful demonstration of aqueous phase green-RTP of **BrPhS-LP** hybrids are outlined in the next section.

4.7. Aqueous Phase and Amorphous-state RTP of BrPhS via Self-assembly

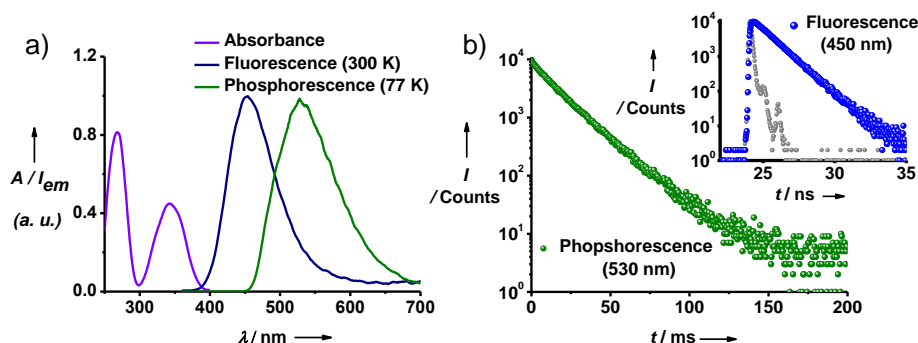


Figure 4.10. a) Absorption spectrum along with the normalized fluorescence (at 300 K in water) and phosphorescence spectra (at 77 K in acetonitrile) of **BrPhS**. ($[\text{BrPhS}] = 0.1 \text{ mM}$, $\lambda_{exc.} = 350 \text{ nm}$, delay time = 10 ms for phosphorescence measurement). b) Phosphorescence decay of 0.1 mM **BrPhS** in acetonitrile at 77 K ($\lambda_{exc.} = 350 \text{ nm}$, $\lambda_{monitored} = 530 \text{ nm}$, average lifetime = 14.3 ms). Inset shows the fluorescence decay profile of 0.1 mM **BrPhS** (without LP, $\lambda_{monitored} = 450 \text{ nm}$, $\lambda_{exc.} = 373 \text{ nm}$) in water.

BrPhS (0.1 mM) absorbs in the 250-400 nm region with absorption maxima at 268 nm (π - π^*) and 346 nm (π - π^*) in water^[29], characteristic of similar benzaldehyde type chromophores (Figure 4.10a). It also shows fluorescence with a maximum at 450 nm ($\lambda_{exc.} = 350 \text{ nm}$), though no phosphorescence is observed under ambient conditions in water (Figure 4.10a). Phosphorescence of **BrPhS**, however, could be realized by minimizing the non-radiative pathways ($\lambda_{exc.} = 350 \text{ nm}$, $\lambda_{max.} = 530 \text{ nm}$), in frozen acetonitrile solution at 77 K (Figure 4.10a). The phosphorescence nature at 77 K is supported by high average lifetime ($\tau_{avg.} = 14.3 \text{ ms}$, $\lambda_{exc.} = 350 \text{ nm}$, $\lambda_{monitored} = 530 \text{ nm}$) as compared to fluorescence lifetime obtained in water ($\tau_{avg.} = 1.1 \text{ ns}$, $\lambda_{exc.} = 373 \text{ nm}$, $\lambda_{monitored} = 450 \text{ nm}$) (Figure 4.10b). Thus, to harvest triplets under ambient conditions, **BrPhS** (0.1 mM) was first anchored with a fixed amount of LP (2.25 wt %) in water (Figure 4.11). Interestingly, we observed appearance of a new red-shifted emission band ($\lambda_{max.} = 510 \text{ nm}$) along with the lifetime of 4.5 ms ($\lambda_{monitored} = 530 \text{ nm}$) hinting towards phosphorescence emission whereas the lower wavelength band showed much shorter lifetime in the nanosecond scale ($\lambda_{monitored} = 450 \text{ nm}$, $\tau_{avg.} = 0.9 \text{ ns}$) ascribing to its fluorescence nature (Figure 4.11a and 4.11b, inset). The phosphorescence nature was further characterized by time-gated emission (delay time = 1 ms) which resembles closely with the low-temperature phosphorescence band of 0.1 mM **BrPhS** taken in acetonitrile at 77 K (Figure 4.10a and Figure 4.11c). To get a further insight into the photophysical properties of **BrPhS** in presence of LP, titrations

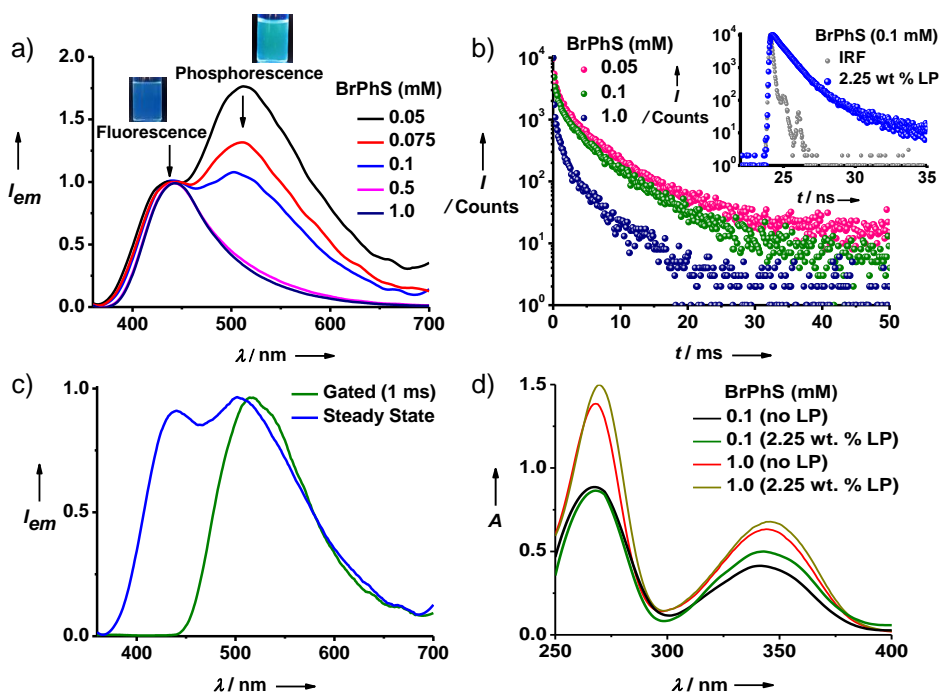


Figure 4.11. a) Normalized emission of **BrPhS-LP** hybrids in water. Inset of (a) show green phosphorescence in aqueous solution in presence of **LP** (right) and only blue fluorescence without **LP** (left), under 365 nm UV illumination. b) Time-resolved phosphorescence decay profiles of **BrPhS-LP** hybrids with different concentrations of **BrPhS** monitored at 530 nm. Inset shows the fluorescence decay profile of 0.1 mM **BrPhS-LP** hybrid monitored at 450 nm ($\lambda_{exc.} = 373$ nm) in water. c) Steady-state and gated emission spectra of 0.1 mM **BrPhS-LP** solution (delay time = 1 ms). d) Absorption spectra of **BrPhS** with and without **LP** at different concentrations. In all cases, $\lambda_{exc.} = 350$ nm and 2.25 wt % **LP** was used unless otherwise mentioned.

were performed by varying the concentration of **BrPhS** from 0.05 mM to 1.0 mM at a fixed weight percentage (2.25 wt %) of exfoliated laponite nanoparticles in water (Figure 4.11a). We observed a gradual decrease in phosphorescence intensity as well as the corresponding lifetime with increasing concentration of **BrPhS** (Figure 4.11a and 4.11b). Decrease in RTP intensity could be due to the non-emissive excimer formation^[3a] between the phosphors at higher concentration range (> 0.1 mM). We could not observe any spectral changes characteristic of inter-chromophoric interactions as observed for dicationic naphthalene diimide derivatives (**pNDI** and **BrNDI**) with large hydrophobic π -conjugated cores as has been seen in the previous section (Figure 4.11d).

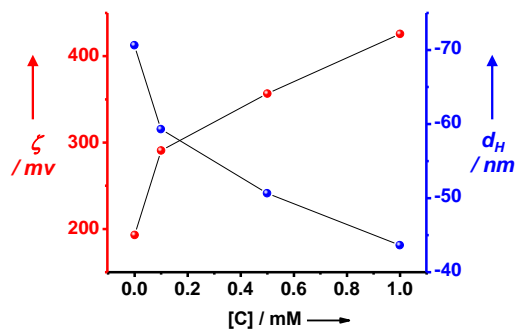


Figure 4.12. Zeta potential and DLS profile of different concentrations of **BrPhS** with 2.25 wt. % **LP** hybrids in water.

Furthermore, zeta potential and dynamic light scattering (DLS) experiments showed gradual decrease of negative charge on the **LP** surface with increasing concentrations of **BrPhS** with concomitant increase in hydrodynamic radius of the particles (Figure 4.12). This observation is a clear indication of extended electrostatic co-assembly between the **LP** particles and **BrPhS**, particularly important for creating a unique supramolecular microenvironment suitable for limited oxygen diffusion and enhanced triplet stability, resulting in efficient aqueous phase phosphorescence under ambient conditions (*vide infra*). It was remarkable to observe that phosphorescence features were retained in the **BrPhS-LP** hybrid thin films, with good quantum yield (3.1 %) and average lifetime (2.03 ms) in air, when the solutions were drop-casted on a glass substrate and dried completely (see Experimental Section, Figure 4.13). As has been seen in case of **BrNDI**, the unique solution-processability of the **BrPhS-LP** soft hybrids is reproduced in this system also, a property most of the ambient organic phosphor materials lack. On the other hand, the neat thin films of **BrPhS** showed only very weak fluorescence without any trace of phosphorescence reiterating the importance of scaffolding provided by inorganic **LP** particles (Figure 4.13a, inset).

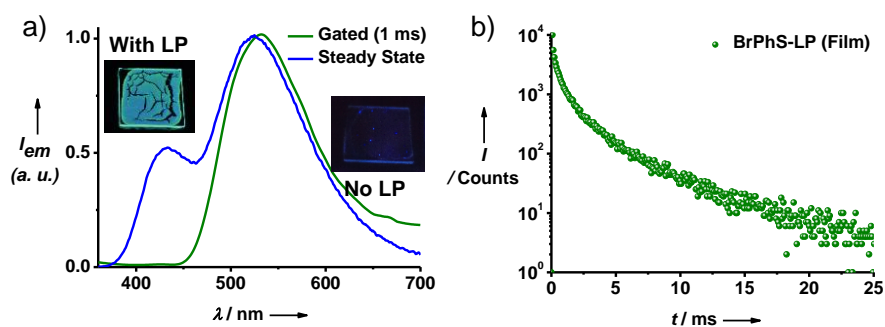


Figure 4.13. a) Steady-state and gated emission and b) phosphorescence decay profile of **BrPhS-LP** hybrid in thin film ($[\text{BrPhS}] = 5 \text{ mM}$, $\text{LP} = 2.25 \text{ wt } \%$, $\lambda_{\text{exc.}} = 350 \text{ nm}$, $\lambda_{\text{monitored}} = 530 \text{ nm}$, delay time = 1 ms). Inset of (a) shows the photograph of dried hybrid thin film under 365 nm UV excitation.

4.8. Conclusions

In conclusion, we have demonstrated a unique organic-inorganic hybrid self-assembly for the controlled molecular organization of chromophores. In the case of **pNDI** without heavy atom substitution, pre-organization of chromophores results in green excimer-like emission. On the other hand, **BrNDI** hybrids showed red-emitting RT phosphorescence as a result of heavy atom effect. The structural rigidity and oxygen tolerance of the inorganic clay particles further minimize the molecular vibrations and triplet quenching of organic phosphors, which in turn stabilizes the phosphorescence in solution phase (water) and films under ambient conditions. Red emitting phosphors with visible light excitation and ambient stability in water are seldom reported and would be of potential use in bio-imaging and sensors. Further, the generalization of our self-assembly approach towards designing aqueous phase RTP systems is exemplified by demonstrating a commonly used bromoaldehyde based green-RTP emitter, **BrPhS**. We also envision, this strategy will provide great success in controlling molecular organization of organic phosphor molecules for long-afterglow in water which has been achieved primarily in crystalline state so far.

4.9. Experimental Section

4.9.1. General Methods

NMR Measurements: ^1H and ^{13}C NMR spectra were recorded on a BRUKER AVANCE-400 fourier transformation spectrometer with 400 and 100 MHz respectively. The spectra are calibrated with respect to the residual solvent peaks. The chemical shifts are reported in parts per million (ppm) with respect to TMS. Short notations used are, s for singlet, d for doublet, t for triplet, q for quartet and m for multiplet.

Optical Measurements: Electronic absorption spectra were recorded on a Perkin Elmer Lambda 900 UV-Vis-NIR Spectrometer and emission spectra were recorded at FLS1000 spectrometer, Edinburgh Instruments. UV-Vis and emission spectra were recorded in 1 mm path length cuvette. Fluorescence spectra of solutions, gels and films were recorded in front-face geometry to avoid self-absorption at high concentrations.

Lifetime and quantum yield measurements: Fluorescence lifetimes were performed on a Horiba Delta Flex time-correlated single-photon-counting (TCSPC) instrument. A 373 nm nano-LED with a pulse repetition rate of 1 MHz was used as the light source. The instrument response function (IRF) was collected by using a scatterer (Ludox AS40 colloidal silica, Sigma-Aldrich). Phosphorescence lifetime ($\lambda_{\text{exc.}} = 380 \text{ nm}$ or 350 nm) and gated emission was measured on FLSP920 spectrometer, Edinburgh Instruments equipped with a micro flash lamp (μF2) set-up.

Quantum yield was measured using an integrated sphere equipped either with a CCD spectrometer by Edmund Optics (BrNDI) or in the same FLS1000 instrument (BrPhS).

Dynamic Light Scattering (DLS): DLS and Zeta potential measurements were carried out using a NanoZS (Malvern UK) employing a 532 nm laser at a back scattering angle of 173°.

Transmission Electron Microscopy (TEM): TEM measurements were performed on a JEOL, JEM 3010 operated at 300 kV. Samples were prepared by placing a drop of the gels on carbon coated copper grids followed by drying at room temperature.

Powder X-Ray Diffraction (PXRD): Powder XRD pattern of the compounds were recorded by in Bruker D8 Discover (40 kV, 30 Ma) instrument using Cu K α radiation ($2\theta = 0.8\text{--}35^\circ$).

High Resolution Mass Spectroscopy (HRMS): HR-MS was carried out using Agilent Technologies 6538 UHD Accurate-Mass Q-TOFLC/MS.

Computational Details: Ground state (S_0) geometries of **pNDI** and **BrNDI** were optimized using density functional theory (DFT) and the electronic absorption spectra was calculated using time-dependent DFT (TDDFT) methods as implemented in the Gaussian 16 software.^[30] All calculations were performed employing B3LYP^[31-33] exchange-correlation functional with 6-31+g(d) basis set for all atoms except Br, for which LANL2DZ basis set along with the corresponding ECP was used. Frequency calculations were performed to confirm the absence of any unstable normal mode. The solvent (water) effects were taken into account by polarized continuum model (PCM) using the integral equation formalism variant (IEFPCM).^[34] The extended alkyl chain attached to the imide N atoms are replaced by methyl groups, which does not impose any change in the electronic structure of the NDI core. The first excited singlet (S_1) state were optimized at the TDDFT level of theory, while the triplet excited state geometries were optimized at the TDDFT level within the Tamm-Dancoff approximation (TDA) which overcomes the triplet instability issue.^[35] The spin-orbit coupling (SOC) was considered as perturbation based on the scalar relativistic Kohn-Sham orbitals after SCF and TDDFT calculations.^[36-38] SOC matrix elements (SOCME) were calculated using B3LYP with TZP basis set for all atoms as implemented in ADF package.^[39]

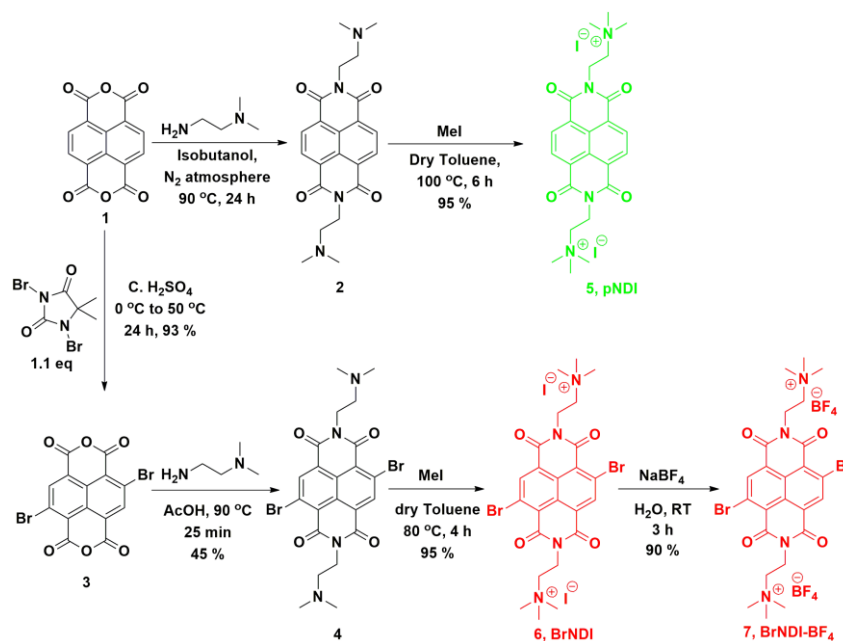
4.9.2. Protocol of Sample Preparation: First a stock solution was prepared by suspending 360 mg of **LP** in 9 ml Millipore distilled water (4 wt. %) under intense sonication followed by treating the suspension with 12 mg of sodium polyacrylate. Further 2.25 wt. % samples were prepared from this 4 wt. % stock solution and required amount of **pNDI** and **BrNDI** aqueous solutions were added to it and sonicated for 5 minutes to get clear **dye-LP** hybrid solution. For **pNDI-LP** gels, required amount of **pNDI** (>3 mM) solid samples were added into 2.25 wt. % **LP** solution and sonicated for 10 minutes. On standing for 30 minutes these samples turned into transparent

hydrogels. For thin film preparation, these solution or gel hybrids were drop casted on clean glass substrates and dried under vacuum overnight at 50 °C.

4.9.3. Synthetic Schemes and Procedures

The synthesis of **pNDI** and **BrNDI** is shown in Scheme 4.1.

Materials: Naphthalene dianhydride and 1,1-dimethyl-3,3-dibromohydantoin (DBH) were purchased from Sigma-Aldrich; N,N dimethyl ethylene diamine was purchased from Alfa-Aeser and Methyl Iodide and Sodium Tetrafluoroborate were purchased from Spectrochem and used without further purification. Laponite XLG was purchased from Rockwood Additives, UK.



Scheme 4.1. Synthetic scheme for **pNDI**, **BrNDI** and **BrNDI-BF₄**.

Synthetic Procedures:

Compound **3** and **4** were synthesized according to literature procedure.^[40]

Synthesis of pNDI: Naphthalene dianhydride **1** (0.65 g, 2.42 mmol) and N,N-dimethyl ethylene diamine (2.07 g, 23.6 mmol) were taken in 40 mL of isobutanol and stirred at 90 °C under N₂ atmosphere for 24 h. The resultant solution was filtered and washed with ethanol and water and dried. The obtained diimide **2** was then taken in 50 mL of dry toluene with excess of methyl iodide and refluxed for 4 h. The obtained residue was filtered and dried under vacuum to obtain **5** as yellow solid.

pNDI: Yellow solid (1.51 g, yield 90 %); ^1H NMR (DMSO- d_6 , 400 MHz, ppm), $\delta_{\text{H}} = 8.73$ (s, 4H), 4.49 (t, 4H, $J = 7.2$ Hz), 3.64 (t, 4H, $J = 7.6$ Hz), 3.24 (s, 18H); ^{13}C NMR (DMSO- d_6 , 100 MHz, ppm), $\delta_{\text{C}} = 162.87, 130.71, 126.69, 61.89, 52.72, 34.11, 30.85$. HRMS (ESI): m/z calculated for 692.0356; observed 565.1282 $[\text{M-I}]^+$.

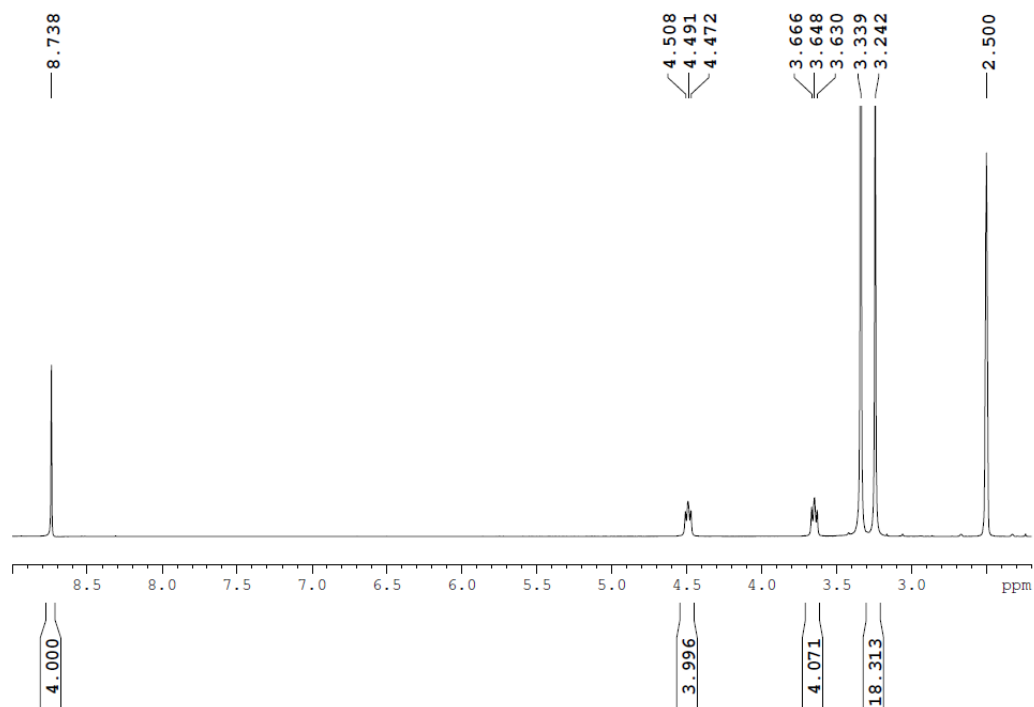


Figure 4.14. ^1H NMR spectra of pNDI in DMSO- d_6 .

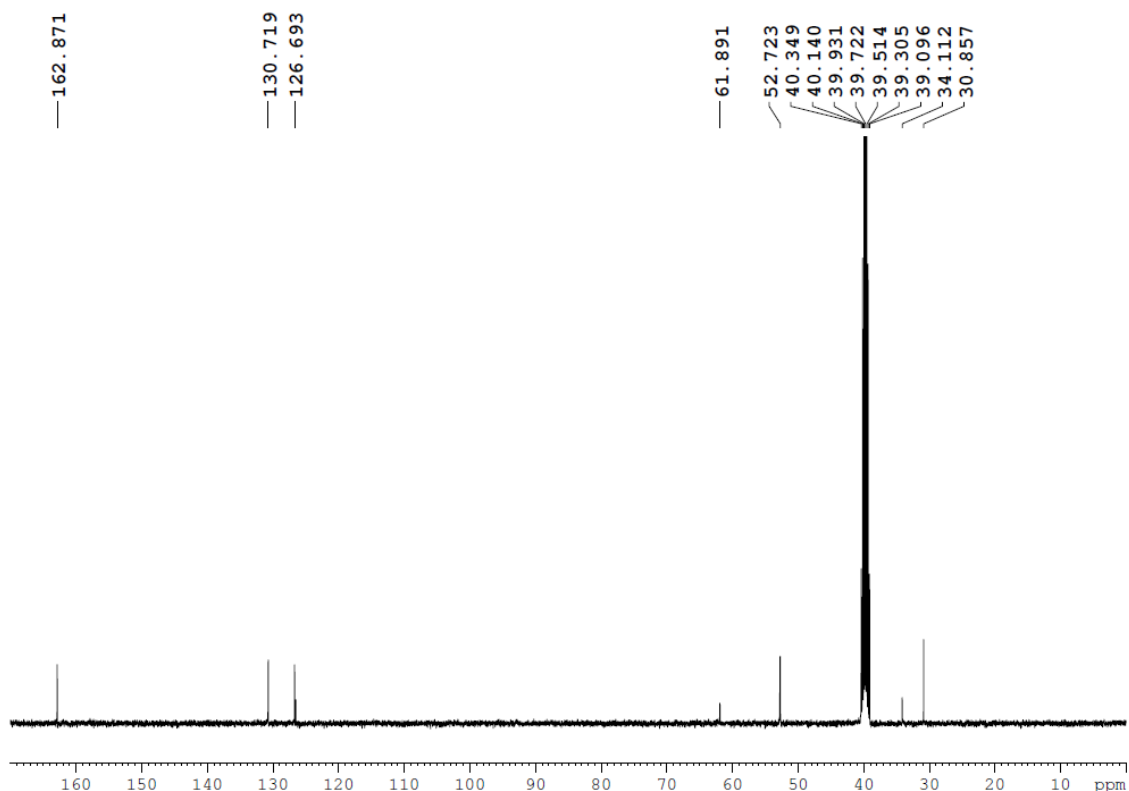


Figure 4.15. ^{13}C NMR spectra of *pNDI* in $\text{DMSO-}d_6$.

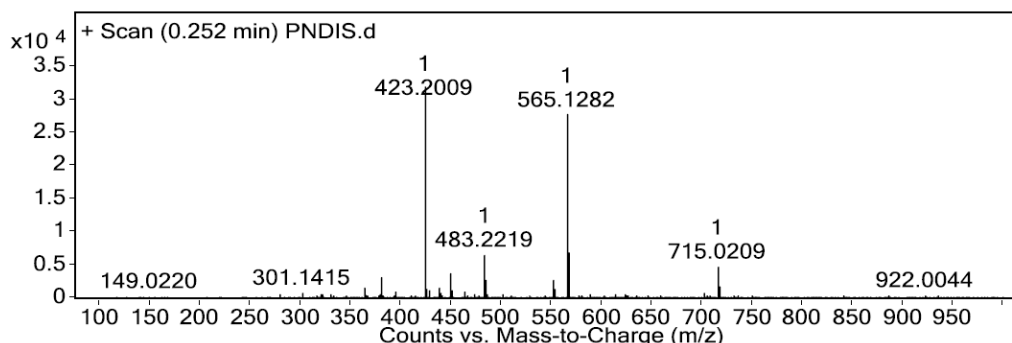


Figure 4.16. ESI-HRMS spectra of *pNDI*.

Synthesis of BrNDI: Brominated naphthalene diimide **4** (75 mg, 0.176 mmol) was taken in 100 ml dry toluene with excess methyl iodide and refluxed for 6 h. The obtained suspension was evaporated to dryness and washed with chloroform to get **6** as brown solid.

BrNDI: Brown solid (142 mg, yield 95 %); ^1H NMR (D_2O , 400 MHz, ppm): δ_{H} = 9.03 (s, 2H), 4.69 (t, 4H, J = 6.8 Hz), 3.73 (t, 4H, J = 7.6 Hz), 3.37 (s, 18H); ^{13}C NMR ($\text{DMSO-}d_6$, 100 MHz, ppm): δ_{C} = 160.70, 160.56, 136.86, 127.57, 126.30, 125.79, 124.31, 61.18, 52.41, 34.24. HRMS (ESI): m/z calculated for $\text{C}_{24}\text{H}_{28}\text{Br}_2\text{I}_2\text{N}_4\text{O}_4$: 849.8546; observed 722.9536 $[\text{M-I}]^+$.

Synthesis of BrNDI-BF₄: 6 (85 mg, 0.1 mmol) was solubilized in 5 ml distilled water and NaBF₄ (13 mg, 0.12 mmol) was added to it. This was stirred for 3 h at 50 °C to obtain an off-white precipitate. This was filtered and washed with distilled water to remove excess NaBF₄ and dried under vacuum to get **7** as off-white solid.

BrNDI-BF₄: off-white solid (70 mg, yield 90 %); HRMS (ESI): *m/z* calculated for C₂₄H₂₈B₂Br₂F₈N₄O₄: 770.0510, observed 683.0438 [M-BF₄]⁺.

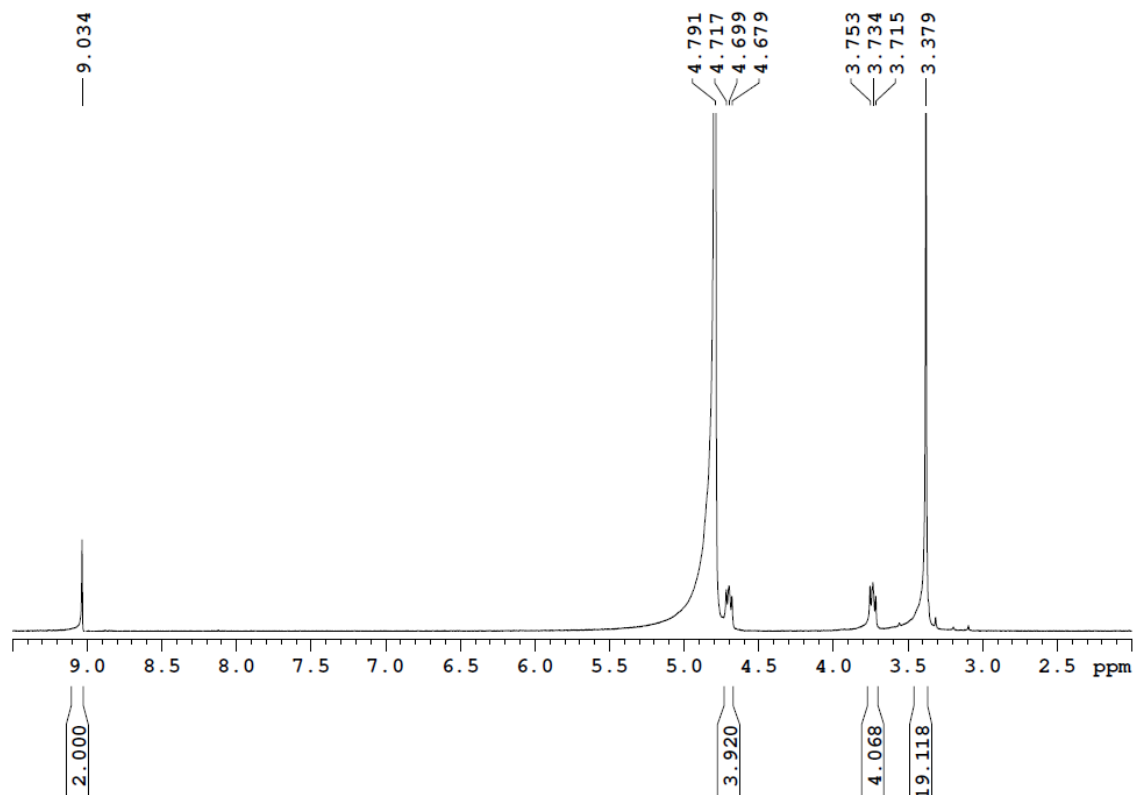


Figure 4.17. ¹H NMR spectra of BrNDI in D₂O.

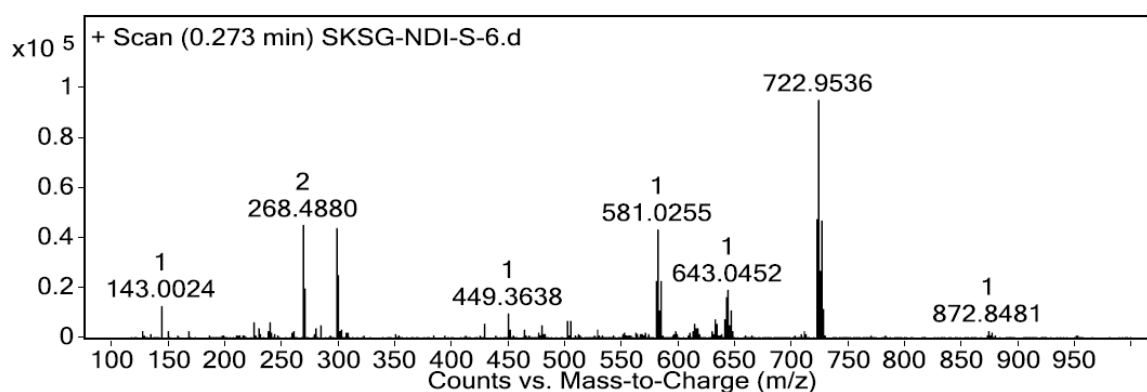


Figure 4.18. ESI-HRMS spectra of BrNDI.

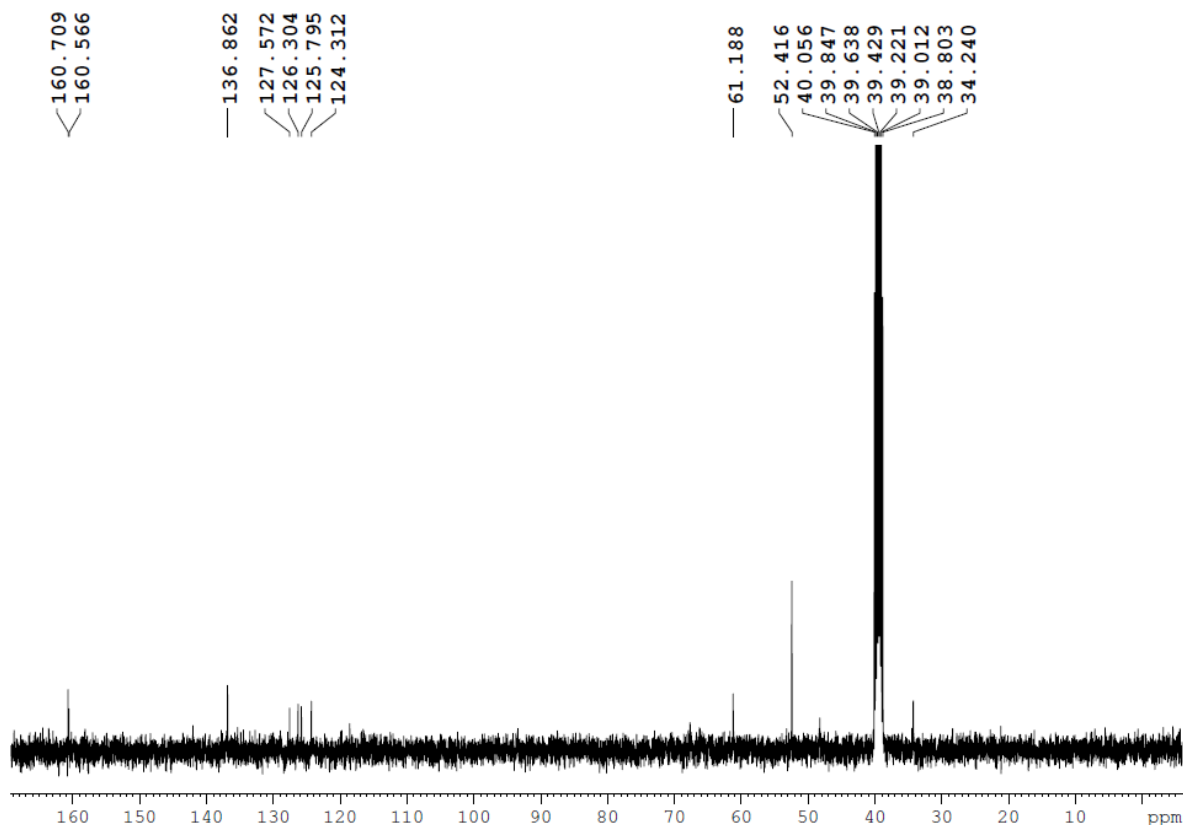


Figure 4.19. ^{13}C NMR spectra of **BrNDI** in $\text{DMSO-}d_6$.

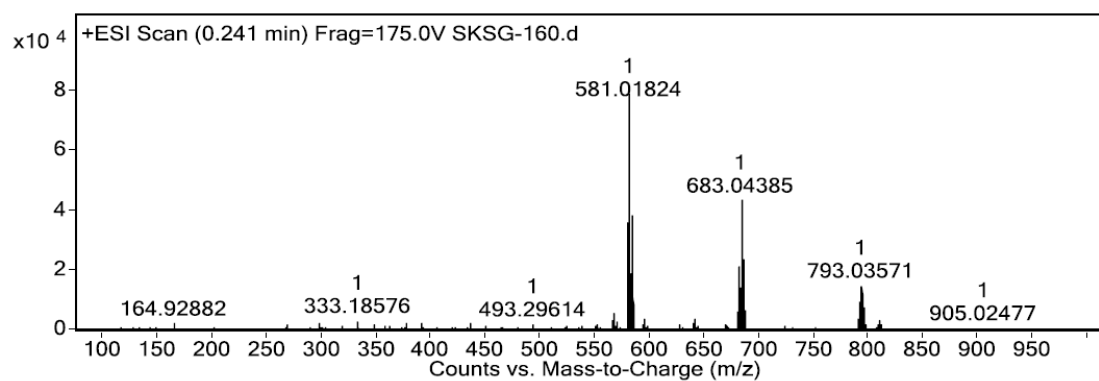
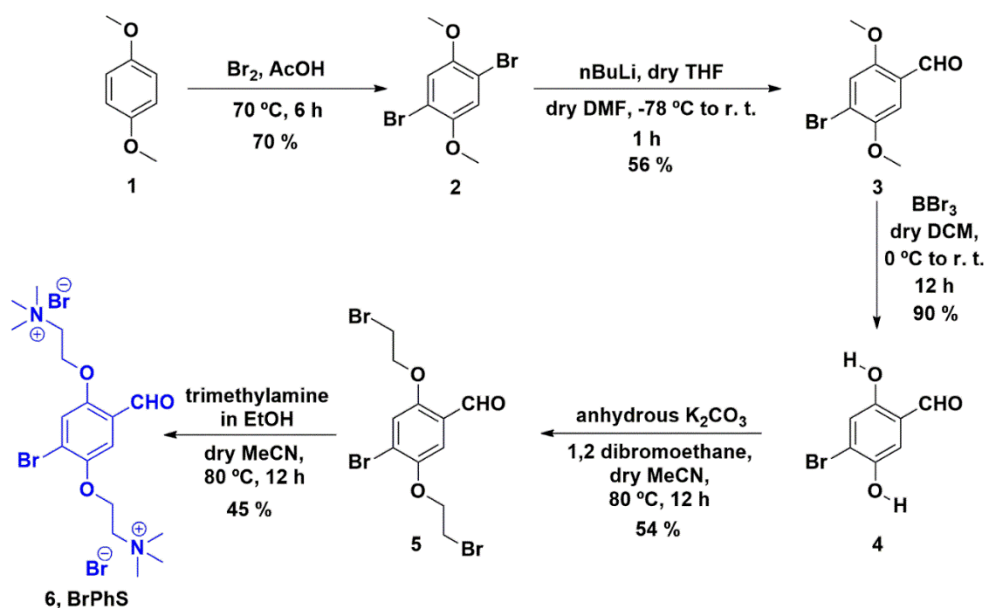


Figure 4.20. ESI-HRMS spectra of **BrNDI-BF4**.

4.9.3b. Synthesis of **BrPhS**

Materials: Dimethylhydroquinone, Br_2 , $n\text{BuLi}$ (2 M in cyclohexane), 1,2-dibromoethane were purchased from Sigma-Aldrich; BBr_3 (1 M in dichloromethane) and K_2CO_3 were purchased from Spectrochem and used without further purification.



Scheme 4.2. Synthetic scheme for **BrPhS**.

Synthetic Procedure

Compound **1-5** were synthesized according to literature procedures.^[3a, 41]

4.1 Synthesis of BrPhS (6): Compound **5** (250 mg, 0.58 mmol) was taken in a 100 ml two neck round bottom flask equipped with a reflux condenser. 50 ml of dry MeCN and 14 ml (58.1 mmol, 100 eqv.) of trimethyl amine (33 % w/w in ethanol) was then added sequentially into the flask under nitrogen atmosphere. This mixture was then refluxed overnight at 80 °C and monitored by ¹H NMR until it converts completely to ammonium salt. Finally, the reaction mixture was evaporated under vacuum to get a brown coloured solid crude. This was then dissolved in 1.5 ml distilled water followed by precipitation using 100 ml cold ethanol. The brown precipitate obtained was then filtered and washed repeatedly with ethanol and finally dried under vacuum at 60 °C for 12 h to get brown powder of **BrPhS** (170 mg, 45 % yield).

¹H NMR (400 MHz, DMSO-*d*₆, ppm): δ_H = 10.35 (s, 1H), 7.69 (s, 1H), 7.43 (s, 1H), 4.63 (brt, J = 3.2 Hz, 2H), 4.57 (brt, J = 3.6 Hz, 2H) 3.89 (t, J = 4.4 Hz, 2H), 3.85 (t, J = 4.4 Hz, 2H), 3.23 (s, 9H), 3.21 (s, 9H); ¹³C NMR (100 MHz, DMSO-*d*₆, ppm): δ_C = 188.7, 154.4, 148.7, 123.9, 119.48, 119.46, 111.03, 64.17, 63.99, 63.31, 63.15, 53.28, 53.04; HRMS (ESI): m/z calculated for C₁₇H₂₉Br₃N₂O₃: 547.9708: observed 469.0515 [M-Br]⁺, 373.1126 [M-CH₃-2Br]⁺, 194.0680 [M-2Br]²⁺.

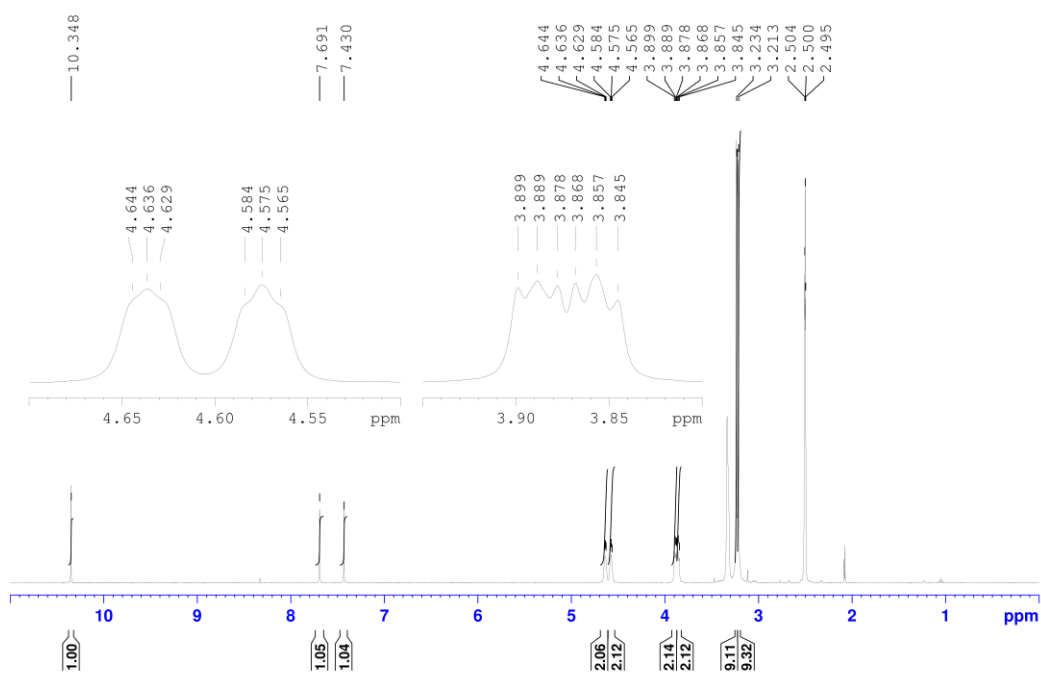


Figure 4.21. ^1H NMR spectrum of **BrPhS** in $\text{DMSO-}d_6$.

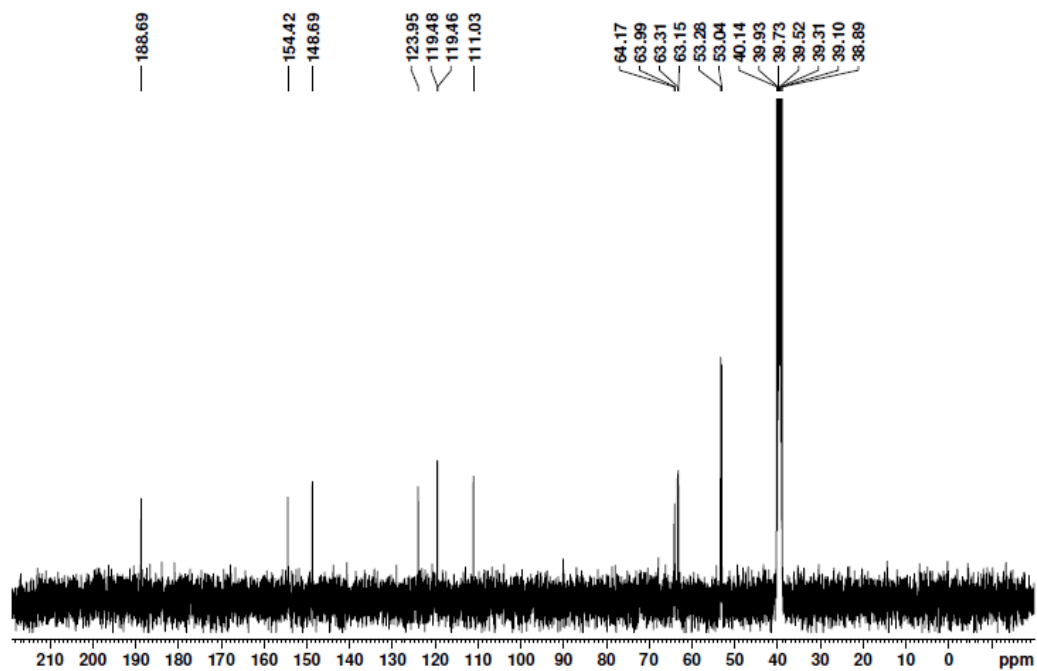


Figure 4.22. ^{13}C NMR spectrum of **BrPhS** in $\text{DMSO-}d_6$.

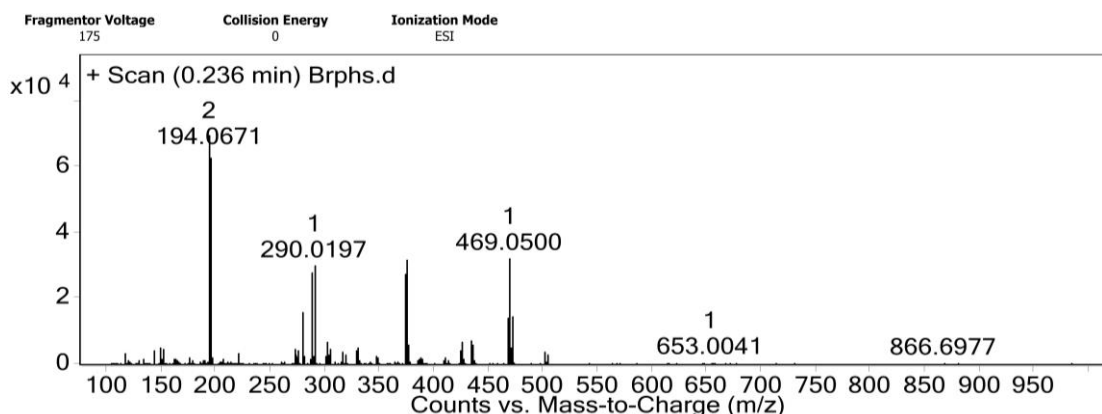


Figure 4.23. ^{13}C NMR spectrum of *BrPhS* in $\text{DMSO-}d_6$.

4.10. References

- [1] a) S. Hirata, *Adv. Opt. Mater.* **2017**, *5*, 1700116; b) S. Xu, R. Chen, C. Zheng, W. Huang, *Adv. Mater.* **2016**, *28*, 9920; c) G. Zhang, G. M. Palmer, M. W. Dewhirst, C. L. Fraser, *Nat. Mater.* **2009**, *8*, 747; d) Kenry, C. Chen, B. Liu, *Nat. Commun.* **2019**, *10*, 2111.
- [2] N. J. Turro, *Modern Molecular Photochemistry*, University Science Books, Sausalito, **1991**, pp. 99-100.
- [3] a) O. Bolton, K. Lee, H. J. Kim, K. Y. Lin, J. Kim, *Nat. Chem.* **2011**, *3*, 205; b) W. Z. Yuan, X. Y. Shen, H. Zhao, J. W. Y. Lam, L. Tang, P. Lu, C. Wang, Y. Liu, Z. Wang, Q. Zheng, J. Z. Sun, Y. Ma, B. Z. Tang, *J. Phys. Chem. C* **2010**, *114*, 6090; c) Z. An, C. Zheng, Y. Tao, R. Chen, H. Shi, T. Chen, Z. Wang, H. Li, R. Deng, X. Liu, W. Huang, *Nat. Mater.* **2015**, *14*, 685; d) Y. Gong, G. Chen, Q. Peng, W. Z. Yuan, Y. Xie, S. Li, Y. Zhang, B. Z. Tang, *Adv. Mater.* **2015**, *27*, 6195; e) M. Baroncini, G. Bergamini, P. Ceroni, *Chem. Commun.* **2017**, *53*, 2081-2093; f) E. Lucenti, A. Forni, C. Botta, L. Carlucci, C. Giannini, D. Marinotto, A. Previtali, S. Righetto, E. Cariati, *J. Phys. Chem. Lett.* **2017**, *8*, 1894.
- [4] N. Gan, H. Shi, Z. An, W. Huang, *Adv. Funct. Mater.* **2018**, *28*, 1802657.
- [5] a) S. Hirata, K. Totani, J. Zhang, T. Yamashita, H. Kaji, S. R. Marder, T. Watanabe, C. Adachi, *Adv. Funct. Mater.* **2013**, *23*, 3386; b) S. Hirata, M. Vacha, *Adv. Opt. Mater.* **2017**, *5*, 1600996; c) S. Hirata, K. Totani, H. Kaji, M. Vacha, T. Watanabe, C. Adachi, *Adv. Opt. Mater.* **2013**, *1*, 438.
- [6] a) X. Ma, J. Wang, H. Tian, *Acc. Chem. Res.* **2019**, *52*, 738; b) D. Li, F. Lu, J. Wang, W. Hu, X. M. Cao, X. Ma, H. Tian, *J. Am. Chem. Soc.* **2018**, *140*, 1916.

- [7] a) M. Gmelch, H. Thomas, F. Fries, S. Reineke, *Sci. Adv.* **2019**, *5*, eaau7310; b) H. Thomas, D. L. Pastoetter, M. Gmelch, T. Achenbach, A. Schlögl, M. Louis, X. Feng, S. Reineke, *Adv. Mater.* **2020**, DOI: 10.1002/adma.202000880; c) Y. Katsurada, S. Hirata, K. Totani, T. Watanabe, M. Vacha, *Adv. Opt. Mater.* **2015**, *3*, 1726; d) A. Steinegger, I. Klimant, S. M. Borisov, *Adv. Opt. Mater.*, *5*, 1700372.
- [8] a) R. Kabe, N. Notsuka, K. Yoshida, C. Adachi, *Adv. Mater.* **2016**, *28*, 655; b) B. Song, W. Shao, J. Jung, S. J. Yoon, J. Kim, *ACS Appl. Mater. Interfaces* *12*, 6137.
- [9] a) J. Xu, A. Takai, Y. Kobayashi, M. Takeuchi, *Chem. Commun.* **2013**, *49*, 8447; b) G. D. Gutierrez, G. T. Sazama, T. Wu, M. A. Baldo, T. M. Swager, *J. Org. Chem.* **2016**, *81*, 4789; c) Y. Yu, M. S. Kwon, J. Jung, Y. Zeng, M. Kim, K. Chung, J. Gierschner, J. H. Youk, S. M. Borisov, J. Kim, *Angew. Chem. Int. Ed.* **2017**, *56*, 16207; d) X. Zhen, Y. Tao, Z. An, P. Chen, C. Xu, R. Chen, W. Huang, K. Pu, *Adv. Mater.* **2017**, *29*, 1606665.
- [10] a) S. J. Barrow, S. Kasera, M. J. Rowland, J. del Barrio, O. A. Scherman, *Chem. Rev.* **2015**, *115*, 12320; b) Y. Gong, H. Chen, X. Ma, H. Tian, *ChemPhysChem* **2016**, *17*, 1934; c) H. Chen, X. Ma, S. Wu, H. Tian, *Angew. Chem. Int. Ed.* **2014**, *53*, 14149; d) S. S. Babu, V. K. Praveen, A. Ajayaghosh, *Chem. Rev.* **2014**, *114*, 1973; e) L. Yang, X. Tan, Z. Wang, X. Zhang, *Chem. Rev.* **2015**, *115*, 7196; f) F. Biedermann, E. Elmalem, I. Ghosh, W. M. Nau, O. A. Scherman, *Angew. Chem. Int. Ed.* **2012**, *51*, 7739.
- [11] a) N. Mizoshita, T. Taniab, S. Inagaki, *Chem. Soc. Rev.* **2011**, *40*, 789-800; b) J. E. Martin, A. J. Patil, M. F. Butler, S. Mann, *Adv. Func. Mater.* **2011**, *21*, 674-681; c) K. V. Rao, A. Jain, S. J. George, *J. Mater. Chem. C* **2014**, *2*, 3055-3064.
- [12] a) K. K. R. Datta, C. Kulkarni, M. Eswaramoorthy, *Chem. Commun.* **2010**, *46*, 616-618; b) A. Eckert, T. Rudolph, J. Guo, T. Mang, A. Walther, *Adv. Mater.* **2018**, *30*, 1802477.
- [13] a) K. V. Rao, K. K. R. Datta, M. Eswaramoorthy, S. J. George, *Angew. Chem. Int. Ed.* **2011**, *50*, 1179-1184; b) K. V. Rao, K. K. R. Datta, M. Eswaramoorthy, S. J. George, *Chem. Eur. J.* **2012**, *18*, 2184-2194; c) K. V. Rao, K. K. R. Datta, M. Eswaramoorthy, S. J. George, *Adv. Mater.* **2013**, *25*, 1713-1718.
- [14] a) D. Lee, O. Bolton, B. C. Kim, J. H. Youk, S. Takayama, J. Kim, *J. Am. Chem. Soc.* **2013**, *135*, 6325; b) M. S. Kwon, D. Lee, S. Seo, J. Jung, J. Kim, *Angew. Chem. Int. Ed.* **2014**, *53*, 11177; c) M. S. Kwon, Y. Yu, C. Coburn, A. W. Phillips, K. Chung, A. Shanker, J. Jung, G. Kim, K. Pipe, S. R. Forrest, J. H. Youk, J. Gierschner, J. Kim, *Nat. Commun.* **2015**, *6*, 8947.

- [15] Q. Wang, J. L. Mynar, M. Yoshida, E. Lee, M. Lee, K. Okuro, K. Kinbara, T. Aida, *Nature* **2010**, *463*, 339-343.
- [16] a) Y. Ishida, T. Shimada, D. Masui, H. Tachibana, H. Inoue, S. Takagi, *J. Am. Chem. Soc.* **2011**, *133*, 14280-14286. b) A. J. Patil, E. Muthusamy, S. Mann, *Angew. Chem. Int. Ed.* **2004**, *43*, 4928-4933; c) T. Tsukamoto, E. Ramasamy, T. Shimada, S. Takagi, V. Ramamurthy, *Langmuir* **2016**, *32*, 2920-2927; d) K. Sano, Y. O. Y. Ishida, Y. Ebina, M. Osada, T. Sasaki, T. Hikima, T. Aida, *Angew. Chem. Int. Ed.* **2018**, *57*, 12508.
- [17] a) M. M. Lezhnina, T. Grewe, H. Stoehr, U. Kynast, *Angew. Chem. Int. Ed.* **2012**, *51*, 10652; b) M. V. Martínez, F. L. Arbeloa, J. P. Prieto, I. L. Arbeloa, *J. Phys. Chem. B* **2005**, *109*, 7443.
- [18] a) F. Würthner, S. Ahmed, C. Thalacker, T. Debaerdemaeker, *Chem. Eur. J.* **2002**, *8*, 4742-4750; b) N. Sakai, J. Mareda, E. Vauthey, S. Matile, *Chem. Commun.* **2010**, *46*, 4225.
- [19] K. V. Rao, *Supramolecular Synthesis of Novel Organic and Hybrid Materials of π -Systems for Optoelectronic Functions* (PhD thesis), Bangalore, JNCASR, **2013**, pp. 176-177.
- [20] M. Kumar, S. J. George, *Chem. Eur. J.* **2011**, *17*, 11102.
- [21] a) R. Zhang, D. Tang, P. Lu, X. Yang, D. Liao, Y. Zhang, M. Zhang, C. Yu, V. W. W. Yam, *Org. Lett.* **2009**, *11*, 4302; b) M. Kumar, S. J. George, *Nanoscale* **2011**, *3*, 2130.
- [22] M. A. El-Sayed, *J. Chem. Phys.* **1963**, *38*, 2834.
- [23] a) G. D. Gutierrez, G. T. Sazama, T. Wu, M. A. Baldo, T. M. Swager, *J. Org. Chem.* **2016**, *81*, 4789; b) K. Kanosue, S. Ando, *ACS Macro Lett.* **2016**, *5*, 1301.
- [24] F. Würthner, S. Ahmed, C. Thalacker, T. Debaerdemaeker, *Chem. Eur. J.* **2002**, *8*, 4742.
- [25] R. E. Dawson, A. Hennig, D. P. Weimann, D. Emery, V. Ravikumar, J. Montenegro, T. Takeuchi, S. Gabutti, M. Mayor, J. Mareda, C. A. Schalley, S. Matile, *Nat. Chem.* **2010**, *2*, 533.
- [26] a) V. Martínez-Martínez, R. S. Llano, S. Furukawa, Y. Takashima, I. L. Arbeloa, S. Kitagawa, *ChemPhysChem* **2014**, *15*, 2517; b) J.-Z. Liao, L. Meng, J.-H. Jia, D. Liang, X.-L. Chen, R.-M. Yu, X.-F. Kuang, C.-Z. Lu, *Chem. Eur. J.* **2018**, *24*, 10498.
- [27] Fluorescence decay profile by exciting at charge-transfer band ($\lambda_{\text{exc.}} > 450$ nm) could not be done because of very low absorption co-efficient at this wavelength.
- [28] X. Chen, C. Xu, T. Wang, C. Zhou, J. Du, Z. Wang, H. Xu, T. Xie, G. Bi, J. Jiang, X. Zhang, J. N. Demas, C. O. Trindle, Y. Luo, G. Zhang, *Angew. Chem. Int. Ed.* **2016**, *55*, 9872.

- [29] S. Sarkar, H. P. Hendrickson, D. Lee, F. DeVine, J. Jung, E. Geva, J. Kim, B. D. Dunietz, *J. Phys. Chem. C* **2017**, *121*, 3771.
- [30] Gaussian 16, Revision A.03, M. J. Frisch, G. W. Trucks, H. B. Schlegel, G. E. Scuseria, M. A. Robb, J. R. Cheeseman, G. Scalmani, V. Barone, G. A. Petersson, H. Nakatsuji, X. Li, M. Caricato, A. V. Marenich, J. Bloino, B. G. Janesko, R. Gomperts, B. Mennucci, H. P. Hratchian, J. V. Ortiz, A. F. Izmaylov, J. L. Williams; F. Ding; F. Lipparini, F. Egidi, J. Goings, B. Peng, A. Petrone, T. Henderson, D. Ranasinghe, V. G. Zakrzewski, J. Gao, N. Rega, G. Zheng, W. Liang, M. Hada, M. Ehara, K. Toyota, R. Fukuda, J. Hasegawa, M. Ishida, T. Nakajima, Y. Honda, O. Kitao, H. Nakai, T. Vreven, K. Throssell, J. A. Montgomery Jr., J. E. Peralta, F. Ogliaro, M. J. Bearpark, J. J. Heyd, E. N. Brothers, K. N. Kudin, V. N. Staroverov, T. A. Keith, R. Kobayashi, J. Normand, K. Raghavachari, A. P. Rendell, J. C. Burant, S. S. Iyengar, J. Tomasi, M. Cossi, J. M. Millam, M. Klene, C. Adamo, R. Cammi, J. W. Ochterski, R. L. Martin, K. Morokuma, O. Farkas, J. B. Foresman, D. J. Fox, Gaussian, Inc., Wallingford CT, **2016**.
- [31] A. D. Becke, *J. Chem. Phys.* **1993**, *98*, 1372.
- [32] C. Lee, W. Yang, R. G. Parr, *Phys. Rev. B* **1988**, *37*, 785.
- [33] B. Miehlich, A. Savin, H. Stoll, H. Preuss, *Chem. Phys. Lett.* **1989**, *157*, 200.
- [34] G. Scalmani, M. J. Frisch, *J. Chem. Phys.* **2010**, *132*, 114110.
- [35] S. Hirata, M. Head-Gordon, *Chem. Phys. Lett.* **1999**, *314*, 291.
- [36] E. van Lenthe, R. Van Leeuwen, E. J. Baerends, *Int. J. Quan. Chem.* **1996**, *57*, 281.
- [37] E. van Lenthe, J. G. Snijders, E. J. Baerends, *J. Chem. Phys.* **1996**, *105*, 6505.
- [38] F. Wang, T. Ziegler, E. van Lenthe, S. van Gisbergen, E. J. Baerends, *J. Chem. Phys.* **2005**, *122*, 204103.
- [39] ADF2017, SCM, *Theoretical Chemistry*, Vrije Universiteit, Amsterdam, The Netherlands, <http://www.scm.com>.
- [40] F. Doria, I. Manet, V. Grande, S. Monti, M. Freccero, *J. Org. Chem.* **2013**, *78*, 8065.
- [41] H. Shi, Z. An, P.-Z. Li, J. Yin, G. Xing, T. He, H. Chen, J. Wang, H. Sun, W. Huang, Y. Zhao, *Cryst. Growth Des.* **2016**, *16*, 808.

Part B

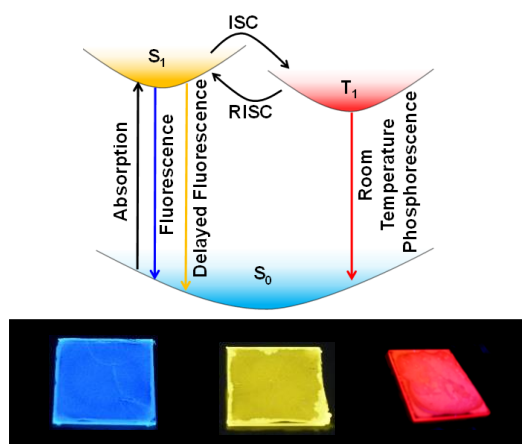
Thermally Activated Delayed Fluorescence

CHAPTER 5

Efficient Thermally Activated Delayed Fluorescence (TADF) from Donor-Acceptor Arylene Diimides*

Abstract

A systematic investigation has been done on various arylene diimides in order to understand and harvest their triplet excitons. Donor-acceptor charge-transfer design based on these electron-deficient arylene diimides are shown to exhibit small singlet-triplet gap facilitating efficient thermally activated delayed fluorescence (TADF) properties. Detailed theoretical calculation was performed to reinforce the role of a phenyl spacer between the donor (phenylcarbazole) and acceptor (arylene diimides) towards maintaining both strong charge-transfer nature of the molecules as well as emission oscillator strength. Moreover, analysis of the emissive phosphorescence bands of these molecules suggest that the confinement of charge-transfer states within the vicinity of locally-excited triplet states are critical in order to harvest the triplet excitons via TADF process.



*Manuscript based on this work has appeared in *Chem. Eur. J.* **2019**, 25, 16007 and other manuscript is under preparation.

5.1. Introduction

Arylene diimides are a very important class of molecules in functional organic and supramolecular materials.^[1] These class of materials have been extensively used in organic FETs and photovoltaic applications as air-stable, n-type semiconductors.^[2] Among the various arylene diimides, 1,4,5,8-Naphthalenetetracarboxylic acid diimides (NDIs) have attracted a lot of attention in recent years due to improved synthetic methodologies for a library of core-substituted NDIs (cNDIs) with tunable energetic levels.^[1b] These molecules have further expanded the scope of cNDIs to various optoelectronic and sensor applications and also as a model system in supramolecular chemistry.^[3] Novel anion- π interactions have been experimentally realized in electron deficient cNDIs and later used in halide sensing, organocatalysis and for anion transport through lipid bilayers.^[4-6] Remarkably, air-stable radical anions of cNDI derivatives are now synthetically feasible^[7] and may be of potential use in artificial photosynthetic cascades for efficient solar energy conversion.^[8] Apart from its electronic properties, the tunable fluorescence of cNDIs in solution are used in energy transfer and circularly polarized luminescence.^[9] However, for advanced luminescence applications such as organic light emitting diodes (OLEDs), triplet harvesting of these molecules is an important requirement to improve the efficiency in devices.^[10] In this respect, however, NDIs are relatively unexplored in spite of the presence of multiple carbonyl groups in its core to promote fast intersystem crossing (ISC) and despite having excellent triplet yield.^[11] Very recently, we have successfully demonstrated the method of stabilizing these NDI triplets by heavy atom substitution in confined supramolecular microenvironments, to harvest ambient room temperature phosphorescence (RTP).^[12] However, molecular engineering of cNDIs to modulate the excited state energy levels (S_n and T_n) and emission wavelengths and also to realize other means of triplet harvesting such as thermally activated delayed fluorescence (TADF) and triplet-triplet annihilation (TTA) up-conversion still remains a challenge in these derivatives. We also envisage that low lying triplets of cNDIs would also benefit in the design of red to NIR triplet emitters, which are difficult to achieved.^[13] Charge-transfer (CT) states created by the spatially separated donor and acceptor subunits is a crucial design to obtain a small singlet-triplet gap (ΔE_{ST}) to aid triplet mediated delayed emission from chromophores.^[10a,14]

In this Chapter, we first introduce a donor-acceptor molecular design to harvest the triplets in cNDI derivatives, by substituting the electron-deficient NDI cores with carbazole (Cz) donor moieties. Remarkably, these core-substituted NDI derivatives **CzNDI** and **CzPhNDI**, showed red-emitting delayed fluorescence (DF) and room temperature phosphorescence (RTP), phenomena rarely reported in NDI based molecules (Figure 5.1). With detailed time dependent

density functional theory (TDDFT) calculations and time-resolved emission spectroscopy, further we provide a structure-property study on how to increase the oscillator strength of emission in these cNDI derivatives, which depends heavily on the excited state geometry of the chromophores. Our design clearly demonstrate importance of a spacer phenyl group between the donor and acceptor units in order to adjust the strong charge-transfer nature of the molecule as well as high oscillator strength of emission. Based on these findings, we further explored other structural analogues of **CzPhNDI**, namely, **CzPhPmDI** and **CzPhNMI**, where electron-deficient pyromellitic diimide and naphthalene monoimide were substituted with same donor unit carbazole (Figure 5.1). We observed an important correlation regarding the energetics of the singlet charge-transfer (^1CT) and locally excited triplet (^3LE) states of the acceptor units constituting these chromophores, that suggest that confinement of the CT state is critical towards obtaining efficient triplet harvesting from these molecules. In addition, a solution-processed OLED device prototype is shown utilizing **CzPhPmDI** to further reiterate the promising applications of this class of chromophores for future solid-state lighting materials.

5.2. Design Strategy and Synthesis

The molecular structures of all donor-acceptor charge-transfer molecules (**CzNDI**, **CzPhNDI**, **CzPhPmDI** and **CzPhNMI**) studied in this Chapter are given in Figure 5.1. **CzNDI** was synthesized in a single step from the corresponding dibromo naphthalene diimide using Pd-catalysed Buchwald-Hartwig amination (see Experimental Section 5.7) reaction. The other phenyl spacer derivatives were synthesized using Pd-catalysed Suzuki coupling reaction from respective bromo-substituted arylene diimides (see Experimental Section 5.7). All our studies were mainly focused on the solid state emission characteristics and polymethyl methacrylate (PMMA) was used as a host material in order to reduce the aggregation-induced optical losses and improve ambient triplet stability.

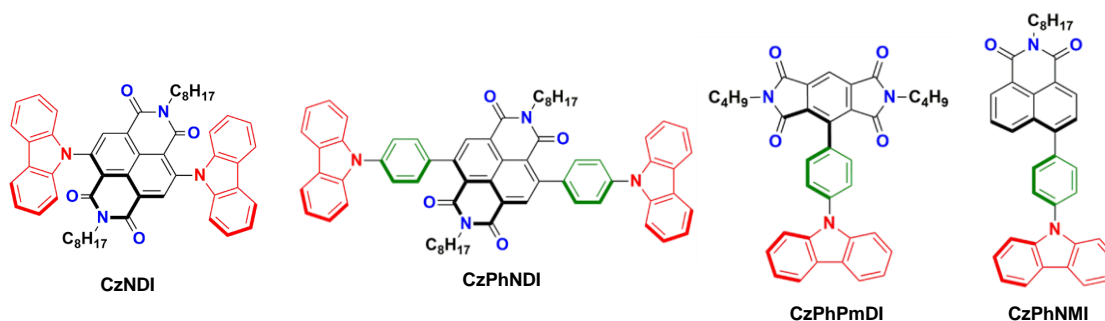


Figure 5.1. Chemical structures of the donor-acceptor charge transfer molecules studied for triplet harvesting in this chapter.

5.3. Thermally Activated Delayed Fluorescence and Room Temperature Phosphorescence from Core-substituted Naphthalene Diimides : A Structure-property Study

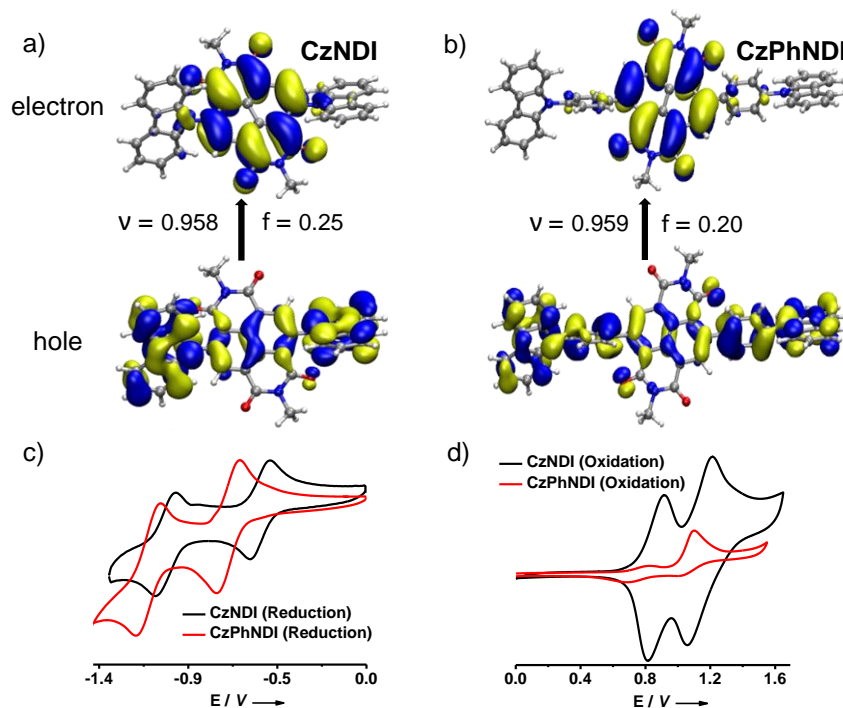


Figure 5.2. Natural transition orbitals for S_1 state at the optimized S_0 geometry for optical absorption of a) **CzNDI** and b) **CzPhNDI**, calculated using $\omega^*B97XD/6-31+g(d)$ level of theory in vacuum. Hole and electron wave functions with the largest weight (v) and the oscillator strength for the transition (f) are also provided. Cyclic voltammetry measurements of **CzNDI** and **CzPhNDI**. c) Reduction cycle and d) oxidation cycle. $[CzNDI]$ and $[CzPhNDI] = 1$ mM in DCM.

Considering the basic design principle of a typical covalently linked donor and acceptor moiety we first designed carbazole-substituted (donor) NDI (acceptor) derivatives, with (**CzPhNDI**) or without (**CzNDI**) the phenyl spacer (Figure 5.1). Next (TDDFT) calculations were performed to understand the ground state geometries (S_0) of these chromophores which revealed dihedral angles of 57° and 61° between donor (Cz) and acceptor (NDI) moieties for **CzPhNDI** and **CzNDI**, respectively. Further, natural transition orbital (NTO) analysis was performed to understand the nature of transitions in these chromophores. In both these chromophores for optical absorption to S_1 state, the hole NTO is localized on carbazole units and the electron NTO is localized on NDI core, in consistent with the molecular design having suitable charge-transfer transitions (Figure 5.2a, 5.2b). This was further supported experimentally

by cyclic voltametry (CV) studies where highest occupied (HOMO) and lowest unoccupied (LUMO) molecular orbital energies were estimated (Figure 5.2c, 5.2d). The calculated HOMO energies of **CzNDI** and **CzPhNDI** were -5.26 eV and -5.17 eV, respectively (see Experimental Section). The calculated LUMO energies of **CzNDI** and **CzPhNDI** were -3.86 eV and -3.71 eV, respectively (see Experimental Section). The HOMO and LUMO energy levels closely match with the HOMO level of carbazole and NDI LUMO levels, respectively.^[15] This observation also shows the spatial separation of HOMO-LUMO for a suitable charge-transfer state formation in the molecules in their ground states.^[13c]

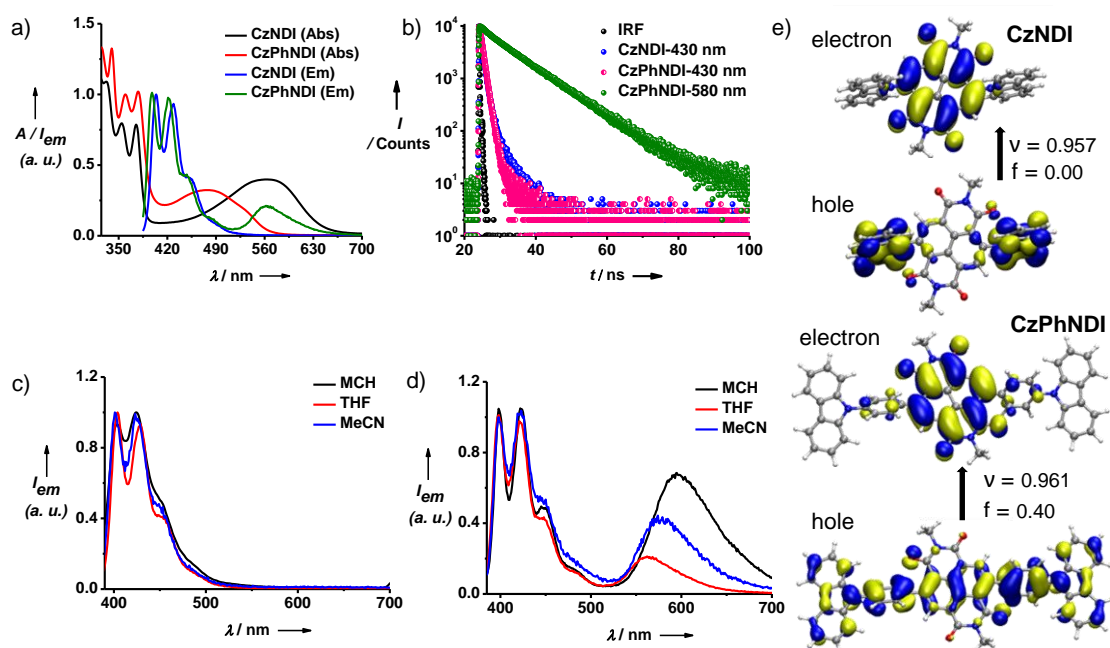


Figure 5.3. a) Absorption and normalized emission spectra of **CzNDI** and **CzPhNDI** in THF ($[\text{CzNDI}]$ and $[\text{CzPhNDI}] = 0.05 \text{ mM}$, $\lambda_{\text{exc.}} = 380 \text{ nm}$) and b) corresponding fluorescence decay spectra collected at the locally excited emission wavelength (430 nm) and charge-transfer emission wavelength (580 nm). IRF is the instrument response function and $\lambda_{\text{exc.}} = 373 \text{ nm}$. Effect of solvent polarity in the emission spectra of c) **CzNDI** and d) **CzPhNDI**. ($[\text{CzNDI}] = [\text{CzPhNDI}] = 0.05 \text{ mM}$, $\lambda_{\text{exc.}} = 380 \text{ nm}$). e) Natural transition orbitals for S_1 states at optimized S_1 state geometry for emission of **CzNDI** (top) and **CzPhNDI** (down) using $\omega^* \text{B97XD/6-31+g(d)}$ level of theory in vacuum. Hole and electron wave functions with the largest weight (v), the oscillator strength for the transitions (f) are also provided.

In solution state (THF), both **CzNDI** and **CzPhNDI** show a locally excited (LE) absorption band at around 300-400 nm and a charge-transfer (CT) band in the longer wavelengths (420-650 nm) (Figure 5.3a). Both the molecules showed characteristic LE emission bands with sharp vibrational features at 400-500 nm with short lifetime (0.99 ns and 0.90 ns for **CzNDI** and

CzPhNDI, respectively) on excitation at 380 nm (Figures 5.3b). Interestingly, **CzPhNDI** showed a CT emission with a maximum at 580 nm, whereas **CzNDI** does not show any CT emission in THF ($\lambda_{\text{exc.}} = 380$ nm, Figure 5.3c, 5.3d). The CT nature of **CzPhNDI** emission is evident from the long lifetime of 9.3 ns and its solvatochromic behaviour ($\lambda_{\text{exc.}} = 373$ nm, $\lambda_{\text{monitored}} = 580$ nm) (Figure 5.2b, 5.2d). In order to get further insight into this remarkable difference in emission characteristics, we theoretically investigated the nature of excited states using TDDFT methods. In the excited state of **CzNDI**, the Cz and NDI units are found to be perpendicular to each other (dihedral angle $\sim 90^\circ$), thus forming a stable twisted intramolecular charge transfer (TICT) state (S_1), with complete spatial separation of hole and electron wavefunctions (Figure 5.3e, top panel); a geometry that weakens the transition dipole moment matrix element as evident from the low oscillator strength of emission ($f = 0.00$). On the contrary, due to the presence of a phenyl spacer in **CzPhNDI**, the TICT state is not stable and both the Cz and NDI units tend to adapt a more planar conformation (dihedral angle $\sim 2^\circ$) in its optimized excited (S_1) state. This leads to a comparatively higher spatial overlap between hole and electron wavefunctions with large oscillator strength ($f = 0.40$) for $S_1 \rightarrow S_0$ transition leading to emissive CT for **CzPhNDI** (Figure 5.3e, bottom panel). Thus it is evident that a balance between twist angle and HOMO-LUMO overlap is crucial for high photoluminescence quantum yield in the cNDI derivatives.

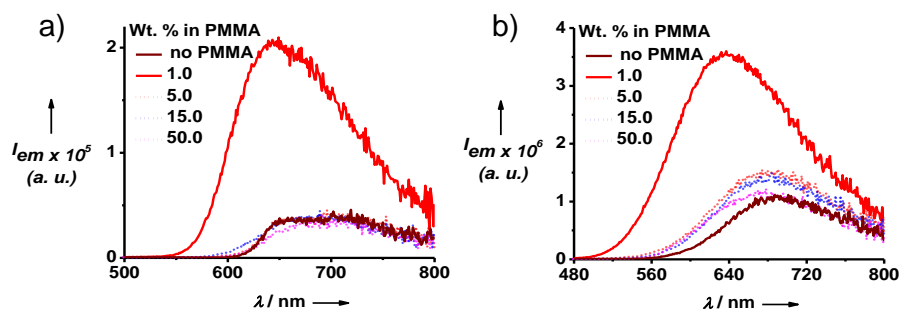


Figure 5.4. Emission ($\lambda_{\text{exc.}} = 380$ nm) of a) **CzNDI** and b) **CzPhNDI** films composed of different wt. % in PMMA.

In an attempt to harvest the triplets in these cNDI derivatives, we further studied them in solid state as non-radiative pathways arising from vibrational relaxation can quench the triplet excitons in solution state. However, neat thin films of both **CzNDI** and **CzPhNDI**, made from chloroform solutions showed only weak emission due to the aggregation induced quenching (Figure 5.4). On the other hand, emission spectra of **CzNDI** and **CzPhNDI** dispersed in poly(methylmethacrylate) (PMMA, 1 wt. % dye to polymer ratio, $\lambda_{\text{exc.}} = 380$ nm) showed a substantial blue-shift (30 nm and 50 nm for **CzNDI** and **CzPhNDI**, respectively) and concomitant enhancement in charge-transfer (CT) emission intensity compared to neat films

(Figure 5.4) suggesting less aggregation and also a plausible triplet state stabilization due to reduced oxygen diffusion contributing effectively in the total emission (*vide infra*).^[16] Unlike the solution state, the intensity of LE emission (400-500 nm) in PMMA films was less compared to the CT emission and hence all further studies were focussed on CT emission. **CzPhNDI** films showed higher emission quantum yield of 32% compared to the 2% of **CzNDI**.

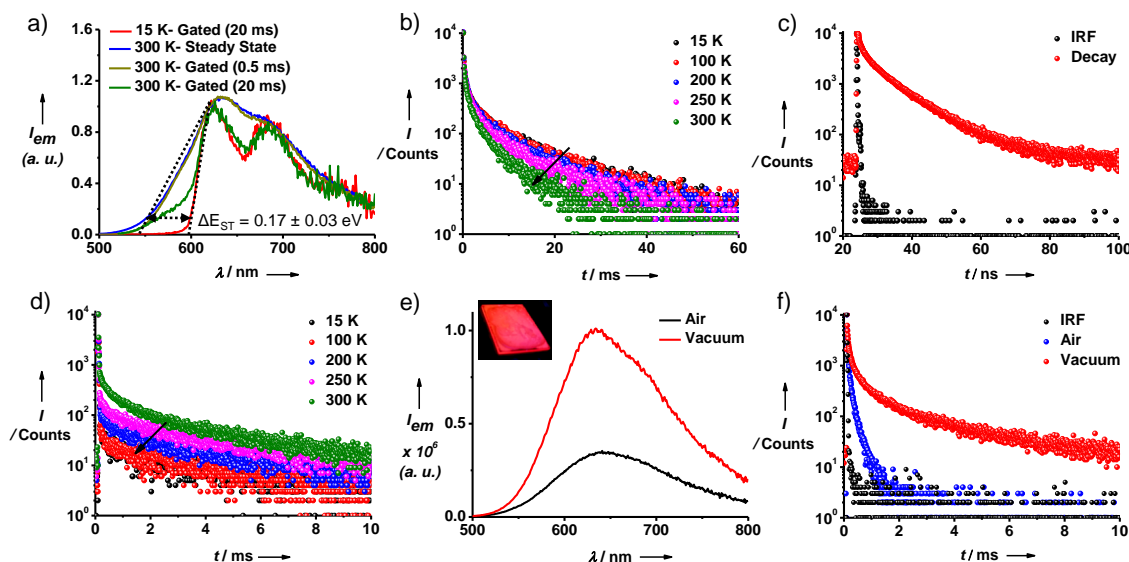


Figure 5.5. a) Normalized emission spectra of the PMMA films of **CzPhNDI** at different temperature with varying delay times (0.5 ms and 20 ms) showing TADF and phosphorescence. b) Temperature dependent lifetime profiles of **CzPhNDI** monitored at 640 nm confirming the phosphorescence nature ($\lambda_{exc.} = 380$ nm). c) Time-resolved decay profile of **CzPhNDI** film (1 wt. % in PMMA) showing the prompt charge-transfer (CT) fluorescence ($\lambda_{exc.} = 373$ nm, $\lambda_{monitored} = 640$ nm). d) Temperature dependent lifetime profiles of **CzPhNDI** monitored at 550 nm confirming the TADF nature. ($\lambda_{exc.} = 380$ nm). e) Comparison of steady-state emission intensity of **CzPhNDI** in air and under vacuum and the inset shows the photograph of **CzPhNDI** film under 365 nm UV-lamp. f) Time-resolved decay profile of PMMA film of **CzPhNDI** (1 wt. %) in air ($\tau_{avg.} = 80.3$ μ s) and vacuum ($\tau_{avg.} = 2.43$ ms). ($\lambda_{exc.} = 380$ nm, $\lambda_{monitored} = 640$ nm). IRF = Instrument Response Function. In all cases 1 wt. % **CzPhNDI**-PMMA composition was used and the excitation wavelength was 380 nm unless otherwise mentioned.

To elucidate the triplet contribution in the emission of **CzPhNDI** detailed time-resolved and temperature dependent fluorescence spectroscopy measurements were performed by exciting the LE state at 380 nm. Steady-state emission at 300 K, showed a broad emission (500-800 nm) with a maximum at 640 nm (Figure 5.5a). Interestingly, a gated emission spectrum with a short time delay (0.5 ms) showed similar emission spectrum suggesting the presence of a delayed emission in **CzPhNDI** chromophores (Figure 5.5a). Further, the gated emission with a longer

delay time of 20 ms at 300 K, revealed vibronic features in the 600-800 nm range, accompanied by a broad structureless emission band at 550-600 nm with reduced intensity, hinting towards the presence of an additional low energy excited state (Figure 5.5a, green curve). Low temperature (15 K) gated emission (20 ms delay) further showed that the emission band in the 600-800 nm region retains its vibronic spectral features with the complete disappearance of the emission contribution in the 550-600 nm suggesting its phosphorescence nature. This was further confirmed by temperature dependent, time-resolved emission measurements at different temperatures ($\lambda_{\text{monitored}} = 640$ nm), which showed a decrease in average lifetime on increasing temperature ($\tau_{\text{avg.}} = 6.45$ ms and 2.43 ms at 15 K and 300 K, respectively, Figure 5.5b).^[17] Along with this long lifetime component, **CzPhNDI** also showed a prompt CT fluorescence with an average lifetime of 7.3 ns ($\lambda_{\text{exc.}} = 373$ nm, $\lambda_{\text{monitored}} = 640$ nm) (Figure 5.5c). On the other hand, average lifetime of the delayed emission at lower wavelength region, selectively monitored at 550 nm showed an increase in lifetime with increase in temperature ($\lambda_{\text{exc.}} = 380$ nm, $\tau_{\text{avg.}} = 78$ μ s and 1.2 ms at 15 K and 300 K, respectively) characteristic of molecules with delayed fluorescence (DF) mediated via triplet excitons (Figure 5.5d) consistent with its small singlet-triplet energy gap ($\Delta E_{\text{ST}} = 0.17 \pm 0.03$ eV). In addition, a threefold increase in emission intensity and corresponding increase in average lifetime under vacuum compared to the emission under ambient conditions, reiterates the contribution from triplet states in **CzPhNDI** emission (Figures 5.5e and 5.5f).^[13c]

Having a conclusive evidence of a delayed fluorescence feature in the **CzPhNDI** derivative, we further investigated the nature of the triplet state that is involved in the excitonic upconversion process. Low temperature solvatochromism studies with individual donor(**CzPh**) and acceptor (**NDI-butyl**) control molecules revealed the locally excited character of the lowest energy triplet state, originating from the acceptor NDI unit rather than charge-transfer in nature (Figure 5.6). The LE or CT nature of any phosphorescence emission band is generally proven by collecting the emission spectra of the chromophores in frozen solvent (77 K) with different polarity.^[18] Therefore, we first obtained the phosphorescence band of 0.05 mM **CzPhNDI** in frozen THF ($\lambda_{\text{exc.}} = 380$ nm, delay time = 20 ms) which matches with the phosphorescence spectrum of 1 wt. % PMMA thin film at 15 K, validating the correlation between solid and solution state properties (Figure 5.6a). Further, a low temperature solvatochromism study of 0.05 mM **CzPhNDI** was done at 77 K (Figure 5.6b). **CzPhNDI** phosphorescence retains its structured emission in all the solvents without any significant shift in the emission maxima which unambiguously proves its LE nature (Figure 5.6b). In general, such triplet LE bands originate from either of the donor or acceptor subunits in these kinds of CT chromophores exhibiting TADF.^[19] Therefore, phosphorescence spectra of individual donor and acceptor units were

obtained in frozen THF solvent at 77 K ($\lambda_{exc.} = 340$ nm, delay time = 20 ms) (Figures 5.6c and 5.6d). The electron donor control molecule (**CzPh**) shows a high energy phosphorescence band at 420-500 nm region, whereas the acceptor control molecule (**NDI-butyl**) shows a low-lying triplet at 600-800 nm region with strong vibronic features.^[20] Remarkably, this phosphorescence band from **NDI-butyl** closely matches with gated emission band obtained from **CzPhNDI** films (1 wt. % in PMMA) at both 300 K and 15 K. This unique feature also suggests that the lowest triplet state involved in DF is originating from the acceptor subunit NDI which is emissive even at 300K resulting in RTP (Figure 5.6e).^[18] Based on the experimentally obtained energy levels

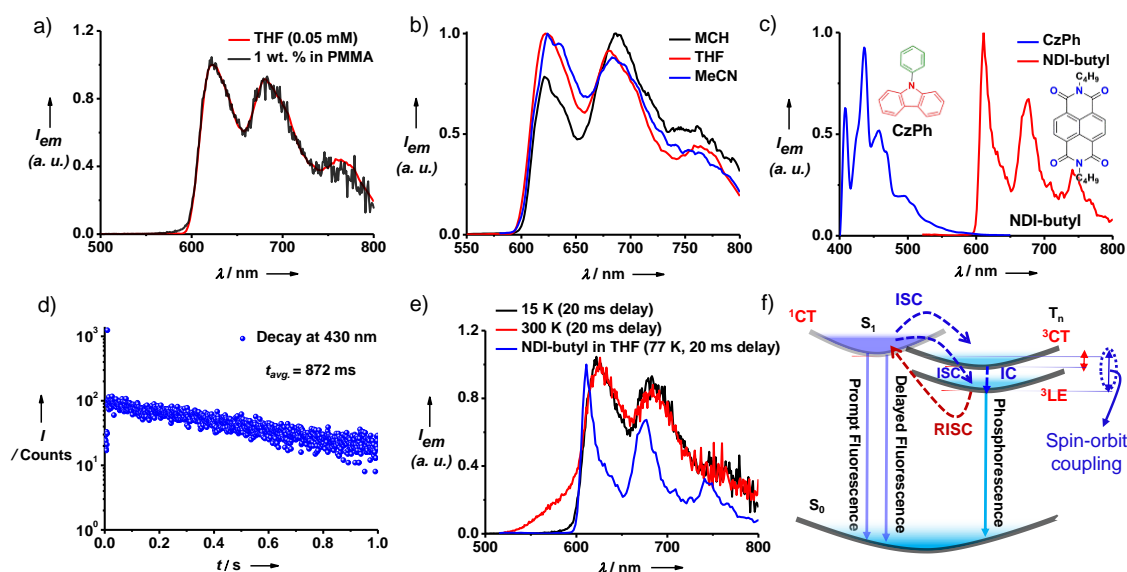


Figure 5.6. a) Phosphorescence spectra of **CzPhNDI** in film state (1 wt. % in PMMA) at 15 K and in THF solution at 77 K. b) Solvatochromism studies of the **CzPhNDI** phosphorescence at 77 K. (For all samples $\lambda_{exc.} = 380$ nm, delay time = 20 ms). [**CzPhNDI**] = 0.05 mM in all cases. Phosphorescence nature (3LE) of the control donor (**CzPh**) and acceptor (**NDI-butyl**) molecules in solution state: c) phosphorescence spectra of control donor and acceptor units in THF at 77 K ($\lambda_{exc.} = 340$ nm, delay time = 20 ms, ([**CzPh**] and [**NDI-Butyl**] = 0.05 mM). d) Time-resolved emission (phosphorescence) decay profile of 0.05 mM **CzPh** ($\lambda_{exc.} = 340$ nm, $\lambda_{monitored} = 430$ nm, $\tau_{avg.} = 872$ ms) 77 K in THF. e) Comparison of phosphorescence spectra ($\lambda_{exc.} = 380$ nm) obtained at 15 K and 300 K for **CzPhNDI** thin films (1 wt. % in PMMA, red and black curves) with the phosphorescence spectrum ($\lambda_{exc.} = 340$ nm) of acceptor moiety (**NDI-butyl**) collected at 77 K in THF. [**NDI-butyl**] = 0.05 mM. f) Simplified Jablonski diagram for **CzPhNDI** indicating various excited state process involving the triplet exciton harvesting. A favourable ISC/RISC process is envisioned due to efficient spin-orbit coupling between the closely-lying 1CT and 3LE states (according to El-Sayed's Rule). (IC = internal conversion, ISC = intersystem crossing, RISC = reverse intersystem crossing). ISC between the 1CT and 3CT is expected to be weak.

of different singlet and triplet manifolds obtained in the case of **CzPhNDI**, we proposed a simplified Jablonski diagram to highlight a plausible spin-orbit coupling between the ^1CT and ^3LE states, which is believed to be a strong contributor towards effective reverse intersystem crossing in TADF molecules (Figure 5.6f).^[21] These experiments provide an unequivocal proof for the co-existence of both DF and RTP emission in the red-wavelength region with high quantum yield. To the best of our knowledge, this is the first report of dual DF and RTP from donor-acceptor cNDI derivatives under ambient conditions.^[12]

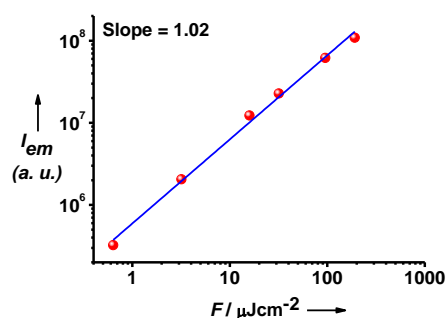


Figure 5.7. Intensity dependent emission profile of 1 wt. % **CzPhPmDI**-PMMA film ($\lambda_{exc.} = 355$ nm, ($\lambda_{monitored} = 500\text{-}700$ nm).

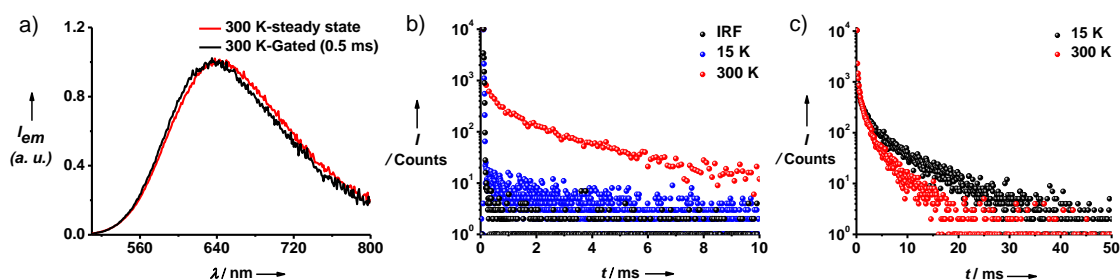


Figure 5.8. Emission characteristics of **CzPhNDI** (1 wt. % in PMMA) films upon excitation at the charge-transfer absorption wavelength ($\lambda_{exc.} = 500$ nm). a) Steady state and gated (delay time = 0.5 ms) emission spectra, suggesting similar delayed emission characteristics as that of 380 nm (locally excited) excitation. Lifetime spectra at different temperatures while monitoring b) at 550 nm ($\tau_{avg.} = 2.26$ ms at 300 K, decay at 15 K too low for accurate fitting) and c) at 640 nm ($\tau_{avg.} = 2.06$ ms at 300 K, $\tau_{avg.} = 4.92$ ms at 15 K) showing similar trend of delayed fluorescence and phosphorescence while exciting the CT band at 500 nm (CT absorption band has sufficient oscillator strength according to theoretical calculations, *vide infra*).

In addition, a linear increase (slope = 1.02) in the emission intensity with the incident excitation ($\lambda_{exc.} = 355$ nm) intensity suggests unimolecular thermally activated delayed fluorescence nature of **CzPhNDI**, rather than a bimolecular triplet-triplet annihilation

upconversion process (Figure 5.7).^[22] Direct excitation at the charge-transfer band at 500 nm, also resulted in similar spectroscopic features suggesting that triplet state harvesting is possible via exciting at the CT absorption band selectively and it reiterates the close proximity of ¹CT-³LE state (Figure 5.8).

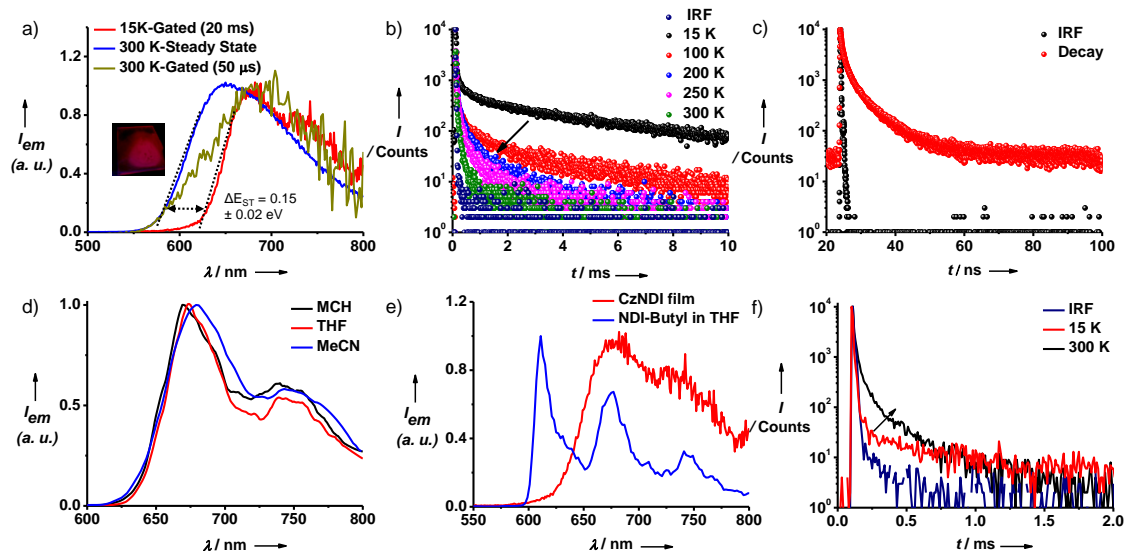


Figure 5.9. a) Normalized emission spectra of PMMA films of CzNDI at different temperatures with different delay times (50 μ s and 20 ms) showing DF and phosphorescence. Inset: Photograph of CzNDI in film state under 365 nm UV-lamp. b) Lifetime spectra of CzNDI at different temperatures ($\lambda_{\text{monitored}} = 680$ nm). c) Time-resolved fluorescence decay profile of prompt charge-transfer (CT) fluorescence of CzNDI (1 wt. % in PMMA) film ($\lambda_{\text{exc.}} = 373$ nm, $\lambda_{\text{monitored}} = 680$ nm, $\tau_{\text{avg.}} = 3.5$ ns). d) Low temperature solvatochromism studies on the phosphorescence emission of CzNDI at 77 K ($\lambda_{\text{exc.}} = 380$ nm, delay time = 20 ms, [CzNDI] = 0.05 mM). Absence of any significant change in the emission spectra with solvent polarity suggest the presence of a locally excited (³LE) triplet state. e) Phosphorescence spectrum ($\lambda_{\text{exc.}} = 380$ nm, delay time = 20 ms) of CzNDI film (1 wt. % in PMMA) at 15 K and (³LE) phosphorescence spectrum of NDI-butyl (acceptor) in THF at 77 K ([NDI-butyl] = 0.05 mM, $\lambda_{\text{exc.}} = 340$ nm, delay time 20 ms). f) Temperature dependent delayed fluorescence decay spectra of CzNDI film (1 wt. % in PMMA) monitored at 570 nm, where phosphorescence has negligible contribution ($\lambda_{\text{exc.}} = 380$ nm). Increasing lifetime ($\tau_{\text{avg.}} = 89.5$ μ s) at 300 K compared to 15 K (lifetime spectra could not be fitted at this temperature because of low intensity) suggests a DF behaviour at this wavelength range. IRF = Instrument Response Function. In all cases 1 wt. % CzNDI-PMMA composition was used and the excitation wavelength was 380 nm unless otherwise mentioned.

On the other hand, PMMA (1 wt. %) films of **CzNDI** showed a weak CT emission ($\lambda_{\text{exc.}} = 380$ nm) in the 550-800 nm region unlike its non-fluorescent nature in solution state (Figures 5.2a and 5.3a) with a prompt lifetime of 3.45 ns ($\lambda_{\text{exc.}} = 373$ nm, $\lambda_{\text{monitored}} = 680$ nm), probably due to a non-orthogonal, excited state conformation in the solid-state (Figure 5.9a). Delayed emission feature is also observed for **CzNDI** films at 300 K as confirmed by a gated emission spectrum (delay time = 50 μ s, $\lambda_{\text{exc.}} = 380$ nm) in the same wavelength region (550-800 nm, $\lambda_{\text{max.}} = 680$ nm) hinting towards similar DF and RTP characteristics as that of **CzPhNDI** (Figures 5.9b and 5.9c). Time-gated emission spectra (20 ms delay time, $\lambda_{\text{exc.}} = 380$ nm) obtained at 15 K showed a 80 nm red- shift compared to room temperature steady-state emission (Figure 5.9b). This low energy emission with a maximum at 680 nm, can be attributed to the locally excited phosphorescence because of its high lifetime ($\tau_{\text{avg.}} = 3.1$ ms, $\lambda_{\text{exc.}} = 380$ nm, $\lambda_{\text{monitored}} = 680$ nm) (Figure 5.9c, Figure S9d). In addition, gradual decrease in the lifetime on increasing the temperature (Figure 5.9c) reiterates (3.1 ms at 15 K to 80.5 μ s at 300 K, $\lambda_{\text{exc.}} = 380$ nm, $\lambda_{\text{monitored}} = 680$ nm) its phosphorescence character similar to **CzPhNDI** at this wavelength. However, unlike **CzPhNDI**, this phosphorescence band neither originates from carbazole (donor) or NDI (acceptor) components (Figure 5.9e). Nonetheless, similar phosphorescence behaviour at low temperatures has been recently shown in donor-acceptor cNDI derivatives by Higginbotham and co-workers, wherein certain conformations of the molecule lead to enhanced conjugation between the donor (triphenyl amine) and acceptor sub-units (NDI) resulting in a new locally excited triplet state.^[13b] A TADF feature is also exhibited by **CzNDI** as evident from decreasing lifetime while decreasing the temperature at 570 nm (Figure 5.9f, 89.5 μ s at 300 K, $\lambda_{\text{exc.}} = 380$ nm).^[23] However, overall quantum yield (2 %) was found to be much weaker than **CzPhNDI** suggesting of its weak oscillator strength of emission.

5.4. Triplet Harvesting from Core-substituted Pyromellitic Diimide via TADF and RTP

Successful demonstration of strong TADF and RTP properties through a donor-acceptor charge-transfer design prompted us to investigate other arylene diimide based molecules towards triplet harvesting. Pyromellitic anhydride, in this regard, has not been studied for triplet harvesting extensively, particularly as TADF emitters. Since, pyromellitic diimide is known as strong acceptor unit and has been exploited in many photovoltaic applications because of its rich electrochemistry,^[24] a suitable donor-substitution was envisaged towards CT emission and TADF. Therefore, with a similar donor-acceptor design principle utilizing the phenyl carbazole (PhCz) as donor unit, we synthesized **CzPhPmDI** over 5 steps starting from Durene (Figure 5.10 and see experimental section).

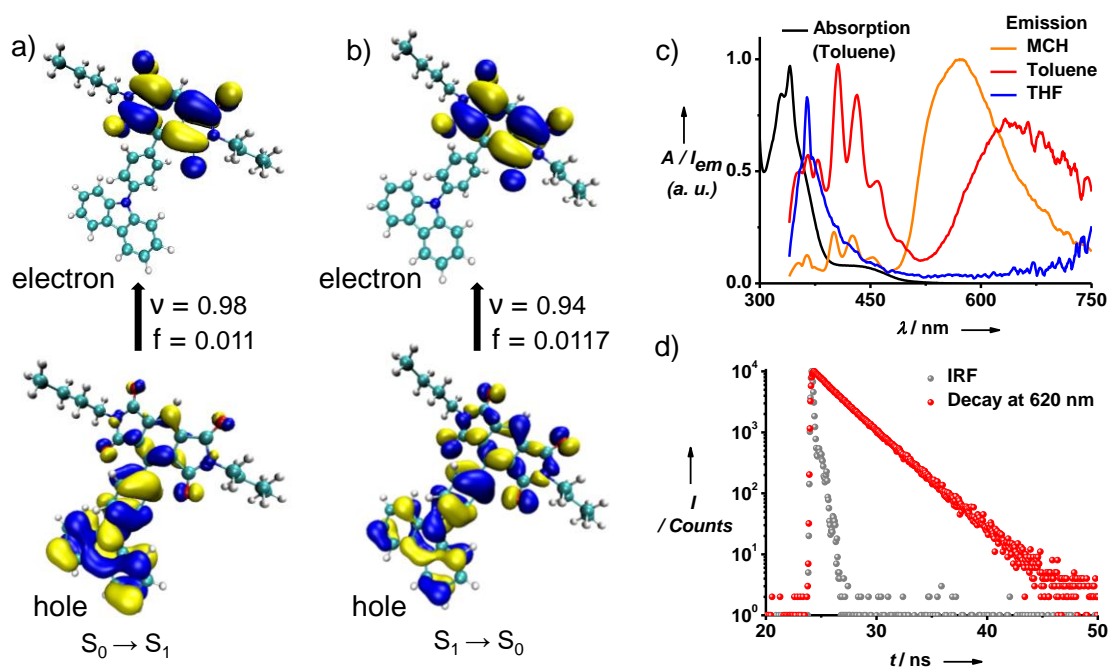


Figure 5.10. Natural transition orbitals for S_1 state at the optimized a) S_0 geometry for optical absorption and b) S_1 state geometry for emission of **CzPhPmDI** (right) using ω B97XD/6-31+g(d) level of theory in vacuum. Hole and electron wave functions with the largest weight (v), the oscillator strength for the transitions (f) are also provided. c) Absorption (toluene) and normalized emission spectra of 0.05 mM **CzPhPmDI** in different solvents showing strong solvatochromic effect ($\lambda_{exc.} = 340$ nm). d) Fluorescence lifetime profile of 0.05 mM **CzPhPmDI** in toluene ($\lambda_{exc.} = 373$ nm, $\lambda_{monitored} = 620$ nm).

At first, to have a qualitative understanding of the geometric and electronic density distribution of **CzPhPmDI**, time-dependent density functional theory (TDDFT) calculations were performed using ω B97XD/6-31G(d) level of theory. As shown in Figure 5.10a, **CzPhPmDI** adopts a twisted geometry in the ground state (S_0). The calculated dihedral angle between CzPh (donor-bridge) and PmDI (acceptor) units at optimized ground-state geometry was 59.7° . Such pre-twisted geometry is an essential criteria for a suppressed delocalization of highest occupied and lowest unoccupied molecular orbitals (HOMOs and LUMOs). As previously studied TADF-emitting NDI derivatives, spatial separation of the HOMO and LUMO orbitals lead to strong charge-transfer transition in the ground state ($S_0 \rightarrow S_1$ transition, $f = 0.013$ Figure 5.10a). Here, the HOMO was mainly localized over carbazole unit with small contribution from the spacer phenyl group. On the other hand, LUMO was exclusively delocalized on the acceptor unit (PmDI). Interestingly, in the optimized S_1 excited state, we observed increased spatial overlap of the HOMO and LUMO, plausibly due to decreased dihedral angle between the donor and acceptor units (41.2°) (Figure 5.10b). This increased overlap is a critical factor to maintain both sufficient charge-transfer transition in the molecule (ΔE_{ST}) as well as higher oscillator strength of emission ($f = 0.0186$, *vide infra*).

CzPhPmDI (0.05 mM, Toluene) show characteristic LE absorption band at 300-390 nm region and a weak CT absorption band at longer wavelength (390-480 nm region, Figure 5.10c). Solvatochromism study further reiterates the CT nature of the emission of **CzPhPmDI** at 460-750 nm region with a broad structureless features (Figure 5.10c). Fluorescence decay analysis of this band ($\lambda_{exc.} = 373$ nm, $\lambda_{monitored} = 620$ nm) shows an average lifetime of 2.41 ns although no high lifetime component (μ s or ms range) at room temperature was observed as expected from an additional delayed-emitting species (Figure 5.10d).

However, **CzPhPmDI** doped PMMA films showed remarkably strong delayed emission feature which is reminiscent of triplet excited state contribution, as evident from increased emission intensity under vacuum ($\lambda_{exc.} = 340$ nm, Figure 5.11a). Similar to previous experiments, the neat films of **CzPhPmDI** showed a quenched emission as compared to corresponding doped films in a solid polymer host (PMMA) at low concentration (1 wt. % with respect to PMMA) and hence, all further studies were performed at this composition (Figure 5.11a). To elucidate the triplet exciton contribution in the total emission profile of **CzPhPmDI**-PMMA films, time-resolved emission spectroscopy was performed at different temperatures. At first, time-resolved decay experiments of 1 wt. % **CzPhPmDI**-PMMA film were performed at two different time-ranges ($\lambda_{exc.} = 340$ nm, $\lambda_{monitored} = 570$ nm). In the short-time range (1 ns-20 μ s) this hybrid film showed a bi-exponential decay with clear prompt fluorescence with a lifetime of 38.3 ns (37 %)

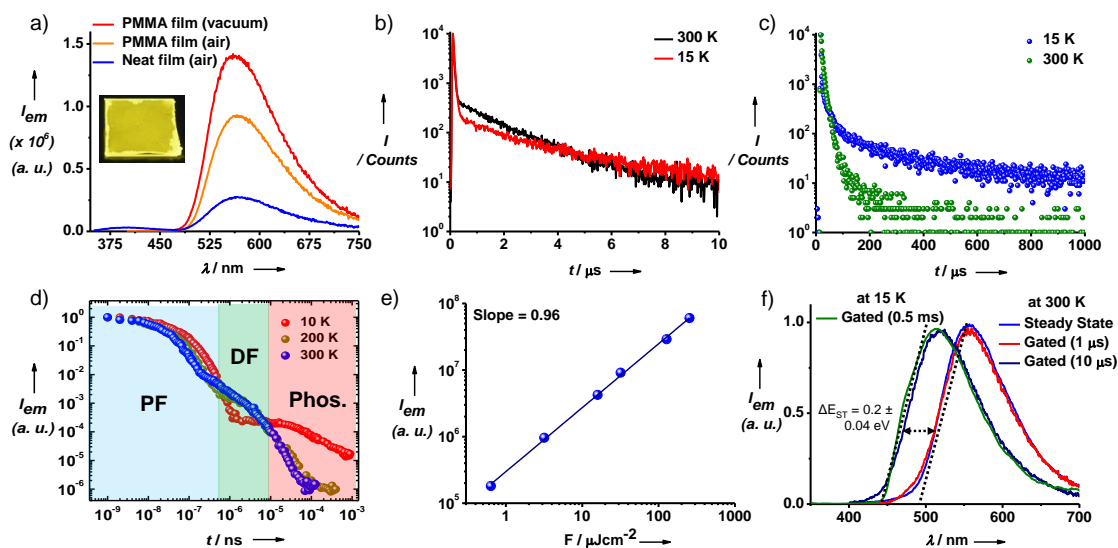


Figure 5.11. a) Emission spectra of **CzPhPmDI** in neat film as well as in doped-PMMA film under aerated and vacuum conditions ($\lambda_{exc.} = 340$ nm). Inset: Photograph of **CzPhPmDI** in film state under 365 nm UV-lamp. Lifetime profiles of **CzPhPmDI**-PMMA hybrid film obtained at different temperatures while monitoring at b) short time-range and c) longer time-range, showing TADF and RTP characteristics, respectively ($\lambda_{exc.} = 340$ nm, $\lambda_{monitored} = 570$ nm). d) Temperature dependent emission decay profile of **CzPhPmDI**-PMMA hybrid film obtained at different delay times showing prompt fluorescence at early-time and delayed fluorescence or phosphorescence at longer time-delays. e) Excitation intensity dependent emission profile of **CzPhPmDI**-PMMA film excited at 355 nm. f) Normalized emission spectra of PMMA films of **CzPhPmDI** at different temperatures with variable time-delays (1 μ s, 10 μ s and 0.5 ms) showing TADF and phosphorescence ($\lambda_{exc.} = 355$ nm). In all cases 1 wt. % **CzPhPmDI**-PMMA was used.

and a delayed emission with lifetime of 1.48 μ s (63 %). The relative contribution of these two components are written in the parenthesis (Figure 5.11b). Interestingly, along with this long-lived delayed emission component, an additional delayed lifetime component was identified in the longer time-range (0.05-1 ms) (Figure 5.11c). In order to underpin the origin of these two different delayed emission components, temperature-dependent transient lifetime experiments were performed at the same wavelength (570 nm) and time-ranges. Interestingly, at the shorter lifetime range the observed delayed emission component (1.48 μ s, 63 % at 300 K) reduces to 1.41 μ s (39 %) at 15 K suggesting the acceleration of RISC from the triplet to singlet excited states following a conventional TADF process. On the other hand, when similar experiments were conducted at longer time-range, a sharp increase in the average lifetime was observed with decreasing temperature (from 143 μ s at 15 K to 23.8 μ s at 300 K) at same monitoring wavelength ($\lambda_{exc.} = 340$ nm, $\lambda_{monitored} = 570$ nm). This contrasting behaviour of delayed emission arising from

the same **CzPhPmDI-PMMA** film hints towards a significant RTP contribution in the longer time-range. Furthermore, temperature dependent time-resolved emission spectra was obtained by examining the emission intensity ($\lambda_{\text{exc.}} = 355 \text{ nm}$) at different time-delays to comprehensively elucidate the time-scales of various processes occurring in the **CzPhPmDI-PMMA** hybrid films (Figure 5.11d). As evident from Figure 5.11d, at early delay-time (0-100 ns), prompt fluorescence is dominating without any significant change in the emission intensity with temperature. However, upon increasing the delay time (1-10 μs range), we observed an increase in delayed emission intensity with increasing temperature reiterating the DF nature of the emission at this time-range. Further increase in the delay-time (10 μs -50 μs) showed a decrease in delayed emission intensity with increasing temperature which is in line with the phosphorescence nature of the emission at this longer-time range where all shorter-lived components are excluded. In order to elucidate the mechanism behind observed DF an excitation-intensity dependent DF measurement was performed ($\lambda_{\text{exc.}} = 355 \text{ nm}$, Figure 5.11e). A linear dependence of the DF intensity with a slope of 0.96, unambiguously prove the thermally activated nature of the emission, in contrast to a bimolecular triplet-triplet annihilation (TTA) mechanism where a quadratic dependence is usually observed.^[22] Having obtained a comprehensive understanding of the both TADF and RTP characteristics of the **CzPhPmDI-PMMA** films, we further investigated the nature of the phosphorescence emission which is crucial to understand the RISC process between triplet and singlet excited states (*vide infra*). Time-resolved emission profile of these films show a striking blue-shift at high time-delay (>10 μs). Interestingly, at shorter delay time (<10 μs) the emission profile completely matches with the steady-state emission of the **CzPhPDI-PMMA** films (Figure 5.11f). This observation hints towards an additional higher energy state as compared to the singlet charge-transfer (¹CT) state which represent the phosphorescence and fluorescence (both prompt and delayed) bands of **CzPhPDI-PMMA** films, respectively.

In order to understand the nature triplet excited state that lead to efficient RTP in **CzPhPmDI**, time-resolved emission at low temperature (15 K) was conducted. Interestingly, the phosphorescence band (delay time = 0.5 ms, ($\lambda_{\text{exc.}} = 340 \text{ nm}$) at 15 K, clearly matches with the RTP emission profile (Figure 5.12a). In addition, solvatochromism studies of **CzPhPmDI** (dissolved in THF or MCH at 0.05 mM concentration) was performed at 77 K, to distinguish the LE or CT nature of the phosphorescence band. As can be seen from Figure 5.12b, the phosphorescence bands of **CzPhPmDI** in MCH, toluene and THF do not show any significant shift with respect to the change in polarity, therefore hinting towards the LE nature of the emission. In addition to this crucial observation, strong vibronic features and identical phosphorescence profile of **CzPhPmDI** with the phosphorescence profile of individual donor

(CzPh) and acceptor (PmDI) units unambiguously confirm its locally excited nature (^3LE). Hence, together with a strong DF feature, the **CzPhPmDI-PMMA** hybrid thin films exhibit strong RTP as well. Such RTP emission from higher-lying excited triplet state (T_n , $n>1$) is commensurate with the LE nature of the band involving multiple carbonyl groups, as has been previously reported by Dias and co-workers.^[16] Based on the emission profile (both at room temperature and 15 K), a simplified Jablonski diagram is proposed in Figure 5.12c. As can be seen from Figure 5.12c, while exciting at the LE absorbance band (340 nm), first ^1CT is first formed (via internal conversion) which competes with an ISC to the nearby ^3LE state.

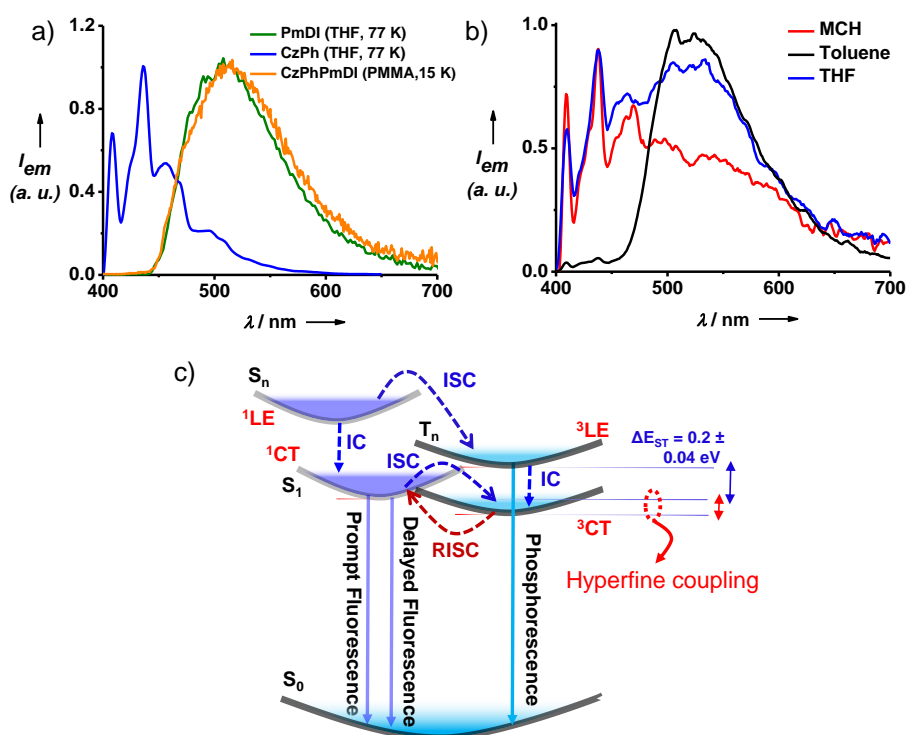


Figure 5.12. a) Phosphorescence spectrum ($\lambda_{exc.} = 340$ nm, delay time = 0.5 ms) of **CzPhPmDI** film (1 wt. % in PMMA) at 15 K and (^3LE) phosphorescence spectrum of **CzPh** (donor) and **PmDI-butyl** (acceptor) in THF at 77 K ($[\text{PmDI-butyl}] = 0.05$ mM, $\lambda_{exc.} = 340$ nm, delay time 20 ms). b) Low temperature solvatochromism studies on the phosphorescence emission of **CzPhPmDI** at 77 K ($\lambda_{exc.} = 380$ nm, delay time = 1 ms, $[\text{CzPhPmDI}] = 0.05$ mM). Absence of any significant change in the emission spectra with solvent polarity suggest these phosphorescence bands are of locally excited (^3LE) character. c) Simplified Jablonski diagram for **CzPhPmDI** indicating various excited state process involving the triplet exciton harvesting. In case of **CzPhPmDI**, higher energy ^3LE plausibly does not participate in reverse intersystem crossing (RISC) process with the ^1CT state through spin-orbit coupling mechanism, however, a hyperfine coupling between the ^1CT and ^3CT states is proposed to mediate spin-flipping process.^[13b]

Phosphorescence from lower-lying CT state was not observed because of inherently low oscillator strength of ^3CT . Since the locally excited triplet state is higher in energy as compared to the ^1CT state ($E_{3\text{LE}} - E_{1\text{CT}} = 0.2 \pm 0.04$ eV), the fast delayed fluorescence component of **CzPhPmDI**-PMMA hybrids could be arising from the small energy gap expected between the ^1CT and ^3CT states and a hyperfine coupling mechanism is envisioned to promote the spin-flipping process between these two CT states having similar molecular orbital characteristics.^[16,18]

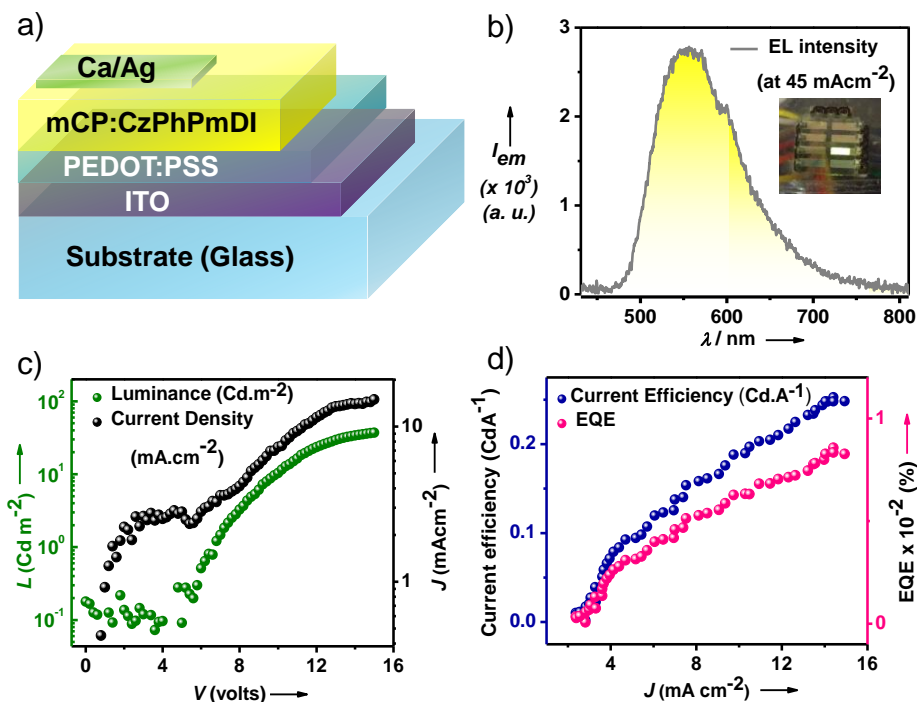


Figure 5.13. Electroluminescence characteristics of the solution-processable OLED device using **CzPhPmDI** as emitting layer: a) Schematic representation of the multi-layered device structure b) Electroluminescence spectrum of the OLED device at 45 mA cm^{-2} injection current density. The inset shows a glowing pixel of the OLED. (c) J-V-L characteristic and the d) EQE of the device, where the maximum luminescence intensity achieved is 37 cd m^2 with the maximum current efficiency 0.25 of CdA^{-1} .

The novel emission characteristics with strong triplet exciton contribution and high photoluminescence quantum efficiency (64 %) encouraged us to further explore the device application of **CzPhPmDI** as emitter in a solution-processed OLEDs. Figure 5.13 show the electroluminescence properties of **CzPhPmDI** with a multi-layered device structure (ITO/PEDOT:PSS/mCP: 20 wt. % **CzPhPmDI**/Ca/Ag). The electroluminescence spectrum of **CzPhPmDI** doped mCP is shown in Figure 5.13b, at an injection current density of 45 mA cm^{-2} . The current density-voltage-luminance (J-V-L) characteristics of the device is shown in Figure

5.13c, where the maximum luminescence intensity achieved is 37 Cdm^{-2} with the maximum current efficiency of 0.25 CdA^{-1} . The maximum EQE of the device was 0.01% (Figure 5.13d). Optimizations of the device performance is currently underway.

5.5. Blue-emitting solid-state Charge-transfer Emission from Donor-Acceptor Core-substituted Naphthalene Monoimide

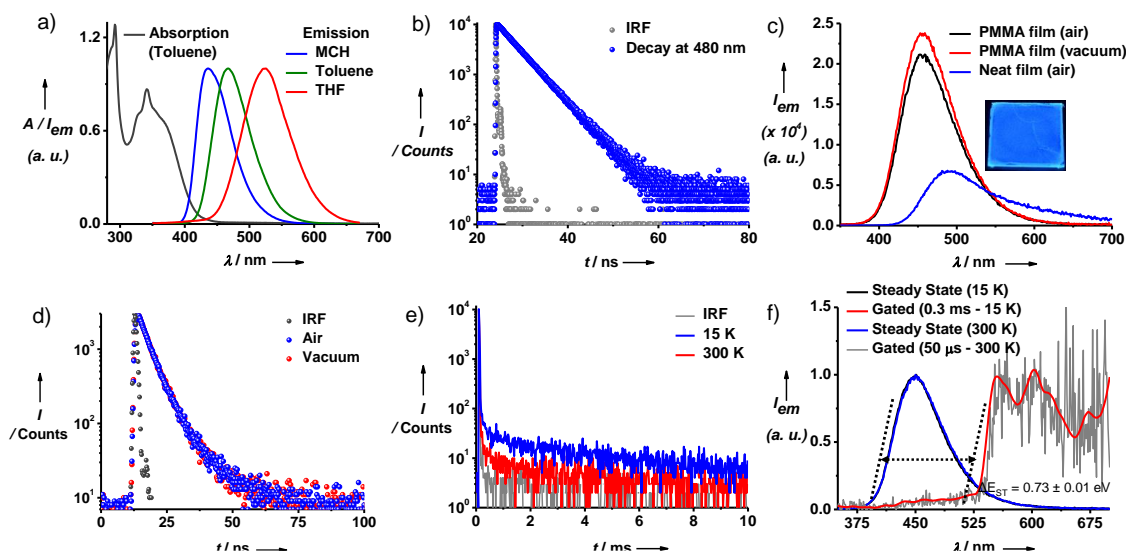


Figure 5.14. a) Absorption (toluene) and normalized emission spectra of 0.05 mM **CzPhNMI** in different solvents showing strong solvatochromic effect ($\lambda_{exc.} = 340 \text{ nm}$). b) Fluorescence lifetime profile of 0.05 mM **CzPhNMI** in toluene ($\lambda_{exc.} = 373 \text{ nm}$, $\lambda_{monitored} = 480 \text{ nm}$). c) Emission spectra of **CzPhNMI** in neat film and 1 wt. % PMMA film under air and vacuum conditions ($\lambda_{exc.} = 340 \text{ nm}$). Inset: Photograph of **CzPhNMI**-doped PMMA film under 365 nm UV-lamp. d) Fluorescence (at room temperature, $\lambda_{monitored} = 450 \text{ nm}$) and e) temperature dependent phosphorescence decay profiles ($\lambda_{monitored} = 570 \text{ nm}$) of **CzPhPmDI**-PMMA hybrid film excited at 340 nm. f) Normalized emission spectra of **CzPhPmDI**-PMMA film at different temperatures with different delay times (50 μs and 0.3 ms) showing very weak phosphorescence ($\lambda_{exc.} = 340 \text{ nm}$). In all cases 1 wt. % **CzPhNMI**-PMMA composition was used.

Naphthalene monoimides are one of the most exploited fluorophores in the arylene diimide family for various luminescence applications such as optical sensing, bio-imaging and lighting devices, because of their relatively easier synthesis and strong emission quantum yields.^[25] In recent years, naphthalene monoimides have been studied for ambient triplet harvesting via room temperature phosphorescence utilizing heavy-atom substitution or charge-transfer design principles.^[26] However, a systematic study towards triplet harvesting from this novel class of materials by means of thermally activated delayed fluorescence is not well-

explored.^[27] Based on our previous studies on naphthalene as well as pyromellitic diimides, we therefore designed and synthesized a carbazole-substituted naphthalene monoimide (**CzPhNMI**) with a phenyl spacer in between the donor and acceptor units (See Experimental Section) aiming ambient triplet harvesting via TADF mechanism.

In order to understand the photophysical properties of **CzPhNMI**, detailed absorption and time-resolved emission experiments were performed. **CzPhNMI** (toluene, 0.05 mM) shows a locally excited absorption band at 280-350 nm region with sharp vibronic features. In addition a broad structure-less band was observed in the longer wavelength region, which is designated as a CT band. In the excited state, CT nature of **CzPhNMI** was further confirmed by strong solvatochromism with changing the polarity of the solvents (Figure 5.14a). However, as expected, no DF characteristics was observed in solution state from the CT emission band which exhibited only a short average lifetime of 4.3 ns ($\lambda_{\text{exc.}} = 373$ nm, $\lambda_{\text{monitored}} = 480$ nm, Figure 5.14b). In neat film state, **CzPhNMI** showed a cyan-emitting band which blue-shifts significantly with substantial increase in intensity (PLQY = 71%) when it was dispersed in low concentration (1 wt. %) in PMMA (Figure 5.14c). However, PMMA-hybrid films of **CzPhNMI** do not show any delayed emission characteristics even under vacuum as evident from similar spectroscopic features in its emission profile (Figure 5.14c). Furthermore, we did not observe any new delayed emission contribution from the lifetime profile which remain unchanged under vacuum (Figure 5.14d, $\lambda_{\text{exc.}} = 340$ nm, $\lambda_{\text{monitored}} = 450$ nm, $\tau_{\text{avg.}} = 5.79$ ns under air and $\tau_{\text{avg.}} = 5.80$ ns under vacuum). To elucidate the triplet state characteristics of **CzPhNMI** we further investigated phosphorescence profile at low temperature (15 K). As evident from Figure 5.14d and 5.14e, **CzPhNMI** shows a weak phosphorescence at 540-700 nm region with average lifetime of 2.3 ms ($\lambda_{\text{exc.}} = 340$ nm, $\lambda_{\text{monitored}} = 570$ nm). The phosphorescence nature of this band was further reiterated from decreasing average lifetime at room temperature (Figure 5.14e). In addition, a striking similarity of phosphorescence (at 77 K, THF) of the brominated-naphthalene monoimide (**BrNMI**) having sharp and vibronic features, with the phosphorescence band of **CzPhNMI** at 15 K suggests that the lowest triplet excited state of **CzPhNMI** is again LE in nature (Figure 5.15a and 5.15b, *vide infra*) like previously studied NDI derivatives. A simple Jablonksi diagram depicting the lowest excited triplet and singlet manifolds of **CzPhNMI** suggest a large singlet-triplet gap ($\Delta E_{\text{ST}} = 730 \pm 10$ meV) which is unfavourable for any RISC process and hence no TADF component could be observed in case of **CzPhNMI**.

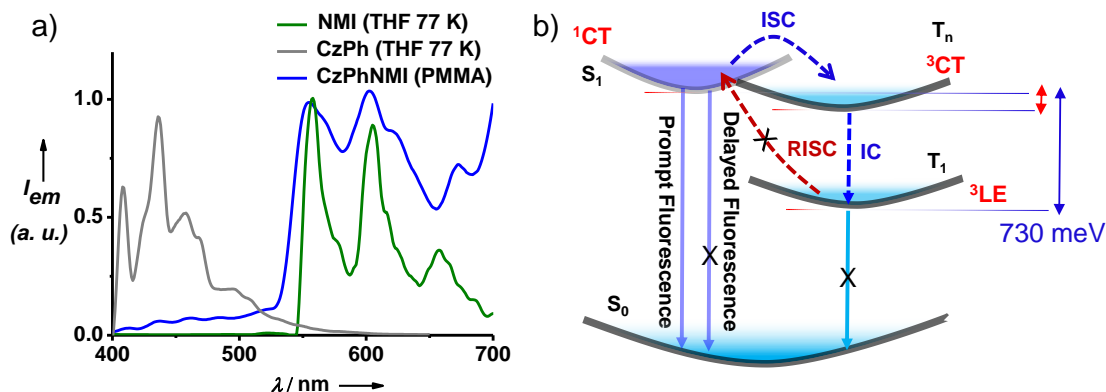


Figure 5.15. a) Phosphorescence spectrum ($\lambda_{exc.} = 340$ nm, delay time = 0.5 ms) of **CzPhNMI** film (1 wt. % in PMMA) at 15 K and (3LE) phosphorescence spectrum of **CzPh** (donor) and **BrNMI** (acceptor) in THF at 77 K ($[BrNMI] = 0.01$ mM, $\lambda_{exc.} = 340$ nm, delay time 20 ms). b) Simplified Jablonski diagram of **CzPhNMI** showing large gap between the 1CT and 3LE states and therefore no reverse intersystem crossing through a spin-orbit coupling mechanism is expected. The hyperfine coupling effect is also envisioned to be negligible as internal conversion from 3CT to lower-lying 3LE will be spin-allowed (Kasha's Rule) and faster process as compared to reverse intersystem crossing to 1CT from 3CT states.

5.6. Conclusions

In conclusion, we have shown an efficient dual DF and RTP emission under ambient and amorphous conditions from cNDI derivatives by a clever molecular design to facilitate the triplet harvesting. Time-resolved photoluminescence studies and TDDFT calculations further provided a structure-property relationship to fine-tune the emission oscillator strength and charge-transfer states of these donor-acceptor molecules. We envisage that this study opens up an exciting, hitherto unexplored triplet harvesting of interesting class of cNDI family, by using the well-established, rich chemistry of core-substitution. In fact, following this design rule, we further studied and successfully demonstrated efficient triplet harvesting from a similar core-substituted, yellow-emitting donor-acceptor pyromellitic diimide derivative with high quantum efficiency. A hyperfine coupling between the two charge-transfer states involved in the reverse intersystem crossing process is envisaged here to result in very fast delayed fluorescence component (~ 1.5 μ s). However, apart from maintaining the oscillator strength through the adjustment of spatial overlap between the donor and acceptor subunits, we underpinned the importance of the confinement of charge-transfer excited states within the vicinity of locally-excited triplet state is crucial for effective triplet harvesting in case of similar donor-acceptor charge-transfer derivative, **CzPhNMI**. Nonetheless, Further extension of these designs to other electron deficient

arylene diimides (especially the perylene family) would be the next step to achieve NIR-emitting triplet-emitting dyes for applications in bio-imaging and OLEDs.^[28]

5.7. Experimental Section

5.7.1. General Methods

NMR Measurements: ¹H and ¹³C NMR spectra were recorded on a BRUKER AVANCE-400 fourier transformation spectrometer with 400 and 100 MHz respectively. The spectra are calibrated with respect to the residual solvent peaks. The chemical shifts are reported in parts per million (ppm) with respect to TMS. Short notations used are, s for singlet, d for doublet, t for triplet, q for quartet and m for multiplet.

Optical Measurements: Electronic absorption spectra were recorded on a Perkin Elmer Lambda 900 UV-Vis-NIR Spectrometer and emission spectra were recorded at FLSP920 spectrometer, Edinburgh Instruments. UV-Vis and emission spectra were recorded in 10 mm path length cuvette. Fluorescence spectra of films were recorded in front-face geometry to avoid self-absorption at high concentrations. Temperature dependent photoluminescence spectra were recorded at the same instrument using a cryostat to control the temperature (Advanced Research Systems).

Lifetime measurements and quantum yield: Fluorescence lifetimes were performed on a Horiba Delta Flex time-correlated single-photon-counting (TCSPC) instrument. A 373 nm nano-LED with a pulse repetition rate of 1 MHz was used as the light source. The instrument response function (IRF) was collected by using a scatterer (Ludox AS40 colloidal silica, Sigma-Aldrich). Phosphorescence, delayed fluorescence lifetime ($\lambda_{exc} = 380$ nm) and gated emission was measured on FLSP920 spectrometer, Edinburgh Instruments equipped with a micro flash lamp (μ F2) set-up. Quantum yield was measured using an integrated sphere. Temperature dependent lifetimes spectra were recorded at the same instrument using a cryostat to control the temperature (Advanced Research Systems).

High Resolution Mass Spectroscopy (HRMS): HR-MS was carried out using Agilent Technologies 6538 UHD Accurate-Mass Q-TOF LC/MS.

Matrix-Assisted Laser Desorption Ionization (MALDI): MALDI was performed on a Bruker daltonics Autoflex Speed MALDI TOF System (GT0263G201) spectrometer using *trans*-2-[3-(4-*tert*-Butylphenyl)-2-methyl-2-propenylidene]malononitrile (DCTB) as the matrix.

Cyclic Voltammetry: The cyclic voltammograms were recorded in dry and degassed dichloromethane (10 ml), with Bu₄NPF₆ (0.1 M) as the supporting electrolyte at room

temperature (scan rate = 100 mV/s). The working electrode was a Pt disc, counter electrode was a Pt wire and the reference electrode was Ag/AgCl wire. The HOMO and LUMO values are estimated by the ferrocene/ferrocenium redox couple as internal standard from the following equations:

$$E_{\text{HOMO}} = -(E^{\text{ox}} + 4.35) \text{ eV} \quad E_{\text{LUMO}} = -(E^{\text{Red}} + 4.35) \text{ eV}$$

Where E^{ox} and E^{Red} are the oxidation and reduction potential from cyclic voltammetry. The CV measurements revealed that both derivatives **CzNDI** and **CzPhNDI** show two electron reversible reduction peaks, whereas two electron quasi reversible peaks are observed during oxidation cycles (Figure 5.2c and 5.2d). In the anodic sweep, the first oxidation peaks for **CzNDI** and **CzPhNDI** were found to be at +0.91 V and +0.82 V, respectively. Similarly, the first reduction peaks for **CzNDI** and **CzPhNDI** were observed at -0.49 V and -0.64 V, respectively. The calculated HOMO energies of **CzNDI** and **CzPhNDI** were -5.26 eV and -5.17 eV, respectively. The calculated LUMO energies of **CzNDI** and **CzPhNDI** were -3.86 eV and -3.71 eV, respectively.

Computational Details: All the molecules were optimized in their ground state using ω B97XD^[29] functional for each molecule and then their optimal ω values for ω B97XD functional were calculated. The optimal ω value was obtained by minimizing J^2 as follows:^[30-31]

$$J^2 = \sum_{i=0}^1 [\epsilon_H(N+i) + IP(N+i)]^2$$

Where ϵ_H and IP are the HOMO energy of and ionization potential of a given molecule or ion, respectively, and N is the number of electron in the molecule or ion. The optimal ω values are provided in Table S1. The ω PB97XD functional with optimal ω value is referred as ω^* PB97XD functional. The optimal ω was used to optical absorption and to optimize their S_1 -state and T_1 -state geometries using TDDFT. Tamm-Dancoff approximation (TDA)^[32] was considered for the calculation for triplet energies to overcome the triplet instability issue. For all the cases optimization of geometries and calculation of optimal ω value were done using 6-31g(d) basis set, whereas the single point energy calculation of ground-state (S_0 -state), S_1 -state and T_1 -state geometries were done using 6-31+g(d) basis set. Nature of the excited states was described using natural transition orbital (NTO) analysis.^[33] All the calculations were performed using Gaussian 16 software.^[34]

Device fabrication: ITO coated glass substrate was used as the bottom electrode for the device and which was pre-cleaned with soap solution, deionized water, Acetone and isopropanol in a sonication bath for 10 min (each step). Then, oxygen plasma ashing was done to remove the

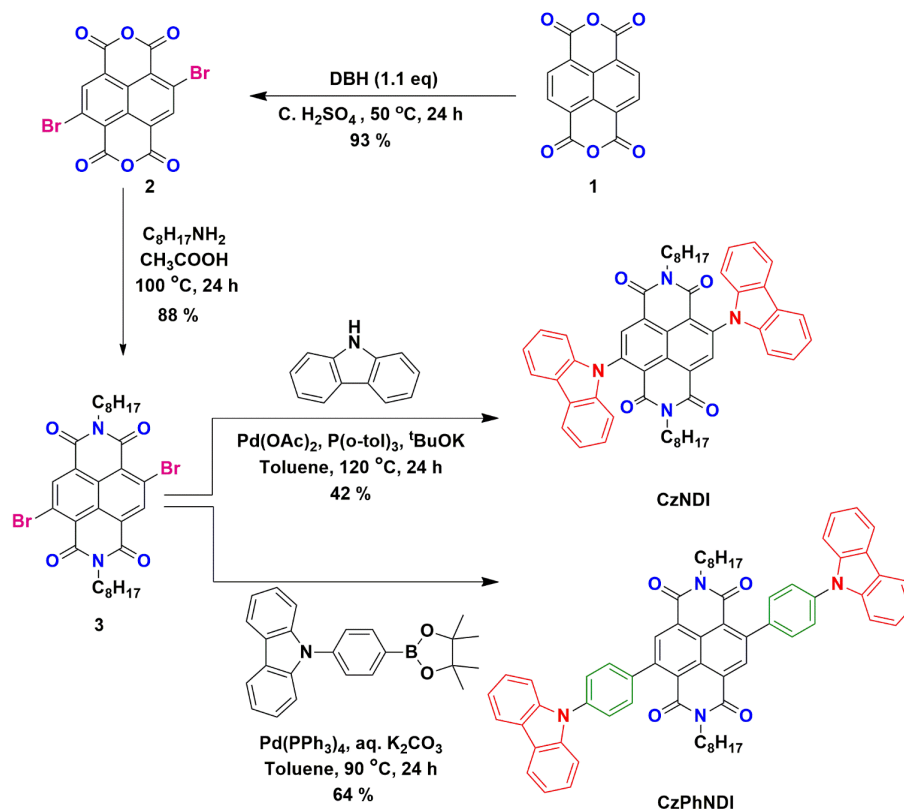
surface impurities and to make the glass surface hydrophilic. Hole injection layer (PEDOT:PSS) was then spin coated at 400 rpm speed for 50 seconds and annealed at 150 °C for 30 minutes under nitrogen atmosphere. Then chloroform solution of **CzPhPmDI** doped in mCP host (20 wt. % **CzPhPmDI** in mCP) was spin-coated at 2000 rpm for 45 seconds inside the nitrogen-filled glove-box and annealed at 80 °C for 20 minutes. The top electrode Ca/Ag (thickness 20 nm and 80 nm, respectively) was deposited using thermal evaporation at 0.1 Å s⁻¹ initial rate. The steady-state J-V-L measurements were done using a Keithley 2400 source-meter and 2000 multi-meter and calibrated silicon detector.

5.7.2. Synthesis

5.7.2a. Synthesis of **CzNDI** and **CzPhNDI**

Naphthalene dianhydride (**1**) and 1,1-dimethyl-5,5-dibromohydantoin (DBH), Pd(OAc)₂, Pd(PPh₃)₄, potassium *tert*-butoxide, tri(*o*-tolyl)phosphine were purchased from Sigma-Aldrich; 9H-Carbazole-9-(4-phenyl)boronic acid pinacol ester, Carbazole were purchased from Alfa Aesar; K₂CO₃, Iodobenzene, Cu, *n*-butyl amine and *n*-octyl amine were purchased from Spectrochem and used without further purification.

5.7.2b Synthetic Scheme:



Scheme 5.1. Synthetic scheme for *CzNDI* and *CzPhNDI*.

5.7.2c. Synthetic Procedure

Compound **2** and **3** were synthesized according to literature procedure.^[20a]

Synthesis of CzNDI: Brominated naphthalene dianhydride, **3** (0.15 g, 0.23 mmol) and carbazole (0.1 g, 0.58 mmol) were taken in 100 mL round bottomed (RB) flask. Anhydrous toluene (12 mL) was added to the above mixture under N₂ atmosphere. This mixture was then purged with N₂ for about 15 min. To this reaction mixture tri(*o*-tolyl)phosphine (6 mg, 8 mol%) and Pd(OAc)₂ (2 mg, 4 mol%) were added and purged with N₂ for another 15 min. To this solution potassium *tert*-butoxide (155 mg, 1.38 mmol) was added and finally purged the whole mixture with N₂ for additional 5 minutes. Later this solution was refluxed at 120 °C for 24 h and monitored by TLC. After completion of starting materials, water was added and extracted with chloroform (150 mL). Organic layer was washed with brine solution and dried over anhydrous Na₂SO₄. Solvent was removed under vacuum and the resulting mixture was purified by silica gel (100-200 mesh) column chromatography.

CzNDI: Dark purple solid (69 mg, yield 42 %); ¹H NMR (400 MHz, CDCl₃, ppm): δ_H = 9.03 (s, 2H), 8.22 (d, *J* = 7.2 Hz, 4H), 7.43-7.36 (m, 8H), 7.19 (d, *J* = 7.6 Hz, 4H), 4.01 (t, *J* = 7.6 Hz, 4H), 1.30-1.21 (m, 24H), 0.84 (t, *J* = 6.4 Hz, 6H); ¹³C NMR (100 MHz, CDCl₃, ppm): δ_C = 161.5, 159.8, 140.5, 139.9, 134.2, 127.9, 127.8, 126.3, 124.7, 121.5, 121.0, 120.9, 109.6, 41.0, 31.7, 29.2, 29.1, 27.9, 26.9, 22.6, 14.0; HRMS (ESI): calculated for C₅₄H₅₂N₄O₄: 820.3989; observed 821.4048 [M+H]⁺. MALDI-TOF (DCTB matrix, negative mode) : 820.904 [M⁻].

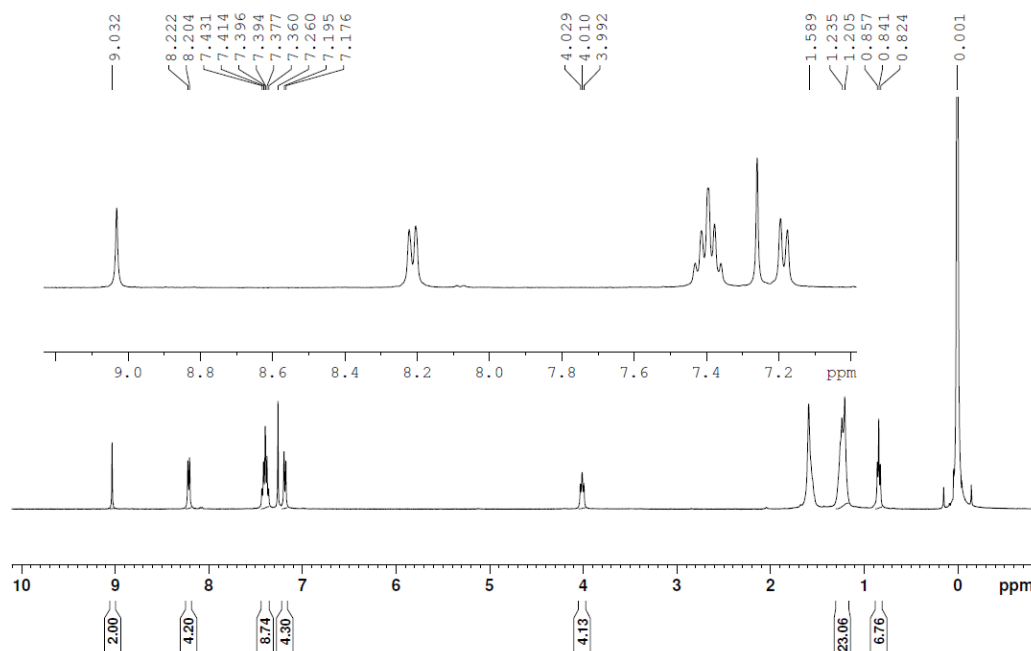


Figure 5.16. ^1H NMR spectrum of *CzNDI* in CDCl_3 .

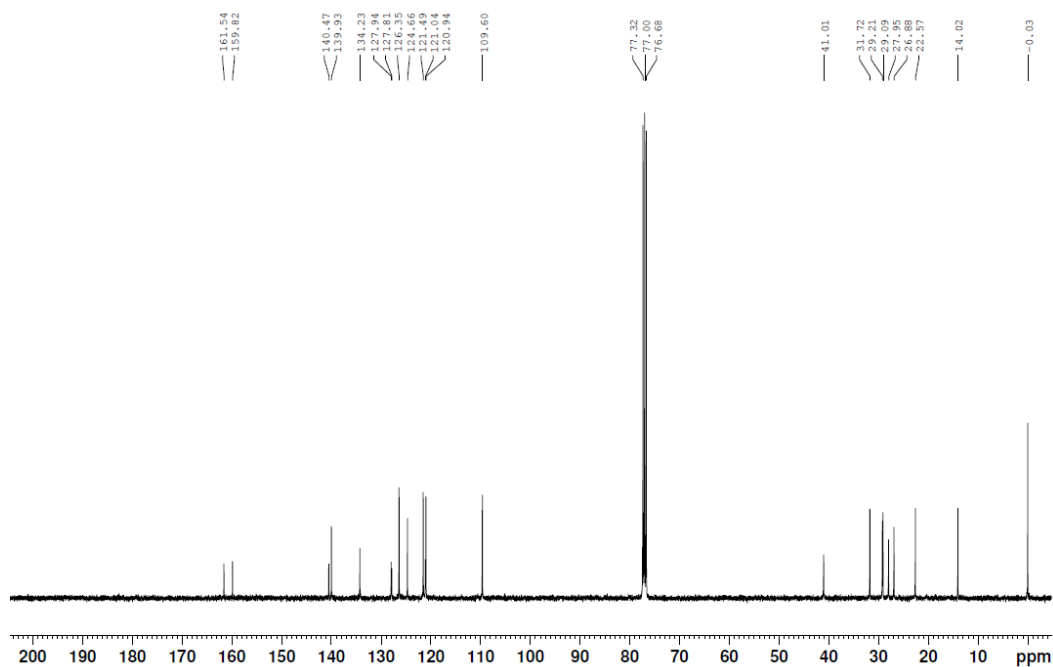


Figure 5.17. ^{13}C NMR spectrum of *CzNDI* in CDCl_3 .

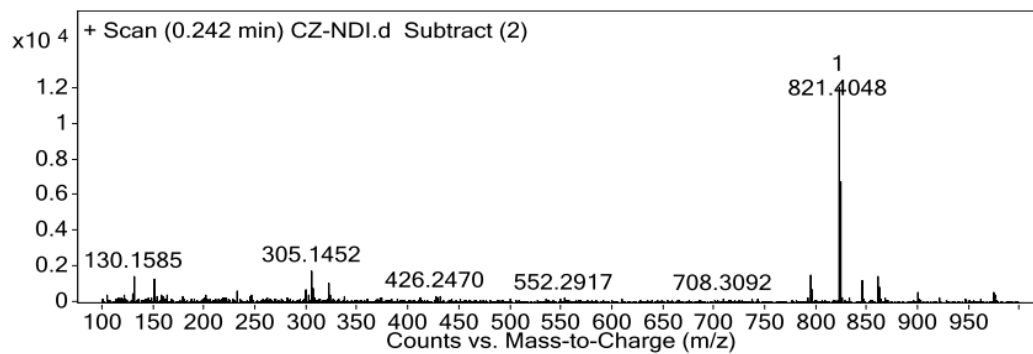


Figure 5.18. ESI-HRMS spectrum of *CzNDI*.

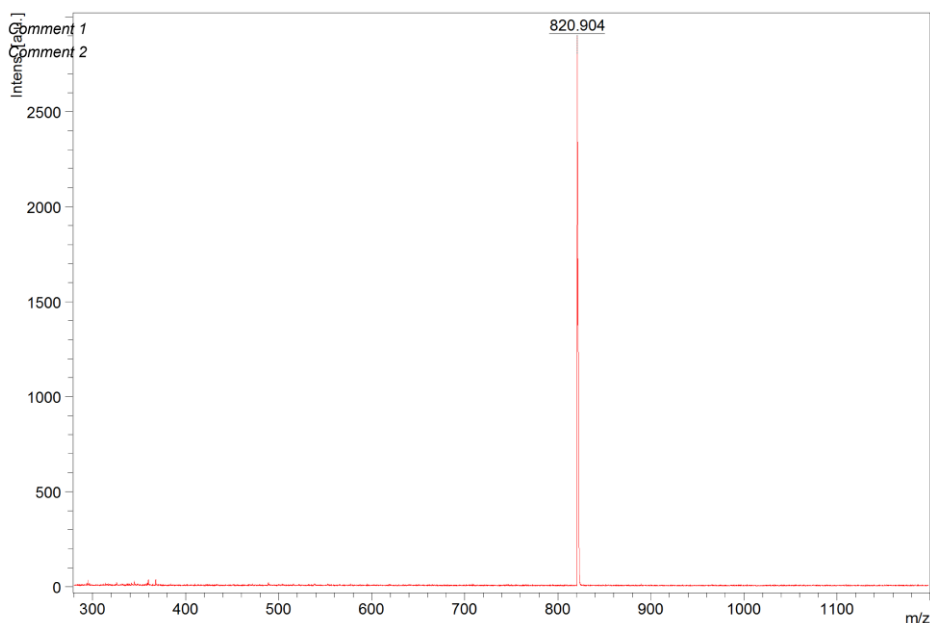


Figure 5.19. MALDI-TOF spectrum of **CzNDI**.

Synthesis of CzPhNDI: Brominated naphthalene diimide **4** (130 mg, 0.2 mmol) and 9H-Carbazole-9-(4-phenyl)boronic acid pinacol ester (0.163 g, 0.44 mmol) were taken in a 100 mL RB flask. Toluene (12 mL) was added to the above mixture under N₂ atmosphere. This mixture was purged with N₂ for about 15 min. K₂CO₃ (0.070 g, 0.50 mmol) was dissolved in millipore water (0.5 mL) and added to the above reaction mixture. Pd(PPh₃)₄ (46 mg, 20 mol%) was then added and purged with N₂ for another 15 min. The solution was refluxed at 120 °C for about 24 h and the reaction was monitored by TLC. After completion of starting material water was added and extracted with chloroform (150 mL). Organic layer was washed with brine solution and then dried over anhydrous Na₂SO₄. Organic layer was concentrated under vacuum and purified by silica gel (100-200 mesh) column chromatography.

CzPhNDI: Red solid (120 mg, yield 64 %); ¹H NMR (400 MHz, CDCl₃, ppm): δ_H = 8.78 (s, 2H), 8.18 (d, *J* = 8.0 Hz, 4H), 7.77 (d, *J* = 8.4 Hz, 4H), 7.69 (d, *J* = 8.0 Hz, 4H), 7.40 (d, *J* = 8.0 Hz, 4H), 7.69 (d, *J* = 8.0 Hz, 4H), 7.48 (t, *J* = 8.0 Hz, 4H), 7.33 (t, *J* = 7.6 Hz, 4H), 4.15 (t, *J* = 7.6 Hz, 4H), 1.76-1.69 (m, *J* = 7.2 Hz, 4H), 1.40-1.29 (m, 20H), 0.86 (t, *J* = 6.8 Hz, 6H); ¹³C NMR (100 MHz, CDCl₃, ppm): δ_C = 162.4, 162.3, 146.8, 140.7, 139.3, 137.8, 135.9, 129.9, 127.4, 126.7, 126.0, 125.8, 123.6, 123.0, 120.3, 120.2, 110.0, 41.1, 31.8, 29.3, 29.2, 28.1, 27.1, 22.6, 14.1; MALDI-TOF (DCTB matrix, negative mode) : m/z calculated for C₆₆H₆₀N₄O₄ : 972.4615; found 972.810 [M⁻].

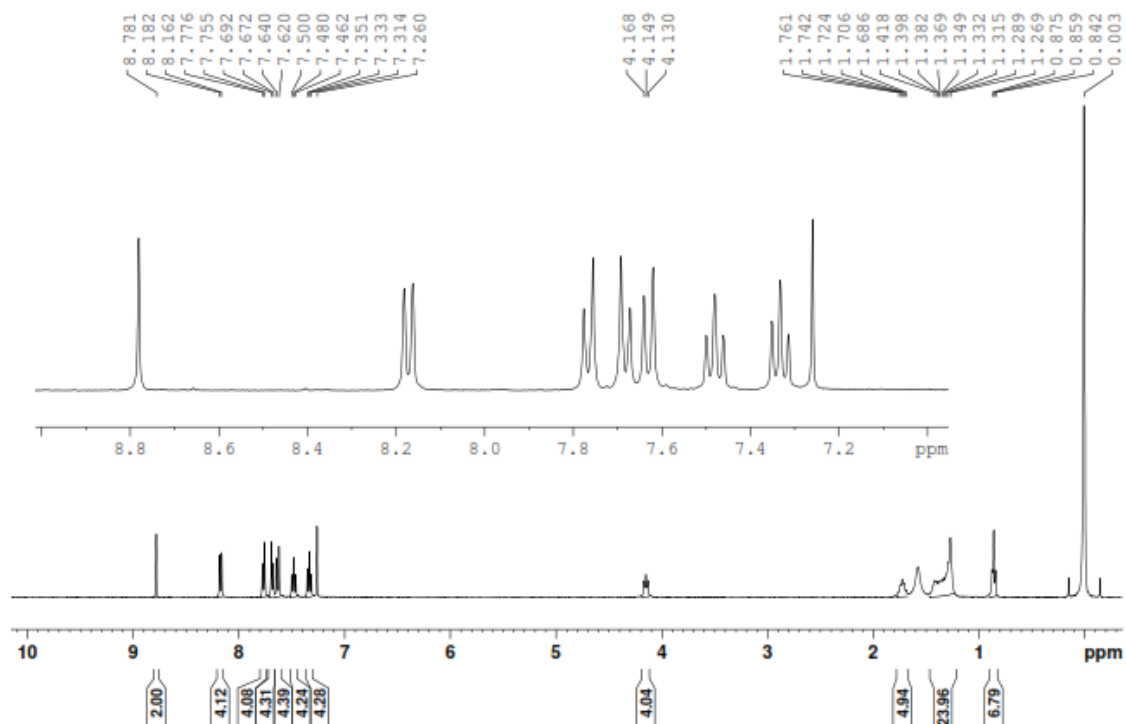


Figure 5.20. ^1H NMR spectrum of *CzPhNDI* in CDCl_3 .

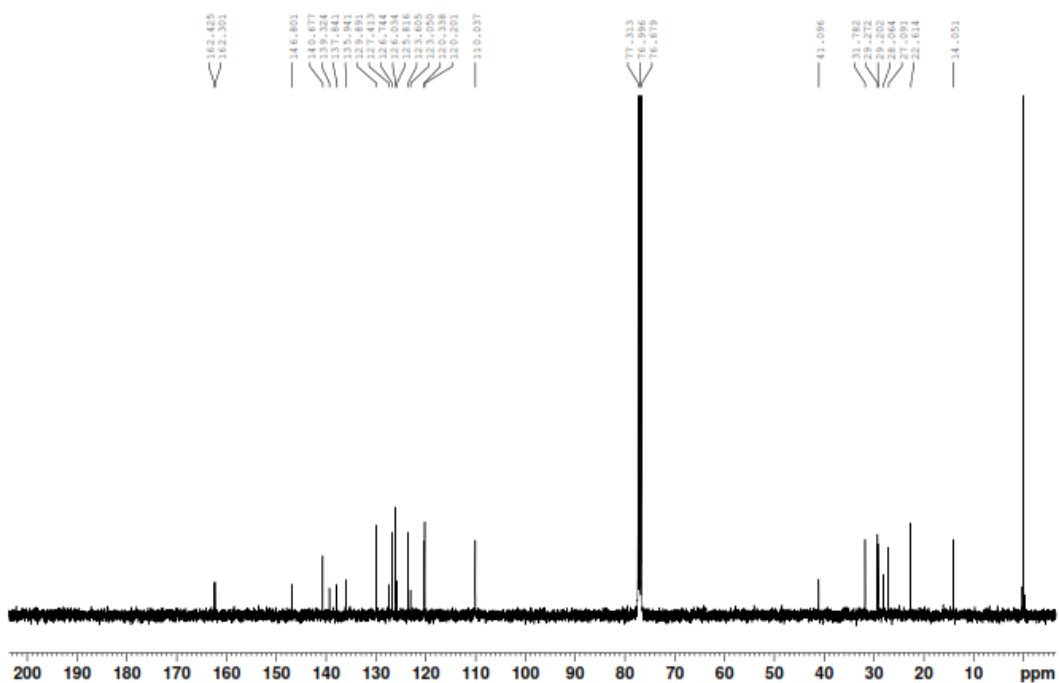


Figure 5.21. ^{13}C NMR spectrum of *CzPhNDI* in CDCl_3 .

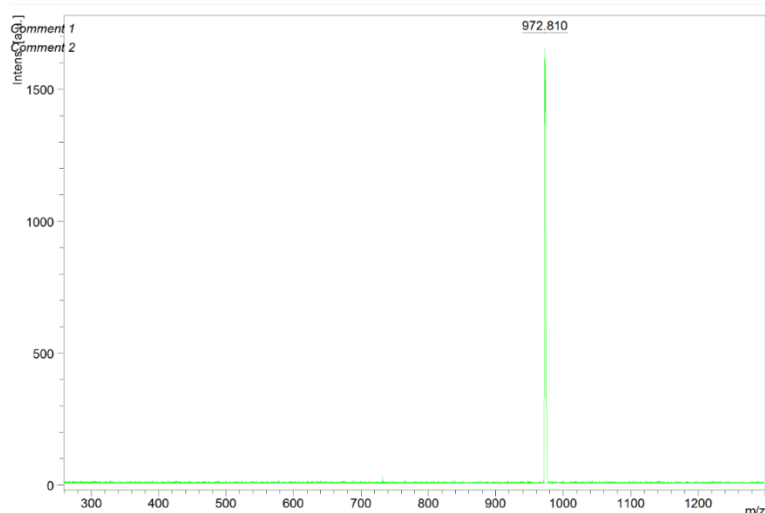


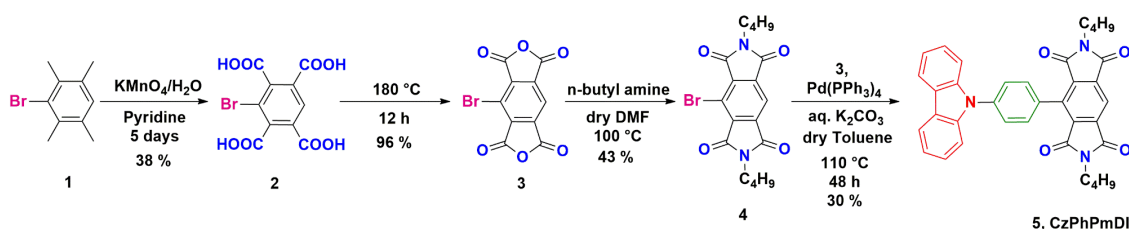
Figure 5.22. MALDI-TOF spectrum of *CzPhNDI*.

The individual donor (*CzPh*), acceptor (NDI-butyl) and (*PmDI*-butyl) molecules were synthesized according to literature procedures.^[20a, 24c, 35]

5.6.2d Synthesis of *CzPmDI*

Durene, Br₂ and Pyridine were purchased from Sigma-Aldrich used without further purification.

5.6.2e Synthetic Scheme:



Scheme 5.2. Synthetic scheme for *CzPhPmDI*.

3 was synthesized according to literature procedure.^[24c]

Synthesis of *BrPmDI* (4): Compound **1** (1 g, 3.37 mmol) was taken in a 250 round bottom flask and 100 mL acetic acid was added into it and stirred at room temperature for 30 minutes. Then *n*-butylamine (0.5 g, 6.73 mmol) was added into the reaction mixture and it was allowed to stir for 16 hours at 100 °C. After completion of the reaction 100 ml water was added into this reaction mixture to result in white precipitate. The precipitate was then filtered and dried under vacuum for 10 hours. The white crude solid was then purified by silica-gel (100-200 mesh) column chromatography using chloroform as an eluent to obtain the pure product as white solid.

BrPmDI: White solid (0.51 g, 43 % yield); $^1\text{H NMR}$ (CDCl_3 , 400 MHz, ppm): δ_{H} 8.2 (s, 1H), 3.74 (t, 4H, $J = 7.4$ Hz), 1.68 (qu, 4H, 7.5 Hz), 1.39 (h, 4H, $J = 7.4$), 0.96 (t, 6H, $J = 7.4$ Hz); $^{13}\text{C NMR}$ (CDCl_3 , 100 MHz, ppm): δ_{C} 165.0, 164.8, 138.9, 134.9, 116.5, 115.5, 38.7, 30.4, 20.1. HRMS (APCI): m/z calculated 406.0528: observed 407.0607 $[\text{M}+\text{H}]^+$.

Synthesis of CzPhPmDI: In a 250 ml two neck round bottom flask **BrPmDI** (500 mg, 1.23 mmol) was taken and 100 ml dry toluene was added into it followed by degassing with nitrogen for 10 minutes. $\text{Pd}(\text{PPh}_3)_4$ (tetrakis(triphenylphosphine)palladium(0)) (150 mg, 0.12 mmol) and 9H-carbazole-9-(4-phenyl) boronic acid pinacol ester (700mg, 1.85 mmol) were added subsequently to the mixture. After 15 minutes of nitrogen purging, K_2CO_3 (340 mg, 2.46 mmol) was added and refluxed for 16 hours. Toluene was removed under reduced pressure and column chromatography was performed using DCM as an eluent to get the pure product as yellow solid.

CzPhPmDI: Yellow solid (210 mg, 30 % yield); $^1\text{H NMR}$ (CDCl_3 , 400 MHz, ppm): δ_{H} 8.31 (s, 1H), 8.14 (d, 2H, $J = 7.7$ Hz), 7.69 (q, 4H, $J = 7.5$ Hz), 7.60 (d, 2H, $J = 8.2$ Hz), 7.44 (m, 2H), 3.69 (t, 4H, $J = 7.4$ Hz), 1.67 (q, 4H, $J = 7.5$), 1.37 (h, 4H, $J = 7.5$), 0.95 (t, 6H, $J = 7.4$ Hz); $^{13}\text{C NMR}$ (CDCl_3 , 100 MHz, ppm): δ_{C} 165.9, 165.8, 140.5, 138.8, 138.1, 133.5, 131.5, 126.0, 125.8, 123.5, 120.3, 120.2, 116.9, 110.1, 38.5, 30.4, 20.1, 13.6. HRMS (ESI): m/z calculated 569.2315: observed 570.2375 $[\text{M}+\text{H}]^+$.

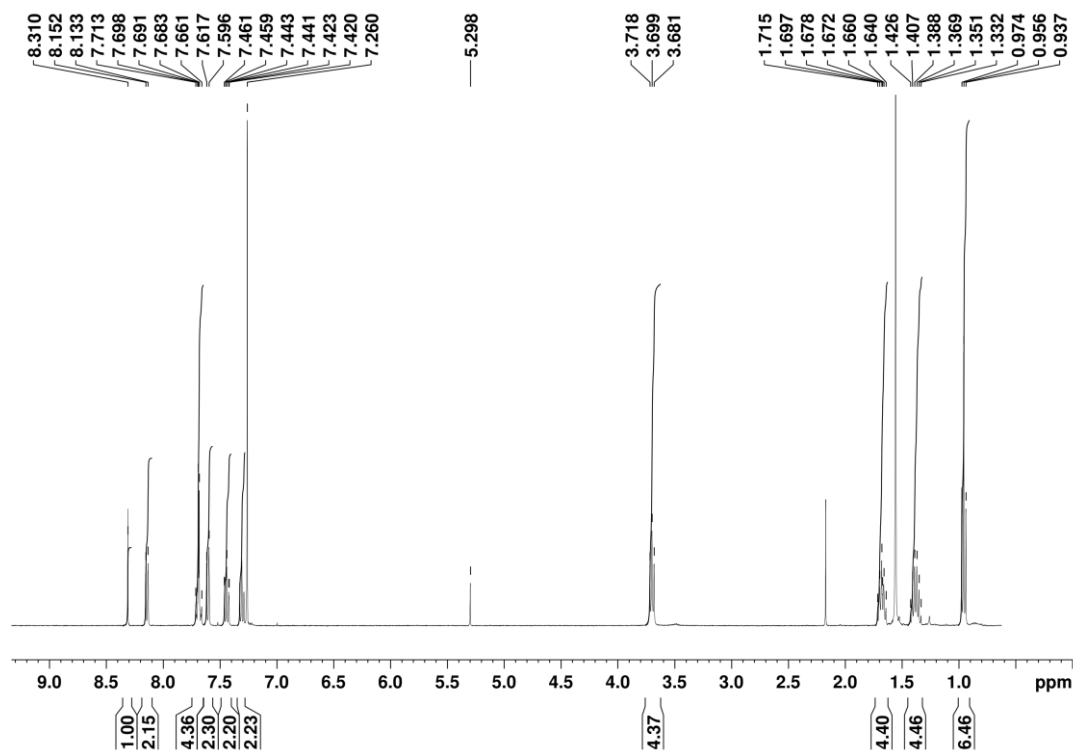


Figure 5.23. $^1\text{H NMR}$ spectrum of **CzPhPmDI** in CDCl_3 .

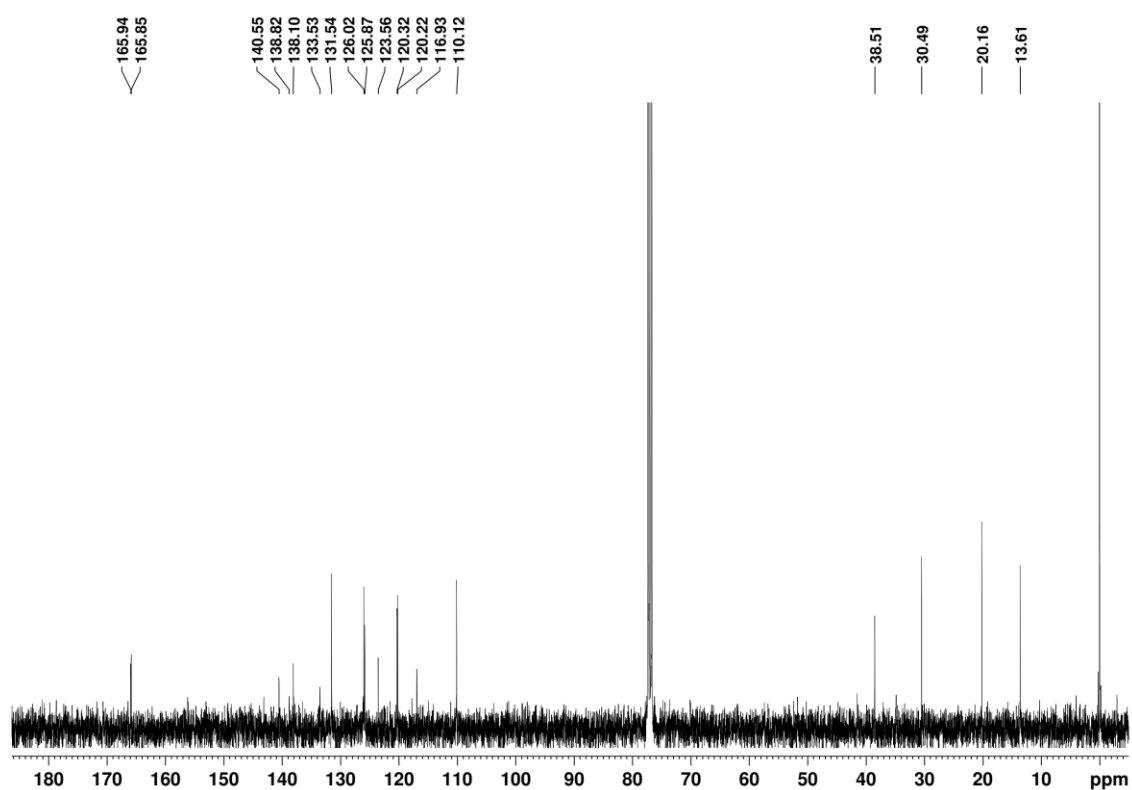
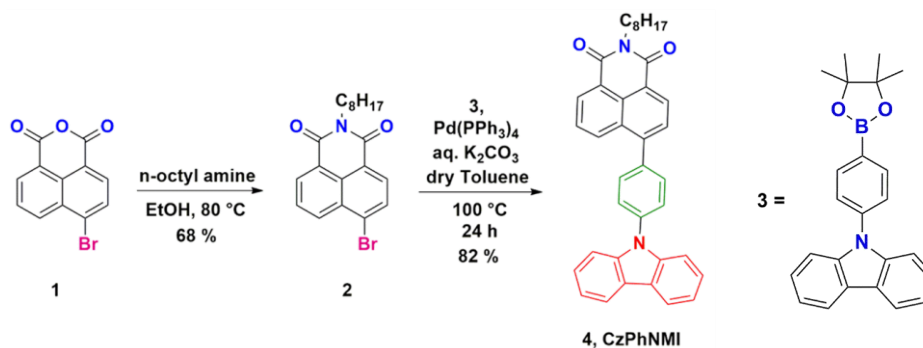


Figure 5.24. ^{13}C NMR spectrum of *CzPhPmDI* in CDCl_3 .

5.7.2f. Synthesis of *CzPhNMI*:

4-Bromo-1,8-naphthalic anhydride and EtOH were purchased from Sigma-Aldrich used without further purification.

5.6.2g. Synthetic Scheme:



Scheme 5.3. Synthetic scheme for *CzPhNMI*.

Synthesis of BrNMI: 4-Bromo-1,8-naphthalic anhydride (**1**) (2 g, 5.15 mmol) was first dispersed in ethanol (50 mL) taken in a 100 mL round bottomed flask. *n*-Octyl amine (, 6.18 mmol) was added to this solution under N₂ atmosphere and refluxed at 80 °C for about 3 hr. Then the reaction mixture was cooled to room temperature and water (100 mL) was added in it. The resulting brown precipitate was then filtered and was washed with ethanol (100 mL). The off-white precipitate was then dried under vacuum at 50 °C for overnight.

BrNMI: Off-white solid, (2.3 g, yield = 82%).

¹H NMR (400 MHz, CDCl₃): δ_H 8.66 (d, *J* = 7.2 Hz, 1H), 8.57 (d, *J* = 8.4 Hz, 1H), 8.42 (d, *J* = 7.6 Hz, 1H), 8.04 (d, *J* = 8.0 Hz, 1H), 7.84 (t, *J* = 7.6 Hz, 1H), 4.16 (t, *J* = 7.6 Hz, 2H), 1.76-1.69 (m, 2H), 1.42-1.22 (m, 10 H), 0.87 (t, *J* = 6.8 Hz, 3H); ¹³C NMR: Due to low solubility ¹³C NMR spectra was not recorded. MALDI-TOF (DCTB matrix, positive mode) (*m/z*): calculated for C₂₀H₂₂BrNO₂ 387.0834; found 388.180 [M+H]⁺.

Synthesis of CzPhNMI: BrNMI (0.2 g, 0.52 mmol) and 9H-Carbazole-9-(4-phenyl)boronic acid pinacol ester (**3**) (0.23 g, 0.62 mmol) was taken in a 100 mL round bottom flask. Toluene (12 mL) was added to the above mixture under N₂ atmosphere. Then the reaction mixture was purged with N₂ for 15-20 minutes. K₂CO₃ (0.11 g, 0.77 mmol) was dissolved in millipore water (0.5 mL) and added to the above reaction mixture followed by the addition of Pd(PPh₃)₄ (0.03 g, 5 mol%). This mixture was farther purged with N₂ for another 15 minutes followed by refluxing under inert condition at 110 °C for about 24 h. After completion of starting material, 25 mL water was added and extracted with chloroform (150 mL). Organic layer was washed with brine solution followed by drying over anhydrous Na₂SO₄. Organic layer was concentrated under vacuum and purified the compound by 100-200 silica-gel column chromatography using chloroform/hexane (10:90 v/v) as eluent.

CzPhNMI: Green Solid (0.155 g, yield = 55%).

¹H NMR (400 MHz, CDCl₃, ppm): δ_H 8.70 (t, *J* = 8.0 Hz, 2H), 8.42 (d, *J* = 8.4 Hz, 1H), 8.20 (d, *J* = 7.6 Hz, 2H), 7.83-7.75 (m, 6H), 7.58 (d, *J* = 8.0 Hz, 2H), 7.47 (t, *J* = 7.6 Hz, 2H), 7.34 (t, *J* = 7.2 Hz, 2H), 4.23 (t, *J* = 7.6 Hz, 2H), 1.80-1.76 (m, 2H), 1.46-1.30 (m, 11H), 0.88 (t, *J* = 6.8 Hz, 3H). ¹³C NMR (100 MHz, CDCl₃, ppm): δ_C 164.2, 164.0, 145.7, 140.7, 138.1, 137.8, 132.3, 131.4, 131.3, 130.8, 130.0, 128.8, 128.0, 127.1, 126.1, 123.6, 123.1, 122.2, 120.5, 120.3, 109.7, 40.6, 31.8, 29.4, 29.2, 28.2, 27.2, 22.6, 14.1. MALDI-TOF (DCTB matrix, negative mode) (*m/z*): calculated for C₃₈H₃₄N₂O₂ 550.2620, found 550.305 [M⁻].

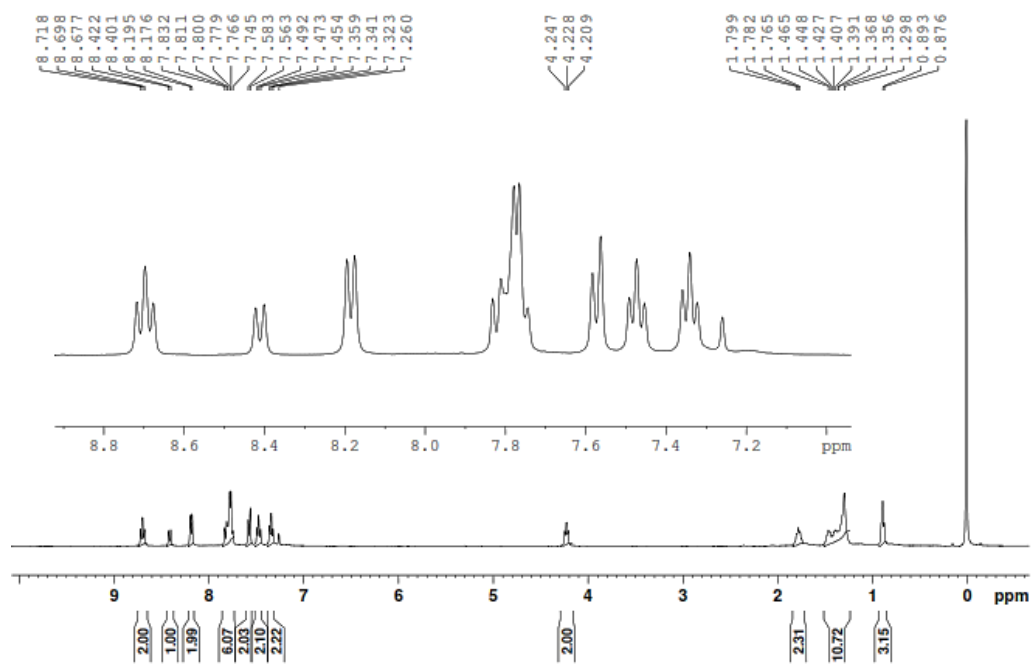


Figure 5.25. ¹H NMR spectrum of *CzPhNMI* in CDCl₃.

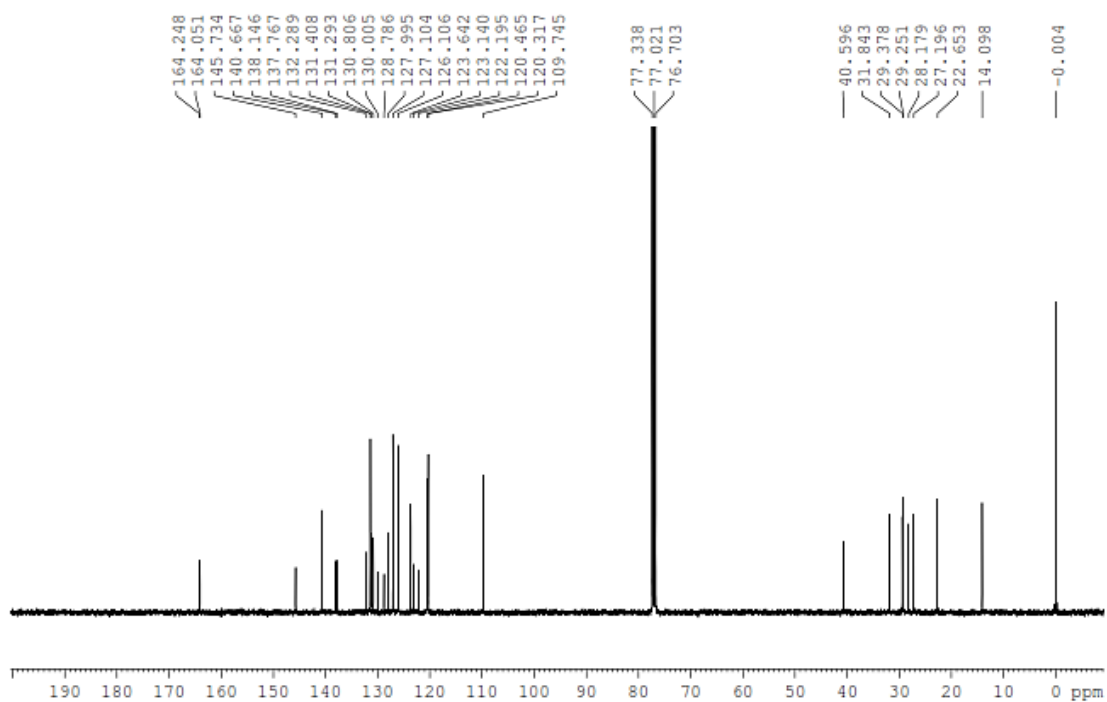


Figure 5.26. ¹³C NMR spectrum of *CzPhNMI* in CDCl₃.

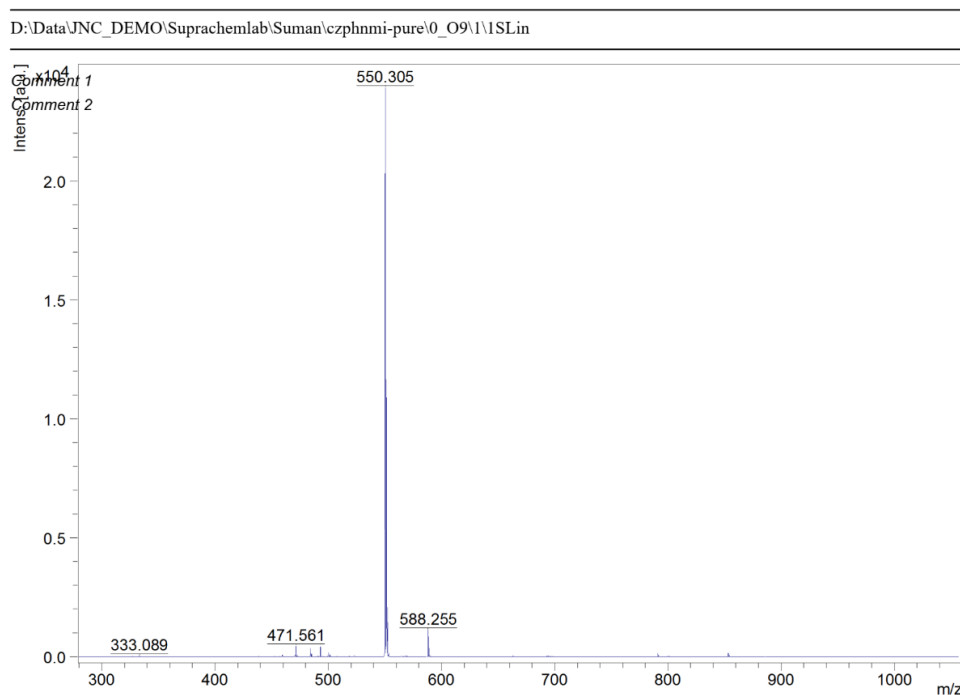


Figure 5.27. MALDI-TOF spectrum of *CzPhNMI*.

5.8. References

- [1] a) X. Zhan, A. Facchetti, S. Barlow, T. J. Marks, M. A. Ratner, M. R. Wasielewski, S. R. Marder, *Adv. Mater.* **2011**, *23*, 268-284; b) N. Sakai, J. Mareda, E. Vauthey, S. Matile, *Chem. Commun.* **2010**, *46*, 4225-4237; c) S. V. Bhosale, C. H. Jani, S. J. Langford, *Chem. Soc. Rev.* **2008**, *37*, 331-342.
- [2] a) J. H. Oh, S.-L. Suraru, W.-Y. Lee, M. Könemann, H. W. Höffken, C. Röger, R. Schmidt, Y. Chung, W.-C. Chen, F. Würthner, Z. Bao, *Adv. Funct. Mater.* **2010**, *20*, 2148-2156; b) T. He, M. Stolte, F. Würthner *Adv. Mater.* **2013**, *25*, 6951-6955; c) H. Yan, Z. Chen, Y. Zheng, C. Newman, J. R. Quinn, F. Dötz, M. Kastler, A. Facchetti, *Nature* **2009**, *457*, 679-686.
- [3] a) S.-L. Suraru, F. Würthner, *Angew. Chem. Int. Ed.* **2014**, *53*, 7428-7448; b) F. Würthner, S. Ahmed, C. Thalacker, T. Debaerdemaeker, *Chem. Eur. J.* **2002**, *8*, 4742-4750; b) C. Röger, F. Würthner, *J. Org. Chem.* **2007**, *72*, 8070-8075; c) R. S. K. Kishore, V. Ravikumar, G. Bernardinelli, N. Sakai, S. Matile, *J. Org. Chem.* **2008**, *73*, 738-740; d) A. Takai, T. Yasuda, T. Ishizuka, T. Kojima, M. Takeuchi, *Angew. Chem. Int. Ed.* **2013**, *52*, 9167-9171.
- [4] a) S. Guha, S. Saha, *J. Am. Chem. Soc.* **2010**, *132*, 17674-17677; b) S. Guha, F. S. Goodson, L. J. Corson, S. Saha, *J. Am. Chem. Soc.* **2012**, *134*, 13679-13691.

- [5] a) Y. Zhao, Y. Domoto, E. Orentas, C. Beuchat, D. Emery, J. Mareda, N. Sakai, S. Matile, *Angew. Chem. Int. Ed.* **2013**, *52*, 9940-9943; b) L. Liu, Y. Cotellet, A.-B. Bornhof, C. Besnard, N. Sakai, S. Matile, *Angew. Chem. Int. Ed.* **2017**, *56*, 13066-13069.
- [6] R. E. Dawson, A. Hennig, D. P. Weimann, D. Emery, V. Ravikumar, J. Montenegro, T. Takeuchi, S. Gabutti, M. Mayor, J. Mareda, C. A. Schalley, S. Matile, *Nat. Chem.* **2010**, *2*, 533-538.
- [7] a) Y. Kumar, S. Kumar, K. Mandal, P. Mukhopadhyay, *Angew. Chem. Int. Ed.* **2018**, *57*, 16318-16322; b) S. Kumar, M. R. Ajayakumar, G. Hundal, P. Mukhopadhyay, *J. Am. Chem. Soc.* **2014**, *136*, 12004-12010; c) G. Bêlanger-Chabot, A. Ali, F. P. Gabbai, *Angew. Chem. Int. Ed.* **2017**, *56*, 9958-9961.
- [8] P. D. Frischmann, K. Mahata, F. Würthner, *Chem. Soc. Rev.* **2013**, *42*, 1847-1870.
- [9] a) A. Sarkar, S. Dhiman, A. Chalishazar, S. J. George, *Angew. Chem. Int. Ed.* **2017**, *56*, 13767-13771; b) R. Sethy, J. Kumar, R. Métivier, M. Louis, K. Nakatani, N. Mohan, T. Mecheri, A. Subhakumari, K. G. Thomas, T. Kawai, T. Nakashima, *Angew. Chem. Int. Ed.* **2017**, *56*, 15053-15056; c) A. Takai, M. Takeuchi, *Bull. Chem. Soc. Jpn.* **2018**, *91*, 44-51.
- [10] a) H. Uoyama, K. Goushi, K. Shizu, H. Nomura, C. Adachi, *Nature* **2012**, *492*, 234-238; b) M. Y. Wong, E. Zysman-Colman, *Adv. Mater.* **2017**, *29*, 1605444.
- [11] a) P. Ganesan, J. Baggerman, H. Zhang, E. J. R. Sudhölter, H. Zuilhof, *J. Phys. Chem. A* **2007**, *111*, 6151-6156; b) O. Yushchenko, G. Licari, S. Mosquera-Vazquez, N. Sakai, S. Matile, E. Vauthey, *J. Phys. Chem. Lett.* **2015**, *6*, 2096-2100.
- [12] a) S. Kuila, K. V. Rao, S. Garain, P. K. Samanta, S. Das, S. K. Pati, M. Eswaramoorthy, S. J. George, *Angew. Chem. Int. Ed.* **2018**, *57*, 17115-17119
- [13] a) J. H. Kim, J. H. Yun, J. Y. Lee, *Adv. Opt. Mater.* **2018**, *6*, 1800255; b) H. F. Higginbotham, P. Pander, R. Rybakiewicz, M. K. Etherington, S. Maniam, M. Zagorska, A. Pron, A. P. Monkman, P. Data, *J. Mater. Chem. C* **2018**, *6*, 8219-8225; c) F. B. Dias, J. Santos, D. R. Graves, P. Data, R. S. Nobuyasu, M. A. Fox, A. S. Batsanov, T. Palmeira, M. N. Berberan-Santos, M. R. Bryce, A. P. Monkman, *Adv. Sci.* **2016**, *3*, 1600080.
- [14] a) Y. Tao, K. Yuan, T. Chen, P. Xu, H. Li, R. Chen, C. Zheng, L. Zhang, W. Huang, *Adv. Mater.* **2014**, *26*, 7931-7958; b) Y. Im, M. Kim, Y. J. Cho, J.-A. Seo, K. S. Yook, J. Y. Lee, *Chem. Mater.* **2017**, *29*, 1946-1963; c) T. J. Penfold, F. B. Dias, A. P. Monkman, *Chem. Commun.* **2018**, *54*, 3926-3935.

- [15] J. Shukla, M. R. Ajayakumar, P. Mukhopadhyay, *Org. Lett.* **2018**, *20*, 7864-7868. Attempt has been made towards synthesizing similar derivative; however triplets are not explored in this work.
- [16] D. Lee, O. Bolton, B. C. Kim, J. H. Youk, S. Takayama, J. Kim, *J. Am. Chem. Soc.* **2013**, *135*, 6325-6329.
- [17] L. Yu, Z. Wu, C. Zhong, G. Xie, Z. Zhu, D. Ma, C. Yang, *Adv. Opt. Mater.* **2017**, *5*, 1700588.
- [18] H. Noda, H. Nakanotani, C. Adachi, *Sci. Adv.* **2018**, *4*, eaao6910.
- [19] P. L. dos Santos, M. K. Etherington, A. P. Monkman, *J. Mater. Chem. C* **2018**, *6*, 4842-4853.
- [20] a) S. Guo, W. Wu, H. Guo, J. Zhao, *J. Org. Chem.* **2012**, *77*, 3933-3943; b) V. Martinez-Martinez, R. S. Llano, S. Furukawa, Y. Takashima, I. L. Arbeloa, S. Kitagawa, *ChemPhysChem* **2014**, *15*, 2517-2521; c) J. Du, F. Liao, Z. Wu, W. Huang, F. Li, J. Dou, H. Miao, X. Chen, X. Zhang, J. Jiang, G. Zhang, *ChemRxiv*, **2019**, <https://doi.org/10.26434/chemrxiv.9784865.v1>.
- [21] M. K. Etherington, J. Gibson, H. F. Higginbotham, T. J. Penfold, A. P. Monkman, *Nat. Commun.* **2016**, *7*, 13680-13687.
- [22] V. Jankus, E. W. Snedden, D. W. Bright, V. L. Whittle, J. A. G. Williams, A. Monkman, *Adv. Funct. Mater.* **2013**, *23*, 384-393.
- [23] Lifetime was too small to be fitted accurately at 15 K.
- [24] a) S. Kola, N. J. Tremblay, M.-L. Yeh, H. E. Katz, S. B. Kirschner, D. H. Reich, *J. Am. Chem. Soc.* **2008**, *130*, 14410-14411; b) S. Kola, J. H. Kim, R. Ireland, M.-L. Yeh, K. Smith, W. Guo, H. E. Katz, *ACS Macro Letters* **2013**, *2*, 664-669; c) X. Guo, M. D. Watson, *Macromolecules* **2011**, *44*, 6711-6716; d) A. R. Mohebbi, C. Munoz, F. Wudl, *Org. Lett.* **2011**, *13*, 2560-2563; e) K. Kanosue, S. Ando, *ACS Macro Lett.* **2016**, *5*, 1301-1305.
- [25] a) P. Gopikrishna, N. Meher, P. K. Iyer, *ACS Appl. Mater. Interfaces* **2018**, *10*, 12081-12111; b) J. M. Delente, D. Umadevi, S. Shanmugaraju, O. Kotova, G. W. Watson, T. Gunnlaugsson, *Chem. Commun.* **2020**, *56*, 2562-2565; c) M. Poddar, G. Sivakumar, R. Misra, *J. Mater. Chem. C* **2019**, *7*, 14798-14815; d) N. Meher, P. K. Iyer, *Nanoscale* **2019**, *11*, 13233-13242.
- [26] a) X. Chen, C. Xu, T. Wang, C. Zhou, J. Du, Z. Wang, H. Xu, T. Xie, G. Bi, J. Jiang, X. Zhang, J. N. Demas, C. O. Trindle, Y. Luo, G. Zhang, *Angew. Chem. Int. Ed.* **2016**, *55*, 9872 - 9876; b) B. Ventura, A. Bertocco, D. Braga, L. Catalano, S. O'Agostino, F. Grepioni, P. Taddei,

J. Phys. Chem. C **2014**, *118*, 18646-18658; c) X. Zhang, L. Du, W. Zhao, Z. Zhao, Y. Xiong, X. He, P. F. Gao, P. Alam, C. Wang, Z. Li, J. Leng, J. Liu, C. Zhou, J. W.Y. Lam, D. L. Phillips, G. Zhang, B. Z. Tang, *Nat. Commun.* **2019**, *10*, 5161; d) S. Yang, D. Wu, W. Gong, Q. Huang, H. Zhen, Q. Ling, Z. Lin, *Chem. Sci.* **2018**, *9*, 8975–8981; e) Goudappagouda, A. Manthanath, V. C. Wakchaure, K. C. Ranjeesh, T. Das, K. Vanka, T. Nakanishi, S. S. Babu, *Angew. Chem. Int. Ed.* **2019**, *58*, 2284-2288.

[27] a) W. Zhang, Y. Xu, M. Hanif, S. Zhang, J. Zhou, D. Hu, Z. Xie, Y. Ma, *J. Phys. Chem. C* **2017**, *121*, 23218-23223; b) W. Zeng, H.-Y. Lai, W.-K. Lee, M. Jiao, Y.-J. Shiu, C. Zhong, S. Gong, T. Zhou, G. Xie, M. Sarma, K.-T. Wong, C.-C. Wu, C. Yang, *Adv. Mater.* **2018**, *30*, 1704961; c) Y.-F. Wang, H.-Y. Lu, C. Chen, M. Li, C.-F. Chen, *Org. Electronics* **2019**, *70*, 71–77.

[28] a) M. Schulze, A. Steffen, F. Würthner, *Angew. Chem. Int. Ed.* **2015**, *54*, 1570-1573; b) X. Zhen, Y. Tao, Z. An, P. Chen, C. Xu, R. Chen, W. Huang, K. Pu, *Adv. Mater.* **2017**, *29*, 1606665; c) N. Gan, H. Shi, Z. An, W. Huang, *Adv. Funct. Mater.* **2018**, *28*, 1802657.

[29] J.-D. Chai, M. Head-Gordon, *Phys. Chem. Chem. Phys.* **2008**, *10*, 6615-6620.

[30] P. K. Samanta, D. Kim, V. Coropceanu, J. L. Brédas, *J. Am. Chem. Soc.* **2017**, *139*, 4042-4051.

[31] K. Lee, D. Kim, *J. Phys. Chem. C* **2016**, *120*, 28330-28336.

[32] S. Hirata, M. Head-Gordon, *Chem. Phys. Lett.* **1999**, *314*, 291-299.

[33] R. L. Martin, *J. Chem. Phys.* **2003**, *118*, 4775-4777.

[34] Gaussian 16, Revision A. 03, M. J. Frisch, G. W. Trucks, H. B. Schlegel, G. E. Scuseria, M. A. Robb, J. R. Cheeseman, G. Scalmani, V. Barone, G. A. Petersson, H. Nakatsuji, X. Li, M. Caricato, A. V. Marenich, J. Bloino, B. G. Janesko, R. Gomperts, B. Mennucci, H. P. Hratchian, J. V. Ortiz, A. F. Izmaylov, J. L. Williams; F. Ding; F. Lipparini, F. Egidi, J. Goings, B. Peng, A. Petrone, T. Henderson, D. Ranasinghe, V. G. Zakrzewski, J. Gao, N. Rega, G. Zheng, W. Liang, M. Hada, M. Ehara, K. Toyota, R. Fukuda, J. Hasegawa, M. Ishida, T. Nakajima, Y. Honda, O. Kitao, H. Nakai, T. Vreven, K. Throssell, J. A. Montgomery Jr., J. E. Peralta, F. Ogliaro, M. J. Bearpark, J. J. Heyd, E. N. Brothers, K. N. Kudin, V. N. Staroverov, T. A. Keith, R. Kobayashi, J. Normand, K. Raghavachari, A. P. Rendell, J. C. Burant, S. S. Iyengar, J. Tomasi, M. Cossi, J. M. Millam, M. Klene, C. Adamo, R. Cammi, J. W. Ochterski, R. L. Martin, K. Morokuma, O. Farkas, J. B. Foresman, D. J. Fox, Gaussian, Inc., Wallingford CT, **2016**.

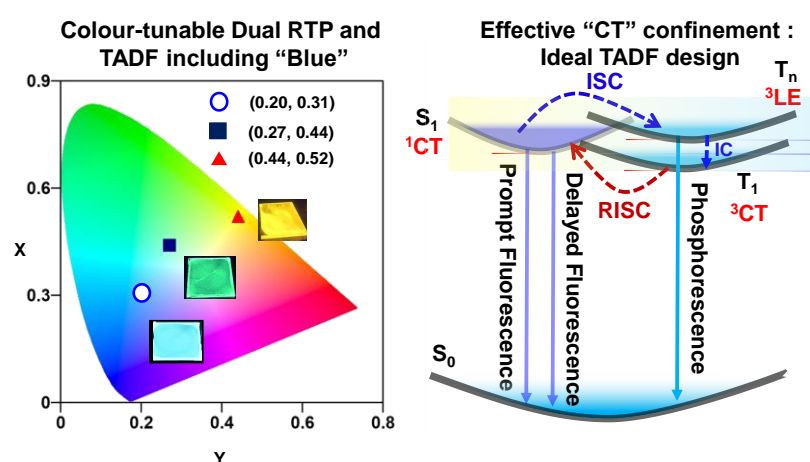
[35] N. Venkatramaiah, G. D. Kumar, Y. Chandrasekaran, R. Ganduri, S. Patil, *ACS Appl. Mater. Interfaces* **2018**, *10*, 3838–3847.

CHAPTER 6

Triazatruxene Based Donor-Acceptor Charge-transfer Chromophores: A Step towards Efficient Blue-emissive Thermally Activated Delayed Fluorescent Molecules*

Abstract

Based on the high triplet energy of electron-rich triazatruxene (TAT), we proposed a rational design principle to harvest blue-emissive thermally activated delayed fluorescence (TADF) by a donor-acceptor charge-transfer (CT) strategy. First, we selected two acceptor units, benzophenone (BP) and diphenyltriazine (TRZ), known for their weak electron-deficient character as well as high triplet energy. Substitution of triazatruxene with $-NH$ s was done successfully to obtain blue-emitting **TAT-3BP** with CIE colour co-ordinate of (0.20, 0.31) and green-emitting **TAT-3TRZ** with excellent photoluminescence quantum yield over 60 % and fast delayed fluorescence lifetime of $\sim 1.7 \mu\text{s}$, in addition to strong room temperature phosphorescence (RTP). The requirement of CT excited state confinement within the vicinity of locally excited (LE) triplet states of donor/acceptor units is maintained in these chromophores in order to facilitate efficient reverse intersystem crossing (RISC) process. Further, we also showed the versatility of TAT as an emerging class of donor moiety towards solution-processable TADF materials by substituting its core with naphthalene monoimide (**TAT-NMI**) which exhibit yellowish-orange emissive TADF with high photoluminescence quantum yield (65 %).



*Manuscripts based on this work is under preparation.

6.1. Introduction

Energy efficient organic light emitting diodes (OLEDs) have sparked a tremendous attention towards the development of high-performance materials and lack of availability of stable pure-blue emitters severely limits their mass production.^[1] Unravelling these blue-emitting electroluminescent materials in turn would accomplish the commercialization of stable, efficient, cost-effective white OLED displays and other solid state lighting applications.^[2] So far, attempts towards realising high-performance blue-emitters are based on certain Ir-complexes, although their instability often considered to be the bottleneck of their further developments.^[3] Therefore, most of the OLED devices use a combination of traditional pure-blue fluorescent molecules and green or red-emitting organometallic compounds to counter the issues of low operational lifetime and device efficiency of blue-emitting organometallic compounds.^[4] Although, the traditional metal-free organic blue-emitters perform well due to their high electro- and photochemical stabilities, inherent triplet exciton losses limits their internal quantum efficiency (IQE) within 25 %, according to the spin-statistical restrictions.^[5] Therefore, recent developments in the field of TADF materials can effectively surmount these triplet losses by utilizing the triplet excitons through a RISC process, and achieve 100 % IQE.^[6] However, inherently broad spectral feature of CT TADF emitters renders the rapid development pure blue-emission and demands a rational approach.^[7] With that objective, in this Chapter we have tried to utilize our understanding of charge-transfer state confinement in order to obtain high-energy TADF emission. The basic design strategy we have taken under consideration is to utilize the donor and acceptor chromophores having high triplet-energy and which emit phosphorescence in the deep-blue region of the visible spectrum. Therefore, previously studied in Chapter 3, TAT is one such electron-rich heterocyclic material with strong propensity to emit pure-blue RTP from their monomer triplet state.^[8] TAT derivatives has been extensively utilized as efficient hole-transporting materials in organic and perovskite solar cells^[9] although their photoluminescence properties have not been explored yet. Moreover, ease in the synthetic efforts to functionalize both the nitrogen centres as well as the core of triazatruxene makes it a suitable candidate for developing TADF emitters using a wide range of acceptor units. Here, we utilized two different acceptors (benzophenone and diphenyltriazine) with high-triplet state energy, to functionalize the nitrogen-centres of TAT leading to blue-emitting **TAT-3BP** and green-emitting **TAT-3TRZ**, respectively.^[7d,10] These molecules show excellent TADF performance in addition to RTP emission under ambient conditions. The confinement of charge-transfer states to the vicinity of LE triplet states is envisioned to provide fast delayed fluorescence (DF) lifetime and further modification of the acceptor units or adjusting the polarity of the host matrix is proposed to tune

the energy of CT states to achieve deep-blue TADF material. In addition, to reiterate the versatility of TAT as a molecular scaffold, we functionalized its core with naphthalene monoimide acceptor (**TAT-NMI**) to obtain a highly solution-processable orange-emitting TADF material.

6.2. Design Strategy and Synthesis

The molecular structures of the donor-acceptor CT molecules (**TAT-3BP**, **TAT-3TRZ** and **TAT-NMI**) using TAT as donor unit are outlined in Figure 6.1. **TAT-3BP** and **TAT-3TRZ** were synthesized by Pd-catalysed Buchwald-Hartwig amination (see Experimental Section) reaction and on the other hand, to synthesize the core-substituted analogue, **TAT-NMI**, Pd-catalyzed Suzuki coupling reaction was utilized (see Experimental Section). All the studies were mainly focused on the solid state emission characteristics in order to obtain the triplet emission and polymethyl methacrylate (PMMA) was used as a host material in order to reduce the aggregation-induced quenching effects as well as to improve ambient triplet stability of the chromophores.

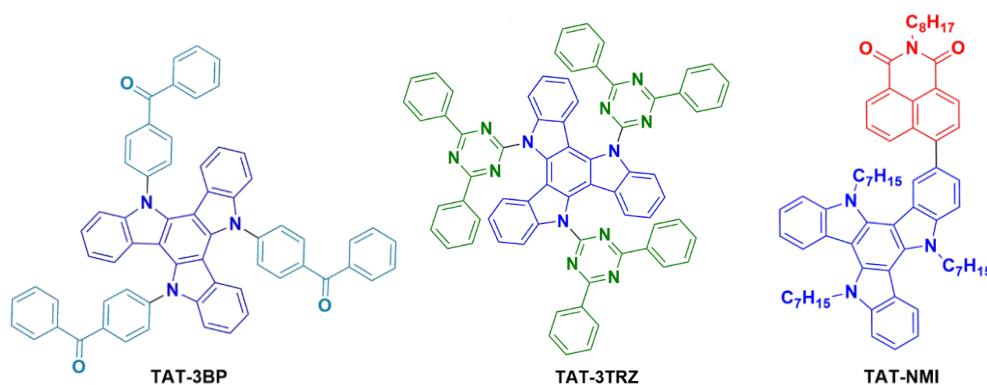


Figure 6.1. Chemical structures of the donor-acceptor charge transfer molecules studied for triplet harvesting using TAT as central donor-scaffold.

6.3. Blue-emitting TADF and RTP from Benzophenone-substituted Triazatruxene (**TAT-3BP**)

Triazatruxene has shown to be a very efficient deep-blue-phosphorescence emitter in Chapter 3. Therefore, to design a blue-emitting CT emitter, we exploited a relatively weak acceptor unit with high triplet-energy, benzophenone (BP).^[10] BP has also been utilized as blue-emitting phosphorescence emitter by Tang and co-workers^[10] and its weak electron-accepting carbonyl group was envisioned to produce high energy charge-transfer states when conjugated with the donor, triazatruxene (**TAT**). With a single step Buchwald- Hartwig amination

methodology, all three $-NH$ groups of **TAT**, were substituted with benzophenone (see Experimental Section) to obtain **TAT-3BP**. The optical properties of **TAT-3BP** was further analysed with detailed absorption and time-resolved emission spectroscopy.

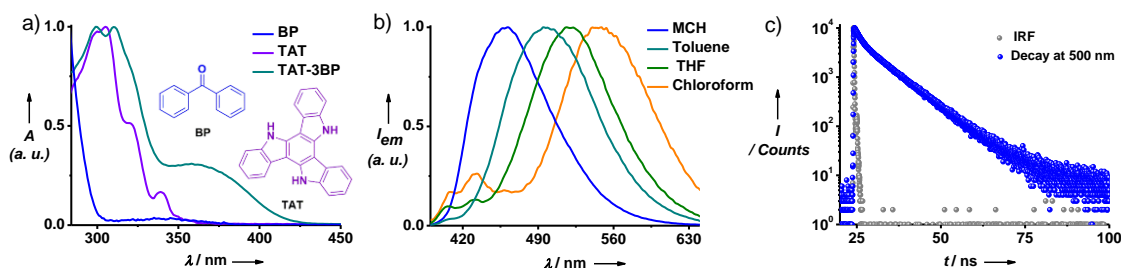


Figure 6.2. a) Normalized absorption spectra of **TAT** (D), **BP** (A) and **TAT-3BP** (D-A) showing characteristic locally-excited and charge-transfer bands ($[TAT]$, $[BP]$ and $[TAT-3BP]$ = 0.05 mM in THF). Inset shows the molecular structures of benzophenone (**BP**) and triazatruxene (**TAT**). b) Normalized emission spectra of **TAT-3BP** showing strong solvatochromic effects in solvents with different polarity ($[TAT-3BP]$ = 0.05 mM, $\lambda_{exc.}$ = 310 nm). c) Fluorescence decay profile of 0.05 mM **TAT-3BP** dissolved in toluene ($\lambda_{exc.}$ = 373 nm, $\lambda_{monitored}$ = 500 nm). IRF is the instrument response function. D= donor, A= acceptor.

In solution state, **TAT-3BP** (0.05 mM, THF) shows a LE absorption band in the 280-350 nm region and CT absorption band in the 350-450 nm region. Significant spectral-shift ($\lambda_{max.}$ = 450 nm in MCH to $\lambda_{max.}$ = 560 nm in THF, $\lambda_{exc.}$ = 310 nm) in its polarity-dependent emission profile is suggestive of a strong CT nature in the excited state (Figure 6.2a and 6.2b). However, in the solution state, only prompt (CT) fluorescence was observed with average lifetime of 7.1 ns ($\lambda_{exc.}$ = 373 nm, $\lambda_{monitored}$ = 500 nm) (Figure 6.2c). Therefore, triplet emission characteristics of **TAT-3BP** was further explored in solid film state. Since, the neat films were less-emissive, plausibly due to the aggregation of the molecules, **TAT-3BP** was dispersed in PMMA in low concentration and we observed a substantial improvement (~ 15 fold increase) in the emission profile (Figure 6.3a). All further experiments were, therefore, performed in 1 wt. % **TAT-3BP-PMMA** composition.

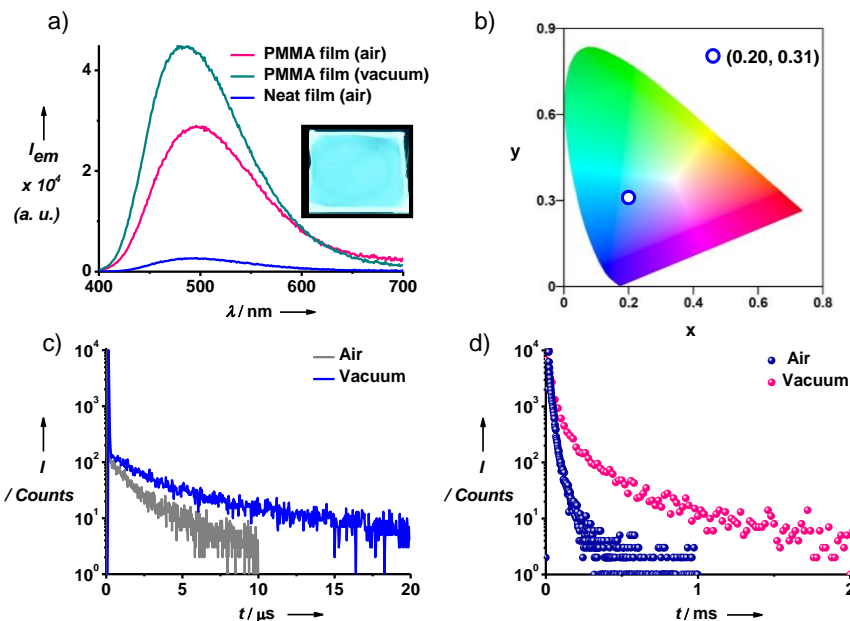


Figure 6.3. a) Comparison of steady-state emission intensity of 1 wt. % TAT-3BP-PMMA hybrid film in air and under vacuum along with the corresponding neat film emission taken in air ($\lambda_{exc.} = 310$ nm). The inset shows the photograph of PMMA film of TAT-3BP (1 wt. %) hybrid film under 365 nm UV-lamp. b) Commission Internationale de l'éclairage colour co-ordinate of 1 wt. % TAT-3BP-PMMA hybrid film. Aerated and vacuum state time-resolved decay profile of PMMA film of TAT-3BP (1 wt. %) at c) short time-range (1 ns -20 μ s range, $\lambda_{exc.} = 405$ nm, $\lambda_{monitored} = 480$ nm) in air and d) longer time-range (5 μ s-2 ms) ($\lambda_{exc.} = 310$ nm, $\lambda_{monitored} = 480$ nm). Delayed lifetime profiles suggest remarkable triplet stability of TAT-3BP in air.

As can be seen from Figure 6.3a, the emission intensity of TAT-3BP-PMMA hybrid film increase substantially under vacuum (~ 1.7 fold), hinting towards high triplet contribution ($\lambda_{exc.} = 310$ nm). Interestingly, Commission Internationale de l'éclairage (CIE) colour co-ordinate of the film was found to be (0.20, 0.31) suggesting blue-emission and in addition, it showed excellent photoluminescence quantum yield of 63 % (Figure 6.3b). Moreover, the lifetime profile further reiterates the triplet contribution in film state as both prompt and delayed emission components could be observed (Figure 6.3c and 6.3d). At shorter time-range (1 ns - 20 μ s), we observed a bi-exponential decay with a prompt fluorescence (17.1 ns, 46 %) and a delayed emission lifetime (1.5 μ s, 54 %) which was further increased under vacuum (2.54 μ s, 61 %) ($\lambda_{exc.} = 405$ nm, $\lambda_{monitored} = 480$ nm, Figure 6.3c).^[11] A similar enhancement of average lifetime (22.8 μ s in air to 0.37 ms under vacuum, $\lambda_{exc.} = 340$ nm, $\lambda_{monitored} = 480$ nm, Figure 6.3d) was evident at the longer time range (5 μ s-2 ms). Such differential delayed lifetime components further hint towards the dual-state TADF and RTP characteristics. In order to elucidate this observation, we further performed detailed temperature-dependent lifetime analyses at both time ranges. At the

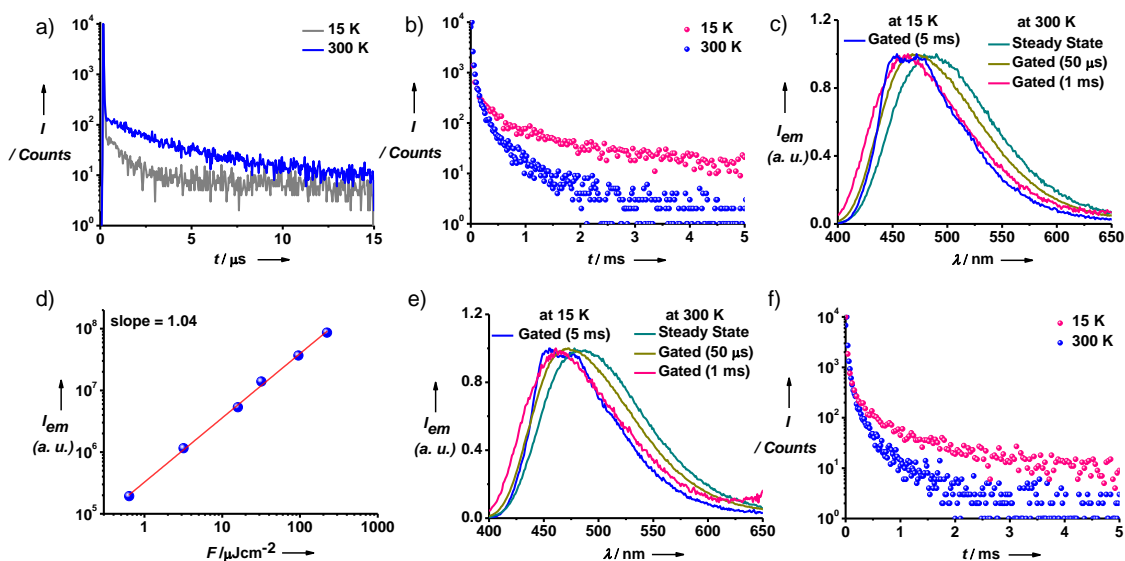


Figure 6.4. Lifetime profiles of **TAT-3BP-PMMA** hybrid film obtained at different temperatures while monitoring at a) short time-range ($\lambda_{exc.} = 405$ nm, $\lambda_{monitored} = 480$ nm) and b) longer time-range ($\lambda_{exc.} = 310$ nm, $\lambda_{monitored} = 480$ nm), showing TADF and RTP characteristics, respectively. c) Normalized steady-state and gated emission spectra of PMMA films of **TAT-3BP** at different temperatures with variable time-delays (50 μ s, 1 ms and 5 ms) showing TADF and RTP ($\lambda_{exc.} = 310$ nm). d) Excitation intensity dependent delayed emission profile of **TAT-3BP-PMMA** film excited at 355 nm. e) Normalized steady-state and gated emission spectra of **TAT-3BP-PMMA** hybrid film with different time-delays (50 μ s, 1 ms and 5 ms) and f) corresponding lifetime profile ($\lambda_{monitored} = 480$ nm, $\tau_{avg.} = 0.9$ ms at 15 K, $\tau_{avg.} = 0.23$ ms at 300 K) at different temperatures while excited at charge-transfer absorption wavelength ($\lambda_{exc.} = 380$ nm). In all cases 1 wt. % **TAT-3BP-PMMA** was used.

shorter time-range, we found a substantial decrease in delayed emission component with cooling down the sample temperature to 15 K (1.19 μ s, 22 %) from 300 K (2.54 μ s, 61 %) ($\lambda_{exc.} = 405$ nm, $\lambda_{monitored} = 480$ nm, Figure 6.4a).^[11] This observation unambiguously proves the DF nature of **TAT-3BP**.^[6d] On the other hand, at longer time-range, a reverse trend was observed where the average lifetime at 300 K ($\tau_{avg.} = 0.37$ ms) sharply increases to $\tau_{avg.} = 1.49$ ms at 15 K, proving the RTP characteristics of **TAT-3BP** ($\lambda_{exc.} = 310$ nm, $\lambda_{monitored} = 480$ nm, Figure 6.4b). Next, time-gated emission at both 300 K (room temperature) and 15 K was measured to understand the energy-levels of emissive triplet and charge-transfer singlet states which has a direct influence on the ISC and RISC processes ($\lambda_{exc.} = 310$ nm, Figure 6.4c).^[6] Calculated ΔE_{ST} between the emissive singlet and triplet levels was observed to be very low (50 ± 30 meV). Notably, at 300 K, a substantial blue-shift in the emission profile of **TAT-3BP** film was observed at high delay-time (1 ms) as compared to charge-transfer singlet state (1CT) suggesting a new long-lived

excited state (Figure 6.4c). In addition, the nearly-identical spectral feature of the gated emission at 300 K (delay-time = 1 ms) and 15 K (delay-time = 5 ms) further reiterates the presence of RTP characteristics along with a strong delayed emission at lower time-delay (50 μ s) (Figure 6.4c). Furthermore, the unimolecular TADF nature was unveiled by the linear increase (slope = 1.04) in the DF intensity with the corresponding incident laser intensity ($\lambda_{exc.} = 355$ nm, Figure 6.4d).^[6e] Here it is also to be noted that, direct excitation at the CT absorption band ($\lambda_{exc.} = 380$ nm) also result in RTP, which reiterates a close proximity between the 1CT and 3LE states (Figure 6.4e and 6.4f).

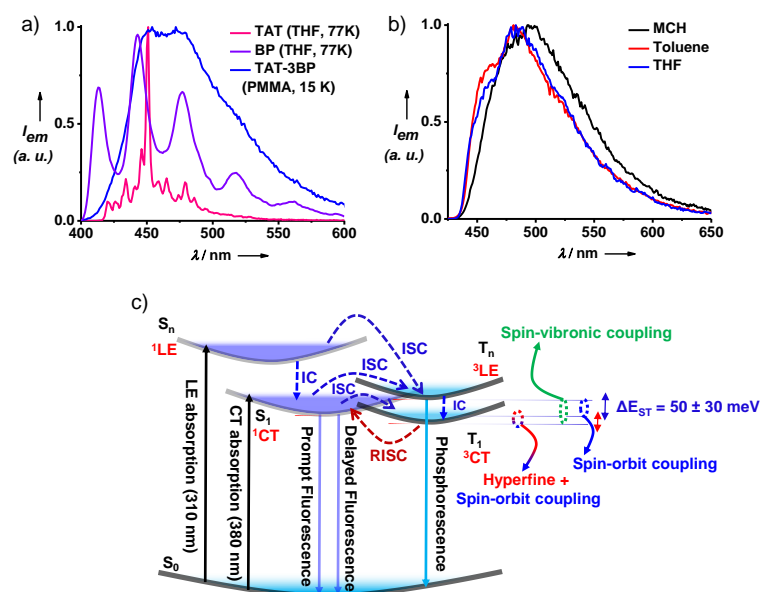


Figure 6.5. a) Phosphorescence spectrum ($\lambda_{exc.} = 310$ nm, delay-time = 5 ms) of **TAT-3BP** film (1 wt. % in PMMA) at 15 K and (3LE) phosphorescence spectrum of **TAT** (donor) and **BP** (acceptor) in THF at 77 K ($[TAT]$ and $[BP] = 0.05$ mM, $\lambda_{exc.} = 300$ nm, delay-time = 20 ms). b) Low temperature solvatochromism studies on the phosphorescence emission of **TAT-3BP** at 77 K ($\lambda_{exc.} = 310$ nm, delay time = 5 ms, $[TAT-3BP] = 0.05$ mM). Absence of any significant change in the emission spectra with solvent polarity suggests these phosphorescence bands are of locally excited (3LE) in character. c) Simplified Jablonski diagram for **TAT-3BP** indicating various excited state process involved the triplet exciton harvesting. In case of **TAT-3BP**, a higher energy 3LE undergoes spin-vibronic coupling with low-lying 3CT (green dotted circle). This in turn, influences the spin-flipping process between the 1CT and 3CT states to result in fast RISC by a combined hyperfine and spin-orbit coupling (red-blue dotted circle). The access to the 3LE states can be done by exciting both at locally-excited (310 nm) as well as at charge-transfer (380 nm) absorption wavelengths. The spin-orbit coupling between the 1CT and 3LE is shown by the blue-dotted circle and the denoted energy gap (ΔE_{ST}) between these two states is 50 ± 30 meV. ISC = intersystem crossing, RISC = reverse intersystem crossing, IC = internal conversion.

Having obtained a comprehensive evidence of a TADF features in **TAT-3BP** derivative, we further investigated the nature of the triplet state that is involved in the intersystem crossing processes. First, a low temperature (15 K) time-gated (delay-time = 5 ms) emission study revealed that the phosphorescence of **TAT-3BP** do not entirely match with the phosphorescence ($\lambda_{\text{exc.}} = 300$ nm, delay-time = 20 ms) of individual donor (triazatruxene, **TAT**) and acceptor subunits (benzophenone, **BP**) (Figure 6.5a). However, low temperature solvatochromism ($\lambda_{\text{exc.}} = 310$ nm) studies show that the phosphorescence profiles are insensitive to the change in solvent polarity (Figure 6.5b). Therefore, the phosphorescence nature of **TAT-3BP** is assigned to belocally-excited (LE) in nature, although it does not identify itself with any of donor or acceptor units. Such observations are previously reported when a substantial conjugation between the donor and acceptor units exists at a certain preferred conformation of the molecule. This results in a different triplet excited state (with respect to individual donor/acceptor triplet states) with electronic/molecular orbital configuration comprizing the wavefunctions of both donor and acceptor units.^[12]

Based on the emission profile we observed for **TAT-3BP** (both at room temperature and 15 K), a simplified Jablonski diagram is proposed in Figure 6.5c. While exciting at the LE absorbance band (310 nm), first ^1CT is formed (via internal conversion) and a competitive ISC channel also opens up to populate the nearby ^3LE state. This ^3LE state is also accessible by directly exciting the film at CT absorption wavelength (380 nm) since the energy gap between these two states are very low (50 ± 30 meV). In addition, phosphorescence from lower-lying triplet CT state could not be observed due to low oscillator strength generally expected from a triplet charge-transfer (^3CT) state.^[13] However, a fast delayed fluorescence lifetime (2.54 μs) while excited at charge-transfer absorption wavelength (405 nm)^[14] is suggestive of hyperfine-coupling between the closely-lying charge-transfer states. In addition, the close vicinity of ^3LE state to the charge-transfer states also plausibly participating in spin-vibronic coupling between the ^3LE and ^3CT states.^[15] Current theoretical understanding in TADF molecules proposes that hyperfine coupling is a dominant process between two CT states as the spin-orbit coupling (SOC) between two spin-states with same molecular orbital configurations (e. g. ^1CT and ^3CT) would be weak, if not zero.^[13, 15a] Therefore, spin-vibronic coupling between the ^3CT and closely-lying ^3LE is hypothesized to indirectly improve the SOC between the two CT states, facilitating the intersystem (and reverse intersystem) crossing processes. In the present scenario, the close-proximity (50 ± 30 meV) between the ^3LE and ^3CT , is envisaged to offer reasonable spin-vibronic coupling which further enhance the fast RISC from the $^3\text{CT} \rightarrow ^1\text{CT}$ and fast TADF emission.

6.4. Green-emitting Ambient TADF and RTP from Triazine-substituted Triazatruxene (TAT-3TRZ)

With an objective to achieve blue-emitting TADF emission, next we explored another acceptor unit diphenyl triazine which is known to have high triplet energy.^[7d] We envisioned conjugating triazatruxene unit with diphenyltriazine (**TAT-3TRZ**, Figure 6.1) would provide suitable charge-transfer transitions and lead to TADF emission in the blue-region of the emission spectrum. Hence, the photophysical properties of **TAT-3TRZ** was further understood by examining various absorption and time-resolved emission measurements both at solution and solid film state.

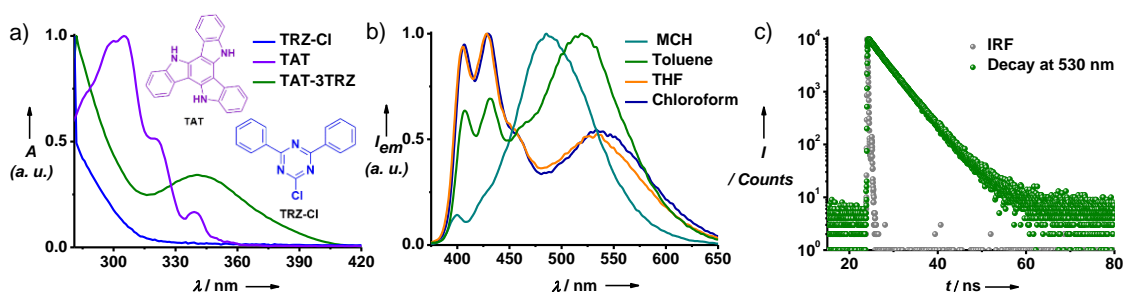


Figure 6.6. a) Normalized absorption spectra of 0.05 mM **TAT** (D), **TRZ-Cl** (A) and **TAT-3TRZ** (D-A) in THF. Inset show the molecular structures of individual donor (**TAT**) and acceptor (**TRZ-Cl**) control molecules. b) Normalized emission spectra of **TAT-3TRZ** showing strong solvatochromic effects in different solvents ($[TAT-3TRZ] = 0.05$ mM, $\lambda_{exc.} = 300$ nm). The LE bands exhibit sharp vibronic features (390-470 nm region) and do not shift with the change in polarity. c) Fluorescence decay profile of 0.05 mM **TAT-3TRZ** taken in toluene ($\lambda_{exc.} = 373$ nm, $\lambda_{monitored} = 530$ nm). IRF is the instrument response function.

In solution state (0.05 mM, THF), **TAT-3TRZ** shows a LE absorption band which closely matches with the acceptor control molecule (i. e. diphenyl triazine chloride, **TRZ-Cl**) at 280-320 nm region along with a red-shifted charge-transfer band at 320-410 nm region, characteristic of TADF chromophores (Figure 6.6a). Further, the solvatochromism studies show substantial Stokes-shift of the charge-transfer band with increasing solvent polarity reiterating the strong CT nature of the emission at longer wavelength ($\lambda_{exc.} = 300$ nm, Figure 6.6b). As expected, the strong vibronic feature of the LE emission band at 390-470 nm region do not change with solvent polarity. Lifetime analysis of the CT band of 0.05 mM toluene solution showed only the prompt fluorescence ($\tau_{avg.} = 4.0$ ns) and no delayed emission component was observed since vibrational and rotational quenching effects deactivate the triplet states rapidly ($\lambda_{exc.} = 373$

nm, $\lambda_{\text{monitored}} = 530$ nm, Figure 6.6c). Therefore, solid state properties were envisaged to surmount these quenching effects and result in strong ambient triplet emission.

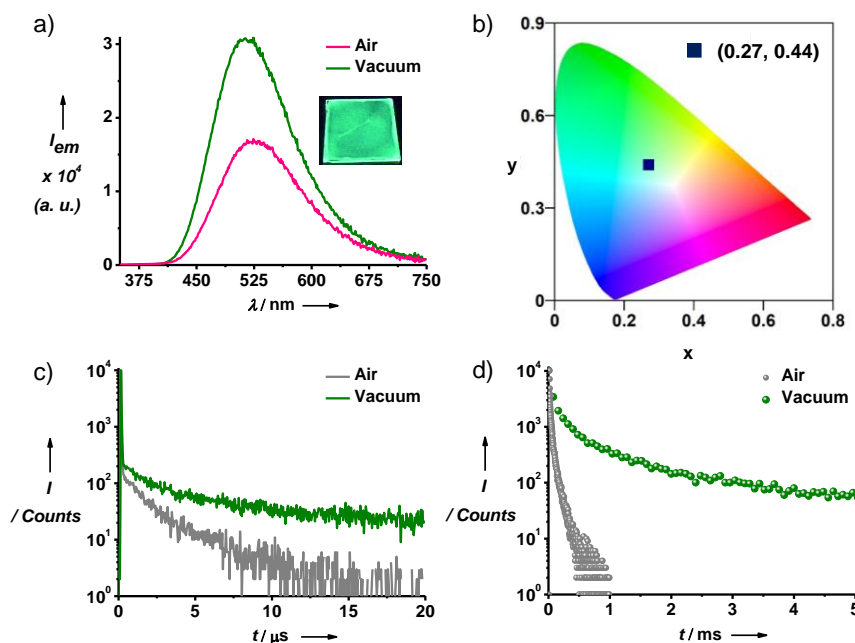


Figure 6.7. a) Comparison of steady-state emission intensity of **TAT-3TRZ-PMMA** hybrid film in air and under vacuum ($\lambda_{\text{exc.}} = 300$ nm). The inset shows the photograph of **TAT-3TRZ-PMMA** hybrid film under 365 nm UV-lamp. b) Commission Internationale de l'éclairage (CIE) colour co-ordinate of **TAT-3TRZ-PMMA** hybrid film. Time-resolved decay profile of **TAT-3TRZ-PMMA** hybrid film at c) short time-range (1 ns -20 μ s, $\lambda_{\text{exc.}} = 405$ nm, $\lambda_{\text{monitored}} = 510$ nm) and d) longer time-range (5 μ s-40 ms, $\lambda_{\text{exc.}} = 300$ nm, $\lambda_{\text{monitored}} = 510$ nm) taken both in air and under vacuum conditions. In all cases, 1 wt. % **TAT-3TRZ-PMMA** composition was used.

The emission properties of dilute **TAT-3TRZ-PMMA** (1 wt. % **TAT-3TRZ** doped in PMMA) hybrid films were studied substantial triplet contribution envisaging reduced non-radiative decay in the solid state with enhanced triplet stability. We observed a ~ 1.5 -fold increase in the emission intensity under vacuum, which is characteristic of triplet contribution in the emission profile (Figure 6.7a, *vide infra*) and the corresponding CIE colour co-ordinate is in the green-region (0.27, 0.44) (Figure 6.7b). As studied previously, in case of **TAT-3BP**, we observed both a relatively short-lived delayed emission component (1 ns-20 μ s time range) and a long-lived component (5 μ s -40 ms time-range) in the lifetime profile (Figure 6.7c and 6.7d). However, strong DF component even in air suggest excellent air-stability of the triplet states of **TAT-3TRZ**. As can be seen in Figure 6.7c, at short lifetime range, the lifetime profile can be fitted biexponentially with a prompt component of 21.5 ns (44 %) and a delayed component of 1.6 μ s

(56 %) in air ($\lambda_{exc.} = 405$ nm, $\lambda_{monitored} = 510$ nm).^[11] The delayed component increases substantially to 3.15 μ s (67 %) under vacuum. On the other hand, at longer time-range, the average delayed emission lifetime increased from 56.8 μ s in air to 3.4 ms under vacuum ($\lambda_{exc.} = 300$ nm, $\lambda_{monitored} = 510$ nm, Figure 6.7d). Therefore, the differential delayed lifetime components hint towards a dual DF and RTP which is even stable in air, as observed in the previous case (**TAT-3BP**).

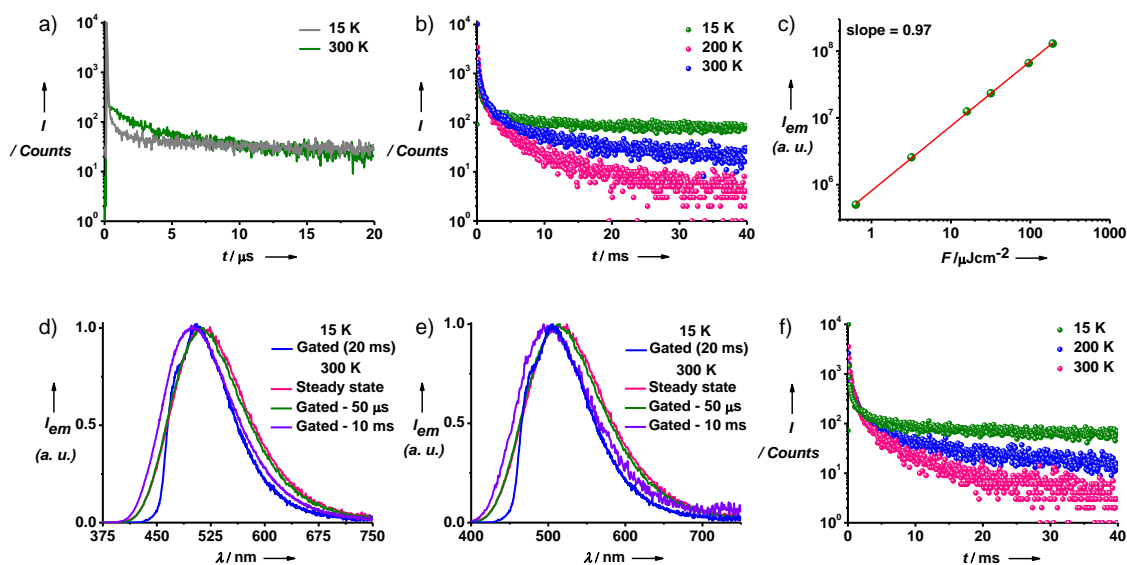


Figure 6.8. Lifetime profiles of **TAT-3TRZ-PMMA** hybrid film obtained at different temperatures while monitoring at a) short time-range ($\lambda_{exc.} = 405$ nm, $\lambda_{monitored} = 510$ nm) and b) longer time-range ($\lambda_{exc.} = 300$ nm, $\lambda_{monitored} = 510$ nm), showing TADF and RTP characteristics, respectively. c) Excitation intensity dependent emission profile of **TAT-3TRZ -PMMA** film excited at 355 nm. Normalized steady-state and gated emission spectra of **TAT-3TRZ-PMMA** hybrid film at different temperatures with different time-delays (50 μ s, 10 ms and 20 ms) while excited at d) locally-excited ($\lambda_{exc.} = 300$ nm) and e) charge-transfer ($\lambda_{exc.} = 360$ nm) absorption wavelengths, showing the presence of both TADF and room temperature phosphorescence. f) Temperature dependent lifetime profile of **TAT-3TRZ-PMMA** hybrid film excited at 360 nm ($\lambda_{monitored} = 510$ nm, $\tau_{avg.} = 1.0$ s at 15 K, $\tau_{avg.} = 2.58$ ms at 300 K). In all cases 1 wt. % **TAT-3TRZ-PMMA** was used.

To elucidate the delayed fluorescence and RTP characteristics of **TAT-3TRZ** comprehensively, we then performed temperature dependent time-resolved emission measurements. In Figure 6.8a, it can be seen that, the delayed emission component decreases from 3.15 μ s (67 %) at 300 K to 1.75 μ s (27 %) at 15 K.^[11] Therefore, the delayed lifetime component at this range corresponds to delayed fluorescence. On the other hand, the average

lifetime in the longer time range increases from 3.4 ms (at 300 K) to 1.58 s (at 15 K) confirming its phosphorescence nature ($\lambda_{\text{exc.}} = 300$ nm, $\lambda_{\text{monitored}} = 510$ nm) (Figure 6.8b). In addition, the linear dependence (slope = 0.97) of delayed fluorescence intensity with the excitation ($\lambda_{\text{exc.}} = 355$ nm) intensity proves the thermally activated nature of the emission (Figure 6.8c). Fast delayed fluorescence lifetime further prompted us to investigate the energy levels of emissive charge-transfer singlet and triplet states involved in the excited state spin-flipping process. Therefore, the phosphorescence spectrum was obtained by a time-gated emission measurement ($\lambda_{\text{exc.}} = 300$ nm, delay-time = 20 ms) at 15 K (Figure 6.8d). Interestingly, the onset of phosphorescence spectrum is observed to be higher in energy as compared to steady-state charge-transfer emission (Figure 6.8d). In addition, the time-gated emission at 300 K also shows a blue-shift with high delay-time (>50 μs) and reiterate the RTP emission spectrum to be higher in energy ($\Delta E_{\text{ST}} = 20 \pm 10$ meV) as compared to the steady-state and delayed fluorescence spectrum (Figure 6.8d). It is to be noted that, the RTP was also seen while exciting at charge-transfer absorption wavelength ($\lambda_{\text{exc.}} = 360$ nm) and similar blue-shift in the emission profile was also evident leading to identical phosphorescence feature at 15 K (Figure 6.8e and 6.8f).

To further understand the triplet state of **TAT-3RZ**, we analyzed the individual phosphorescence spectrum of donor and acceptor units and compared the spectral profile with the phosphorescence band of the **TAT-3TRZ**. As evident from Figure 6.9a, the phosphorescence spectrum of **TAT-3TRZ** ($\lambda_{\text{exc.}} = 300$ nm) at 15 K, is different from both the donor (0.05 mM **TAT** in THF) and acceptor (0.05 mM **BP** in THF) subunits at 77 K (Figure 6.9b). Nonetheless, the solvatochromism studies at 77 K further suggest a locally-excited nature of the phosphorescence, as the emission profiles do not change with solvent polarity. To summarize the excited state processes that lead to dual TADF and RTP characteristics of **TAT-3TRZ**, a simple Jablonski diagram is proposed in Figure 6.9c. Assuming the small energy gap between the ^1CT and ^3CT states a hyperfine coupling mechanism is envisaged to play key role for efficient spin-flipping process. However, the close proximity between the CT states and the ^3LE state (energy gap between the ^1CT and ^3LE is just 20 ± 10 meV), ideal for effective spin-vibronic coupling between the ^3CT and ^3LE states which in turn facilitates reverse intersystem crossing between the ^1CT and ^3CT states by an additional spin-orbit coupling effect (*vide infra*).^[15]

From the discussions above, we reiterate the importance of triazatruxenes as an emerging class of materials, with not just strong TADF, but as ambient phosphorescence emitters. The high photoluminescence quantum yield of both **TAT-3BP** (63 %) and **TAT-3TRZ** (58 %) and fast delayed fluorescence lifetime (~ 2.5 - 3.1 μs) is also highly suitable for their further translation to OLED devices. The CIE color co-ordinate of **TAT-3BP** is (0.20, 0.31) is still not close to deep-blue emission, and we are therefore plan to achieve this goal by suitable functionalization of

acceptor (BP), e. g. by introducing weak electron-donating functional groups or by adjusting the polarity of the host matrix.^[16]

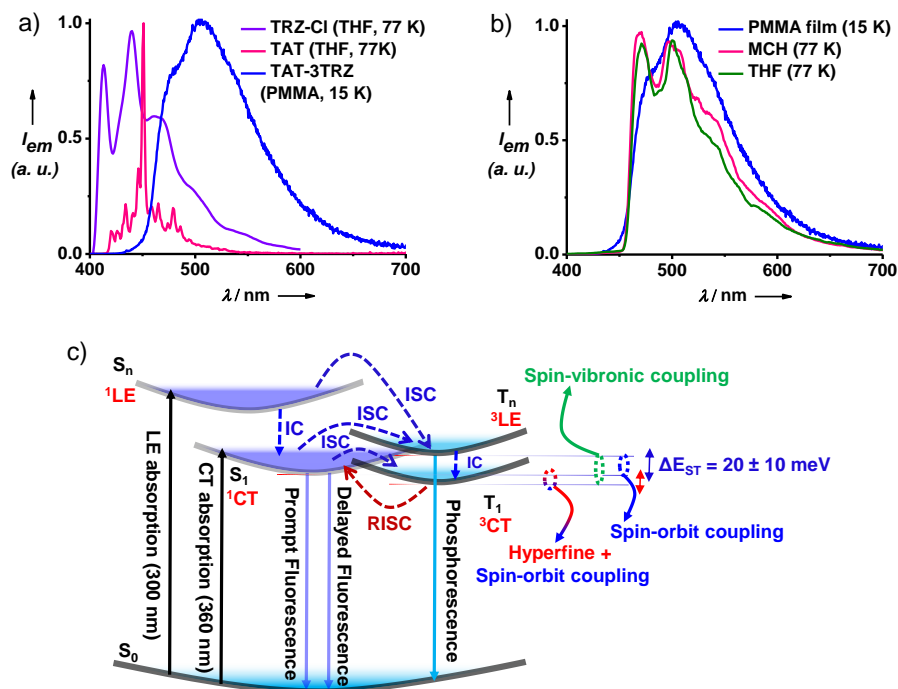


Figure 6.9. a) Phosphorescence spectrum ($\lambda_{exc.} = 300$ nm, delay-time = 20 ms) of **TAT-3TRZ** film (1 wt. % in PMMA) at 15 K and (3LE) phosphorescence spectrum of **TAT** (donor) and **TRZ-CI** (acceptor) in THF at 77 K ($[TAT]$ and $[TRZ-CI] = 0.05$ mM, $\lambda_{exc.} = 300$ nm, delay-time = 20 ms). b) Low temperature solvatochromism studies showing no significant shift on the phosphorescence emission profile of **TAT-3TRZ** at 77 K ($\lambda_{exc.} = 300$ nm, delay time = 10 ms, $[TAT-3TRZ] = 0.05$ mM). c) Simplified Jablonski diagram for **TAT-3TRZ** indicating various excited state processes leading to the triplet exciton harvesting. A higher energy 3LE undergoes spin-vibronic coupling with low-lying 3CT (green dotted circle). This in turn influences the spin-flipping process between the 1CT and 3CT states to result in fast RISC by a combined hyperfine and spin-orbit coupling (red-blue dotted circle). The access to the 3LE states can be done by exciting both at locally-excited (300 nm) as well as at charge-transfer (360 nm) absorption wavelengths. The spin-orbit coupling between the 1CT and 3LE is shown by the blue-dotted circle and the denoted energy gap (ΔE_{ST}) between these two states is 20 ± 10 meV. ISC = intersystem crossing, RISC = reverse intersystem crossing, IC = internal conversion.

6.5. Yellow-emissive Solution-processable TADF from Core-substituted Triazatruxene (TAT-NMI)

With a comprehensive overview on the TAT-based TADF emitters by the -NH substitution, we further explored the possibility of its core-substitution which is especially beneficial for designing solution-processable OLED materials. Hence, we selected previously studied naphthalene monoimide as an acceptor which did not show any TADF with a relatively weak donor unit, carbazole (**CzPhNMI**, Chapter 5). Utilizing a Suzuki coupling between the tetramethyl boronic ester derivative of TAT and bromo-naphthalimide, we synthesized donor-acceptor **TAT-NMI** in good yields (Figure 6.1, see Experimental Section). The long-alkyl side-chains of both donor and acceptor units are suitable for high-solubility in common organic solvents which is in line with the desired solution-processable TADF design.

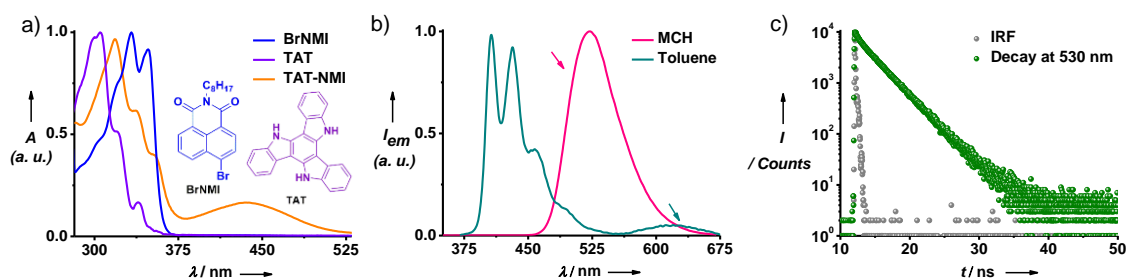


Figure 6.10. a) Normalized absorption and emission spectra of **TAT** (D), **BrNMI** (A) and **TAT-NMI** (D-A). ($[TAT]$ and $[BrNMI] = 0.05$ mM in THF, $[TAT-NMI] = 0.05$ mM, in toluene. Inset shows the molecular structures of bromo-naphthalimide (**BrNMI**) and triazatruxene (**TAT**). Emission spectra of show strong solvatochromic effects in solvents with different polarity ($[TAT-NMI] = 0.05$ mM, $\lambda_{exc.} = 330$ nm). The locally excited bands in toluene exhibit sharp vibronic features in the 380-520 nm region. Arrows indicate the CT emission bands. c) Fluorescence decay profile of 0.05 mM **TAT-NMI** dissolved in MCH ($\lambda_{exc.} = 373$ nm, $\lambda_{monitored} = 530$ nm). IRF is the instrument response function. D = donor, A = acceptor.

In solution state, **TAT-NMI** shows characteristic locally-excited absorption at 280-375 nm region with vibronic features and a broad charge-transfer band at 370-500 nm region (Figure 6.10a). The corresponding emission spectra show strong solvatochromic shift of the charge-transfer emission band ($\lambda_{exc.} = 330$ nm) and the average lifetime of the charge-transfer band is 2.77 ns ($\lambda_{exc.} = 373$ nm, $\lambda_{monitored} = 530$ nm, 0.05 mM MCH) (Figure 6.10b and 6.10c).

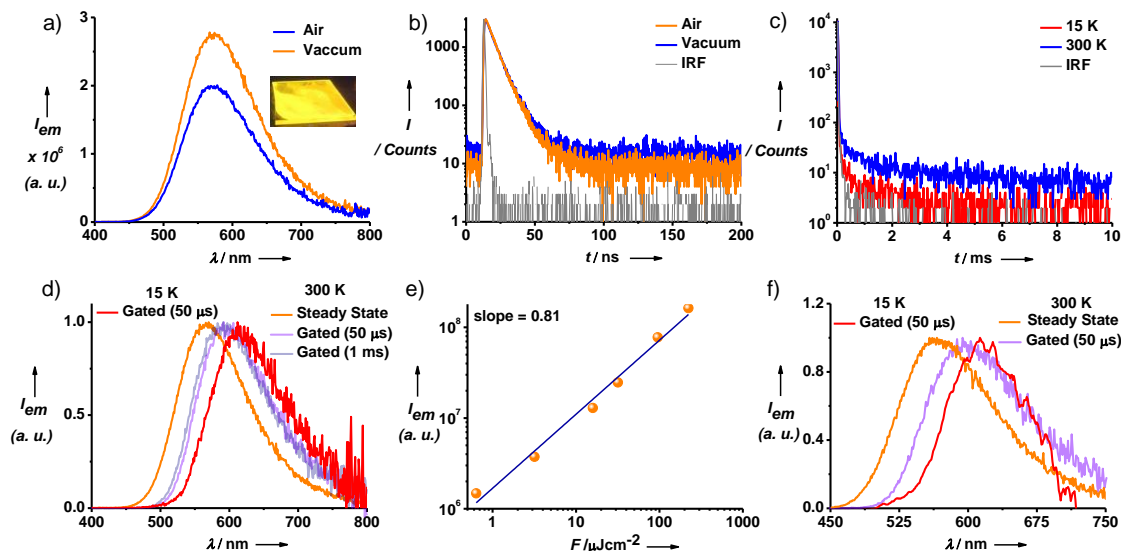


Figure 6.11. a) Comparison of steady-state emission intensity of **TAT-NMI-PMMA** hybrid film in air and under vacuum ($\lambda_{exc.} = 330$ nm. The inset shows the photograph of **TAT-NMI-PMMA** hybrid film under 365 nm UV-lamp. b) Fluorescence decay profile of **TAT-NMI-PMMA** hybrid film when monitored both in air and under vacuum ($\lambda_{exc.} = 340$ nm, $\lambda_{monitored} = 570$ nm) c) Temperature dependent lifetime profile at longer time-range ($\lambda_{exc.} = 330$ nm, $\lambda_{monitored} = 570$ nm) showing delayed fluorescence characteristic. The lifetime at 15 K was too weak for accurate fitting. Normalized steady-state and gated emission spectra of **TAT-NMI-PMMA** hybrid film at different temperatures with different time-delays (50 μ s and 1 ms) while excited at d) locally-excited ($\lambda_{exc.} = 330$ nm) and g) charge-transfer ($\lambda_{exc.} = 430$ nm) absorption wavelengths. e) Excitation intensity dependent emission profile of **TAT-NMI-PMMA** film excited at 355 nm. In all cases 1 wt. % **TAT-NMI-PMMA** was used. IRF = instrument response function.

Next, we performed the solid state emission characteristics of **TAT-NMI** doped in PMMA in low concentration (1 wt. % **TAT-NMI-PMMA** composition). Increase in emission intensity (~ 1.4 fold) of the hybrid film hints towards enhanced triplet stability under vacuum ($\lambda_{exc.} = 330$ nm) (Figure 6.11a) and therefore detailed time-resolved lifetime characteristics were performed to elucidate the triplet contribution. Lifetime profile of **TAT-NMI** shows a prompt fluorescence emission with average lifetime of 7.5 ns which does not increase under vacuum (Figure 6.11b, $\lambda_{exc.} = 340$ nm, $\lambda_{monitored} = 570$ nm) (Figure 6.11b).

On the other hand, a longer-lived component with average lifetime of 2.04 ms was observed under vacuum^[17] which decreases with lowering the temperature suggesting the delayed fluorescence characteristic of **TAT-NMI** (Figure 6.11c, $\lambda_{exc.} = 330$ nm, $\lambda_{monitored} = 570$ nm).^[18] Time-gated emission (delay-time = 50 μ s) profile at 15 K shows a substantial red-shift as compared to the charge-transfer emission band and assigned as the phosphorescence band of

TAT-NMI (Figure 6.11d). At room temperature, time-gated emission profile ($\lambda_{\text{exc.}} = 330 \text{ nm}$) (delay-time = 50 μs) also show a red-shift, although, very different from the phosphorescence band even at longer time-delay (1 ms) (Figure 6.11d). Therefore, the gated emission spectra (delay-time = 50 μs and 1 ms) at 300 K is assigned to the delayed fluorescence band. The reason behind such a high bathochromic shift ($\lambda_{\text{max.}} = 568 \text{ nm}$ to $\lambda_{\text{max.}} = 590 \text{ nm}$) is not very clear at this moment, although similar observation has been seen in a few TADF systems, reported by Adachi and co-workers.^[19] The plausible reason behind this shift has been proposed as the difference in the nuclear configuration of singlet and triplet states. To elaborate this hypothesis, it is explained by the following: The delayed fluorescence is obtained by the reverse intersystem crossing from triplet states after a substantially long-time (in this case, in the ms scale), which has different nuclear configuration from initial singlet state that lead to prompt fluorescence. The polarization in the host medium for initial singlet state (leading to prompt fluorescence) might be different than the singlet excited states formed by RISC (leading to delayed fluorescence), since the polarization in the host matrix varies with time.^[19c] Therefore, it is expected that the Frank-Condon factor for prompt fluorescence and delayed fluorescence in such scenario (temporal-change of polarization of these singlet states in the the host medium) would result in shifts in prompt and delayed fluorescence spectrum.^[19a] Nonetheless, a linear dependence (slope = 0.81) of the DF intensity confirms the TADF nature of the emission despite the relatively large singlet-triplet gap ($220 \pm 20 \text{ meV}$) (Figure 6.11d and 6.11e).

As evident from Figure 6.12a, the phosphorescence profile of **TAT-NMI** is different from both donor and acceptor subunits. therefore this observation suggests towards a substantial contribution from both the donor and acceptor subunits in the T_1 state (*vide infra*) and solvatochromism studies further confirm the LE nature of the phosphorescence emission from the T_1 state (Figure 6.12b). From the proposed Jablonski diagram (Figure 6.12c), we see a substantially high energy gap between the lowest ^1CT state and ^3LE state ($220 \pm 20 \text{ meV}$) which in turn explains the very slow DF lifetime (and RISC) as well as weak DF component (~30 % of the total emission) in the total emission.^[20]

However, its worthwhile to mention that, the core-substitution does lead to CT emission reiterating the high oscillator strength with relatively more planar structure (**TAT-NMI**) as compared to N-substituted compounds (**TAT-3BP** and **TAT-3TRZ**). Therefore, bringing the steric effects into the future designs are envisioned to hold the key for the development of new solution-processable OLED materials based on these novel class of molecules. Moreover, ample opportunity to substitute the core as well as $-\text{NH}$ positions with suitable acceptors (and even donors) would lead us to understand the concept of multi-resonance effects in order to yield high triplet harvesting through TADF with desired (fast) RISC rates.^[21]

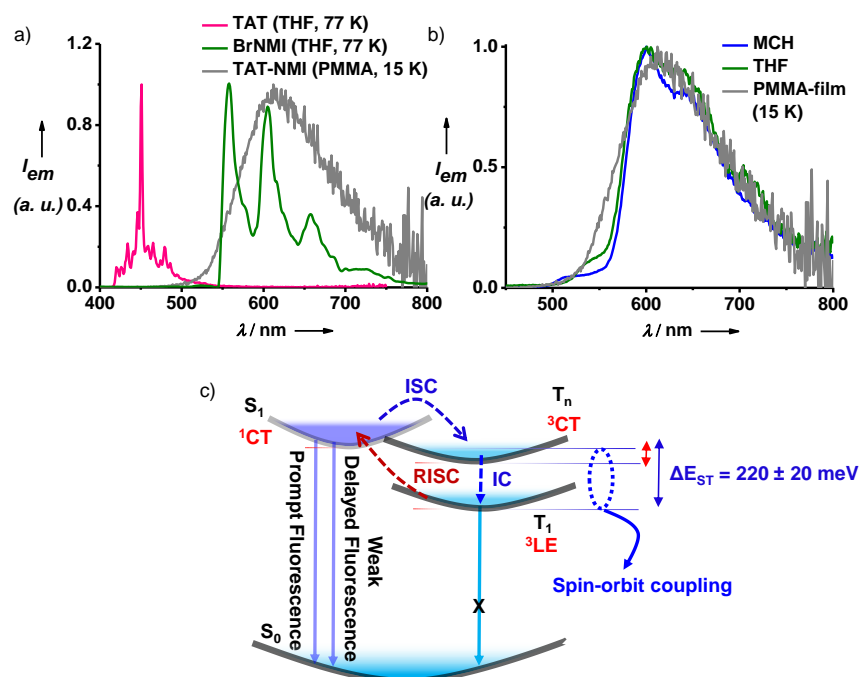


Figure 6.12. a) Phosphorescence spectrum ($\lambda_{exc.} = 330$ nm, delay-time = 1 ms) of **TAT-NMI** film (1 wt. % in PMMA) at 15 K and (3LE) phosphorescence spectrum of **TAT** (donor) and **BrNMI** (acceptor) in THF at 77 K ($[TAT]$ and $[BrNMI] = 0.05$ mM, $\lambda_{exc.} = 300$ nm for **TAT** and $\lambda_{exc.} = 340$ nm for **BrNMI**, delay-time = 20 ms for both). b) Low temperature solvatochromism studies on the phosphorescence emission of **TAT-NMI** at 77 K ($\lambda_{exc.} = 330$ nm, delay-time = 1 ms, $[TAT-NMI] = 0.05$ mM). Absence of any significant change in the emission spectra with solvent polarity suggest these phosphorescence bands are of locally-excited (3LE) character. c) Simplified Jablonski diagram for **TAT-NMI** indicating various excited state process involving the triplet exciton harvesting. Here, a large difference between the T_1 (3LE) and T_1 (1CT), communicating through spin-orbit coupling, slows down the RISC process as well as lead to poor triplet harvesting. ISC between the 1CT and 3CT states are expected to be mediated by weak hyperfine coupling mechanism. However, the lower-lying 3LE will be majorly populated according to Kasha's rule and hence the RISC is very poor in this case due to large gap.

6.6. Conclusions

In conclusion, we have shown the importance of charge-transfer excited state confinement within the vicinity of LE triplet states to achieve fast DF characteristics in case of **TAT-3BP** and **TAT-3TRZ**. Although we could not achieve a deep-blue emission from these molecules, the CT energy can be tuned by suitable host-polarity. Nonetheless, increased electron-deficient nature of triazine units (**TAT-3TRZ**) further red-shifts the CT states as compared to the benzophenone derivative (**TAT-3BP**), suggesting that the tuning of the benzophenone core might

lead to the desired confinement of the charge-transfer energy to deep-blue region. Here, it is also worth mentioning that, the phosphorescence bands of both **TAT-3TRZ** and **TAT-3BP** do not match with the individual donor/acceptor units and we envision the contribution from both donor and acceptor units lead to such difference in the T_1 state where the conformation of the molecules play a crucial role. Hence a detailed theoretical calculation is underway in order to elucidate the excitation configurations corresponding to the T_1 states by natural transition orbital analyses. Next, we also showed that triazatruxenes can be utilized as a versatile donor scaffold for future development of solution processable TADF materials by synthesizing a yellowish-orange emitting **TAT-NMI** derivative where we substituted its $-NH$ positions with long-alkyl chains and substituting its core with a strong acceptor unit, naphthalene monoimide. As a perspective, we envision that relatively unexplored triazatruxene moieties hold a great promise for designing the state-of-the-art TADF materials considering their excellent chemical tunability and also high charge-transport ability.

6.7. Experimental Section

6.7.1. General Methods

NMR Measurements: 1H and ^{13}C NMR spectra were recorded on a BRUKER AVANCE-400 fourier transformation spectrometer with 400 and 100 MHz respectively. The spectra are calibrated with respect to the residual solvent peaks. The chemical shifts are reported in parts per million (ppm) with respect to TMS. Short notations used are, s for singlet, d for doublet, t for triplet, q for quartet and m for multiplet.

Optical Measurements: Electronic absorption spectra were recorded on a Perkin Elmer Lambda 900 UV-Vis-NIR Spectrometer and emission spectra were recorded at FLS1000 spectrometer, Edinburgh Instruments. UV-Vis and emission spectra were recorded in 10 mm path length cuvette. Fluorescence spectra of films were recorded in front-face geometry to avoid self-absorption at high concentrations. Temperature dependent photoluminescence spectra were recorded at the same instrument using a cryostat to control the temperature (Advanced Research Systems). For laser fluence dependent measurements with 355 nm excitation source with a delay-time of 1 μs and integration time of 10 μs .

Lifetime measurements and quantum yield: Solution state fluorescence lifetimes were performed on a Horiba DeltaFlex time-correlated single-photon-counting (TCSPC) instrument. A 373 nm nano-LED with a pulse repetition rate of 1 MHz was used as the light source. The instrument response function (IRF) was collected by using a scatterer (Ludox AS40 colloidal silica, Sigma-Aldrich). Phosphorescence, delayed fluorescence lifetime and gated emission was

measured on FLS1000 spectrometer, Edinburgh Instruments equipped with a micro-flash lamp ($\mu\text{F}2$) set-up. For **TAT-3BP** and **TAT-3TRZ**, 405 nm pulsed diode laser-source with a pulse repetition rate of 10 KHz was used in MCS mode, in order to measure the delayed fluorescence lifetime. On the other hand, for **TAT-NMI** micro-flash lamp was used ($\lambda_{\text{exc.}} = 380 \text{ nm}$) for delayed fluorescence lifetime measurement. Quantum yield was measured using an integrated sphere in the same FLS1000 spectrometer. Temperature dependent lifetimes spectra for all the samples were recorded at the same instrument equipped with a cryostat set-up (Advanced Research Systems) to control the temperature.

High Resolution Mass Spectroscopy (HRMS): HR-MS was carried out using Agilent Technologies 6538 UHD Accurate-Mass Q-TOF LC/MS.

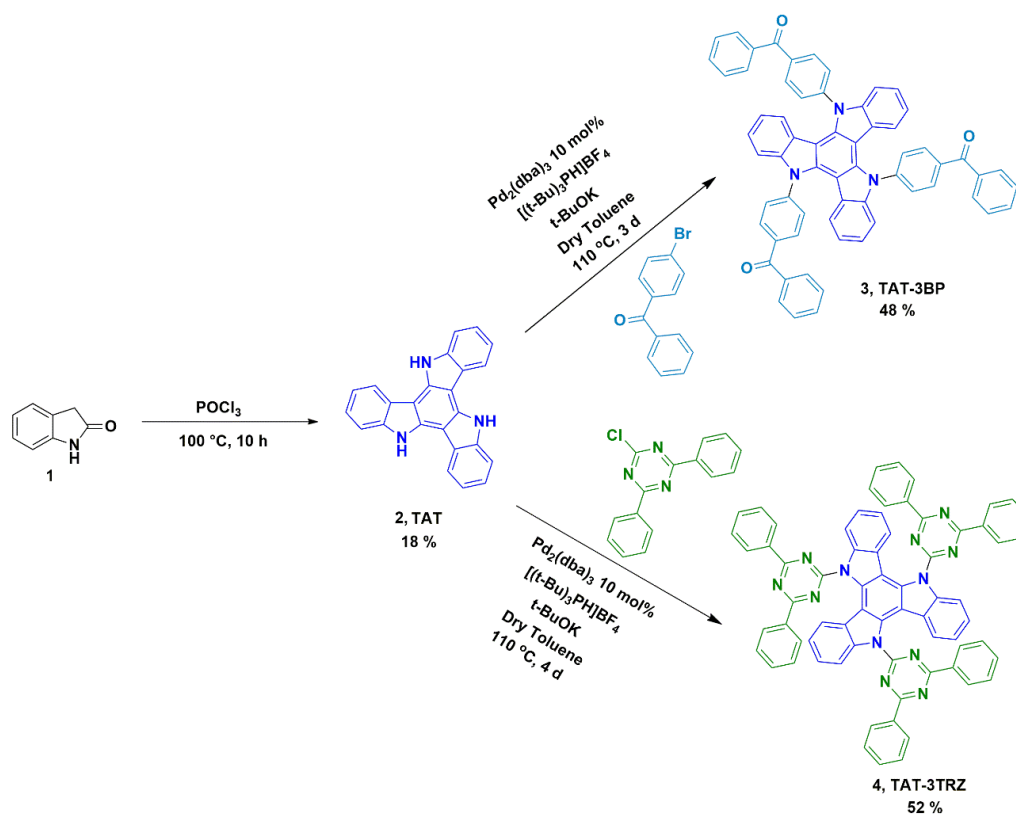
Matrix-Assisted Laser Desorption Ionization (MALDI): MALDI was performed on a Bruker daltonics Autoflex Speed MALDI TOF System (GT0263G201) spectrometer using *trans*-2-[3-(4-*tert*-Butylphenyl)-2-methyl-2-propenylidene]malononitrile (DCTB) as the matrix.

6.7.2. Synthesis

6.7.2a Synthesis of **TAT-3BP** and **TAT-3TRZ**

2-Oxindole, 4-Bromobenzophenone, Bromobenzene, Benzophenone, Phenylmagnesium bromide, 2,4,6-Trichloro-1,3,5-triazine, Tris(dibenzylideneacetone)dipalladium(0), Tri-*tert*-butylphosphonium tetrafluoroborate, Potassium *tert*-butoxide, POCl_3 , as well as deuterated solvents CDCl_3 , $\text{DMSO-}d_6$, were purchased from Sigma-Aldrich and Alfa-Aesar and used without further purification.

6.7.2a Synthetic scheme:

**Scheme 6.1.** Synthetic scheme of **TAT-3BP** and **TAT-3TRZ**.

Synthesis of **TAT (2)** is given in Chapter 3.

Synthesis of **TAT-3BP**:

In a two-neck RB flask equipped with a reflux condenser, Pd₂(dba)₃ (0.174 g, 0.19 mmol, 30 mol %) was taken and 30 mL of dry toluene was added followed by purging with N₂ at room temperature for 10 minutes under stirring. To this pink suspension, the ligand [(t-Bu)₃PH]BF₄ (0.110 g, 0.38 mmol, 60 mol %) was added and purged with N₂ for another 10 minutes. Subsequently, a mixture of triazatruxene (0.200 g, 0.58 mmol, 1 equiv.) and 4-Bromobenzophenone (0.509 g, 1.95 mmol, 3.36 equiv.) were added to the reaction mixture and purged with N₂ for 15 minutes. Finally, to this brown suspension, t-BuOK (0.306 g, 2.73 mmol, 4.7 equiv.) was added, purged with N₂ for 10 minutes and finally allowed to reflux at 110 °C for 3 days. The resulting dark brown suspension was filtered, the residue was washed with DCM, obtained the clear dark brown filtrate, which was extracted with water. The collected organic layer was dried over anhydrous Na₂SO₄ and evaporated under reduced pressure. The dark brown solid thus obtained, was purified by 100-200 mesh silica gel column chromatography by using 10 %-50 % EtOAc:Hexane solvent mixture as eluent to obtain pale yellow solid. This solid was further washed with EtOAc to obtain pure **TAT-3BP**.

TAT-3BP: Yellow-solid (0.24 g, 48 % yield); ^1H NMR (400 MHz, CDCl_3 , ppm): δ_{H} 8.08 (d, 8.4 Hz, 6H), 7.94 (d, 7.2 Hz, 6H), 7.80 (d, 8.4 Hz, 6H), 7.66-7.62 (m, 3H), 7.56-7.51 (m, 9H), 7.31 (t, 3H), 6.95-6.91 (m, 3H), 6.30 (d, 8 Hz, 3H); ^{13}C NMR (100 MHz, CDCl_3): δ_{C} 195.83, 144.30, 141.50, 137.43, 137.28, 137.17, 133.01, 131.94, 130.34, 128.67, 128.41, 124.10, 122.85, 122.72, 120.69, 110.21, 105.54; HRMS (ESI): m/z calculated for $\text{C}_{63}\text{H}_{39}\text{N}_3\text{O}_3$: 885.2991; Observed 886.3284 ($\text{M}+\text{H}$) $^+$.

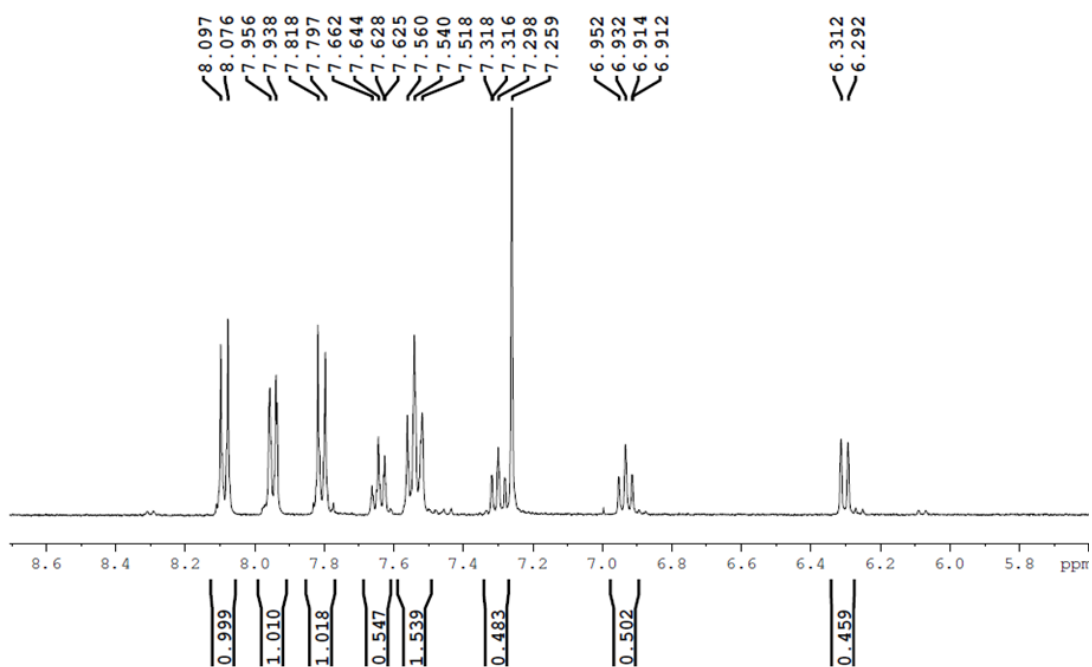


Figure 6.13. ^1H NMR spectrum of TAT-3BP in CDCl_3 .

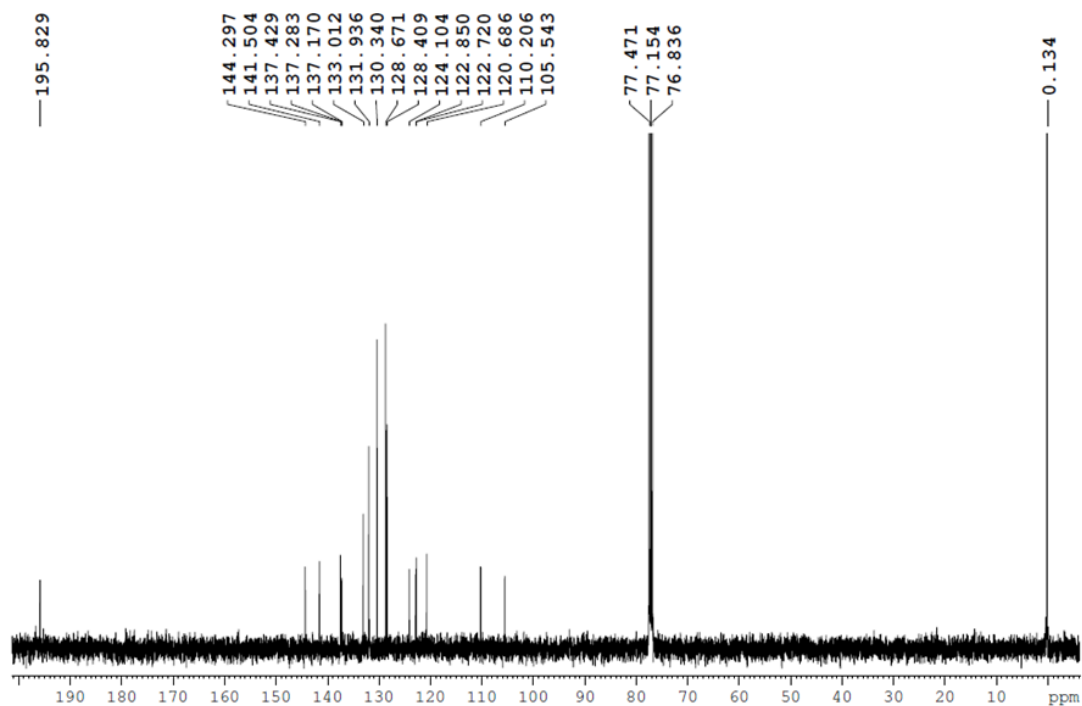


Figure 6.14. ^{13}C NMR spectrum of *TAT-3BP* in CDCl_3 .

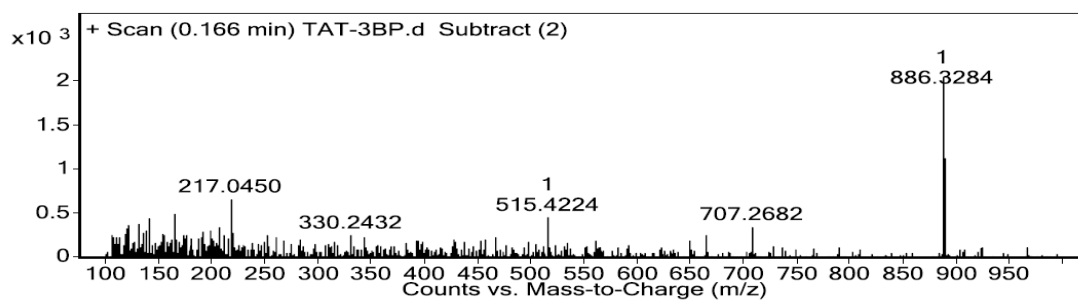
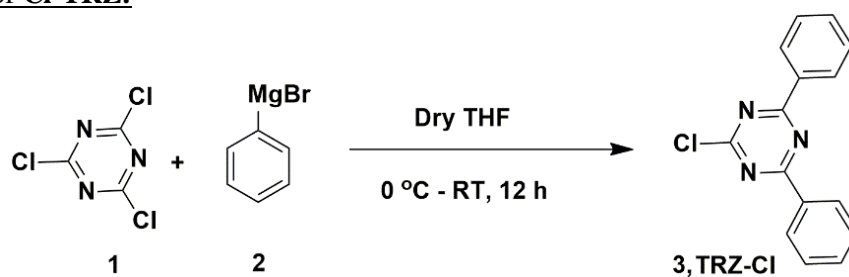


Figure 6.15. ESI-HRMS spectrum of *TAT-3BP*.

Synthesis of **Cl-TRZ**:



Scheme 6.2. Synthetic scheme of *TRZ-Cl*.

Synthesis of TRZ-Cl: In a two-neck round bottom flask 2,4,6-Trichloro-1,3,5-triazine (1 g, 5.37 mmol) was taken in 15 mL of dry THF under N₂ atmosphere. The mixture was then allowed to stir at 0 °C for 5 minutes. To this solution, 1(M) Phenylmagnesium bromide in THF (11 mL, 10.75 mmol) was added slowly through syringe at 0 °C over 30 minutes. The reaction mixture was stirred at room temperature for 12 h to get a dark-red solution which was poured in ice-water and extracted with DCM. The combined organic layer was dried over anhydrous Na₂SO₄ and evaporated under reduced pressure. The obtained crude was purified by 100-200 silica-gel column chromatography by using 20 %- 50 % CHCl₃:Hexane solvent mixture as eluent to obtain 2-chloro-4,6-diphenyl-1,3,5-triazine, **TRZ-Cl** as white crystalline solid.

TRZ-Cl: White crystalline solid (0.97 g, Yield = 68%); ¹H NMR (400 MHz, CDCl₃, ppm): δ_H 8.62 (d, 7.2 Hz, 4H), 7.65-7.61 (m, 2H), 7.56-7.53 (m, 4H); ¹³C NMR (100 MHz, CDCl₃, ppm): δ_C 173.56, 172.33, 134.53, 133.69, 129.55, 128.96; HRMS (ESI): *m/z* calculated for C₁₅H₁₀ClN₃: 267.0563; Observed 268.0704 (M+H)⁺.

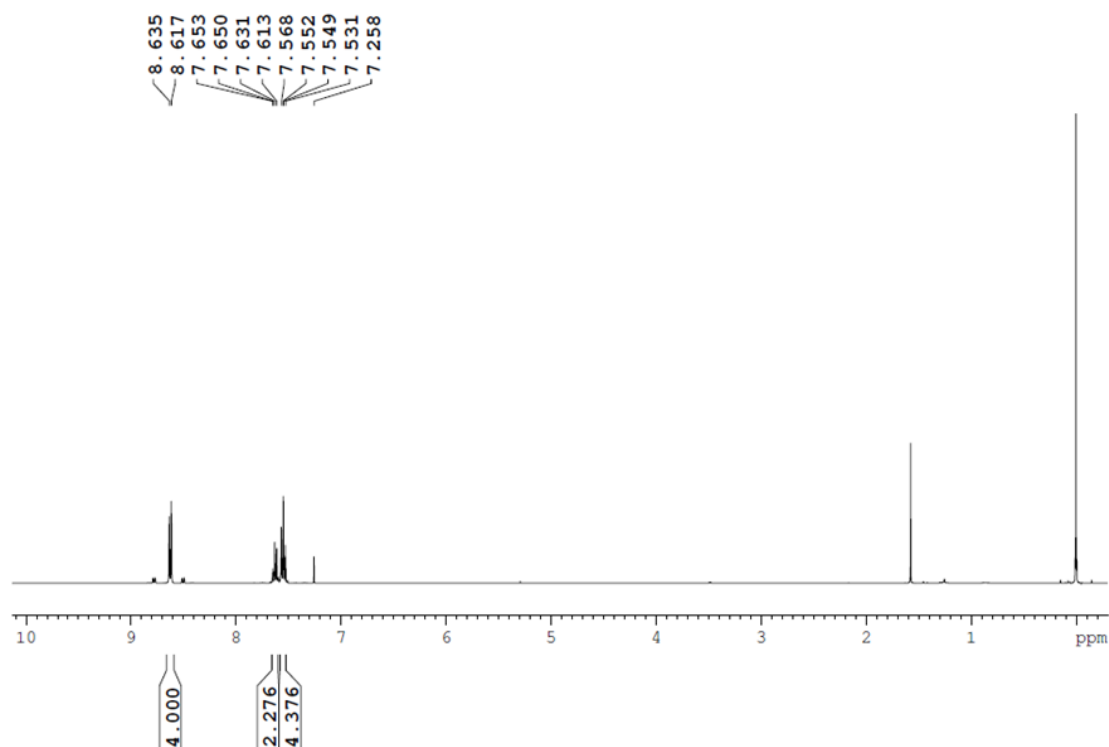


Figure 6.16. ¹H NMR spectrum of **TRZ-Cl** in CDCl₃.

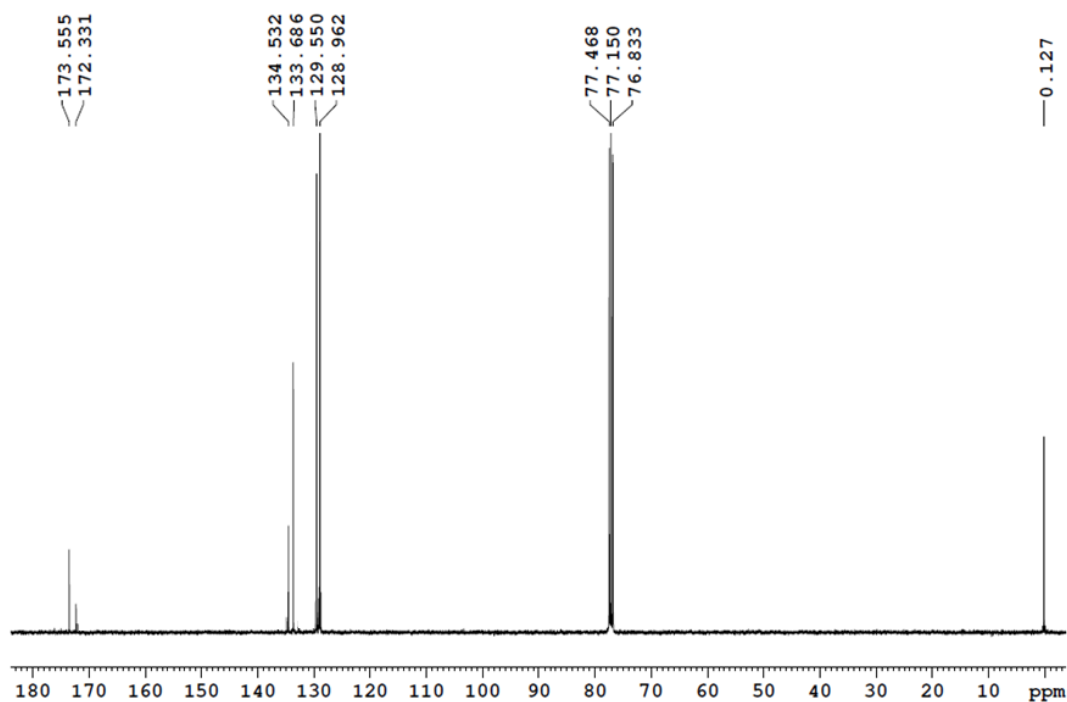


Figure 6.17. ^{13}C NMR spectrum of **TRZ-Cl** in CDCl_3 .

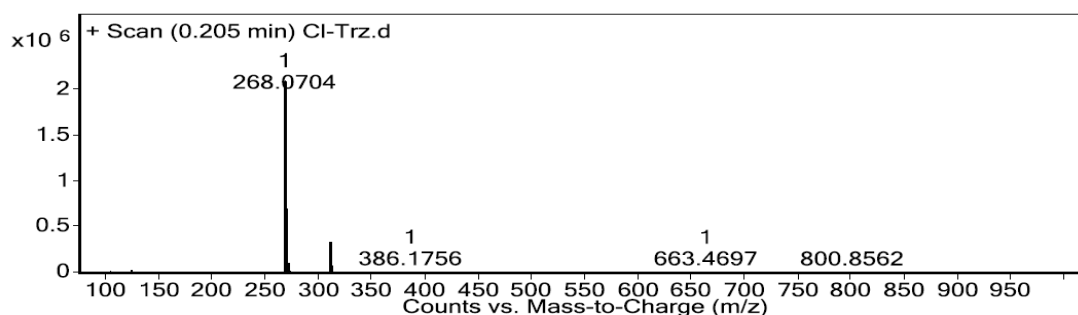


Figure 6.18. ESI-HRMS spectrum for **TRZ-Cl**.

Synthesis of **TAT-3TRZ**:

In a 100 mL two-neck RB flask equipped with reflux condenser, the catalyst $\text{Pd}_2(\text{dba})_3$ (0.174 g, 0.19 mmol, 30 mol %) was dissolved in 30 mL of dry toluene and purged with N_2 at room temperature for 10 min under stirring. To this pink suspension, $[(\text{t-Bu})_3\text{PH}]\text{BF}_4$ (0.110 g, 0.38 mmol, 60 mol %) was added and purged with N_2 for 10 minutes. Subsequently, a mixture of triazatruxene (0.200 g, 0.58 mmol, 1 equiv.) and 2-chloro-4,6-diphenyl-1,3,5-triazine (0.523 g, 1.95 mmol, 3.36 equiv.) were added to the reaction suspension and purged with N_2 for additional 15 minutes. Finally, to this reaction suspension, t-BuOK (0.306 g, 2.73 mmol, 4.7 equiv.) was added, purged with N_2 for 10 minutes and allowed to stir at 110 °C for 4 days under reflux and inert atmosphere. The resulting dark brown suspension was filtered and the residue was washed

with DCM to obtain a clear dark brown filtrate. The filtrate was then extracted with water and combined organic layer was dried under anhydrous Na_2SO_4 and evaporated under reduced pressure. The obtained dark brown solid was purified by 100-200 silica-gel column chromatography by using 10 % -50 % CHCl_3 :Hexane solvent mixture to obtain **TAT-3TRZ** as pale-yellow solid.

TAT-3TRZ: pale yellow solid (0.33 g, 52 % yield); ^1H NMR (400 MHz, CDCl_3 , ppm): δ_{H} 9.07 (d, 8.4 Hz, 3H), 8.43 (m, 12H), 7.52 (m, 6H), 7.50-7.38 (m, 6H), 7.36-7.34 (m, 9H), 7.10-7.01 (m, 6H); ^{13}C NMR (100 MHz, CDCl_3 , ppm): δ_{C} 173.12, 165.45, 142.23, 141.06, 135.83, 132.89, 129.31, 128.76, 127.98, 127.37, 126.69, 125.77, 123.69, 123.32, 122.52; HRMS (ESI): m/z calculated for $\text{C}_{69}\text{H}_{42}\text{N}_{12}$: 1114.3968: Observed 1039.3817 (M-Phenyl+H) $^+$.

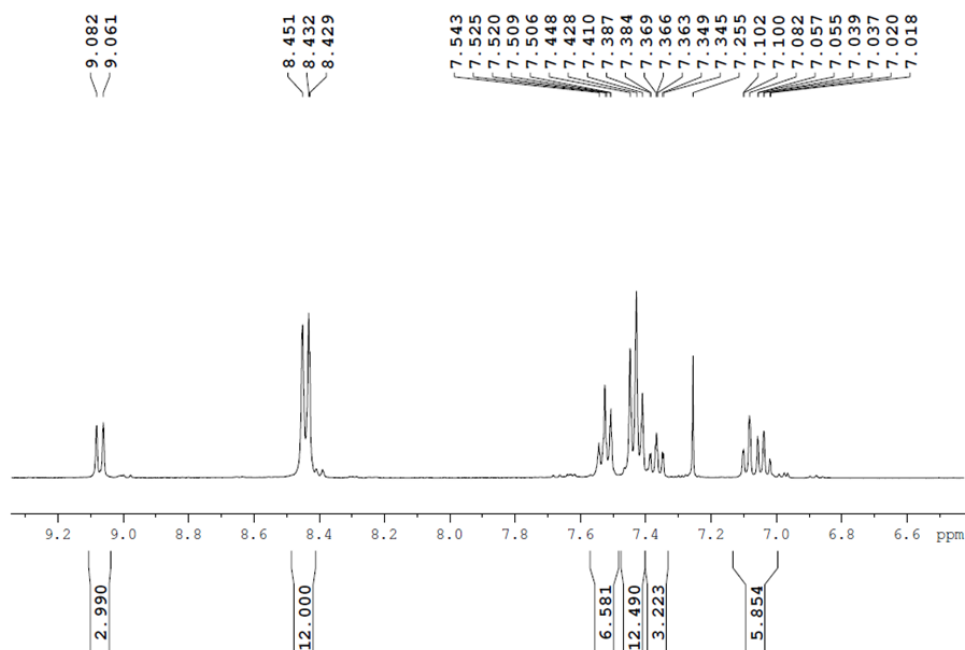


Figure 6.19. ^1H NMR spectrum of **TAT-3TRZ** in CDCl_3 .

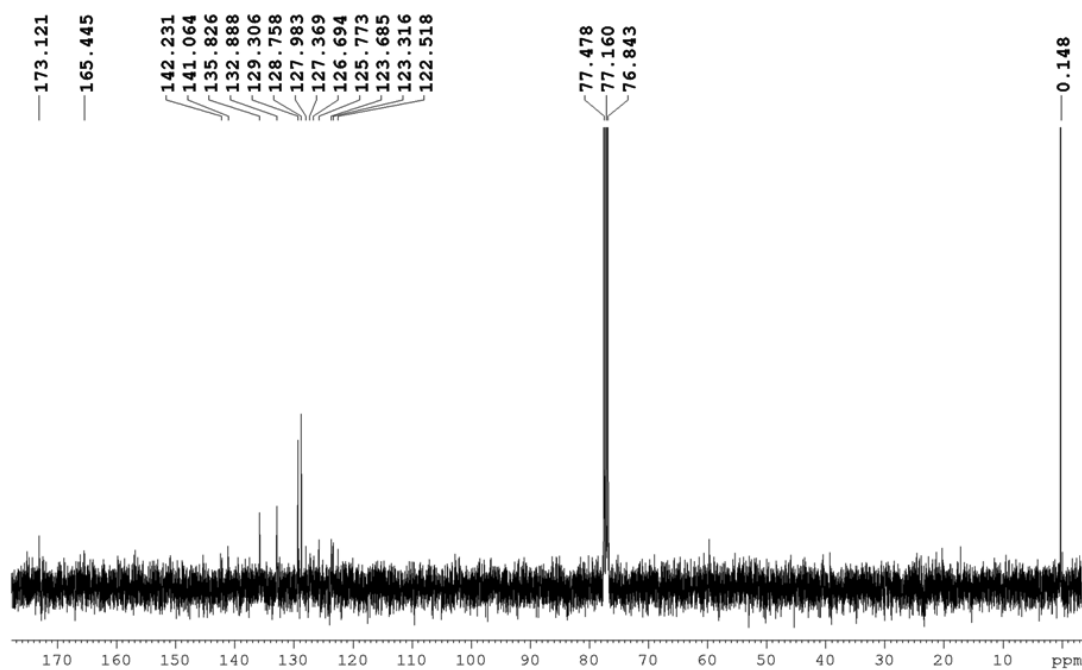


Figure 6.20. ^{13}C NMR spectrum of *TAT-3TRZ* in CDCl_3 .

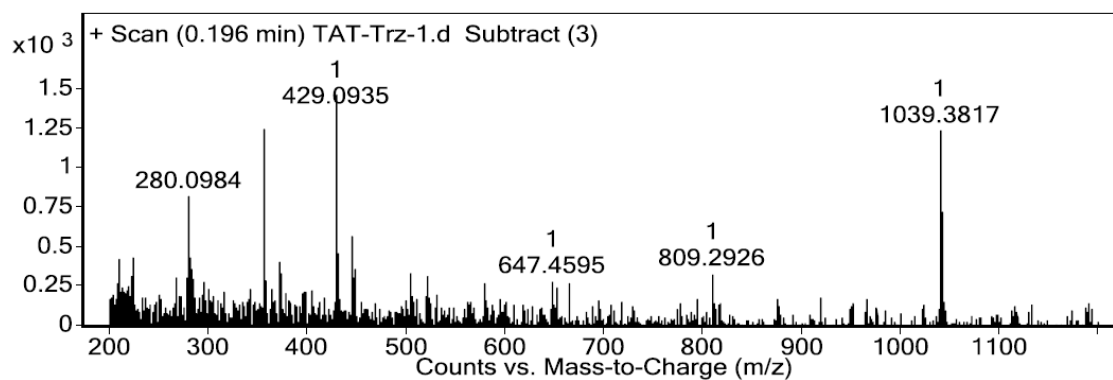
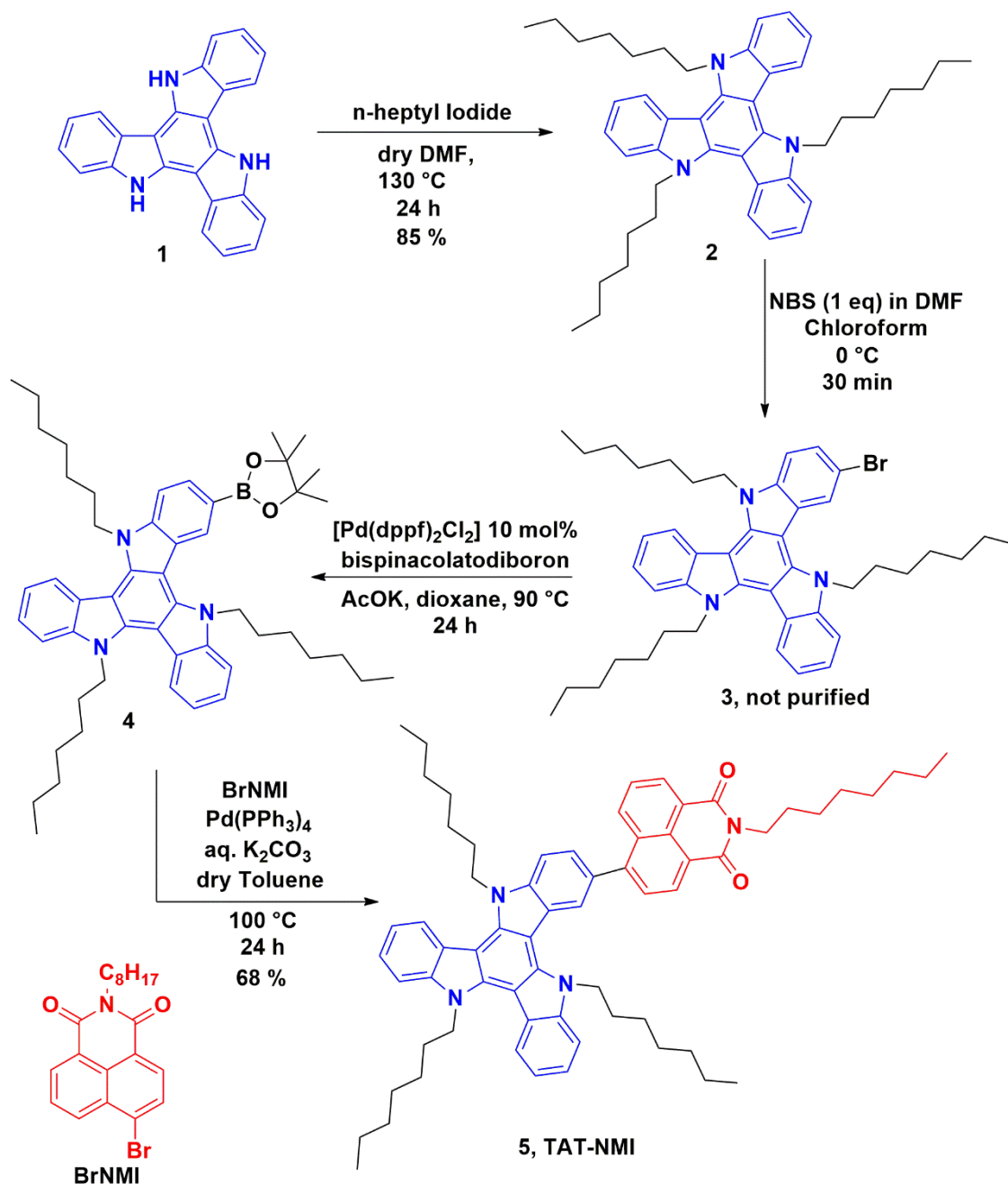


Figure 6.21. ESI-HRMS spectrum of *TAT-3TRZ*.

6.7.2b. Synthesis of **TAT-NMI**:

NBS, $[\text{Pd}(\text{dppf})_2\text{Cl}_2]$, $\text{Pd}(\text{PPh}_3)_4$, K_2CO_3 and AcOK were purchased from Spectrochem, bispinacolatodiboron were and NBS (N-bromosuccinimide) were purchased from Alfa-Aesar and used without further purification.



Scheme 6.3. Synthetic scheme of **TAT-NMI**.

3 was synthesized according to literature procedure.^[22] Synthesis of **BrNMI** is given in Chapter 5.

Synthesis of 4: **3** was (420 mg, 0.58 mmol), bis(pinacolato)diboron (271 mg, 1.45 mmol) and potassium acetate (161 mg, 1.65 mmol) were dissolved in anhydrous dioxane (20 mL) and purged with nitrogen for 15 minutes. To this mixture, [Pd(dppf)₂Cl₂] (45 mg, 10 mol %) was then added and stirred further at 90°C for 24 h. The solution was cooled down to room temperature upon completion and the solvent was then evaporated to dryness. The resulting crude was then dissolved in DCM and finally washed with water (3 x 30 mL) and followed by drying over anhydrous Na₂SO₄. The combined organic layer was then concentrated under reduced pressure to obtain a brown viscous oil. This was finally purified by silica-gel column chromatography using 30% Chloroform-Hexane mixture as the eluent.

4: Colourless oil (270 mg); ¹H NMR (400 MHz, CDCl₃, ppm): δ_H 8.27 (d, 7.2 Hz, 3H), 8.0 (s, 1H), 7.7 (d, 6.6 Hz, 1H), 7.6 (d, 8.4 Hz, 2H), 7.4 (t, 6.6 Hz, 2H), 4.98 (t, 8.4 Hz, 2H), 4.8 (m, 3H), 1.9 (m, 6H), 1.42 (s, 12 H), 1.26-1.18 (m, 22 H), 0.78 (m, 9H); ¹³C NMR (100 MHz, CDCl₃, ppm): δ_C 141.0, 140.5, 139.6, 138.9, 126.0, 122.7, 121.6, 121.5, 120.7, 119.8, 119.7, 110.6, 110.5, 103.3, 103.2, 103.19, 83.8, 47.1, 48.9, 31.76, 31.72, 29.08, 28.97, 26.75, 26.71, 25.05, 22.56, 14.07; MALDI-TOF: *m/z* calculated for C₅₁H₆₈BN₃O₄: 765.5405; Observed: 765.637 (M⁺).

Synthesis of (TAT-NMI): BrNMI (0.2 g, 0.52 mmol) and **4** (0.23 g, 0.62 mmol) were taken in a 100 mL round bottom flask. To this mixture anhydrous Toluene (12 mL) was added above under N₂ atmosphere, followed by purging with N₂ for 15-20 minutes with vigorous stirring. K₂CO₃ (0.11 g, 0.77 mmol) was dissolved in millipore water (0.5 mL) and added to the above reaction mixture followed by the addition of Pd(PPh₃)₄ (0.03 g, 5 mol%). This resulting suspension was further purged with N₂ for 15 minutes before refluxing under inert condition at 110 °C for about 24 h. After completion of starting material, 15 mL water was added and extracted with chloroform (50 mL). Organic layer was washed with brine solution followed by drying over anhydrous Na₂SO₄. Organic layer was concentrated under reduced pressure and the resulting crude product was purified by 100-200 silica-gel column chromatography using 5 % chloroform-hexane as eluent to obtain **TAT-NMI** as orange solid.

TAT-NMI: Red solid (0.17 g, 68 % yield); ¹H NMR (600 MHz, CDCl₃, ppm): δ_H 8.7 (d, 11 Hz, 1H), 8.0 (d, 9.6 Hz, 1H), 8.53 (dd, 1.8 Hz, 1H), 8.4 (d, 12 Hz, 1H), 7.9 (d, 11 Hz, 1H), 7.76-7.65 (m, 4H), 7.50-7.35 (m, 5H), 4.9 (t, 4.8 Hz, 6H), 4.2 (d, 12 Hz, 2H), 2.03-1.99 (m, 8H), 1.29-0.73 (m, 46H); ¹³C NMR (100 MHz, CDCl₃, ppm): δ_C 147.9, 141.0, 140.9, 139.6, 139.2, 138.7, 133.17, 133.12, 131.15, 130.8, 130.5, 128.9, 128.2, 126.7, 123.39, 123.68, 123.36, 123.0, 122.9, 121.7, 121.6, 121.5, 121.4, 119.8, 111.9, 110.6, 110.57, 103.54, 103.2, 102.9, 47.0, 40.5, 31.8, 31.6,

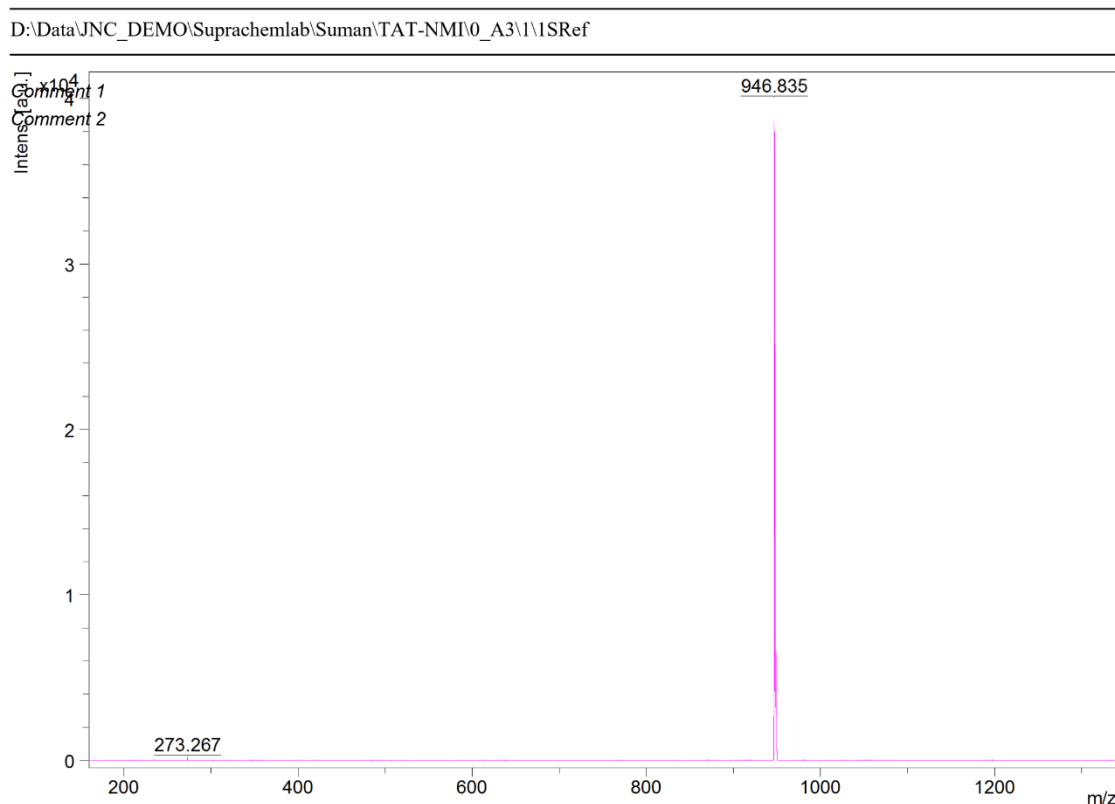


Figure 6.24. MALDI-TOF spectrum of *TAT-NMI*.

6.8. References

- [1] a) S. Reineke, *Nat. Mater.* **2015**, *14*, 459; b) S. Reineke, *Nat. Photonics* **2014**, *8*, 269; c) M. Zhu, C. Yang, *Chem. Soc. Rev.* **2013**, *42*, 4963; d) Y. Im, S. Y. Byun, J. H. Kim, D. R. Lee, C. S. Oh, K. S. Yook, J. Y. Lee, *Adv. Funct. Mater.* **2017**, *27*, 1603007; e) W. C. Chen, C. S. Lee, Q. X. Tong, *J. Mater. Chem. C* **2015**, *3*, 10957.
- [2] a) X. Cai, S.-J. Su, *Adv. Funct. Mater.* **2018**, *28*, 1802558; b) J.-H. Lee, C.-H. Chen, P.-H. Lee, H.-Y. Lin, M.-K. Leung, T.-L. Chiu, C.-F. Lin, *J. Mater. Chem. C* **2019**, *7*, 5874.
- [3] a) Y. Yamada, H. Inoue, S. Mitsumori, T. Watabe, T. Ishisone, T. Hara, T. Takahashi, H. Nakashima, S. Seo, *SID Symp. Dig. Tech. Pap.* **2016**, *47*, 711; b) G. Li, K. Klimes, T. Fleetham, Z. Q. Zhu, J. Li, *Appl. Phys. Lett.* **2017**, *110*, 113301; c) T. B. Fleetham, L. Huang, K. Klimes, J. Brooks and J. Li, *Chem. Mater.* **2016**, *28*, 3276; d) J. Lee, C. Jeong, T. Batagoda, C. Coburn, M. E. Thompson, S. R. Forrest, *Nat. Commun.* **2017**, *8*, 15566; e) P. Heimel, A. Mondal, F. May, W. Kowalsky, C. Lennartz, D. Andrienko, R. Lovrincic, *Nat. Commun.* **2018**, *9*, 4990; f) Y. Zhang, J. Lee and S. R. Forrest, *Nat. Commun.* **2014**, *5*, 5008; g) K. Udagawa, H. Sasabe, C. Cai and J. Kido, *Adv. Mater.* **2014**, *26*, 5062; h) J. Lee, H. F. Chen, T. Batagoda, C. Coburn, P. I.

Djurovich, M. E. Thompson, S. R. Forrest, *Nat. Mater.* **2016**, *15*, 92; Z. Chen, L. Wang, S. Su, X. Zheng, N. Zhu, C. L. Ho, S. Chen, W. Y. Wong, *ACS Appl. Mater. Interfaces* **2017**, *9*, 40497.

[4] a) S. Reineke, F. Lindner, G. Schwartz, N. Seidler, K. Walzer, B. Lüssem, K. Leo, *Nature* **2009**, *459*, 234; b) D. Y. Kondakov, *J. Soc. Inf. Disp.* **2009**, *17*, 137; c) D. Di, L. Yang, J. M. Richter, L. Meraldi, R. M. Altamimi, A. Y. Alyamani, D. Credgington, K. P. Musselman, J. L. MacManus-Driscoll, R. H. Friend, *Adv. Mater.* **2017**, *29*, 1605987; d) B. Y. Lin, C. J. Easley, C. H. Chen, P. C. Tseng, M. Z. Lee, P. H. Sher, J. K. Wang, T. L. Chiu, C. F. Lin, C. J. Bardeen, and J. H. Lee, *ACS Appl. Mater. Interfaces* **2017**, *9*, 10963; e) J. Y. Hu, Y. J. Pu, F. Satoh, S. Kawata, H. Katagiri, H. Sasabe, J. Kido, *Adv. Funct. Mater.* **2014**, *24*, 2064; f) Q. Wei, N. Fei, A. Islam, T. Lei, L. Hong, R. Peng, X. Fan, L. Chen, P. Gao, Z. Ge, *Adv. Opt. Mater.* **2018**, *6*, 1800512; g) R. Hamze, J. L. Peltier, D. Sylvinson, M. Jung, J. Cardenas, R. Haiges, M. Soleilhavoup, R. Jazzar, P. I. Djurovich, G. Bertrand, M. E. Thompson, *Science* **2019**, *363*, 601.

[5] a) C. W. Tang, S. A. Van Slyke, *Appl. Phys. Lett.* **1987**, *51*, 913; b) R. H. Friend, R. W. Gymer, A. B. Holmes, J. H. Burroughes, R. N. Marks, C. Taliani, D. D. C. Bradley, D. A. Dos Santos, J. L. Bredas, M. Logdlund, W. R. Salaneck, *Nature* **1999**, *397*, 121; c) M. A. Baldo, D. F. O'Brien, Y. You, A. Shoustikov, S. Sibley, M. E. Thompson, S. R. Forrest, *Nature* **1998**, *395*, 151; d) M. A. Baldo, M. E. Thompson, S. R. Forrest, *Nature* **2000**, *403*, 750.

[6] a) M. Y. Wong, E. Zysman-Colman, *Adv. Mater.* **2017**, *29*, 1605444; b) Z. Yang, Z. Mao, Z. Xie, Y. Zhang, S. Liu, J. Zhao, J. Xu, Z. Chi, M. P. Aldred, *Chem. Soc. Rev.* **2017**, *46*, 915; c) Y. Im, M. Kim, Y. J. Cho, J.-A. Seo, K. S. Yook, J. Y. Lee, *Chem. Mater.* **2017**, *29*, 1946; d) H. Uoyama, K. Goushi, K. Shizu, H. Nomura, C. Adachi, *Nature* **2012**, *492*, 234; e) F. B. Dias, K. N. Bourdakos, V. Jankus, K. C. Moss, K. T. Kamtekar, V. Bhalla, J. Santos, M. R. Bryce, A. P. Monkman, *Adv. Mater.* **2013**, *25*, 3707; f) Q. Zhang, B. Li, S. Huang, H. Nomura, H. Tanaka, C. Adachi, *Nat. Photonics* **2014**, *8*, 326.

[7] a) H. Nakanotani, T. Higuchi, T. Furukawa, K. Masui, K. Morimoto, M. Numata, H. Tanaka, Y. Sagara, T. Yasuda, C. Adachi, *Nat. Commun.* **2014**, *5*, 4016; b) Y. J. Cho, B. D. Chin, S. K. Jeon, J. Y. Lee, *Adv. Funct. Mater.* **2015**, *25*, 6786; c) W. Song, J. Y. Lee, *Adv. Opt. Mater.* **2017**, *5*, 1600901; d) L. S. Cui, H. Nomura, Y. Geng, J. U. Kim, H. Nakanotani, C. Adachi, *Angew. Chem. Int. Ed.* **2017**, *56*, 1571; e) T.-A. Lin, T. Chatterjee, W.-L. Tsai, W.-K. Lee, M.-J. Wu, M. Jiao, K.-C. Pan, C.-L. Yi, C.-L. Chung, K.-T. Wong, C.-C. Wu, *Adv. Mater.* **2016**, *28*, 6976.

[8] a) S. Kuila, S. Garain, S. Bandi, S. J. George, *Adv. Funct. Mater.* **2020**, 2003693; b) P. L. Dos Santos, J. S. Ward, D. G. Congrave, A. S. Batsanov, J. Eng, J. E. Stacey, T. J. Penfold, A. P. Monkman, M. R. Bryce, *Adv. Sci.* **2018**, *5*, 1700989.

[9] a) F. J. Ramos, K. Rakstys, S. Kazim, M. Grätzel, M. K. Nazeeruddin, S. Ahmad, *RSC Adv.* **2015**, *5*, 53426; b) K. Rakstys, A. Abate, M. I. Dar, P. Gao, V. Jankauskas, G. Jacopin, E. Kamarauskas, S. Kazim, S. Ahmad, M. Grätzel, M. K. Nazeeruddin, *J. Am. Chem. Soc.* **2015**, *137*, 16172; c) A. Connell, Z. Wang, Y.-H. Lin, P. C. Greenwood, A. A. Wiles, E. W. Jones, L. Furnell, R. Anthony, C. P. Kershaw, G. Cooke, H. J. Snaith, P. J. Holliman, *J. Mater. Chem. C* **2019**, *7*, 5235; d) X.-C. Li, C.-Y. Wang, W.-Y. Lai, W. Huang, *J. Mater. Chem. C* **2016**, *4*, 10574; e) K.-H. Lin, A. Prlj, C. Corminboeuf, *J. Phys. Chem. C* **2017**, *121*, 21729.

[10] W. Z. Yuan, X. Y. Shen, H. Zhao, J. W. Y. Lam, L. Tang, P. Lu, C. Wang, Y. Liu, Z. Wang, Q. Zheng, J. Z. Sun, Y. Ma, B. Z. Tang, *J. Phys. Chem. C* **2010**, *114*, 6090.

[11] The percentages indicate relative contributions of the prompt and delayed emission components.

[12] a) H. F. Higginbotham, P. Pander, R. Rybakiewicz, M. K. Etherington, S. Maniam, M. Zagorska, A. Pron, A. P. Monkman, P. Data, *J. Mater. Chem. C* **2018**, *6*, 8219; b) S. Kuila, A. Ghorai, P. K. Samanta, R. B. K. Siram, S. K. Pati, K. S. Narayan and S. J. George, *Chem. Eur. J.* **2019**, *25*, 16007; c) X.-K. Chen, Y. Tsuchiya, Y. Ishikawa, C. Zhong, C. Adachi, J.-L. Brédas, *Adv. Mater.* **2017**, *29*, 1702767.

[13] P. K. Samanta, D. Kim, V. Coropceanu, J.-L. Brédas, *J. Am. Chem. Soc.* **2017**, *139*, 4042.

[14] Similar lifetime-profile exciting at locally-excited wavelength (below 330 nm) could not be as we do not have excitation-source at this region.

[15] a) J. Gibson, A. P. Monkman, T. J. Penfold, *ChemPhysChem* **2016**, *17*, 2956; b) M. K. Etherington, J. Gibson, H. Higginbotham, T. J. Penfold, A. P. Monkman, *Nat. Commun.* **2016**, *7*, 13680; c) H. Noda, X.-K. Chen, H. Nakanotani, T. Hosokai, M. Miyajima, N. Notsuka, Y. Kashima, J.-L. Brédas, C. Adachi, *Nat. Mater.* **2019**, *18*, 1084; d) J. U. Kim, I. S. Park, C.-Y. Chan, M. Tanaka, Y. Tsuchiya, H. Nakanotani, C. Adachi, *Nat. Commun.* **2020**, *11*, 1765.

[16] a) P. L. dos Santos, J. S. Ward, M. R. Bryce, A. P. Monkman, *J. Phys. Chem. Lett.* **2016** *7*, 3341; b) T. Chatterjee, K.-T. Wong, *Adv. Optical Mater.* **2019**, *7*, 1800565; c) G. Méhes, K. Goushi, W. J. Potscavage, C. Adachi, *Org. Electron.* **2014**, *15*, 2027.

[17] The triplet stability of **TAT-NMI** in air was very poor and no delayed emission lifetime could be obtained in aerated conditions, unlike the previous molecules **TAT-3BP** and **TAT-3TRZ**.

[18] C. Baleizão, M. N. Berberan-Santos, *J. Chem. Phys.* **2007**, *126*, 204510.

[19] a) K. Goushi, K. Yoshida, K. Sato, C. Adachi, *Nat. Photonics* **2012**, *6*, 253; b) K. Nasu, T. Nakagawa, H. Nomura, C.-J. Lin, C.-H. Cheng, M.-R. Tseng, T. Yasuda, C. Adachi, *Chem. Commun.* **2013**, *49*, 10385; c) C. F. Madigan, V. Bulović, *Phys. Rev. Lett.* **2003**, *91*, 247403.

[20] The increase we see is under vacuum conditions is directly proportional to the total delayed fluorescence emission as no RTP component was observed in the molecule. The calculated DF percentage was 30 % (~1.4 fold increase in the steady-state emission under vacuum, see Figure 6.11a) in the total emission.

[21] a) D.-H. Kim, A. D'Aléo, X.-K. Chen, A. D. S. Sandanayaka, D. Yao, L. Zhao, T. Komino, E. Zaborova, G. Canard, Y. Tsuchiya, E. Choi, J. W. Wu, F. Fages, J.-L. Brédas, J.-C. Ribierre, C. Adachi, *Nat. Photonics* **2018**, *12*, 98; b) T. Hatakeyama, K. Shiren, K. Nakajima, S. Nomura, S. Nakatsuka, K. Kinoshita, J. Ni, Y. Ono, T. Ikuta, *Adv. Mater.* **2016**, *28*, 2777; c) A. Pershin, D. Hall, V. Lemaire, J.-C. Sancho-Garcia, L. Muccioli, E. Zysman-Colman, D. Beljonne, Y. Olivier, *Nat. Commun.* **2019**, *10*, 597.

[22] a) T. Bura, N. Leclerc, S. Fall, P. Lévêque, T. Heiser, R. Ziessel, *Org. Lett.* **2011**, *13*, 6030; b) T. Bura, N. Leclerc, R. Bechara, P. Lévêque, T. Heiser, R. Ziessel, *Adv. Energy Mater.* **2013**, *3*, 1118.

CURRICULUM VITAE



Suman was born on February 25th, 1992 in a small village, named Ramchandrapur in a coastal district (Purba Medinipur) of West Bengal, India. He completed B.Sc. with a First Class division (Honours in Chemistry) from St. Paul's Cathedral Mission College (University of Calcutta), Kolkata in 2012. He subsequently joined in the School of Chemistry, University of Hyderabad, Hyderabad the same year and obtained a M.Sc. degree in Chemistry in 2014. Since August 2014, he is a PhD student (with a research fellowship from *University Grants Commission*, Govt. of India) at the Supramolecular Chemistry Laboratory, New Chemistry Unit, JNCASR, Bangalore under the supervision of Prof. Subi J. George. In July 2018, he was selected to deliver a talk (with a generous funding from the organizers) in the 24th International Conference on Science and Technology of Synthetic Metals (**ICSM-2018**) held in Busan, South Korea. In the following year, he attended 15th International Conference on Organic Electronic (**ICOE-2019**) at Hasselt University, Belgium (June, 2019) with the generous travel grant from JNCASR and awarded with a *best poster presentation*. His research work at Supramolecular Chemistry Laboratory has been focused on developing molecular systems towards harvesting the triplet excitons of purely organic chromophores via room temperature phosphorescence and thermally activated delayed fluorescence. The most important results of this work are presented in this thesis.

LIST OF PUBLICATIONS

From Thesis:

1. All-Organic, Temporally Pure White Afterglow in Amorphous Films Using Complementary Blue and Greenish-Yellow Ultralong Room Temperature Phosphors, **S. Kuila**,⁺ S. Garain,⁺ S. Bandi and S. J. George, *Adv. Funct. Mater.* **2020**, 2003693 (DOI: 10.1002/adfm.202003693. ⁺ contributed equally).
2. Phosphorescence Energy Transfer: Ambient Afterglow Fluorescence from Water-Processable and Purely Organic Dyes via Delayed Sensitization, **S. Kuila** and S. J. George, *Angew. Chem. Int. Ed.* **2020**, 59, 9393.
3. Aqueous Phase and Amorphous State Room Temperature Phosphorescence from a Small Aromatic Carbonyl Derivative, **S. Kuila**, S. Garain, M. Eswaramoorthy and S. J. George, *Mat. Res. Exp.* **2019**, 6, 124003.
4. Red-Emitting Delayed Fluorescence and Room Temperature Phosphorescence from Core-Substituted Naphthalene Diimides, **S. Kuila**, A. Ghorai, P. K. Samanta, R. B. K. Siram, S. K. Pati, K. S. Narayan and S. J. George, *Chem. Eur. J.* **2019**, 25, 16007.
5. Aqueous Phase Phosphorescence: Ambient Triplet Harvesting of Purely Organic Phosphors via Supramolecular Scaffolding, **S. Kuila**, K. V. Rao, S. Garain, P. K. Samanta, S. Das, S. K. Pati, M. Eswaramoorthy and S. J. George, *Angew. Chem. Int. Ed.* **2018**, 57, 17115. (**hot paper**).
6. Colour-tunable Room Temperature Phosphorescence (RTP) from Heavy-atom Substituted Crystalline Carbazoles, **S. Kuila**, S. Roy, P. K. Samanta, J. Mondal, A. De, S. C. Peter and S. J. George, (manuscript under review).
7. Water-processable Afterglow Emission from Dicationic Coronenebisimide, **S. Kuila**, S. Garain and S. J. George, (manuscript under preparation).
8. Activating Dual-state Thermally Activated Delayed Fluorescence and Room Temperature Phosphorescence from Core-substituted Pyromellitic Diimides, **S. Kuila**, G. Barappanavar, S. Garain, B. Garain, S. K. Pati, D. Kabra and S. J. George, (manuscript under preparation).
9. Colour-tunable Thermally Activated Delayed Fluorescence and Room Temperature Phosphorescence from Charge-transfer Triazatruxene Derivatives, **S. Kuila**, S. Bandi and S. J. George, (manuscript under preparation).

Other Publications:

10. Room Temperature Phosphorescence from Heavy-atom Free Benzophenone Boronic Ester Derivatives, S. Garain, **S. Kuila**, A. Sinhababu and S. J. George, *Bull. Mater. Sci.* (Manuscript Accepted).
11. Highly Efficient Orange-red Room Temperature Phosphorescence from Heavy-atom Substituted Pyromellitic Diimides, S. Garain, **S. Kuila**, B. Garain, M. Kataria, A. Borah, S. K. Pati and S. J. George, (manuscript under preparation).
12. Anion- π Emission from Core-substituted Naphthalene Diimide Derivatives, S. Garain, A. Sarkar, **S. Kuila**, S. Das, S. K. Pati and S. J. George, (manuscript under preparation).
13. Recent Advances on the Metal-free Amorphous Afterglow Materials, **S. Kuila** and S. J. George, (Manuscript under Preparation).

14. Solution-State Room Temperature Phosphorescence: A Supramolecular Self-Assembly Approach, S. Garain,⁺ **S. Kuila**,⁺ and S. J. George, (Invited Review under preparation,⁺ contributed equally).

